Dissertation
submitted to the
Combined Faculties of the Mathematics, Engineering and Natural Sciences
of the Ruperto-Carola-University of Heidelberg, Germany,
for the degree of
Doctor of Natural Sciences

Put forward by
Siddhant A. Deshmukh
born in Warrington, United Kingdom

Oral examination: October 26th, 2023

Modelling Non-Equilibrium Molecular Formation and Dissociation for the Spectroscopic Analysis of Cool Stellar Atmospheres

Referees:
Priv. Doz. Dr. Hans-Günter Ludwig
Priv. Doz. Dr. Andreas Koch-Hansen

Examiners:
Priv. Doz. Dr. Hans-Günter Ludwig
Priv. Doz. Dr. Andreas Koch-Hansen
Prof. Dr. Matthias Bartelmann
Prof. Dr. Saskia Hekker

ABSTRACT

Modelling techniques for stellar atmospheres are undergoing continuous improvement. In this thesis, I showcase how these methods are used for spectroscopic analysis and for modelling time-dependent molecular formation and dissociation. I first use CO^{5}BOLD model atmospheres with the LINFOR3D spectrum synthesis code to determine the photospheric solar silicon abundance of 7.57 ± 0.04. This work also revealed some issues present in the cutting-edge methods, such as synthesised lines being overly broadened. Next, I constructed a chemical reaction network in order to model the time-dependent evolution of molecular species in (carbon-enhanced) metal-poor dwarf and red giant atmospheres, again using CO^{5}BOLD. This was to test if the assumption of chemical equilibrium, widely assumed in spectroscopic studies, was still vaild in the photospheres of metal-poor stars. Indeed, the mean deviations from chemical equilibrium are below 0.2 dex across the spectroscopically relevant regions of the atmosphere, though deviations increase with height. Finally, I implemented machine learning methods in order to remove noise and line blends from spectra, as well as to predict the equilibrium state of a chemical reaction network. The methods used and developed in this thesis illustrate the importance of both conventional and machine learning modelling techniques, and merge them to further improve accuracy, precision, and efficiency.

ZUSAMMENFASSUNG

Die Modellierungstechniken für Sternatmosphären werden ständig verbessert. In dieser Arbeit zeige ich, wie diese Methoden für die spektroskopische Analyse und zur Modellierung der zeitabhängigen Molekularformation und -dissoziation benutzt werden. Ich habe zuerst CO^{5}BOLD -Modellatmosphären mit dem LINFOR3D -Spektrumsynthesecode verwendet, um die photosphärische solare Siliziumhäufigkeit von 7.57 ± 0.04zu bestimmen. Diese Untersuchung wurden auch einige Probleme der modernsten Methoden aufgedeckt, wie z. B. synthetische Linien übermäßig verbreitert werden. Als nächstes habe ich ein chemisches Reaktionsnetzwerk konstruiert, um die zeitabhängige Entwicklung der molekularen Spezies in (kohlenstoffverstärkten) metallarmen Zwergen- und Roten-Riesen-Atmosphären zu modellieren, wiederum unter Verwendung von CO^{5}BOLD. Diese sollte getestet werden, ob die Annahme eines chemischen Gleichgewichts, die in spektroskopischen Studien angenommen wird, in den Photosphären metallarmer Sterne noch gültig ist. In der Tat liegen die mittleren Abweichungen vom chemischen Gleichgewicht in den spektroskopisch relevanten Regionen der Atmosphäre unter $0,2$ dex in den spektroskopisch relevanten Bereichen der Atmosphäre, obwohl die Abweichungen mit der Höhe zunehmen. Schließlich habe ich Methoden des maschinellen Lernens eingesetzt, um Rauschen und Linienmischungen aus den Spektren zu entfernen sowie den Gleichgewichtszustand eines chemischen Reaktionsnetzwerks vorherzusagen. Die in dieser Arbeit verwendeten und entwickelten Methoden illustrieren die Bedeutung sowohl konventioneller als auch maschineller Lernverfahren für die Modellierungstechniken und führen sie zusammen, um die Genauigkeit, Präzision und Effizienz.

ACKNOWLEDGMENTS

There are have been many people who have helped me over the past few years, and to whom I owe my thanks.

Firstly, I would like to thank the Landessternwarte (LSW) of the Universität Heidelberg for providing me with the opportunity to pursue a doctoral degree in Astronomy and Astrophysics. Particular thanks goes of course to my supervisor, Dr. Hans-Günter Ludwig, for his limitless patience, care, and many insightful comments over the years. Thank you for teaching me what it means to be a scientist. I would also like to thank Dr. Norbert Christlieb and Dr. Stefan Jordan, both of whom were valuable points of guidance throughout the process. Additionally, I extend my thanks to the staff at the LSW, University, and Max-Planck-Institute for Astronomy, who made me feel welcome here in Heidelberg. I would like to thank the Stars group for many fruitful discussions, specifically to Jeffrey Gerber, Matthew Gent, and Guillaume Guiglion.

I would like to thank all of the members of my Committee by taking the time to read this thesis and express their judgement.

I would like to thank Elan Gin and Jeremy Carter, both of whom believed in me at an early age, and set me upon this incredible journey. I know for sure that this would have been impossible without your guidance. Similarly, I would like to thank Sean Matt and Adam Finley for guiding me throughout my undergradute studies.

I would also like to thank the wonderful friends I have made and retained throughout my life. I have met many fantastic peers as part of the IMPRS-HD program; from my generation, I would like to thank Nicolás Kurtovic, Timmy Delage, Matthew Gent, Arvind Hughes, and Riccardo Franceschi, all of whom have been extremely supportive throughout my time here. And generally, thank you to everyone who partook in Mittwochskultur.

Special thanks goes out to the sci-an team for a great entry into the startup world: Oliver Völkel, Jacob Isbell and Tobias Moldenhauer. From the long nightly discussions in Munich trams to scrambling for tight deadlines, it has been a fantastic time. I would like to extend my thanks to the MAX!mize incubator programme that made it possible to fund this project while I worked there.

I would like to thank the members of Turbo Normal for helping me keep sane through music and good times, despite The Curse. To David Fuksman, Antoine Dumont, Marten Scheuck, Gabriele Pichierri, Jacob Isbell, Riccardo Franceschi and Oliver Völkel, thank you all.

Thinking further back, I would like to thank all the friends who have supported me since my undergraduate days and beyond. To Jacque Dieu and Harry Coad, my old housemates, I hope the adventure never ends. And in another sense of that word, I hope for the same with Sammy Colburn, Daniel Gardener, Sebastian Treacy, and Henry Holmes, as well. I would like to thank James Ashford for useful discussions throughout the years, particularly in the field of machine learning. Looking even further back, I would like to extend my gratitude to Sam Sadow, Aditya Peri, and others – it's crazy to think how quickly the years have flown by.

Finally, none of this would have been possible without the support of my family, particularly my parents Avinash and Himagauri Deshmukh. Thank you for your unending support and love throughout these years.

CONTENTS

Part I

BACKGROUND

OUTLINE

This thesis is divided into four parts. This first part, "Background", lays the foundation for the work. A concise summary of the analysis of stellar atmospheres is given in Chap. 1, which is laid out similar to a review. Chaps. 2 and 3 are based on published work (Deshmukh and Ludwig, 2023; Deshmukh et al., 2022). Chaps. 4,5, and 6 are based on work I conducted during my PhD, and are not yet published. Chap. 7 is a review of the work presented in this thesis.

The second part of the work focuses on using conventional techniques for modelling stellar atmospheric properties. Chap. 2 presents an end-to-end analysis of the determination of the photospheric solar silicon abundance according to the stellar atmosphere code `CO5BOLD` and the spectrum synthesis code `LINFOR3D`. It further explores the various shortcomings of these kinds of codes in general, and presents investigations on potential improvements for future works. This chapter is based on the work appearing in Deshmukh et al. (2022).

Chap. 3 shows the effects of the assumption of chemical equilibrium in the atmospheres of metal-poor and carbon enhanced metal-poor dwarf stellar atmospheres by considering the interplay between chemical kinetics and hydrodynamics. It also introduces a graph theoretical perspective to analyse chemical reaction networks. This chapter is based on the work appearing in Deshmukh and Ludwig (2023).

Chap. 4 extends this methodology to the atmospheres of metal-poor giant stars and explores a novel way to determine the state of chemical equilibrium in a given stellar atmosphere. Chaps. 3 and 4 are directly linked in that the same kind of analysis is performed in different astrophysical contexts, and the results can be directly compared.

The third part explores the use of machine learning techniques for modelling the properties of stellar atmospheres. Chap. 5 showcases the attempts to leverage machine learning algorithms to improve the quality of spectroscopic data. Chap. 5 contains direct links to Chap. 2 in terms of the observational material and the context.

Chap. 6 introduces a novel method of utilising neural networks to speed up chemical kinetics calculations and demonstrates the advantages for the model atmospheres presented in Chaps. 3 and 4. The methodologies in terms of machine learning techniques are similar to those encountered in Chap. 5.

Finally, the fourth part, containing Chap. 7, summarises the key takeaways of this work and presents an outlook on promising future work.

1 STARS AND THEIR ATMOSPHERES

1.1 THE STUDY OF STELLAR ATMOSPHERES

The atmosphere of a star is the region between its core and the interstellar medium (ISM) (Hubeny and Mihalas, 2015). Energy is generated by nuclear fusion in the stellar core, and this energy is transported via conduction, convection, radiation and neutrinos throughout the star, before it finally escapes into the ISM. This energy then propagates through the Universe before being, for example, observed by a species on a life-sustaining planet orbiting one of these luminous objects. What can we learn from observing such an object?

Generally, we do not observe a star's core, but its atmosphere. We would like to know certain intrinsic properties of stars, such as their mass and chemical composition, in order to better understand their evolution; in a broader sense, to understand the evolution of our Universe. However, Mother Nature does not allow us to inspect these properties directly. We must instead make do with observed properties such as the star's luminosity. Various techniques have been developed and refined over the years to better probe these measurements, including photometry and spectroscopy.

1.1.1 *Why model stellar atmospheres?*

The aim of modelling stellar atmospheres comes from the motivation to understand observations of stellar objects. The electrmagnetic (EM) spectrum of a star sheds light on properties such as its temperature, surface gravity, and chemical composition (Gray, 2008). Quantitative spectroscopic analysis allows for greater understanding of the various physical processes that led to the formation of such a spectrum. It is imperative, then, to construct accurate and precise stellar models that result in model spectra that can be compared with observations. Since the scientist is in full control of the parameters of the model, such as the elemental abundances that it is seeded with, the properties of distant stars can be inferred through comparison to a range of astrophysical models.

The evolution of chemical elements in our Universe proceeds in the interiors of stars through stellar nucleosynthesis. Fusion products are eventually brought up (through various pathways) into the stellar atmosphere, and later deposited into the ISM. These fingerprints of chemical evolution are readily present in the atmospheres of stars, and by piecing together our other knowledge about the objects in question, large-scale trends of Galactic chemical evolution can be studied. In short, then, the study of stellar atmospheres involves the quantitative study of stellar spectra, which yields a host of information about the star's properties. The focus in this study is on stellar chemical compositions, developing and improving upon modelling techniques, understanding the implications of various assumptions made in the modelling phase, such as assumptions relating to thermodynamic equilibrium.

1.1.2 *Energy transport*

In order to better understand systems out of thermodynamic equilibrium, we will first detail the primary mechanisms of energy transport in stars. Generally, energy is trans-

ferred through conduction, convection, radiation, or by neutrinos (Hansen, Kawaler, and Trimble, 2004). In cool stellar atmospheres, conduction is relatively inefficient, neutrinos account for just a few percent of energy loss from nuclear reactions, and so energy is transferred primarily via convection and radiation (Hubeny and Mihalas, 2015). Typically, convection is the primary mode of energy transport when the material is very opaque or when large temperature gradients exist (see Sec. 1.2 for a more detailed look at which transport mechanisms are dominant in various stars). We can follow a straightforward line of reasoning to determine where convection is possible.

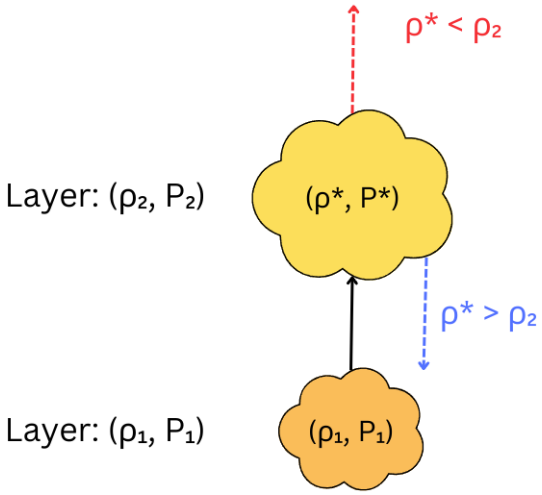

Figure 1: Diagram of a parcel of gas undergoing basic convection.

Consider a parcel of gas in a stratified atmosphere that is displaced from a point with density ρ_1 and pressure P_1 to a point with density ρ_2 and pressure P_2 (Fig. 1). Let the conditions in the parcel after the displacement be its density ρ_* and its pressure P_*. If the parcel is sufficiently large and its displacement is significantly less than the local sound speed, pressure changes equalise at the speed of sound, so $P_* = P_2$, and heat flow is adiabatic inside of the parcel. We therefore need only compare the densities ρ_* and ρ_2 to determine the immediate future motion of the parcel. If $\rho_* < \rho_2$, the parcel is unstable against convection and will continue to rise. If $\rho_* \geqslant \rho_2$, the parcel is stable against convection and will sink back down. We can extend this logic to determine which parts of an atmosphere will be unstable against convection.

For an adiabatic process,

$$\frac{dP}{P} = -\gamma \frac{dV}{V}, \tag{1}$$

where γ is the adiabatic index for an ideal gas [1] and V is the specific volume $V = \frac{1}{\rho}$. Therefore, $dV = -\frac{1}{\rho^2} d\rho$, leading to

$$\frac{dV}{V} = -\frac{d\rho}{\rho}. \tag{2}$$

Substituting for the right-hand side of Eq. 1, we arrive at

$$\frac{dP}{P} = \gamma \frac{d\rho}{\rho}, \tag{3}$$

1 More generally, the definition $\Gamma_1 = \left(\frac{\partial \ln(P)}{\partial \ln(\rho)}\right)_s$ is used, with s as the entropy, and is more general as the definition $\gamma = c_P/c_V$ is specific to ideal gases (where $\Gamma_1 = \gamma$). In the model atmosphere code CO5BOLD , the general definition of Γ_1 is used, though the case of an ideal gas is considered in this example for simplicity.

which directly rates the change in pressure to the change in density. As $\frac{dx}{x} = d\ln(x)$,

$$\frac{d\ln(P)}{d\ln(\rho)} = \gamma. \tag{4}$$

We can now compare the the lograithmic gradients of pressure with respect to density in the star $\left(\frac{d\ln(P)}{d\ln(\rho)}\right)_{star}$ to the adiabatic case $\left(\frac{d\ln(P)}{d\ln(\rho)}\right)_{ad}$. Stability against convection is achieved when the gradient in the star is less steep than in the adiabatic case, that is

$$\left(\frac{d\ln(P)}{d\ln(\rho)}\right)_{star} < \left(\frac{d\ln(P)}{d\ln(\rho)}\right)_{ad}. \tag{5}$$

However, as we are dealing with stellar atmospheres, it will be useful to restate this in terms of the temperature T. Stellar atmospheres are composed of ideal gases (Hubeny and Mihalas, 2015; Maoz, 2016), whose equation of state is given by

$$P = \frac{N_A k_B}{\mu}\rho T, \tag{6}$$

where $N_A = 6.02214076 \times 10^{23}\ \mathrm{mol}^{-1}$ is Avogadro's number, $k_B = 1.380649 \times 10^{-23}\ \mathrm{J\,K}^{-1}$ is the Boltzmann constant, and μ is the mean molecular weight. Differentiating Eq. 6 and dividing through by the original expression, we arrive at the relation

$$\frac{dP}{P} = \frac{dT}{T} + \frac{d\rho}{\rho}. \tag{7}$$

Using Eq. 3 and rearranging, we arrive at

$$\frac{dT}{T} = \frac{dP}{P}\left(\frac{\gamma - 1}{\gamma}\right), \tag{8}$$

which leads to the expression for the adiabatic gradient

$$\nabla_{ad} \equiv \frac{d\ln(T)}{d\ln(P)} = \frac{\gamma - 1}{\gamma}. \tag{9}$$

As in the case of Eq. 5, stablity against convection is achieved when

$$\left(\frac{d\ln(T)}{d\ln(P)}\right)_{star} < \left(\frac{d\ln(T)}{d\ln(P)}\right)_{ad}. \tag{10}$$

In more convenient notation:

$$\frac{d\ln(T)}{d\ln(P)} < \nabla_{ad}. \tag{11}$$

If the gradient $\frac{d\ln(T)}{d\ln(P)}$ ever exceeds $\frac{\gamma-1}{\gamma}$ ($= \frac{2}{5}$ for an ideal monatomic gas), convection will commence. Steep temperature gradients therefore cause the material to become convectively unstable, and convection sets in to flatten the temperature gradient. In the Sun, these are primarily seen in the atmosphere above the nuclear-burning core.

Nuclear reactions in the core, such as the proton-proton (p-p) chain and the CNO cycle release energy as radiation and neutrinos. In the Sun, energy is primarily transported via radiation in the core, as the temperature gradient is not steep enough for convection to occur (Kippenhahn, Weigert, and Weiss, 2012), and radiation transport becomes increasingly important in the higher, optically thin atmospheric layers (Hubeny

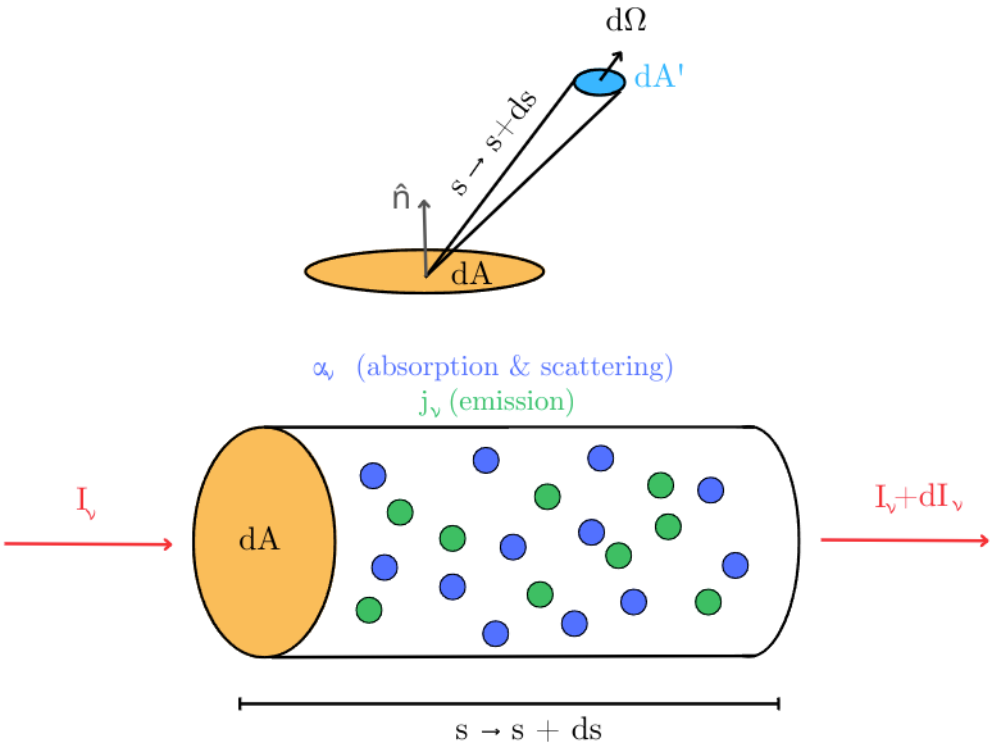

Figure 2: Geometry of the basic radiative transfer problem (top) and the beam of intensity I_ν shining through a medium containing particles capable of absorption, scattering, and emission (bottom).

and Mihalas, 2015). As we are primarily interested in stellar atmospheres, let us consider the general transport of energy via radiation from a bright source shining through a medium, as in Fig. 2.

Consider photons with frequencies in the range ν to $\nu + d\nu$ flowing from dA to dA'. The energy flow is given by

$$dE_\nu = I_\nu(\Omega) d\Omega dt d\nu \hat{n} \Omega dA, \tag{12}$$

where $I_\nu(\Omega)$ is the monochromatic specific intensity (W m^{-2} $ster^{-1}$ Hz^{-1}), $\hat{n}$ is the normal unit vector, Ω and Ω is the solid angle (see again Fig. 2 for a visual explanation). We define the mean intensity

$$J_\nu = \frac{1}{4\pi} \oint I_\nu(\Omega) d\Omega. \tag{13}$$

If the radiation field is isotropic, spherical symmetry ensures $J_\nu = I_\nu$. Consider the material that the photons pass through to be capable of absorbing and scattering radiation within the relevant energy window (Fig. 2). The cross-section presented to the photon beam of unit area of material with a thickness ds is $n\sigma_\nu ds$, where n is the number density of absorbers and σ_ν is their cross-section. This expression is equivalent to the probability of absorption or scattering. We can now define the absorption coefficient (cross-section per unit volume) as

$$\alpha_\nu = n\sigma_\nu \tag{14}$$

and the specific opacity

$$\kappa_\nu = \frac{n\sigma_\nu}{\rho} = \frac{\alpha_\nu}{\rho}, \tag{15}$$

where ρ is the mass density. The photon mean free path is given by

$$\lambda_\nu = \frac{1}{\alpha_\nu}. \tag{16}$$

Conventional distance is not a good measure for these kinds of events, as we require a measure that characterises the extent to which a photon can travel freely, that is, without being absorbed. We therefore define the optical depth τ_ν:

$$\tau_\nu = \int_{s_1}^{s_2} \alpha_\nu \, ds \tag{17}$$

which leads to

$$d\tau_\nu = \alpha_\nu \, ds. \tag{18}$$

The optical depth contains contributions from physical distance as well as the effect of absorbers, thereby naturally representing the opacity. When $\tau >> 1$, the material is said to be optically thick, meaning that many absorption and scattering events occur, so photons do not travel freely through the medium. In contrast, when $\tau << 1$, the material is said to be optically thin, meaning it is extremely unlikely for a single photon to undergo multiple scattering or absorption events, and hence photons can propagate more-or-less freely through the medium. As a simple, terrestrial example, opaque clouds are optically thick, while translucent ones are optically thin. On a foggy day, if you can see the silhouette of the Sun, the fog cannot be optically thick. The stellar photosphere is a region of transition from the deeper, optically thick layers, to the higher, optically thin ones; Secs. 1.4.2 and 1.4.2.1 go into further detail on why this complicates the treatment of radiation transfer.

The loss in intensity as the beam travels through the medium due to absorption and scattering events in terms of the optical depth is therefore

$$I_\nu(\Omega)\alpha_\nu \, ds = I_\nu(\Omega) d\tau_\nu. \tag{19}$$

In stellar atmospheres, the material can also produce radiation that adds to the photon beam. We define the volume emissivity j_ν (W m^{-3} ster^{-1} Hz^{-1}) as the energy emitted per unit time, volume, frequency and solid angle. Note that the exact properties of j_ν and α_ν will depend on atomic physics (see Sec. 1.1.4.1) . The amount of radiation added to the beam as it passes through a distance ds due to emission is simply $j_\nu ds$.

Overall, the radiation transport equation combines these processes of absorption, scattering, and radiation as the photon beam passes through the medium of thickness ds:

$$\frac{dI_\nu}{ds} = \left(\frac{dI_\nu}{ds}\right)_{\text{absorption}} + \left(\frac{dI_\nu}{ds}\right)_{\text{scattering}} + \left(\frac{dI_\nu}{ds}\right)_{\text{emission}}. \tag{20}$$

Substituting the expressions for absorption and emission above leads to

$$\frac{dI_\nu}{d\tau_\nu} = -\alpha_\nu I_\nu + j_\nu, \tag{21}$$

and after rewriting in terms of the optical depth $d\tau_\nu = \alpha_\nu ds$, we arrive at the familiar form

$$\frac{dI_\nu}{d\tau_\nu} = -I_\nu + \frac{j_\nu}{\alpha_\nu}. \tag{22}$$

The last term on the right-hand side is commonly referred to as the source function

$$S_\nu = \frac{j_\nu}{\alpha_\nu} \tag{23}$$

as it characterises the properties of the source material. Further details of the implementation of radiation transport in stellar atmosphere codes is presented in Sec. 1.4.2.

1.1.3 *Atmospheric layers*

The stellar atmosphere contains many layers: starting from the inside and moving outwards, the layers are the photosphere, the chromosphere, the transition region and the corona. We will explore these layers from the perspective of the solar atmosphere, which we can directly observe and which we understand much better compared to distant stars.

The photosphere is the deepest and coolest region of the atmosphere that is still transparent to many photons that travel outwards from the core. The bottom of the photosphere is defined to be where the plasma ceases to be opaque, allowing photons to pass through it and other layers of the atmosphere. The photosphere is typically used to define a star's visual surface. While the temperature can vary by a few thousand Kelvin throughout the photosphere, the effective temperature is used to characterise its temperature with respect to a blackbody. The stellar photosphere contains many phenomena that stem from the interplay between convection, magnetic fields and radiation transfer. The most common phenomena are granules – convection cells with rising hot plasma in their centre and falling cool plasma in the intergranular lanes. In the Sun, we can actually observe the granulation pattern with state-of-the-art telsecopes (Bahng and Schwarzschild, 1961). We generally observe spectral lines from absorption processes in the photosphere (see Sec. 1.1.4).

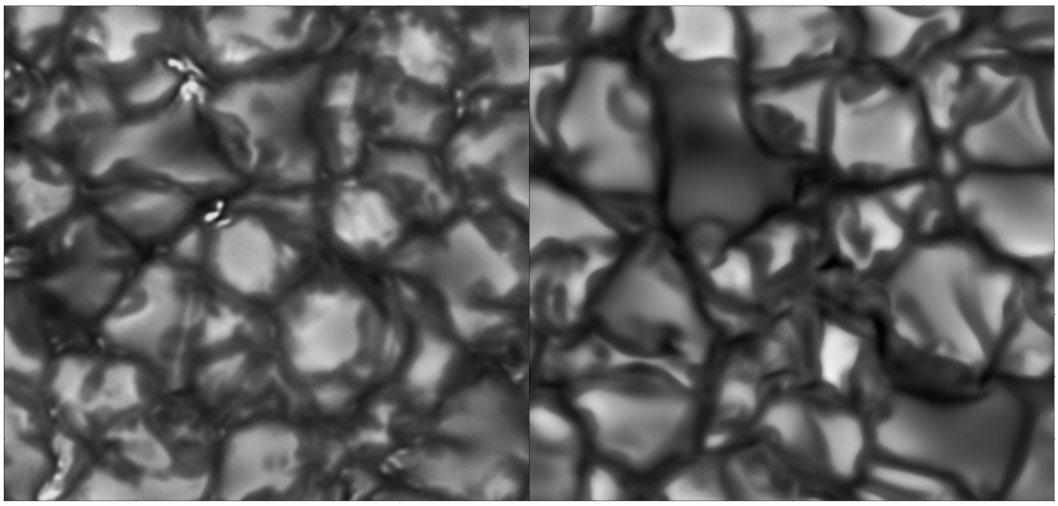

Figure 3: A comparison of solar granulation pattern in emergent intensity observed with the Swedish Solar Telescope (left) and the numerical simulation (right). Both images have a scale of 6 Mm $\times$6 Mm. Original: Fig 1.2 from Magic (2014)

Other phenomena include supergranules, which carry magnetic field bundles to convection cell edges, starspots, which are darker, cooler regions of concentrated magnetic flux that inhibit convection, and faculae, which are brighter spots between granules produced by concentrations of magnetic field lines.

Moving up to the chromosphere, the temperature first decreases slightly and then increases drastically by a factor of $\sim$ 10 (Avrett, 2003; Washinoue, Shoda, and Suzuki,

2022) as it reaches the transition region to the stellar corona. While the photosphere contains many absorption features, the high temperatures of the chromosphere lend itself to many emission features (Jess et al., 2015). In particular, the solar chromosphere has a characteristic pinkish-red colour due to the H$_\alpha$ emission line. The chromosphere is much more difficult to observe, though we can see it and the corona more clearly during a solar eclipse, when the photosphere is obscured. Coronographs on solar telescopes block out the majority of photospheric light so that these higher layers can be observed in further detail (Gray, 2008).

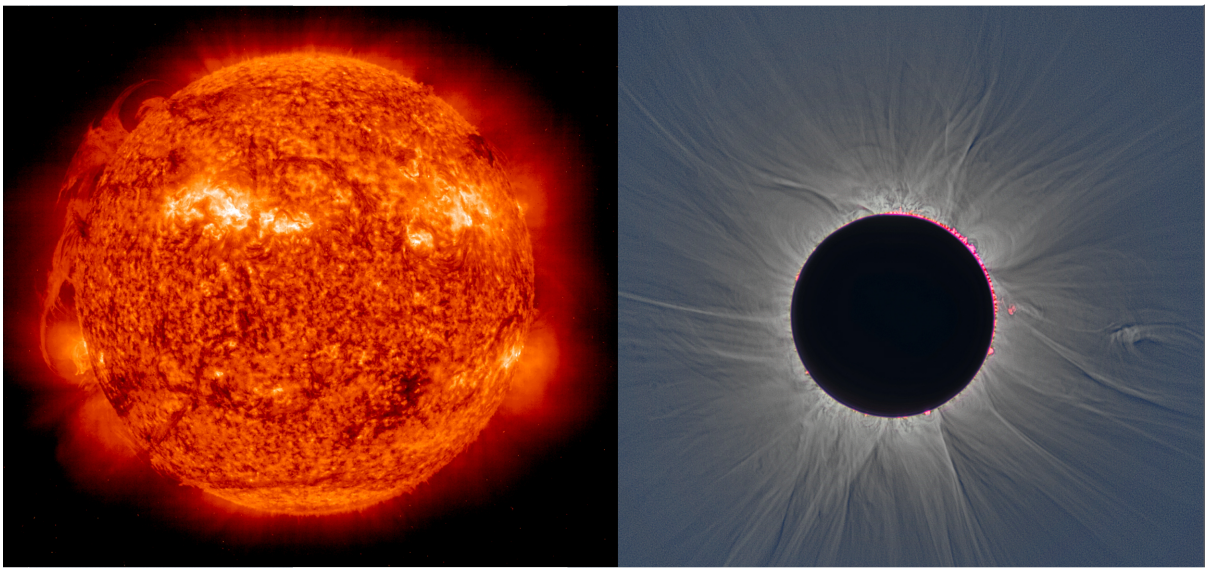

Figure 4: Composite image of the Sun taken with the Solar and Heliospheric Observatory at 304 Å (left, credit NASA SOHO) and a total solar eclipse where parts of the chromosphere, corona, and the solar wind are visible (right, credit Jay Pasachoff (2013)).

Chromospheric phenomena are intimately connected to magnetic activity. These includes plages (regions bright in chromospheric emission (de Grijs and Kamath, 2021)), hair-like spicules (Pereira, Pontieu, and Carlsson, 2012) (also known as fibrils, jets of short-lived plasma that rise quickly and fade away), and chromospheric loops (concentric arches that show intense variability in ultraviolet radiation and expansion (Foukal, 1976)). Of course, while we segment the atmosphere for understanding, no part of the atmosphere is fully independent. The magnetic phenomena observed in the chromosphere are directly related to magnetic concentrations in the photosphere and connect to higher features in the corona.

Above the chromosphere we have the transition region, so named because it describes the steep increase in temperature as well as a few other notable transitions in the atmosphere. Note that the transition region is sometimes described as a component of the chromosphere or corona, since it is difficult to associate it to a particular layer. Below it,

gravity, gas pressure and fluid dynamics dominate the shapes of layers, but throughout the transition region and above, dynamic features caused by magnetic phenomena are dominant.

Finally, the stellar corona describes the outermost region of the atmosphere. It is the final boundary between the star and the ISM, and also marks the beginning of the stellar wind (McComas et al., 2003; de Ferrer, 1809). The temperature of the solar corona is over 1 MK, well above the effective photospheric temperature of 5772 K (Altrock, 2004; Prša et al., 2016). The source of this heating is currently still a matter of debate, known as the coronal heating problem (Aschwanden, 2006; Klimchuk, 2004). Two leading theories include magnetohydrodynamic (MHD) wave heating (Cirtain et al., 2013; Kuperus, Ionson, and Spicer, 1981; Schatzman, 1949), , which suggests magneto-acoustic and Alfvén waves (Alfvén and Lindblad, 1947) transport energy from the photosphere to the corona, and magnetic reconnection (which occurs during events such as solar flares (Kumar and Wang, 2019)), which suggests magnetic field lines induce electric currents in the corona and then collapse, causing the field lines to "reconnect" to other magnetic poles, releasing energy as heat and wave energy in the process (Li, Priest, and Guo, 2021). Currently, the coronal heating problem remains unsolved.

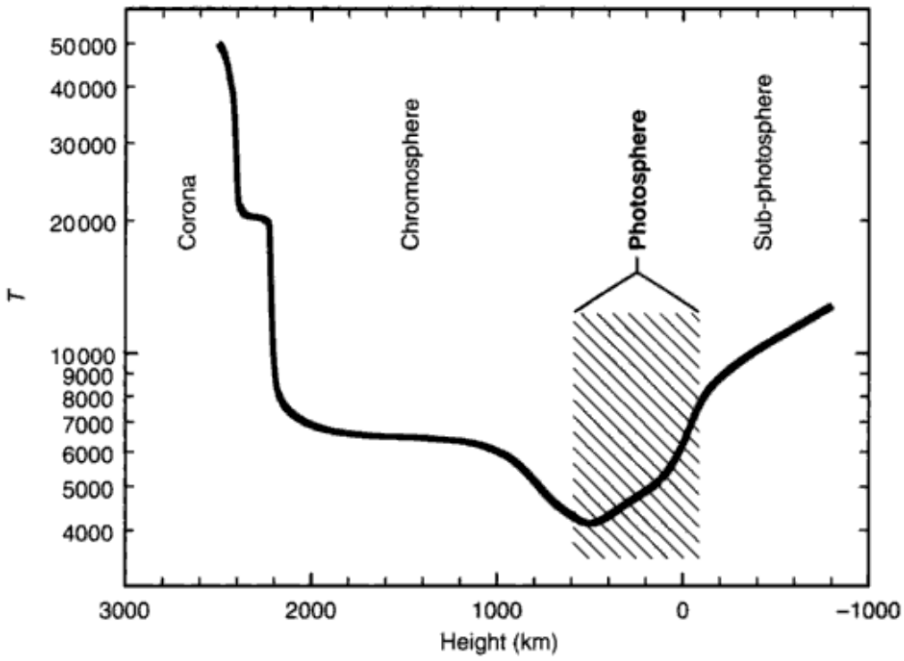

Figure 5: Temperature distribution of the solar atmosphere as a function of height. Original: Fig. 1.1 from Gray (2008).

We will primarily explore the phenomena in the stellar photosphere and the lower chromosphere in our study of stellar abundances and chemical species in these layers, since these layers are spectroscopically relevant for the studies of metal-poor stars. Specifically, we will investigate how stellar spectroscopy is used to study absorption lines to determine abundances, the importance of these studies, and the effect of the assumption of chemical equilibrium in these layers. We will consider the case of the Sun, and metal-poor dwarf and giant stars in order to construct a picture of the evolution of chemical elements. The sample of stars lets us probe some of the first stars that formed after the Big Bang and compare them to a star we have studied extensively and know very well, our own Sun.

1.1.4 *A brief history of spectroscopy*

The modern science of spectroscopy is built upon foundational principles in optics. The idea of using a prism to generate a rainbow of colours was known during Roman times (Seneca and Clarke, 1910) and explaining the rainbow phenomenon seen on Earth can be dated back to the the late 13th and early 14th centuries in the Islamic world and medieval Europe (Bostock and Riley, 1898). The 1600s saw the beginnings of the precise mathematical science of studying a spectrum of light in order to understand its source. In the mid-1600s, multiple individuals studied the solar spectrum (Burgess and Mielenz, 2012), though Sir Isaac Newton is generally regarded as the first to publish a comprehensive review of his experiments and theoretical explanations of the dispersion of light (Newton, 1704). Throughout the 1600s, Robert Hooke and Christiaan Huygens further studied the nature of light (Hooke, 1665; Huygens, 1690), the latter of whom developed the first wave theory of light. Netwon further demonstrated that white light could be separated into a spectrum of colours using a prism, and that these colours could be recombined once more into white light. Newton's scientific setup involved a small aperture from which white light entered, a lens to collimate the light, a glass prism to disperse it, and a screen upon which the resulting spectrum was displayed; modern optical spectrographs use similar methods to observe extremely distant astronomical objects. The precise science of spectroscopy had begun.

Spectroscopy took off again in the 1800s. In 1802, William Wollaston built an improved spectrometer that included an additional lens to focus the solar spectrum onto a screen (Wollaston, 1802). He noticed that patches of colours were missing, and attributed this to natural boundaries between colours. However, in 1815, Joseph von Fraunhofer replaced the prism with a diffraction grating, building off of theories of light interference (BRAND, 1995). This experimental change resulted in a vast improvement in spectral resolution R, defined as

$$R = \frac{\lambda}{\Delta\lambda}, \tag{24}$$

where $\Delta\lambda$ is the smallest difference in wavelength that can be distinguished at wavelength λ. This same core principle of using a diffraction grating to disperse light is used in modern-day spectrographs such as the Space Telescope Imaging Spectrograph (STIS) and the 4-metre Multi-Object Spectroscopic Telescope (4MOST). Fraunhofer's change allowed him to establish a quantitative wavelength scale. He observed the same dark bands that Wollaston had, and mapped over 570 different spectral lines to their wavelengths. These lines are known today as the Fraunhofer lines (Wissenschaften, 1817) , and were the first spectral lines systematically observed in the solar spectrum.

In the 1820s, John Herschel and William Talbot burnt salts in flames and studied their resulting spectra (Herschel, 1823; Talbot, 1826). This linked emergent spectra to materials. Charles Wheatstone noticed in 1835 that bright lines in emission spectra differed between various metals, allowing him to distinguish metals via this new form of flame spectroscopy (Wheatstone, 1836). In 1849, Jean Foucault unified the ideas of absorption and emission features, showing that features appearing at the same wavelength are attributed to the same material (Foucault, 1849). He identified the difference between these two kinds of spectra as relating to the temperature of the source. Anders Jonas Ångström independently postulated in 1852 that a gas could absorb and emit radiation of the same wavelength (Ångström, 1852), and measured an emission spectrum of H.

The 1860s saw the work of Gustav Kirchhoff and Robert Bunsen, who matched the Fraunhofer lines seen in the solar spectrum to laboratory measurements (Kirchhoff, 1861). They went on to link chemical compounds to specific spectra, identifying elements within these chemical compounds (Kirchhoff and Bunsen, 1860), and definitively

linked absorption and emission features by attributing them to particular elements. Kirchhoff later associated the wavelength-specific radiative emission and absorption to a body in thermodynamic equilibrium in his law of thermal radiation (Kirchhoff, 1860). Furthermore, he introduced the three laws of spectroscopy:

1. An incandescent solid, liquid or gas under high pressure produces a continuous spectrum.
2. A hot gas under low pressure seen against a cool background emits an emission-line spectrum.
3. A continuous spectrum viewed through a cool, low-density gas produces an absorption spectrum.

These three laws correctly define the three kinds of spectra we recognise today. The 1860s continued with William and Margaret Huggins determining that the same elements are found in the stars and the Earth (Huggins, 1868). This realisation was arguably where the seeds of modern science of Galactic Archaeology would begin to form – that we can study the chemical composition of stars to understand the chemodynamical evolution of the Universe. Spectroscopy continued to develop as a refined science, with many important discoveries and inventions (Beer, 1852; Larmor, 1897; Rowland, 1882; Thomas, 1991; Zeeman, 1896). Let us now discuss the formation and source of spectra in greater detail.

Spectra are not isolated to stars; many fields in astronomy use spectra to better understand the object of interest. For example, emission spectra from active galactic nuclei (AGN) are used to understand the structure of the accretion disc and jets (Fath, 1909). Transmission spectra (formed when we observe an atmosphere backlit by a separate source) are used in exoplanet studies to probe the content of the planetary atmosphere (Mayorga et al., 2021; de Wit et al., 2016). The study of spectra is common outside of astronomy, too, with techniques such as to identify molecules in chemical analysis (Chen and Yip, 1974; Garcia Ruiz et al., 2020) and to better understand biological phenomena (Hammes, 2005).

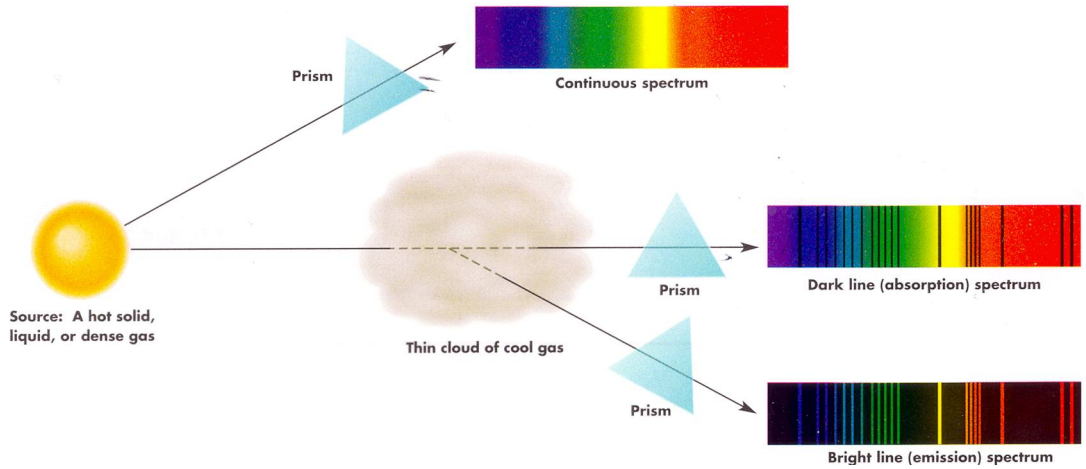

Figure 6: The three kinds of spectra as defined by Kirchhoff's laws. Repurposed from Fix (2010).

So why are these phenomena so ubiquitous in our Universe? Generally, the electromagnetic spectrum is simply a mapping of the wavelength of EM radiation to intensity, and we are fortunate that sources of EM radiation are quite abundant. Note that the word "spectrum" has since been applied to many other kinds of waves, but we will concern ourselves primarily with light here. There are three kinds of spectra, as described

by Gustav Kirchhoff from his three laws of spectroscopy: a continuum spectrum is the light of a hot source (acting as a blackbody radiator) observed directly; an emission spectrum forms when we observe the electromagnetic radiation directly emitted by a non-blackbody source; an absorption spectrum forms when light from a hotter background source is absorbed in a cooler medium, and we observe the resultant light with the absorbed components missing. The transmission spectrum mentioned above is a composite of the stellar and planetary spectra. Fig. 7 shows the conditions under which absorption and emission lines will form.

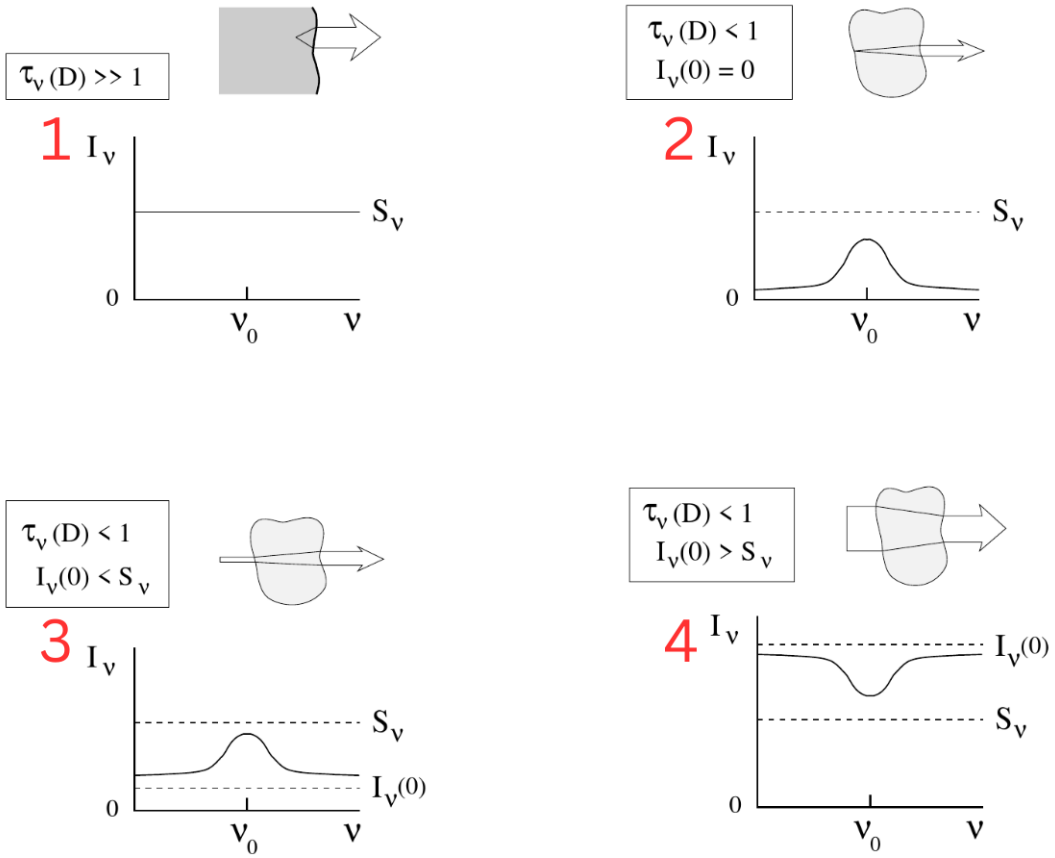

Figure 7: Spectral lines from a homogenous object with a uniform source function. No lines emerge when the object is optically thick (1). When it is optically thin, emission lines emerge when it is not backlit (2) or when it is brighter than its surroundings (3). Absorption lines emerge when the object is backlit by a brighter source (4). Adapted from Fig. 2.2 from https://robrutten.nl/rrweb/rjr-edu/coursenotes/rutten_rtsa_notes_2003.pdf.

More specifically, when photons travel through an absorbing medium between the observer and the source, the resultant absorption spectrum tells us which wavelengths of light have been removed through absorption. This gives us information on which atoms and molecules are present in the medium, given our knowledge of the background source's continuum spectrum. A classic example of this is the solar spectrum.

Here, we see sections of the light generated from the solar core being absorbed by the solar atmosphere. The different wavelengths correspond to different absorbing species, and so we can infer the presence and abundance of atoms and molecules present within the solar atmosphere.

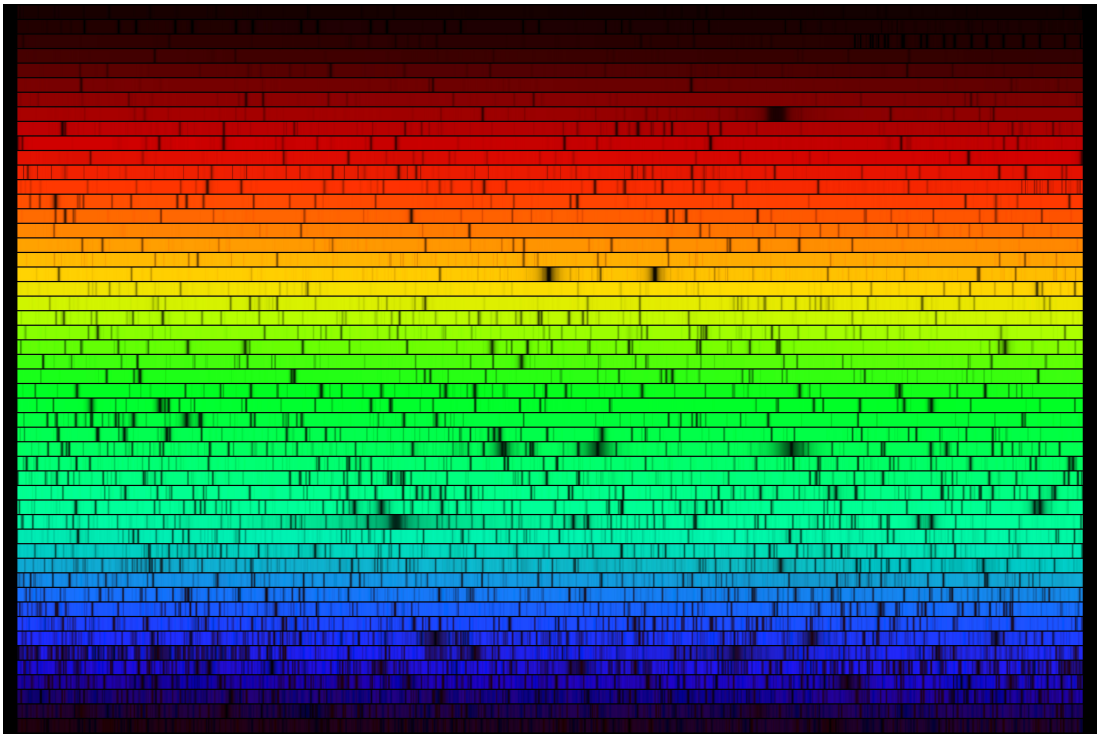

Figure 8: Solar spectrum from a digital atlas observed with the Fourier Transform Spectrometer at the National Solar Observatory at Kitt Peak, Arizona. Credit: N.A.Sharp, NOAO/NSO/Kitt Peak FTS/AURA/NSF.

Emission lines, in contrast, come from hot sources. The solar chromosphere's distinct colour comes from the emission of H_α lines.

1.1.4.1 *The introduction of quantum mechanics*

In the early 20th century, the foundation of quantum mechanics led to a better understanding of the physical processes that lead to the formation of a spectrum. Specifically, one could now associate a spectral line to a given difference in energy levels, providing a unique map of transitions visualised as a spectrum, since transitions are only allowed in discrete steps between energy levels. An emission line is formed when an atom or molecule experiences a transition from higher energy state E_2 to a lower energy state E_1, releasing a photon, and an absorption line is formed in the opposite circumstance, namely when an incident photon causes a transition from a lower energy state E_1 to a higher energy state E_2. In both cases, the wavelength of the photon corresponds to the energy difference $E_2 - E_1$, that is,

$$E_{,} = E_2 - E_1 = \frac{hc}{\lambda_\gamma}. \tag{25}$$

This was studied extensively for H, and many of the series have names associated with their discoverers.

Einstein postulated in 1916 that the formation of an atomic spectral line is governed by three processes: spontaneous emission, absorption, and stimulated emission (Einstein, 1916). These processes were assigned the coefficients A_{21}, B_{12} and B_{21}, respectively, where the numerical subscript convention describes the transition from state $x \to y$. These coefficients are related to the intrinsic properties of the energy levels of the atom or molecule in question.

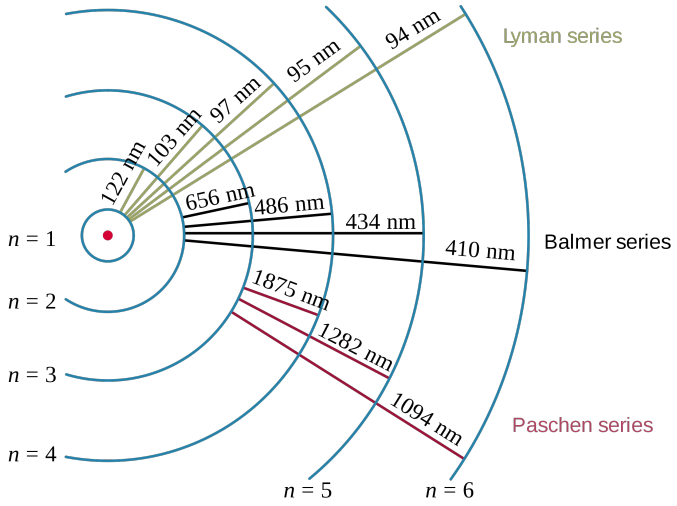

Figure 9: Hydrogen series and their transition wavelengths. Original: https://commons.wikimedia.org/wiki/File:Hydrogen_transitions.svg

Spontaneous emission is the process by which an atom transitions from a higher energy state E_2 to a lower energy state E_1 without external influence, releasing a photon with energy $E_\gamma = E_2 - E_1$. With the energy levels E_2 and E_1 ($E_2 \geqslant E_1$), the change in number density of atoms in state 2 (n_2) per unit time is

$$\left(\frac{d(n_2)}{dt}\right)_{\text{spontaneous}} = -A_{21} n_2, \tag{26}$$

and the change in number density of atoms in state 1 (n_1) per unit time is therefore

$$\left(\frac{d(n_1)}{dt}\right)_{\text{spontaneous}} = A_{21} n_2. \tag{27}$$

The Einstein coefficient A_{21} (s^{-1}) describes the probability per unit time for this process, and is specific to a particular atom. Note that the energy-time uncertainty principle causes photons in a narrow range of frequencies around the central frequency to be generated. This is the source of the "spectral linewidth", or natural broadening (see Sec. 1.1.4.2 below).

Absorption involves an external photon with energy $E_\gamma = E_2 - E_1$ being absorbed by an atom, causing it to jump from state E_1 to E_2. The Einstein coefficient B_{12} (m^3 J^{-1} s−2) is the probability per unit time per unit frequency per unit energy density (of the radiation field) that a photon with the defined energy E_γ will be absorbed, causing the state $1 \to 2$ transition. The change in number density of atoms in state 1 (n_1) per unit time is then

$$\left(\frac{dn_1}{dt}\right)_{\text{positive absorption}} = -B_{12} n_1 \rho(\nu). \tag{28}$$

where $\rho(\nu)$ is the spectral energy density of the isotropic radiation field at the frequency of the transition $\nu = \frac{E_2 - E_1}{h}$.

Stimulated, or induced, emission involves an electronic transition caused by external EM radiation near the energy of transition $E_2 - E_1$. This is equivalent to "negative absorption", that is, the inverse of the absorption process. The Einstein coefficient B_{21}

($m^3\ J^{-1}\ s{-}2$) describes the probability per unit time per unit frequency per unit energy density (of the radiation field) that the presence of an external photon at energy $E_2 - E_1$ causes a decay from state $2 \to 1$, resulting in an emission of a photon at energy $E_\gamma = E_2 - E_1$. The change in number density of atoms in state 1 per unit time is then

$$\left(\frac{dn_1}{dt}\right)_{\text{negative absorption}} = B_{12} n_2 \rho(\nu). \tag{29}$$

Interestingly, Einstein's formulation of stimulated emission was a theoretical discovery at the time. It later helped form the foundation for the invention of the laser (Steen, 1998). In a curious twist of fate, lasers are commonly used in modern-day spectroscopy to excite source material (Rinke-Kneapler and Sigman, 2014).

With these coefficients in hand, we can now consider the balance between these processes at thermodynamic equilibrium. In a closed system, a simple balancing is held such that the net change in the number of excited atoms is zero. That is, the losses and gains between processes are balanced. This leads into the principle of detailed balance, which states that at equilibrium, each elementary kinetic process is in equilibrium with its reverse process (Boltzmann, 2003, 1872; Gorban, 2014). For the processes described above, the fulfilled condition at equilibrium is

$$0 = \left(\frac{d(n_1)}{dt}\right)_{\text{spontaneous}} + \left(\frac{dn_1}{dt}\right)_{\text{positive absorption}} + \left(\frac{dn_1}{dt}\right)_{\text{negative absorption}}, \tag{30}$$

or equivalently,

$$0 = A_{21} n_2 - B_{12} n_1 \rho(\nu) + B_{21} n_2 \rho(\nu). \tag{31}$$

We can combine the notion of these Einstein coefficients into a single quantity known as the oscillator strength, a dimensionless quantity that expresses the probability of absorption or emission between two given energy levels E_1 and E_2 (with $E_2 \geqslant E_1$). It is the ratio between the quantum mechanical transition rate and the classical absorption/emission rate of a single-electron oscillator that has the same frequency as the transition $\nu = \frac{E_2 - E_1}{h}$ (Hilborn, 1982). In the context of spectroscopy, larger oscillator strengths result in stronger transitions. The oscillator strength of the transition between states $1 \leftrightarrow 2$ is related to the cross-section for absorption σ by

$$f_{12} = \frac{4\epsilon_0 m_e c}{e^2} \frac{\sigma}{\varphi_\nu}, \tag{32}$$

where ϵ_0 is the permittivity of free space, m_e is electron mass, c is the speed of light, e is elementary charge and φ_ν is the normalised distribution function in frequency. This can also be expressed in terms of angular frequency, namely

$$f_{12} = \frac{2\epsilon_0 m_e c}{\pi e^2} \frac{\sigma}{\varphi_\omega} \tag{33}$$

with φ_ω as the normalised distribution function in angular frequency. Including the inter-coefficient relations from Eq.31, all three Einstein coefficients (for a given spectral line) can be expressed using the oscillator strength and statistical weights of the levels:

$$A_{21} = \frac{2\pi\nu^2 e^2}{\epsilon_0 m_e c^3} \frac{g_1}{g_2} f_{12}, \tag{34}$$

$$B_{12} = \frac{e^2}{4\epsilon_0 m_e h\nu} f_{12}, \tag{35}$$

$$B_{21} = \frac{e^2}{4\epsilon_0 m_e h} \frac{g_1}{g_2} f_{12}. \tag{36}$$

$$\tag{37}$$

The statistical weight and oscillator strength are further linked by the relation

$$g_1 f_{12} = -g_2 f_{21}. \tag{38}$$

The gf-value hence corresponds to a particular energetic transition (Robinson, 1996). In spectroscopic contexts, the $\log(gf)$ value is an important factor that determines the strength of a particular spectral line, with the other factors being the abundance of the species and the excitation of the lower level. A change in $\log(gf)$ directly translates to an opposite change in measured abundance, making it especially important in abundance analyses to have tight constraints on $\log gf$ values. There have been advances in both theoretical predictions and experimental measurements of these values in recent years (Pehlivan Rhodin, 2018). This is yet another choice that the scientist must make when conducting an abundance analysis, as multiple sources of $\log gf$-values exist for a given set of spectral lines. We will see the effect of this choice in practice for determining the solar photospheric silicon abundance in Chap. 2.

1.1.4.2 *Line broadening*

Let us consider the formation of an absorption feature. In a perfect laboratory environment, a single atom can absorb a photon of a specific wavelength from a background source. The resulting spectral line would be an ideal Dirac peak at the given wavelength. However, the spectral lines we observe in the solar photosphere are never so precisely defined. A few different physical processes lead to the broadening and shifting of spectral lines. In the photosphere, we observe the continuous spectrum of radiation from the solar core shine through a medium with various absorbers at various wavelengths. If we consider just one of these, for example the H_α Fraunhofer C line (now better known as the first line in the Balmer series) at 656.281 nm, the number of absorbers is the number of singly-excited H atoms. The H_α line describes the electronic transition between the $n = 2$ and $n = 3$ states in the H atom. Therefore, photons corresponding to the energy (or wavelength) of 1.89 eV (the energy difference between the $n = 2$ and $n = 3$ levels of neutral atomic H) would be absorbed. A variety of effects local to these absorbers can alter the shape of the spectral line. These physical processes can broaden the line or shift it, and the combination of all of the processes results in the line we finally observe.

The first source of broadening is known as lifetime (or natural) broadening and comes from the uncertainty principle. The lifetime of the state is related to its energy due to spontaneous emission, and so a collection of absorbers will decay at differing rates. This introduces a Lorentzian profile to the spectral line shape due to the exponential decay (Haken and Wolf, 1996). Natural broadening is a consequence of quantum mechanical effects, though there are methods to suppress the decay rates to reduce natural broadening (Gabrielse and Dehmelt, 1985).

The second major source of broadening is thermal or Doppler broadening. The velocities of the particles in the gas follow a Maxwell-Boltzmann distribution, resulting in absorbers being red- and blue-shifted from the line centre based on their velocity away from or towards the observer, respectively. The different velocities result in different Doppler shifts of the absorbed radiation, and the overall line shape is modified by a Gaussian profile. Surprisingly, the Doppler broadening of a spectral line can be useful. Even though it somewhat obscures the nature of the absorption feature, the amount of broadening is dependent on the velocity, and hence the temperature of the gas. Higher gas temperatures result in a higher spread of particle velocities and therefore a broader spectral line shape.

The final source of broadening to consider here is pressure broadening. Absorbing particles will collide with other particles in the gas, shortening the lifetime of the ab-

sorption process. This has an effect similar to natural broadening, and introduces a Lorentzian profile. When all broadening sources are taken into account, the spectral line shape has a Voigt profile (a convolution of a Gaussian and Lorentzian). Fig. 10 shows these three sources of broadening and where their presence is primarily observed.

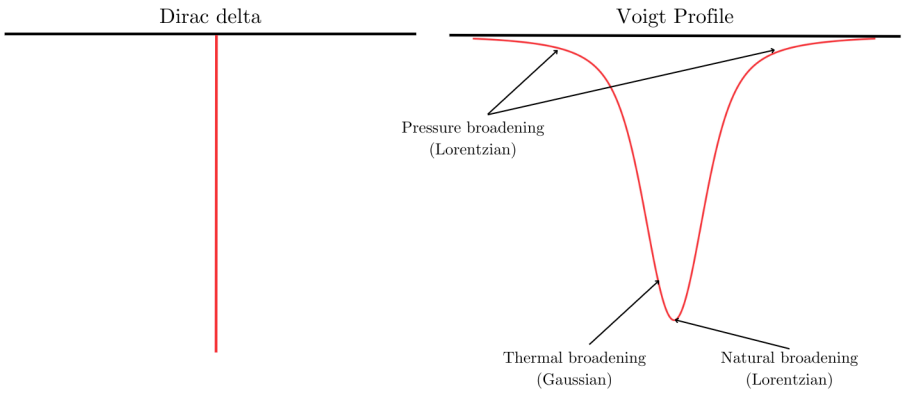

Figure 10: Representative diagram showing how natural broadening, thermal broadening and pressure broadening affect the shape of a spectral line, shifting it from a Dirac delta peak to a Voigt profile.

All of these sources of broadening are present for emission lines as well; the focus was on absorption lines because those are the primary lines we consider in the solar photosphere. There are further sources of broadening, and further distinctions to be made in the sources of broadening considered. These involve energy shifts due to electric fields (Epstein, 1916; Stark and Kirschbaum, 1914) and van der Waals forces (Monier et al., 2010). However, the three sources mentioned above are the main sources of local broadening we will consider for the atmospheric region we are interested in. The effects of broadening on both observed and modelled spectral lines in the solar photosphere is explored in Chap. 2.

1.2 A BRIEF TAXONOMY OF STARS

A star is a luminous astronomical body held together by self-gravity that generates energy through thermonuclear fusion, which gives support against gravity. These properties give constraints on a star's mass, a property which also determines how it will evolve. Observed stellar masses range from as low as 0.09 $M_\odot$ (Close et al., 2007) to as high as 196 $M_\odot$ (Kalari et al., 2022). The theoretical lower limit of a star is $\sim$ 0.08 $M_\odot$ or 75 M_J, the minimum mass required for the conditions for H-burning to begin in the core. Below this mass exist brown dwarfs, which fuse deuterium, but cannot ignite hydrogen. The range of masses for brown dwarfs is roughly $13 - 75$ M_J; below this, the astronomical body is a gas giant planet. These astronomical bodies all form due to cloud collapse, and the initial mass of this cloud is imperative in determining the kind of body that eventually forms. Stars rarely form in isolation, but we will generally consider single-star systems for simplicity.

Stellar evolution, that is, the physical changes a star experiences during its lifetime, depends primarily on its mass and chemical composition. Mass affects almost every aspect of a star's structure and governs many physical processes such as nuclear fusion, while chemical composition affects the amount of available nuclear fuel. In stellar atmospheres, the chemical composition (and more specifically, the metal-content) greatly impacts the effectiveness of radiation transfer.

The structure of a H-burning (main-sequence, MS) star depends on its mass, since this informs the primary form of nuclear energy generation, and this subsequently dictates how heat is efficiently transported outwards from the core. This in turn determines the characteristic temperatures throughout the star, which affects properties such as the ionisation state. The structure of MS stars can be divided into three regimes: very low mass stars ($M_* < 0.3\ M_\odot$), intermediate mass stars ($0.3 \leqslant M_* < 1.5\ M_\odot$), and high mass stars ($1.5\ M_\odot \leqslant M_*$) (Hansen, Kawaler, and Trimble, 2004). The proton-proton chain (pp-chain) is the primary mode of energy generation in very low mass and intermediate stars, and does not establish a steep temperature gradient. The energy generation rate of the pp-chain scales as $\epsilon_{pp} \sim T^4$, where T is the temperature (Maoz, 2016). In intermediate mass stars, this leads to a radiative core and a convective envelope. In very-low mass stars, though, the higher opacities due to lower core temperatures result in radiation transfer being inefficient, and so they are fully convective. Table 1 presents the overall p-p chain and its 3 common branches.

Table 1: Proton-proton (p-p) chain branches with reactions and released energy. The temperature range at which the branch is dominant is shown in each subheading.

Reaction	Energy Released
$p + p + e^- \rightarrow {}^2_1 D + \nu_e$ (net reaction)	1.44 MeV
${}^2_1 D + p \rightarrow {}^3_2 He + \gamma$	5.49 MeV
p-p I branch: $10 - 18$ MK	
${}^3_2 He + {}^3_2 He \rightarrow {}^4_2 He + 2{}^1_1 H$	12.86 MeV
p-p II branch: $18 - 25$ MK	
${}^3_2 He + {}^4_2 He \rightarrow {}^7_4 Be + \gamma$	1.59 MeV
${}^7_4 Be + e^- \rightarrow {}^7_3 Li + \nu_e$	0.861 MeV (90%) / 0.383 MeV (10%)
${}^7_3 Li + {}^1_1 H \rightarrow 2{}^4_2 He$	17.35 MeV
p-p III branch: > 25 MK	
${}^3_2 He + {}^4_2 He \rightarrow {}^7_4 Be + \gamma$	1.59 MeV
${}^7_4 Be + {}^1_1 H \rightarrow {}^8_5 B + \gamma$	*
${}^8_5 B \rightarrow {}^8_4 Be + e^+ + \nu_e$	*
${}^8_4 Be \rightarrow 2{}^4_2 He$	*
*The last three steps contribute a total energy of 18.21 MeV, but much of it is lost to the neutrino	
Overall Reaction	
$4\,{}^1H^+ + 2e^- \rightarrow {}^4 He^{2+} + 2\nu_e$	26.73 MeV

High mass stars signify the point where the carbon-nitrogen-oxygen (CNO) cycle becomes the predominant form of nuclear energy generation, as the core temperature exceeds $\sim 1.8 \times 10^7$ K. The CNO cycle's energy generation scales as $\epsilon_{CNO} = T^{17}$, significantly higher than ϵ_{pp}. This establishes steep temperature gradients in the cores of these stars, causing them to be convective. The outer envelopes have shallower temperature gradients, but are hot enough so that H is nearly fully ionised. This makes them transparent to UV photons (a large portion of the radiative flux). Additionally, the CNO cycle is catalytic, unlike the p-p chain, with the C, N, O isotopes consumed at one point in the cycle being re-generated in later ones. Table 2 shows the branches of the CNO cycle characteristic in stars. Branches CNO-II and CNO-III are only significant in massive stars. About 99 % of the Sun's energy comes from the various p-p chains, with only 1 %

Table 2: Carbon-Oxygen-Nitrogen (CNO) catalytic cycle with the four branches present in stars. The CNO-III and CNO-IV branches are only significant in massive stars.

Reaction	Energy Released
CNO-I branch:	
${}^{12}_{6}\mathrm{C} + {}^{1}_{1}\mathrm{H} \rightarrow {}^{13}_{7}\mathrm{N} + \gamma$	1.95 MeV
${}^{13}_{7}\mathrm{N} \rightarrow {}^{13}_{6}\mathrm{C} + \mathrm{e}^{+} + \nu_{\mathrm{e}}$	1.20 MeV
${}^{13}_{6}\mathrm{C} + {}^{1}_{1}\mathrm{H} \rightarrow {}^{14}_{7}\mathrm{N} + \gamma$	7.54 MeV
${}^{14}_{7}\mathrm{N} + {}^{1}_{1}\mathrm{H} \rightarrow {}^{15}_{8}\mathrm{O} + \gamma$	7.35 MeV
${}^{15}_{8}\mathrm{O} \rightarrow {}^{15}_{7}\mathrm{N} + \mathrm{e}^{+} + \nu_{\mathrm{e}}$	1.73 MeV
${}^{15}_{7}\mathrm{N} + {}^{1}_{1}\mathrm{H} \rightarrow {}^{12}_{6}\mathrm{C} + {}^{4}_{2}\mathrm{He}$	4.96 MeV
CNO-II branch:	
${}^{15}_{7}\mathrm{N} + {}^{1}_{1}\mathrm{H} \rightarrow {}^{16}_{8}\mathrm{O} + \gamma$	12.13 MeV
${}^{16}_{8}\mathrm{O} + {}^{1}_{1}\mathrm{H} \rightarrow {}^{17}_{9}\mathrm{F} + \gamma$	0.60 MeV
${}^{17}_{9}\mathrm{F} \rightarrow {}^{17}_{8}\mathrm{O} + \mathrm{e}^{+} + \nu_{\mathrm{e}}$	2.76 MeV
${}^{17}_{8}\mathrm{O} + {}^{1}_{1}\mathrm{H} \rightarrow {}^{14}_{7}\mathrm{N} + {}^{4}_{2}\mathrm{He}$	1.19 MeV
${}^{14}_{7}\mathrm{N} + {}^{1}_{1}\mathrm{H} \rightarrow {}^{15}_{8}\mathrm{O} + \gamma$	7.35 MeV
${}^{15}_{8}\mathrm{O} \rightarrow {}^{15}_{7}\mathrm{N} + \mathrm{e}^{+} + \nu_{\mathrm{e}}$	2.75 MeV
CNO-III branch:	
${}^{17}_{8}\mathrm{O} + {}^{1}_{1}\mathrm{H} \rightarrow {}^{18}_{9}\mathrm{F} + \gamma$	5.61 MeV
${}^{18}_{9}\mathrm{F} \rightarrow {}^{1}\ {}_{7}{}_{8}\mathrm{O} + \mathrm{e}^{+} + \nu_{\mathrm{e}}$	1.66 MeV
${}^{18}_{8}\mathrm{O} + {}^{1}_{1}\mathrm{H} \rightarrow {}^{15}_{7}\mathrm{N} + {}^{4}_{2}\mathrm{He}$	3.98 MeV
${}^{15}_{7}\mathrm{N} + {}^{1}_{1}\mathrm{H} \rightarrow {}^{16}_{8}\mathrm{O} + \gamma$	12.13 MeV
${}^{16}_{8}\mathrm{O} + {}^{1}_{1}\mathrm{H} \rightarrow {}^{17}_{9}\mathrm{F} + \gamma$	0.60 MeV
${}^{17}_{9}\mathrm{F} \rightarrow {}^{1}\ {}_{7}{}_{8}\mathrm{O} + \mathrm{e}^{+} + \nu_{\mathrm{e}}$	2.76 MeV
CNO-IV branch:	
${}^{18}_{8}\mathrm{O} + {}^{1}_{1}\mathrm{H} \rightarrow {}^{19}_{9}\mathrm{F} + \gamma$	7.99 MeV
${}^{19}_{9}\mathrm{F} + {}^{1}_{1}\mathrm{H} \rightarrow {}^{16}_{8}\mathrm{O} + {}^{4}_{2}\mathrm{He}$	8.11 MeV
${}^{16}_{8}\mathrm{O} + {}^{1}_{1}\mathrm{H} \rightarrow {}^{17}_{9}\mathrm{F} + \gamma$	0.60 MeV
${}^{17}_{9}\mathrm{F} \rightarrow {}^{17}_{8}\mathrm{O} + \mathrm{e}^{+} + \nu_{\mathrm{e}}$	2.76 MeV
${}^{17}_{8}\mathrm{O} + {}^{1}_{1}\mathrm{H} \rightarrow {}^{18}_{9}\mathrm{F} + \gamma$	5.61 MeV
${}^{18}_{9}\mathrm{F} \rightarrow {}^{17}_{9}\mathrm{O} + \mathrm{e}^{+} + \nu_{\mathrm{e}}$	1.66 MeV
Overall Reaction (net)	
$4\,{}^{1}_{1}\mathrm{H} + 2\mathrm{e}^{-} \rightarrow {}^{4}_{2}\mathrm{He}^{2} + 2\nu_{\mathrm{e}} + 7\gamma$	26.73 MeV

coming from the CNO cycle.

1.2.1 *Stellar Classification*

While these intrinsic properties of a star determine its lifetime and evolution, they are not properties readily accessible observationally. We must instead make do with observational properties such as the star's spectrum. The modern-day Morgan-Keenan (MK) classification system is a two-dimensional scale in temperature and luminosity (Gray

and Corbally, 2009), where the luminosity of a star L_* is the total power emitted by the star, which is related to the effective temperature of a blackbody radiating at the temperature T_{eff}:

$$L_* = 4\pi R_*^2 \sigma T_{eff}^4. \tag{39}$$

The temperature classification comes from the older Harvard classification scheme refined by Annie Jump Cannon in 1901 (Cannon and Pickering, 1901). By 1912, her system essentially resembled its modern form (Cannon and Pickering, 1912). In 1925, Cecilia Payne demonstrated that this classification system was in fact a sequence in effective temperature (Payne, 1925). Table 3 shows our modern classification of spectral types based on effective temperature, as well as the typical mass (M_*), radius (R_*) and bolometric luminosity L_* in solar units. The luminosity classification developed from the

Table 3: Modern-day Harvard spectral classification system for stars in order of their effective temperature (Cannon and Pickering, 1912; Payne, 1925). The mass, radius, and bolometric luminosity typical of MS stars of the given spectral type is presented in terms of solar units.

Spectral Class	T_{eff} [K]	$M_{*(MS)}/M_\odot$	$R_{*(MS)}/R_\odot$	$L_{*(MS)}/L_\odot$
O	$\geqslant 30,000$	$\geqslant 16.00$	6.60	$\geqslant 30,000$
B	$10,000 - 30,000$	$2.10 - 16.00$	$1.80 - 6.60$	$25 - 30,000$
A	$7,500 - 10,000$	$1.40 - 2.10$	$1.40 - 1.80$	$5 - 25$
F	$6,000 - 7,500$	$1.04 - 1.40$	$1.15 - 1.40$	$1.5 - 5$
G	$5,200 - 6,000$	$0.80 - 1.04$	$0.96 - 1.15$	$0.6 - 1.5$
K	$3,700 - 5,200$	$0.45 - 0.8$	$0.70 - 0.96$	$0.08 - 0.6$
M	$2,400 - 3,700$	$0.08 - 0.45$	$\leqslant 0.70$	$\leqslant 0.08$

Yerkes system (also called the MK system after its authors) (Morgan, Keenan, and Kellman, 1943), which is based on spectral lines sensitive to temperature and surface gravity. Stars which are denser (higher surface gravity) have spectral lines that are more heavily affected by pressure broadening than stars which have lower densities (lower densities). Given the mass, the observation of the spectrum therefore allows the classification of whether a star is a dwarf (higher surface gravity) or a giant (lower surface gravity). Table 4 depicts the various common luminosity classes in use today. Our Sun is classified as a G2V star. Note that the MK system is the modern-day name for the two-dimensional system for spectral classification using temperature and luminosity (Morgan and Keenan, 1973). Stars are are often grouped as "early-" or "late-type". These are simply synonyms for "hotter" and "cooler" stars, with early-type stars referring to the spectral classes O-A, and late-type to F-M (often synonymous with "cool stars"). Other classification systems are also widely used, such as those based on color indices and magnitudes (Johnson and Morgan, 1953). These frequently refer to the bands in the EM spectrum, and different telescopes are fitted with different filters to observe specific wavelengths. These "colours" can therefore form a photometric classification system.

1.2.1.1 *Hertzsprung-Russell Diagram*

The results of spectral classification can be plotted on a graph known as a Hertzsprung-Russell diagram, named after Ejnar Hertzsprung and Henry Norris Russell who created it independently in 1911 and 1913, respectively (Hertzsprung, 1909, 1911; Russell, 1914). Typically, it is a diagram of T_{eff} and luminosity, though the original diagram was an

Table 4: Modern-day Yerkes luminosity classes used as part of the two-dimensional Morgan-Keenan spectral classification system.

Luminosity Class	Name
0 / Ia^+	hypergiants
Ia	luminous supergiants
Iab	intermediate-size luminous supergiants
Ib	less luminous supergiants
II	bright giants
III	giants
IV	subgiants
V	main-sequence / dwarfs
sd (prefix) / VI	subdwarfs
D (prefix) / VII	white dwarfs

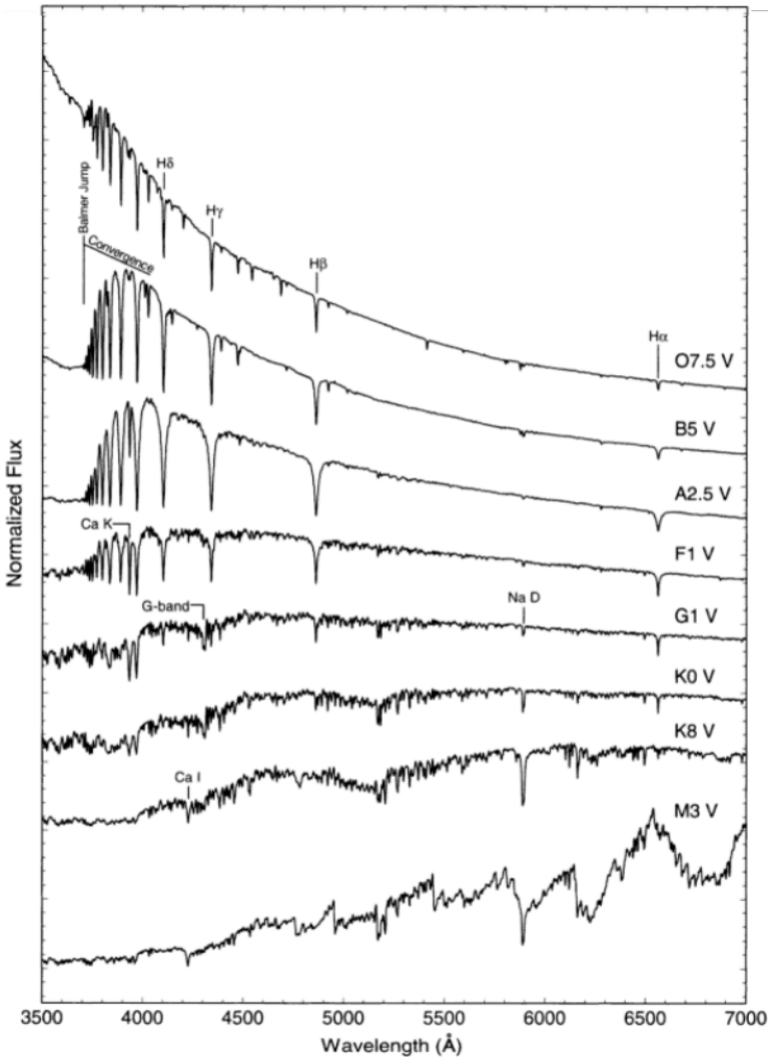

Figure 11: Spectral sequence for OBAFGKM main-sequence stars from Gray and Corbally (2009) showcasing that the sequence is a sequence in temperature.

observational one, depicting spectral type and absolute visual magnitude. Modern observational versions of the H-R diagram plot colour index against magnitude, and are referred to as Colour-Magnitude diagrams (CMDs). The theoretical H-R diagram plots temperature against luminosity (generally with both in log-space). This theoretical diagram is often produced from stellar evolution models, and compared with observations. Transforming the theoretical diagram into the observational one (or vice versa) requires some defined relationship between colour index and temperature, and it is therefore useful to consider the two as separate. Fig. 12 shows a basic H-R diagram with labelled components.

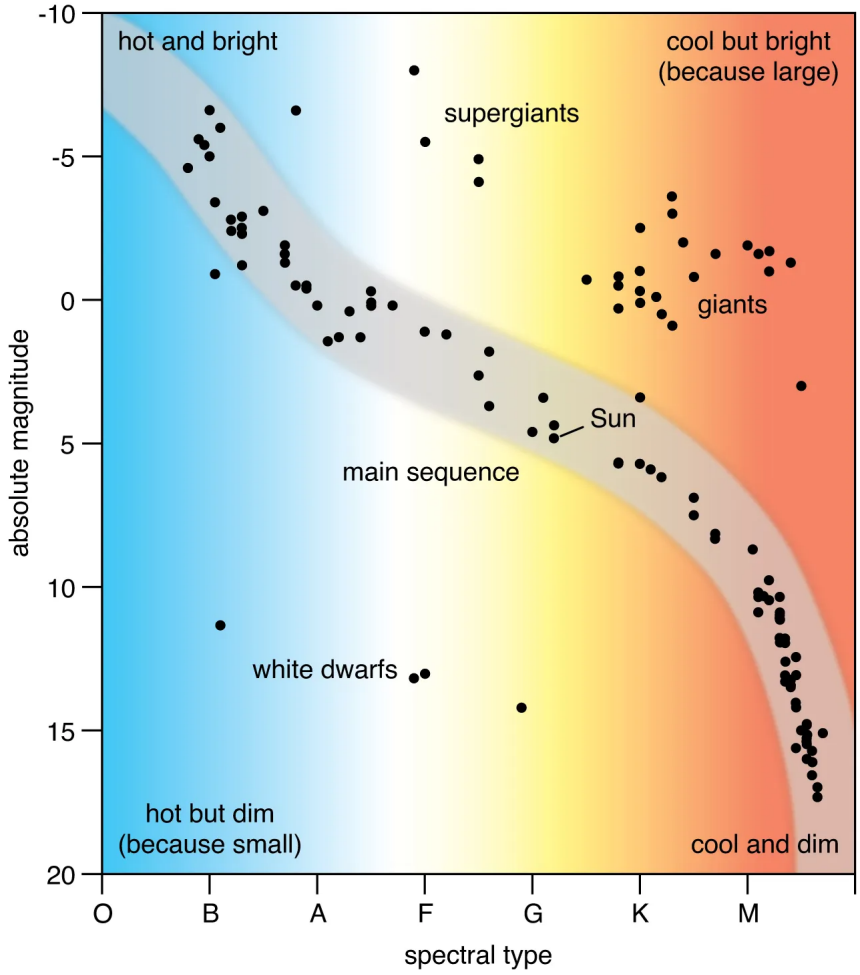

Figure 12: Theoretical H-R diagram illustrating the key components of a star's lifetime. Copyright Encyclopaedia Britannica (https://www.britannica.com/science/Hertzsprung-Russell-diagram).

The evolution of stars based on their mass can also be plotted on the H-R diagram. Loosely, as protostars contract, their temperatures increase, causing them to move leftwards on the H-R diagram. This movement continues until they reach the Zero-Age Main-Sequence (ZAMS), at which point they are hot enough to fuse H to He in their cores. A star spends the majority of its lifetime on the MS, and the various evolutionary phases it goes through after this stage depends on its mass. We will primarily consider the evolutionary stages of 1 $M_\odot$ stars, as they are the ones relevant in this work (see Fig. 13). After the supply of H in the core has run dry, the star begins to fuse H in a thin shell around the He core. During this time, it leaves the MS and becomes a subgiant. Eventually, the core becomes degenerate, causing the H shell to increase in temperature

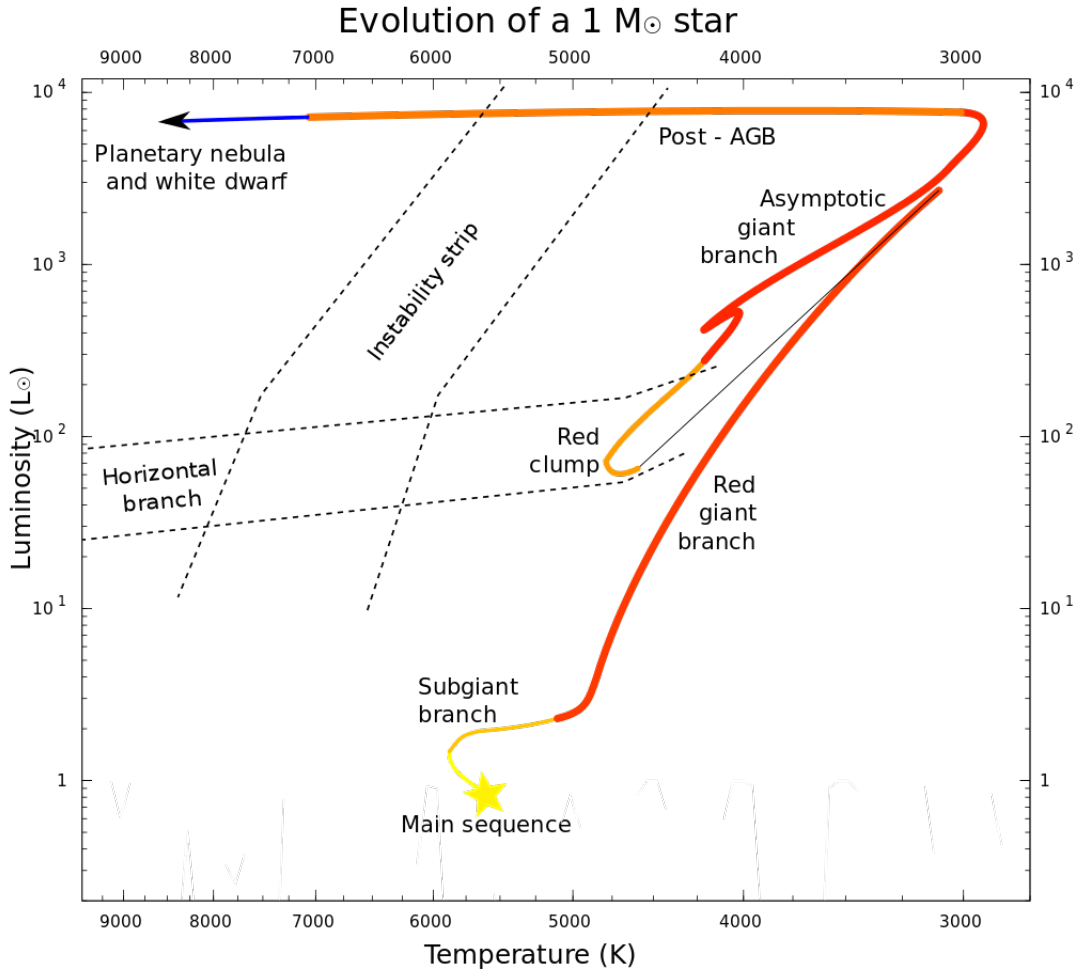

Figure 13: Evolutionary track of a 1 $M_\odot$ star on the H-R diagram after it enters the main-sequence. Original from https://en.wikipedia.org/wiki/Stellar_evolution.

and the star to expand, increasing its luminosity. It now enters the red giant branch (RGB) with an inert, degenerate He core. The vast increase in core temperature due to this process means the CNO cycle is the primary mode of energy generation in the H shell.

As the star continues to fuse H into He, its core becomes more massive and the temperature increases. This in turn results in more rapid H fusion, and the star expands to become more luminous. On the H-R diagram, the star is seen to "ascend" the RGB. Throughout this process, the convective envelope becomes deeper, and the first "dredge-up" event carries the fusion products of the CNO cycle into the atmosphere. This process of H-shell burning will continue until the inert He core becomes massive and hot enough to begin He fusion through the triple-alpha process. He fusion causes an immediate temperature increase, and the core quickly becomes non-degenerate, expanding and producing a "helium flash", where large quantities of He are quickly fused into C during a runaway process. The star now enters the horizontal branch, and remains there as it burns He in its core.

After the supply of He fusion fuel in the core is exhausted, He fusion continues in a shell around the core consisting of C and O. H fusion continues in a second shell outside the He core, which contributes a majority of the energy generation. The star is now on the asymptotic giant branch (AGB). During the AGB phase, a convection zone can form that brings C from the core into the atmosphere (second dredge-up). Some

stars can experience a third dredge-up as well. These stars are "chemically peculiar" carbon stars (see Sec. 1.2.3). AGB stars suffer increased mass loss through strong stellar winds, and these winds carry enriched material from the star into the ISM. Additionally, these stellar winds result in circumstellar envelopes (CSEs) forming around AGB stars, which are host to many interesting and complex chemical reactions.

As the amount of H and He in the shells depletes, the star reaches the tip of the AGB. Since these stars are not hot enough to fuse C to support their mass, the core contracts and becomes hotter. Stellar winds deposit more products into the CSE, and as the star continues to get hotter, the UV radiation it emits ionises the ejected atmosphere, and the object shines as a planetary nebula. The ejected shell of ionised gas continues to travel outwards. Eventually, the star starts to cool, and ceases to produce enough UV radiation to ionise the nebula. The plasma recombines and becomes transparent due to this process and no longer emits. The central stellar remnant cools as a white dwarf, composed primarily of electron-degenerate C and O.

Throughout this entire process, the star has converted primordial H and He into heavier elements through nucleosynthesis. These products are eventually deposited into the ISM. Higher mass stars (above 8 $M_\odot$) can fuse C and slightly heavier elements, including O, Ne, and Si. The heaviest elements in our Universe are naturally synthesised in explosive supernovae (SNe). Over time, the ISM has been continually enriched by processes during stellar evolution, and these characteristics can be observed in the spectra of stars that formed from this enrichment.

1.2.2 *Stellar populations and abundances*

It was a crucial discovery of astronomy in the 1900s that not all stars share the same chemical composition. This led to the discovery of other concepts, such as the importance of chemical composition in stellar evolution (Kippenhahn, Weigert, and Weiss, 2012) and the link between atmospheric composition and birth environment, allowing modern studies to study chemodynamical evolution of our Galaxy (Anders et al., 2014). All stars observed so far have metals (elements heavier than H and He) in their atmospheres. The abundance ε of an element A is defined logarithmically as a ratio of its number density N to that of H

$$\log_{10} \varepsilon(A) = \log_{10}(N_A/N_H) + 12, \tag{40}$$

where $\log_{10} \varepsilon(H)$ is defined to be 12. Stellar abundances are usually presented in comparison to the solar metallicity using a bracket notation

$$[A/H] = \log_{10} \varepsilon(A_*) - \log_{10} \varepsilon(A_\odot). \tag{41}$$

The metal content, or metallicity, is usually defined as the ratio of Fe to H (Hinkel, Young, and Wheeler, 2022)

$$n_{Fe/H} = \log_{10}(N_{Fe}/N_H)_* - \log_{10}(N_{Fe}/N_H)_\odot. \tag{42}$$

A value of $[Fe/H] = -3$ therefore corresponds to an iron abundance of 1/1000 compared to the solar iron abundance. It is useful to consider metallicities and abundances in comparison to our Sun by means of Eq. 41. Table 5 highlights the common terminology presented in Beers and Christlieb (2005). In doing so, it is important to understand our ruler, that is, the solar abundances we use in comparison. These have changed significantly throughout the years as observational and modelling techniques have improved our understanding of the solar conditions. In Chapter 2, we will investigate the

Table 5: Names given to metallicity ranges for stars of super- and sub-solar metallicity. See Beers and Christlieb (2005) and Frebel (2010) for more details on the classification scheme. The classifications highlighted in bold are those studied closely in this work, particularly in Chaps. 3, 4 and 6.

Abbreviation	Terminology	Metallicity ([Fe/H])
SMR	Super metal-rich	$\geqslant 0.5$
Solar	**Solar**	~ 0.0
MP	Metal-poor	$\leqslant -1.0$
VMP	**Very metal-poor**	$\leqslant -2.0$
EMP	**Extremely metal-poor**	$\leqslant -3.0$
UMP	Ultra metal-poor	$\leqslant -4.0$
HMP	Hyper metal-poor	$\leqslant -5.0$
MMP	Mega metal-poor	$\leqslant -6.0$

solar Si abundance in greater detail and come to understand why discrepancies exist between various analyses. That being said, the solar abundances adopted today by various groups differ only slightly due to the availability of high-precision data and significant improvements in modelling techniques. In many works, the standard solar abundances put forward by Asplund et al. (2009) were used. These were updated from the previous standard solar abundances by Asplund, Grevesse, and Sauval (2005). Other solar abundance sets, including the one used in this work, come from Anders and Grevesse (1989), Caffau et al. (2011a), Grevesse et al. (2010), Grevesse and Sauval (1998), and Lodders (2019).

In the beginning, the Universe was composed simply of H, He and trace amounts of Li (Alpher, Bethe, and Gamow, 1948; Peebles, 1966; Steigman, 2007). Every heavier element was nucleosynthesised in the cores of stars through fusion, or through various processes during SNe. It stands to reason, then, that each new generation of stars further enriches the ISM. Older stars would then generally be more metal-poor, while younger stars would be more metal-rich. We can group similar stars together as populations, since stars that share a birth environment are likely to have similar chemical compositions and ages.

The concept of stellar populations was first introduced by Jan Oort in 1926 and further developed into the modern categories by Walter Baade in 1944 (Baade, 1944). The three categories, or populations, are: young, metal-rich Population I (Pop I) stars; older, metal-poor Pop II stars; the hypothetical oldest Pop III stars, which would be the first few generations of stars in our Universe. Only a few hundred million years after the Big Bang, these first stars would from just H, He and trace amounts of Li. They would be extremely massive and luminous, lighting up the Universe and helping to trigger the phase of reionisation (Sokasian et al., 2004). While Pop III stars have not been directly observed (yet!), their presence is inferred from our understanding of stellar evolution and cosmology (Fosbury et al., 2003). However, as they would likely have masses upwards of several hundred solar masses, these stars would only survive for a few million years (Ohkubo et al., 2009). It is possible that some of these massive Pop III stars were also surrounded by lower mass stars (Krumholz et al., 2009). These stars would only be able to survive into the modern-day Galaxy if they had been ejected from their birth cluster before they exceeded $\sim$ 0.8 $M_{\odot}$ (Dutta et al., 2020). While none of these stars have been observed to date, newer operations from state-of-the-art telescopes such as James Webb Space Telescope (JWST) (Rydberg et al., 2013) and spectroscopic surveys

such as SDSS-III [2] may provide us with the first observations of these ancient relics of the primordial Universe.

Since metallicity is a proxy for the age of a star, we can study Pop I and II stars' atmospheres to gain insights into their birth environments. For this, it is important to consider low-mass stars with radiative cores and convective envelopes. In Chapter 3 we will focus on metal-poor and carbon enhanced metal-poor (see Sec. 1.2.3) dwarf stars, while in Chapter 4 we will investigate the atmospheres of giant stars. In both cases, though, we consider stars around solar mass. It is primarily the convective envelope, and specifically the photosphere, that we are interested in studying. Due to a chemical potential μ-barrier, shear forces from differential rotation and magnetic field effects, material from the core and envelope do not mix while a star remains on the main sequence (Garaud, 2020). Giant stars experience dredge-up events where material from the core is mixed into the envelope, though we can still use metals formed past the iron peak to answer questions about their origin. All in all, the atmospheric content of a star provides a wealth of information about its potential formation and age.

1.2.3 *Chemically peculiar stars*

In short, our reasons for studying the atmospheres of metal-poor stars is to understand the conditions of the early Universe. Metal-poor stars provide fundamental limits on various aspects of study within astrophysics. Some of these include the amount of Li present just after the Big Bang (Beers and Christlieb, 2005), the nature of the first stars in the Universe (Bromm and Larson, 2004), the distribution of masses associated with star formation in the early Universe (Chabrier, Hennebelle, and Charlot, 2014; Salpeter, 1955), and the astrophysical sources of heavy elements associated with neutron-capture prediction (Meyer, 1994). Some of these stars have interesting discrepancies in the metal contents of their atmospheres; these are known as chemically peculiar stars. This term is often used to describe hotter, MS stars generally of spectral type A or B (Preston, 1974). However, since we are interested in cool stars, we will use this term to mean stars later than type G (usually off of the MS). Some examples of these stars include carbon stars (Keenan and Morgan, 1941), S-type stars (Keenan, 1954) and barium stars (Bidelman and Keenan, 1951).

In the case of carbon and S-type stars, the peculiarities stem from a mixing of elements from the core to the surface (McClure, 1985). Carbon stars are typically luminous AGB stars with more C than O in their atmospheres. In the atmosphere, these form into the stable molecule CO. Since O is less abundant, only C remains in excess, and it is these absorption features we primarily observe (Keenan, 1993; Keenan and Morgan, 1941). S-type stars contain absorption features that are typical of elements from the slow neutron capture process (s-process) (Keenan, 1954; MacConnell, 1979). These stars have generally equal quantities of C and O. Barium stars and some S-type stars are the result of mass transfer from a binary system (McClure, 1985). Both show enhancements in s-process elements, though barium stars further show stronger CH, CN and C_2 absorption features.

Further interesting trends emerge when we consider increasingly metal-poor stars and their potential chemical peculiarities. We observe larger-than-expected (from metallicity) carbon abundances as metallicity decreases, and in some cases, enhancements in other heavy elements (Beers and Christlieb, 2005; Frebel and Norris, 2013). We will focus on these carbon enhanced metal-poor (CEMP) stars in greater detail. Table 6 describes the different subclasses of MP and CEMP stars. At lower metallicities, atomic spectral

2 https://www.sdss3.org/surveys/

Table 6: Definitions for subclasses of metal-poor stars consolidated from Beers and Christlieb (2005), Aoki et al. (2013) and Frebel and Norris (2013). These are operational definitions useful in this work due to the nature of the chemical compositions studied in Chaps. 3, 4 and 6.

Neutron-capture-rich stars	
r-I	$+0.3 \leqslant$ [Eu/Fe] $\leqslant +1.0$ and [Ba/Eu] < 0
r-II	[Eu/Fe] $\geqslant +1.0$ and [Ba/Eu] < 0
s	[Ba/Fe] $\geqslant +1.0$ and [Ba/Eu] $> +0.5$
r/s	$0.0 <$ [Ba/Eu] $< +0.5$
Carbon-enhanced metal-poor (CEMP) stars	
CEMP	[C/Fe] $\geqslant +0.7$
CEMP-r	[C/Fe] $\geqslant +0.7$ and [Eu/Fe] $\geqslant +1.0$
CEMP-s	[C/Fe] $\geqslant +0.7$, [Ba/Fe] $\geqslant +1.0$ and [Ba/Eu] $> +0.5$
CEMP-r/s	[C/Fe] $\geqslant +0.7$ and $0.0 <$ [Ba/Eu] $< +0.5$
CEMP-no	[C/Fe] $\geqslant +0.7$ and [Ba/Fe] < 0.0

lines become fainter and most of the absorption features are in molecular lines. Fig. 14 shows this trend for similar MS dwarf stars at different metallicities. It is therefore important to consider the effects influencing the formation of molecular features. In this work, particularly in Chaps. 3 and 4, the question of whether molecular species can form into chemical equilibrium in the atmospheres of metal-poor cool stars is addressed.

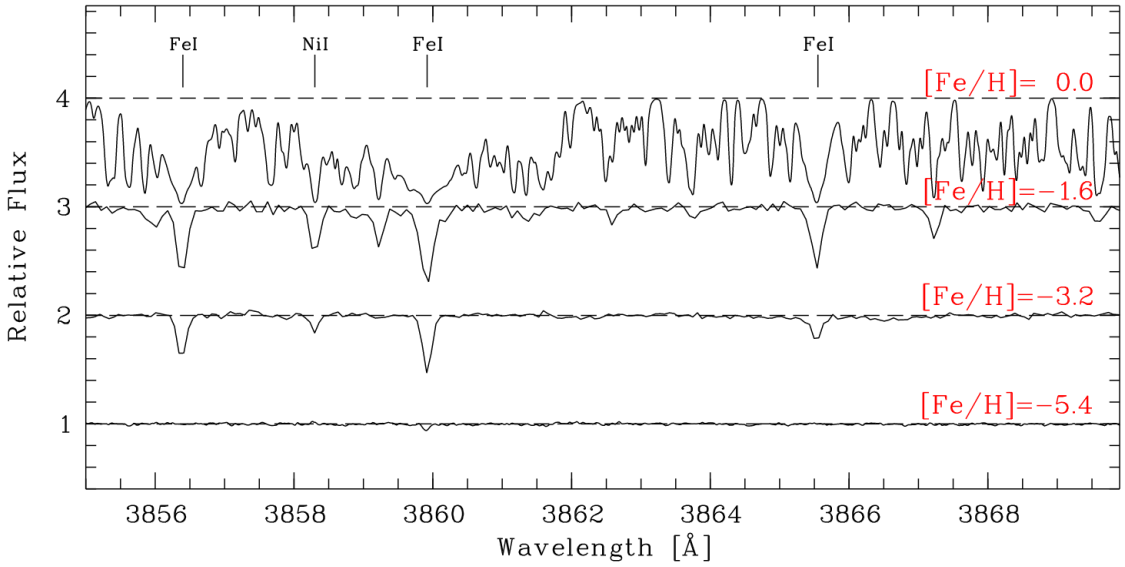

Figure 14: Spectra of MS dwarf stars with varying metallicities. The top panel shows the Sun. Note the reduction, and eventual absence of atomic spectral lines in the region as metallicity decreases. Original: Fig. 1 from Frebel (2010).

Beers and Christlieb (2005) published the first comprehensive review that standardised definitions of CEMP stars. They defined metallicity thresholds from [Fe/H] $= 1.5$ all the way down to [Fe/H] $= -6.0$. At the time of their writing, the abundance range of discovered stars covered $-5.4 \leqslant$ [Fe/H] $\leqslant 0.5$. Now, the lowest metallicity star we have detected is SMSS J0313-6708, found by Keller et al. (2014). The exact metallicity is un-

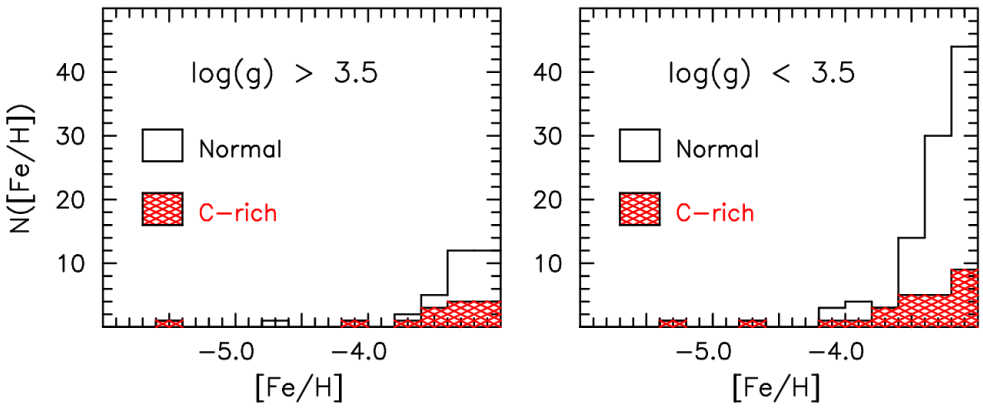

Figure 15: Histogram of stellar metallicity for the dwarf stars (left) and giant stars (right) from Frebel (2010). Red dashed bars indicate C-rich objects. Note the trend of increasing C-rich objects as metallicity decreases, despite the decreasing number of objects at lower metallicity. Original: Frebel and Norris (2013).

known, since there is a complete lack of Fe in its absorption features, but the upper limit is at [Fe/H] $= -7.1$. This star is also carbon enhanced, and adds an important point to an interesting trend seen in the distribution of metallicity and carbon enhancement. We will investigate the distribution of metallicty and stellar populations in the Milky Way in Sec. 1.3.1. But first, it is important for us to understand the structure of our Galaxy.

1.3 Stellar Populations Throughout the Milky Way

We are now equipped with the knowledge required to probe the origins of stars in our Milky Way Galaxy. Let us first consider the structure of the modern Milky Way (as we observe it today), and then work backwards to understand its formation. The Milky Way is a barred spiral galaxy (Gerhard, 2002; Goodwin, Gribbin, and Hendry, 1998; de Vaucouleurs, 1964) of type Sbc in the Hubble classification. From inside out, the Galaxy consists of the Centre, the bulge, the bar, the disk (made up of the thin and thick disk and containing four spiral arms) and the halo. Stellar populations throughout the Galaxy differ, and these differences give us insights into, for example, the presence of star-forming regions (SFRs) and the sites of merger events (Balser et al., 2011; Shen et al., 2010). Using information about radial velocities and chemical gradients allow us to better understand the provenance of these populations and better constrain our understanding of the Galaxy (Anders et al., 2014; Frebel and Norris, 2013; Gaia Collaboration et al., 2022). This field of study is known as Galactic Archaeology – inferring the formation, history and evolution of the Milky Way by understanding currently ongoing processes.

1.3.1 *Milky Way Structure and Galactic Archaeology*

The first Pop III stars were extremely massive, forming from the pristine ISM material of just H, He and trace amounts of Li left over from Big Bang nucleosynthesis (Alpher and Herman, 1948). Their demise naturally led to the enrichment of the ISM with heavier metals, and the population of stars that formed from this enriched gas were the metal-poor Pop II stars. The cycle then continued, with the death of Pop II stars creating an ever more metal-rich environment for the birth of Pop I stars. In the Milky Way, older Pop II stars are primarily located in the bulge and the halo, while younger Pop I stars are predominantly in the thin and thick disk. Studies into the bulge show that a vertical

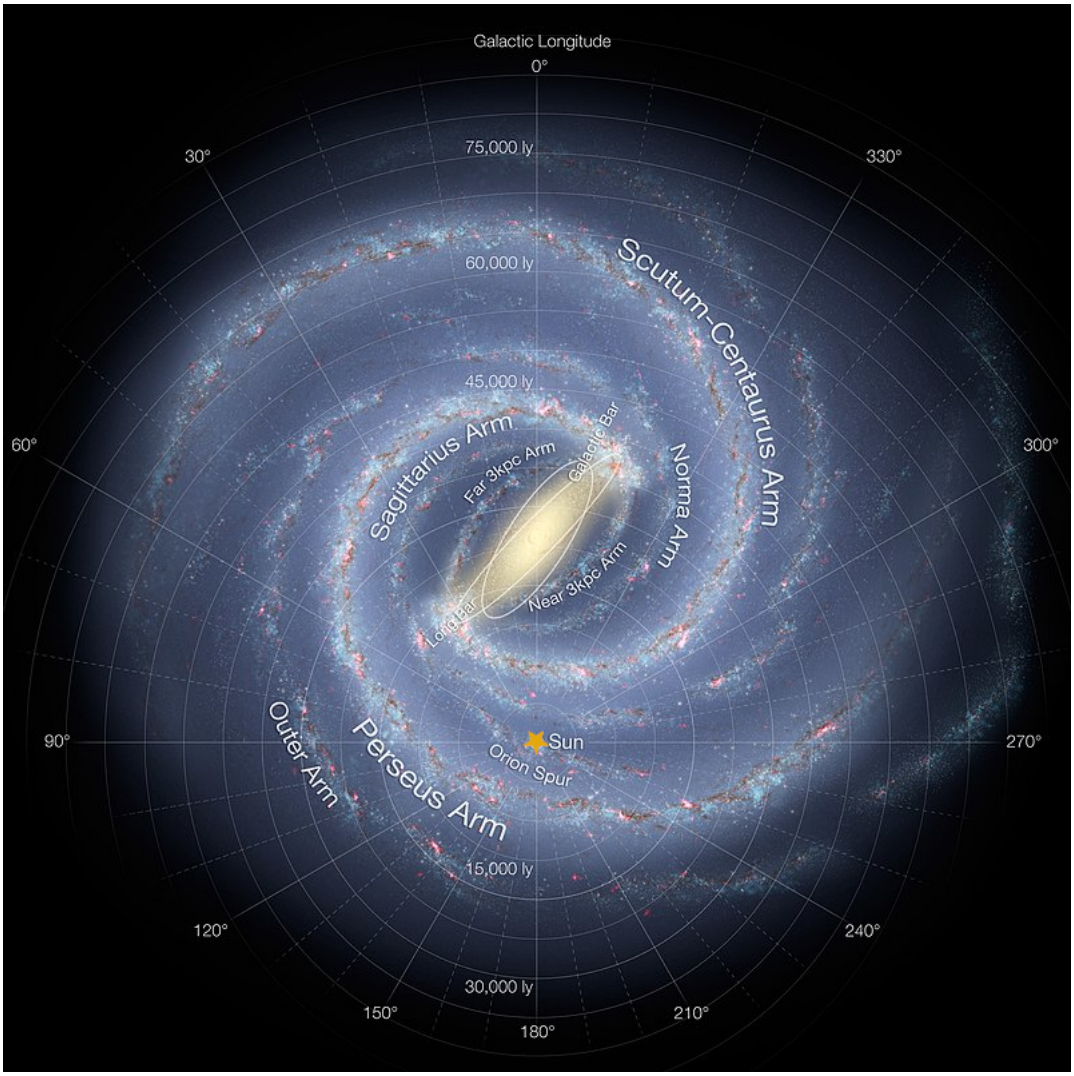

Figure 16: Artist's impression of a top-down view of our Milky Way Galaxy with the position of the Sun highlighted. Original: NASA/JPL-Caltech 2008 (author R. Hurt).

metallicty gradient is present, with metal-rich stars being in the Galactic plane and metal-poor stars existing further from the plane (Ness and Freeman, 2016). Similarly, the spiral arms are located primarily in the Galactic plane and contain more metal-rich stars than the older stars that are part of the halo. This observation already informs us of the change in star formation during the evolution of the Milky Way – in the present-day, there is not enough cool gas present in the halo and the outer bulge to facilitate effective star formation. HII regions, a tracer for recent star formation, are similarly concentrated in the spiral arms (Balser et al., 2011). It stands to reason, then, that our search for the oldest stars coincides with the search for the most metal-poor stars. Let us take a moment to consider the strucutre of the Milky Way in order to understand where these old stars are located.

The Galactic Centre contains the supermassive black hole (SMBH) Sagittarius A* (Sgr A*) with an estimated mass of $\sim 4 \times 10^6$ $M_\odot$ (GRAVITY Collaboration et al., 2019). Observations of the accretion rate of Sgr A* indicate it is an inactive galactic nucleus, though it is still an intense radio source (Kraus, Ko, and Matt, 1954). The Center is also the rotational centre of the Galaxy, with all of the Galaxy's matter revolving around the central SMBH.

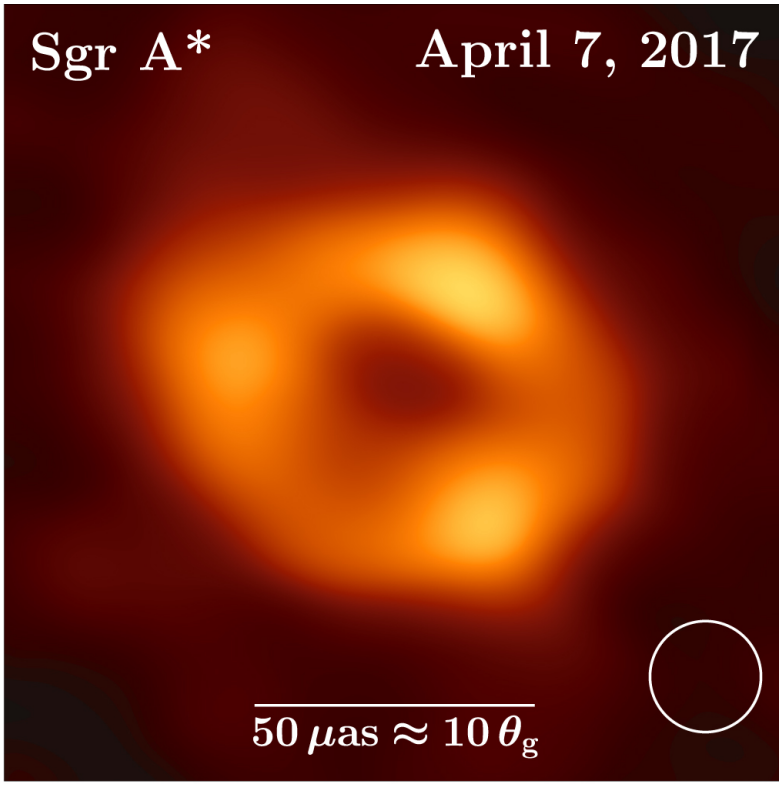

Figure 17: Representative image of the supermassive black hole Sgr A* from the Event Horizon Telescope observations on April 7, 2017. Original: Fig. 3 from Collaboration et al. (2022).

The Galactic bulge and bar describe the structure of stars within ~ 3 kpc of the Centre. It is possible that multiple bars exist (Cabrera-Lavers et al., 2008; Nishiyama et al., 2005). The bulge includes a concentration of old, Population II stars, among other stellar populations (Ness and Freeman, 2016; Vanhollebeke, Groenewegen, and Girardi, 2009). The lack of dust and gas means there is little active star formation in this region (Lian et al., 2020). A 5 kpc ring may surround the bar and would contain the majority of the molecular hydrogen and star formation activity of the Galaxy (Jackson et al., 2006; Kolpak et al., 2002). Through the study of a particular globular cluster HP1, the bulge appears to be approximately 12.8 Gyr old (Kerber et al., 2019).

Surrounding these features are the spiral arms contained within the disk of the Milky Way that primarily host Population I stars. The two major spiral arms are the Perseus Arm and the Scutum-Centaurus Arm (Benjamin, 2008). While there are more spiral arms in the Galaxy, these two are considered as the major ones since they contain significantly more older stars than the other arms. These other arms are the Near 3 kpc arm, the Norma arm, the Outer arm (which contains a later-discovered extension), the Carina-Sagittarius arm, and the Orion-Cygnus arm (which contains the Solar System we call home) (Churchwell et al., 2009). The spiral arms contain greater concentrations of dust and gas, HII regions, and molecular clouds, all key ingredients for star formation (Dame, Hartmann, and Thaddeus, 2001; Russeil, 2003). The exact structure of these spiral arms is not fully known, with various suggested pitch angles of the arms (Drimmel, 2000; Levine, Blitz, and Heiles, 2006) and suggestions that the Milky Way may contain multiple spiral patterns (Mel'Nik, 2005; Mel'nik and Rautiainen, 2009).

We can also divide this disk containing the arms into the thick and thin disk based on kinematics, stellar number densities and chemical compositions (Bensby and Feltzing,

2010). The evolution (or co-evolution) of the disks is still an active field of research (Gent et al., 2022a). Thick disks are found in many disk galaxies (Burstein, 1979), and it was first considered to be a separate galactic structure in 1983 (Gilmore and Reid, 1983). Stars in the thick disk are overall more metal-poor (Kordopatis et al., 2011). The origin of the Milky Way's thick disk is not entirely clear, though various formation scenarios have been considered, including merger events and stellar migration (Kasparova et al., 2016; Schönrich and Binney, 2009; Villalobos and Helmi, 2008). Thin disks are a property of spiral and lenticular galaxies, and the stars here are generally younger and more metal-rich (Sparke and Gallagher, 2000, 2007). More recently, the nature of the formation and content of the disks has been studied. The Milky Way's thick disk contains older, metal-poor stars inside the solar radius (within 8 kpc), but younger, metal-rich stars outside of it (Bensby et al., 2011; Martig et al., 2016). The Milky Way's thin disk may have formed from a collision with a small satellite galaxy approximately 8.8 Gyr ago (Peloso et al., 2005; Sparke and Gallagher, 2007). The Milky Way disk contains a large amount of active star formation, and about 85% of stars in the Galactic plane are located in the thin disk (Allende Prieto, 2010).

Open clusters are similarly mainly located in the disk (Janes and Phelps, 1994). These are clusters of stars that formed from the same giant molecular cloud, providing good constraints on their ages and chemical compositions. They are loosely gravitationally bound, and can be disrupted by encounters with other clusters and gas as they orbit through the Milky Way, which can expel cluster members (Karttunen et al., 2017). Furthermore, many are inherently unstable due to the relatively weak mutual gravitational attraction between members, and they vanish on timescales of a few million to a few hundred million years (Hills, 1980; de La Fuente Marcos, 1998). Open clusters are quite useful for investigating stellar evolution since the various cluster members share important properties such as age, chemical composition, velocity and visual extinction, meaning the variations between members can be isolated to their masses (Carroll and Ostlie, 2014). Young open clusters that are still within their natal molecular cloud illuminate it with the radiation pressure from the newly-formed stars, creating a HII region (Anderson et al., 2009). This is a key feature for tracking star formation throughout the Galaxy, (Bok, 1948; Yun and Clemens, 1990).

The halo is the outermost region of the Milky Way and contains mostly older, Population II field stars and globular clusters (GCs). Most of these are within 30 kpc of the Galactic Centre (Harris, 1996) and around 40% of the globular clusters move on retrograde orbits (Dauphole et al., 1996). GCs are more gravitationally bound than open clusters, as they contain hundreds of thousands of stars in higher densities than seen in open clusters (Gratton et al., 2019). There is no active star formation in the Galactic halo, as there is little cool gas that can result in cloud collapse (Sparke and Gallagher, 2007). Interestingly, modern observations show that nearly all of these clusters have multiple populations (Bastian and Lardo, 2018; Milone and Marino, 2022). In stellar clusters, we assume that all stars are roughly the same age, since they would have formed from the same giant molecular cloud. However, the multiple population suggests that stars in GCs do not all come from the same single star-formation event. The GCs in our Galactic Halo furthermore show differences in composition, and it is likely that these GCs came from interactions and mergers between the Milky Way and the multiple dwarf galaxies that surround it (Kravtsov, 2001). Concerning formation, metal-poor clusters are associated with the Galactic Halo, while metal-rich ones are associated with the Bulge (Harris, 1976).

The existence of many metal-poor GCs in the same plane in the halo supports the idea that these clusters were not all made in-situ in the Milky Way, but were rather captured from a satellite galaxy (Yoon and Lee, 2002). The study of the stars within these clusters

therefore informs our understanding of the dynamics of the Milky Way and its satellite galaxies, as well as the history of star formation within it. These old, metal-poor halo stars are thus integral to understanding the formation and migration of stars in our Galaxy.

Overall, then, the search for the oldest stars will take us to GCs in the Galactic Halo and stars in the Bulge. GCs in the Galactic Halo contain some of the oldest stars in the Galaxy (some so old that they help constrain the known age of the Universe (Bonifacio et al., 2018; Caffau et al., 2011b; Cayrel et al., 2001; Cowan et al., 2002; Ishigaki et al., 2014)). The analysis of the multiple populations of GCs with their kinematic data provides vital information about merger events and interactions (Bekki and Freeman, 2003; Johnson et al., 2020). H-R diagrams of GCs are useful for determining overall properties of the cluster, such as its age. The H-R diagram of a single GC has the interesting property that all stars have roughly the same age, and therefore the independent parameter is the mass. As stellar evolution is governed by mass, with the highest mass stars evolving into giants first, the point at which stars "turn off" of the MS to become giants (the "main-sequence turnoff") can be used to precisely determine a cluster's age (Carroll and Ostlie, 2014; Gontcharov et al., 2021). This lets up build up a picture of age vs chemical composition (or metallicity).

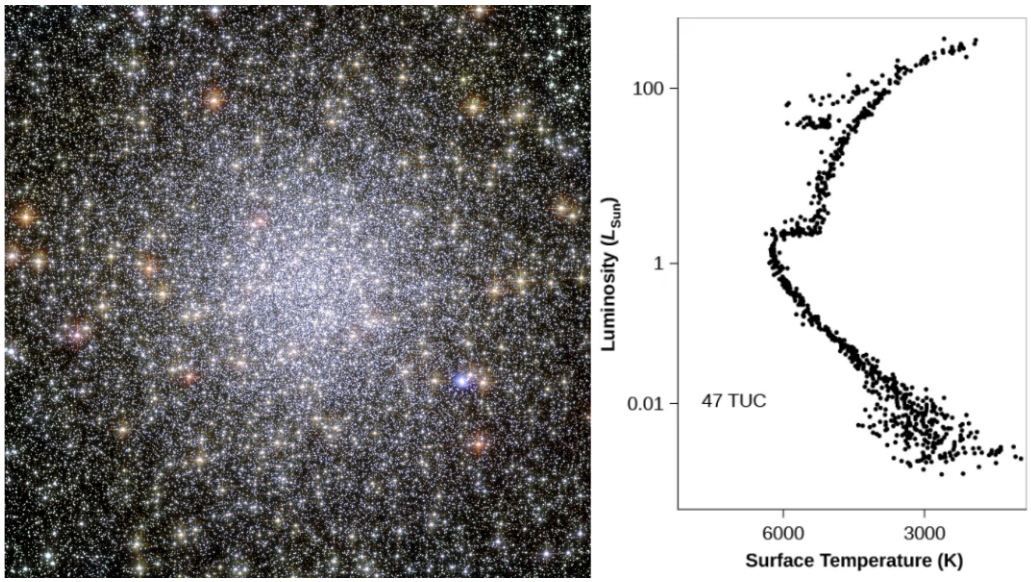

Figure 18: Image of the globular cluster NGC 104 with its associated H-R diagram. Original from OpenStax (2022), image credit NASA, ESA, and the Hubble Heritage (STScI/AURA)-ESA/Hubble Collaboration.

1.3.2 *Chemical Enrichment of the Milky Way*

While the metal content of a star is generally referenced by the ratio of Fe to H, chemical peculiarities in other elements yield insights into other internal and external processes. For example, the presence of excess α-process elements in cool, MS stellar atmospheres informs us that the ISM was previously enriched by them, since these stars would not have sufficient core temperatures to initiate C fusion. α-elements consist of integer number of alpha particles, (hence an even number of protons), imprinting a characteristic "odd-even" elemental abundance pattern. Notable examples are C, O, Mg, Ne, and Si. The most reasonable sources for this enrichment are massive AGB stars, whose stellar ejecta are carried by stellar winds and deposited into the ISM (Boulangier et al., 2019),

and supernovae (Kobayashi, Karakas, and Lugaro, 2020; Truran, Cowan, and Cameron, 1978; Truran and Heger, 2003). α-enrichment is therefore a key indicator of external historic enrichment of the ISM.

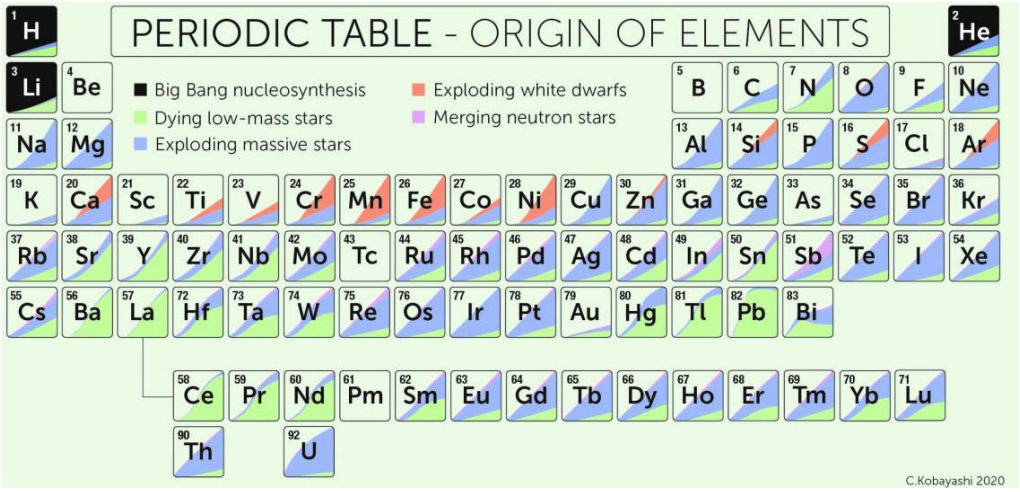

Figure 19: The origins of the elements coloured by nucleosynthetic sites. Original: Kobayashi, Karakas, and Lugaro (2020).

Similar indicators are elements formed through the slow (s) and rapid (r) process. Approximately half the elements heavier than Fe are formed via the s-process, and another half by the r-process. The s-process is known to occur primarily in AGB stars (Burbidge et al., 1957; Kaeppeler et al., 1982). s-process elements in a cool star's atmosphere therefore suggest the ISM was enriched by the stellar wind of an AGB star. During the s-process, α and β^- decay results in the formation of specific elements, thereby imprinting a unique signature whose astrophysical source can be ascertained to this process. The same logic allows us to find elements produced by the r-process. This process can only occur through heavy bombardment of neutrons without being interrupted by radioactive decay. It can therefore only occur in regions with a high density of free neutrons. The most prevalent sources are supernovae and neutron star mergers (Kasen et al., 2017; Thielemann et al., 2011).

In summary, Big Bang nucleosynthesis formed H, He and trace amounts of Li. From these, heavier elements were then primarily synthesised in stars (Alpher and Herman, 1948). During a star's lifecycle, these heavier elements can be deposited into the ISM, enriching the next generation of stars. There are three primary channels of metal enrichment from stellar evolution (Burbidge et al., 1957):

1. Intermediate mass stars: Stars with a mass $0.5M_\odot \leqslant M <\sim 6M_\odot$ produce mainly C, O, other α-elements, and s-process elements that are brought to the surface and lost in a stellar wind or planetary nebula when star enters AGB.

2. Massive stars: Stars with a mass $M \geqslant 6\ M_\odot$ burn He ashes hydrostatically yielding predominantly α-elements. These stars explode as core-collapse Type II SNe with r-process and trans-Fe elements produced through nucleosynthesis.

3. Type Ia SNe: These SNe result in significant Fe yields and are plausibly the result of mass transfer in binary star that pushes SN progenitor over Chandrasekhar limit. Negligible amounts of α-elements are produced.

α-, s- and r-process elements therefore provide information of different astrophysical events that occurred prior to the formation of the star under observation. It is particularly important to study metal-poor stars here, since the enrichment by r- and s-process

elements in these stars will come from just a handful (and perhaps only a single) nucleosynthetic event (Frebel and Ji, 2023), allowing for more precise estimates when searching for the oldest stars in the Galaxy.

Another mystery is the increasing amount of carbon enhancement ([C/Fe]) towards decreasing metallicity. The origin of carbon-enhanced metal-poor (CEMP) stars is a topic still under investigation (Hansen et al., 2016; Rossi et al., 2023; Sharma et al., 2018; Sivarani et al., 2006). Modelling techniques can help us understand the influence of various formation and enrichment processes. Sharma et al. (2018), for example, explore the effects of the three channels of metal enrichment using the EAGLE suite of simulations (Planck Collaboration et al., 2014; Schaye et al., 2015). They find two pathways to form CEMP stars, distinguished by the [C/O] ratio. The first comes from AGB stars, which synthesise C more predominantly than O, resulting in [C/O] > 1. Stellar winds deposit the enriched material into the ISM, which reflects the original pattern. As such, it is possible that the stars are not necessarily C-rich, but rather O-poor. This is further supported by Type II SNe which result in enrichment in both C and O. The enrichment of a generation of stars assumes that the enriching materials have had sufficient time to mix throughout the gas cloud. If however, there are times when star formation is bursty and times when there is little to no star formation due to the lack of pristine gas, there can be sufficient time for enriching material to mix with new accreting gas, and the following generation of stars will reflect the history of enrichment.

The second pathway concerns stars with [C/O] < 1, but still having [C/Fe] > 1. Massive stars can enrich the ISM with material that exhibits these properties. Over time, lower mass Type II SNe will shift the pattern more towards the solar case. However, the first, massive progenitors can enrich the ISM on timescales faster than required for the first AGB events in the Galaxy. As such, a population of stars with [C/Fe] > 1 but [C/O] < 1 emerges. The C/O ratio is a useful tracer of formation processes and also affects processes during a star's lifetime (Akerman et al., 2004; Nakajima and Sorahana, 2016), and can even result in trends for planet formation (Nissen, 2013; Teske et al., 2014). Understanding the relevance of various enrichment processes is therefore paramount in piecing together a larger picture of our Galaxy. The search for pristine metal-poor stars samples goes hand-in-hand with unraveling the mystery of the Galaxy's formation.

In Chapters 3 and 4 we will investigate a different aspect of CEMP stars, namely the effects of chemical composition on the photospheric chemistry. We will utilise state-of-the-art stellar convection simulations to explore whether the observed effect of carbon enhancement might result from an incorrect assumption of chemical equilibrium, and see again how the C/O ratio plays a vital role.

1.4 Modelling techniques for stellar atmospheres

Thus far we have built the groundwork for understanding the atmospheres of stars and the importance of their study. We will now turn our attention to the problem of modelling the complex processes that occur within, and shape, a stellar atmosphere. Primarily, we will concern ourselves with the convection zone, photosphere and low chromosphere. To properly model the phenomena that occur in these regions, such as convection and spectral line formation, it is necessary to introduce concepts in (magneto)hydrodynamics, radiation transfer, and thermodynamics. These are presented in the context of the stellar atmosphere code CO^{5}BOLD(Freytag et al., 2012), a finite-volume magnetohydrodynamics solver which additionally models radiation transport and chemical kinetics.

The modelling techniques introduced here are presented as background for the techniques used in this work. Specific details are presented in: Chapter 2 for spectroscopic

modelling; Chapter 3 for chemical kinetics and coupling to hydrodynamics; Chapter 5 for machine learning techniques in spectroscopy; Chapter 6 for neural network techniques for solving systems of differential equations.

1.4.1 *(Magneto)hydrodynamics*

In the regions of interest, we would like to model the dynamics of a plasma. The equations of fluid dynamics and radiation transport will form the basis of modelling the structure of the atmosphere. Here, we will consider the Newtonian (non-relativistic) limit and introduce the equations in the context of the finite-volume solver `CO5BOLD`(Freytag et al., 2012). From the general set of Navier-Stokes equations, the equations of Eulerian hydrodynamics are often used to model most astrophysical fluid flows (Calder et al., 2002).

For convenience, let the Cartesian coordinates (x, y, z) be represented as $(x_1, x_2, x_3) = \mathbf{x}$. The velocity field $\mathbf{v}$ is then given by

$$\mathbf{v} = (v_1, v_2, v_3)^T = \left(\frac{dx_1}{dt}, \frac{dx_2}{dt}, \frac{dx_3}{dt}\right)^T \tag{43}$$

The 3D Euler equations of hydrodynamics can be expressed as conservation relations (plus source terms) for the mass density (ρ), the momentum densities (ρv_1, ρv_2, ρv_3), and the total energy density e_{tot}. There are three primary equations that govern the evolution of the fluid. These are (including source terms due to gravity) the equation of mass conservation (Eq. 44), the momentum equation (Eq. 45) and the energy equation (Eq. 46):

$$\frac{\partial \rho}{\partial t} + \nabla \cdot (\rho \mathbf{v}) = 0 \tag{44}$$

$$\frac{\partial (\rho \mathbf{v})}{\partial t} + \nabla \cdot (\rho \mathbf{v}\mathbf{v} + \nabla P) = \rho \mathbf{g} \tag{45}$$

$$\frac{\partial (\rho e_{tot})}{\partial t} + \nabla \cdot (\rho e_{tot} \mathbf{v} + P\mathbf{v}) + \nabla \mathbf{F}_{rad} = 0 \tag{46}$$

Other quantities introduced here are the gas pressure P, the gravitational acceleration source term $\mathbf{g} = (g_1, g_2, g_3)$, and the radiative energy flux $\mathbf{F}_{rad} = (F_1, F_2, F_3)$. The gas pressure is calculated from an equation of state (EOS)

$$P = P(\rho, e_{int}), \tag{47}$$

where e_{int} is the internal energy. `CO5BOLD` uses a tabulated EOS. The total energy of the system is governed by

$$\rho e_{tot} = \rho e_{int} + \rho \frac{v_1^2 + v_2^2 + v_3^2}{2} + \rho \Phi, \tag{48}$$

where Φ is the gravitational potential; $\mathbf{g} = -\nabla \Phi$.

The equations of hydrodynamics can be coupled to Maxwell's equations of electrodynamics and Ohm's law to arrive at the equations of ideal magnetohydrodynamics (MHD). Ideal MHD is a widely-used approximation for the modelling of astrophysical

plasmas, as its implication of field lines frozen into the plasma is justified due to the extremely high conductivity of the fluids (Bartelmann, 2013). Essentially, the transport of the magnetic field via advection is significantly more dominant than the magnetic-field diffusion.

Maxwell's equations group together Gauss' Law

$$\nabla \cdot \mathbf{E} = \frac{\rho_c}{\epsilon_0} \tag{49}$$

the forbiddance of magnetic monopoles

$$\nabla \cdot \mathbf{B} = 0 \tag{50}$$

Faraday's law of induction

$$\nabla \times \mathbf{E} = -\frac{\partial \mathbf{B}}{\partial t} \tag{51}$$

and the Maxwell-Ampére circuital law

$$\nabla \times \mathbf{B} = \mu_0(\mathbf{J} + \epsilon_0 \frac{\partial \mathbf{E}}{\partial t}) \tag{52}$$

where $\mathbf{E}$ is the electric field, ρ_c is the charge density, ϵ_0 is the permittivity of free space, $\mathbf{B}$ is the magnetic field, μ_0 is the permeability of free space, and $\mathbf{J}$ is the current density. Additionally, Ohm's law relates the movement of the charged particles to the induced current density on those particles:

$$\mathbf{E} + \mathbf{v} \times \mathbf{B} = \eta \mathbf{J}, \tag{53}$$

where η in this context is the electrical resistivity. The ideal MHD equations ignore resistivity due to the current density, and are mass conservation

$$\frac{\partial \rho}{\partial t} + \nabla \cdot (\rho \mathbf{v}) = 0, \tag{54}$$

the momentum equation

$$\frac{\partial (\rho \mathbf{v})}{\partial t} + \nabla \cdot (\rho \mathbf{v}\mathbf{v} + (P + \frac{\mathbf{B} \cdot \mathbf{B}}{2})\mathbf{I} - \mathbf{B}\mathbf{B}) = \rho \mathbf{g}, \tag{55}$$

the induction equation

$$\frac{\partial \mathbf{B}}{\partial t} + \nabla \cdot (\mathbf{v}\mathbf{B} - \mathbf{B}\mathbf{v}^T) = 0, \tag{56}$$

and the energy equation

$$\frac{\rho e_{tot}}{\partial t} + \nabla \cdot ((\rho e_{tot} + P + \frac{\mathbf{B} \cdot \mathbf{B}}{2})\mathbf{v} - (\mathbf{v} \cdot \mathbf{B})\mathbf{B} + \mathbf{F}_{rad}) = 0. \tag{57}$$

Eq. 50 is a solenoidality constraint that must be fulfilled. Additionally, the advective term in Eq. 56 ($\mathbf{v}\mathbf{B} - \mathbf{B}\mathbf{v}^T$) is non-zero due to the ions and electrons in the plasma being affected by the Lorentz force

$$\mathbf{F} = q(\mathbf{E} + \mathbf{v} \times \mathbf{B}), \tag{58}$$

where q is the elementary charge. The motion of the charged particles change the frozen-in magnetic field lines, resulting in a non-stationary magnetic field. The term $\mathbf{B}\mathbf{v}^T$ is the dyadic tensor product of the two vectors $\mathbf{B}$, $\mathbf{v}$ resulting in the tensor $\mathbf{C}$ with elements $c_{mn} = B_m v_n$, and the n-th component of the divergence of $\mathbf{C}$ is $(\nabla \cdot \mathbf{C})_n = \sum_n \partial c_{mn}/\partial x_m$. The total energy is now given by

$$\rho e_{tot} = \rho e_{int} + \rho \frac{\mathbf{v} \cdot \mathbf{v}}{2} + \frac{\mathbf{B} \cdot \mathbf{B}}{2} + \rho \Phi \tag{59}$$

CO5BOLD includes an MHD module that solves these equations (Freytag et al., 2012; Schaffenberger et al., 2005).

1.4.1.1 *Finite-Volume Solvers*

There are a few different common methods for solving (M)HD problems in astrophysics. Three common, similar methods for solving the set of partial differential equations are the finite-difference (FD), finite-element (FE), and finite-volume (FV) methods. In each case, the goal is to discretise the equations on a grid of some kind so that a numerical solution can be computed. For a review on these kinds of solvers, see, e.g., Ferziger, Perić, and Street (2020). FV methods, such as the one implemented in `CO`^{5}`BOLD`, utilise the divergence theorem to change volume integrals with divergence terms into surface integrals, that is:

$$\iiint_V (\nabla \cdot \mathbf{F}) dV = \oiint_S (\mathbf{F} \cdot \hat{\mathbf{n}}) dS. \tag{60}$$

As such, they are inherently conservative, as the flux of the vector field $\mathbf{F}$ (right-hand side of the equation) entering a volume is identical to that leaving the adjacent volume. FV methods evaluate exact expressions given the average values of quantities across a volume, and these are then combined to provide an overall approximate solution (LeVeque, 2002).

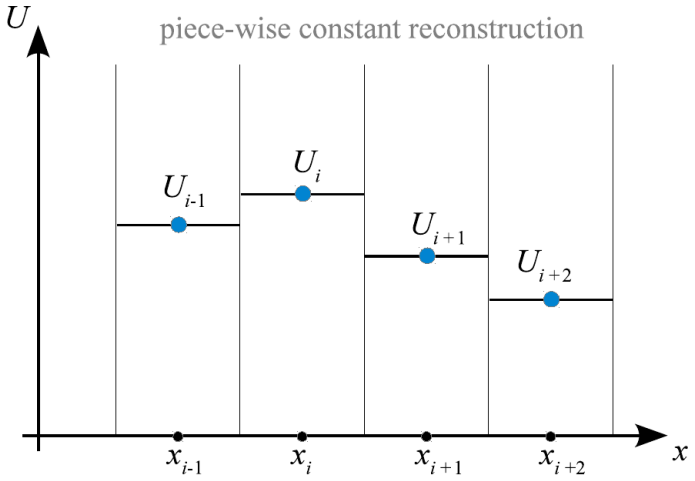

Figure 20: Finite-volume discretisation with a piece-wise constant reconstruction scheme applied to the cell-centred quantities U_i. Adapted from lecture notes at Heidelberg University (MVComp1).

Consider a 1D Cartesian grid with equidistant spacing. The value of a quantity is calculated at the centre of each grid cell and represents the average across the cell volume. However, simply using these values would lead to discontinuity between adjacent cells (see Fig. 20). FV methods use reconstruction methods to combine the cell-averaged values in order to produce a smooth, continuous function of the quantity across the domain. The order of the reconstruction scheme further determines the accuracy of the approximation (LeVeque, 2002) Certain functions (aptly named slope limiters) are used to limit the slopes computed on the state quantities (e.g. density and pressure) as these can produce spurious oscillations in the vicinity of sharp features such as shock waves.

Hydrodynamical flows often result in converging and diverging flows. In such cases, the densities, pressures and velocities are rapidly changing and introduce discontinuities in numerical solvers. It is necessary to utilise so-called shock-capturing methods (Toro, 2009) to model the characteristics correctly. In these methods, phenomena such as shock waves and contact discontinuities can be modelled correctly through the Rankine-Hugoniot jump conditions (Rankine, 1870; Toro, 2009).

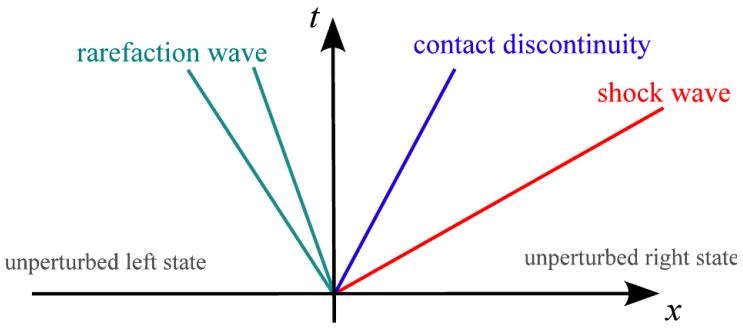

Figure 21: Characteristics of a typical Riemann problem. Adapted from lecture notes at Heidelberg University (MVComp1).

For the computation of a self-consistent stellar atmosphere, it is important to consider the conservation of mass, momentum and energy between grid cells. CO^{5}BOLD employs a FV method with directional operator splitting to reduce a 3D problem into a 1D one (Strang, 1968). From this, the approximate fluxes across each cell boundary are calculated with an approximate 1D Riemann solver of Roe type (Roe, 1986), which is modified to account for the realistic EOS, the non-equidistant grid (primarily in the vertical direction) and the presence of source terms such as gravity. The partial waves are reconstructed and advected with upwind-centred fluxes, and a slope limiter is applied to decrease the order of the scheme near discontinuities to ensure stability while preserving accuracy (Colella and Woodward, 1984; LeVeque, 1992).

1.4.2 *Radiation transport*

Convection and radiation are two primary modes of energy transport in cool stellar atmospheres. Transport via radiation becomes increasingly important in optically thin layers (above the convective zone). Radiation transport is hence an integral component of stellar atmosphere codes. CO^{5}BOLD can handle non-local radiation transport with frequency-dependent opacities κ_ν (Ludwig and Steffen, 2013). This is particularly important when creating an accurate 3D, time-dependent model for spectroscopic modelling in order to capture the intricacies introduced by the large number of spectral lines present. The basics of radiation transport were discussed in Sec. 1.1.2. Here, the finer details regarding opacities and optical depth and their implementation in stellar atmosphere codes is presented.

It is unfortunately infeasible to precisely model every spectral line present in a cool stellar atmosphere. The Sun, for example, has over 10^6 absorption features, each of which affect the overall intensity. To make the problem computationally tractable, it is necessary to approximate the true opacities. There are a few methods to do this, including multigroup methods (González et al., 2015), opacity distribution functions (ODFs) (Leenaarts, 2020), and opacity binning methods (Ludwig and Steffen, 2013). The latter is used in CO^{5}BOLD. The opacities are group-averaged and are given as a function of temperature T and pressure P

$$\kappa_\nu = \kappa_\nu(T, P). \tag{61}$$

CO^{5}BOLDuses tabulated opacities and opacity binning with an ODF that sorts opacities in a given frequency interval based on line strengths. A number of frequency bins and ODF sub-intervals can then be defined to control the accuracy of the scheme. The lower limit of frequency-independent opacity reverts to the grey approximation. More details

on the implementation in CO^{5}BOLD are presented in Freytag et al. (2012), Ludwig and Steffen (2013), and Steffen (2017).

The average opacity is necessary for computing the solution to the transport equation (Eq. 22). There are two methods of defining an average opacity, each of which are calculated using a certain weighting scheme. The Planck opacity uses the normalised Planck distribution as the weighting function,

$$B_\nu(T) = \frac{2h\nu^3}{c^2}\frac{1}{\exp(\frac{h\nu}{k_B T}) - 1}, \tag{62}$$

and averages κ_ν directly as

$$\kappa_{\text{Planck}} = \frac{\int_0^\infty \kappa_\nu B_\nu(T) d\nu}{\int_0^\infty B_\nu(T) d\nu}, \tag{63}$$

or equivalently,

$$\kappa_{\text{Planck}} = \left(\frac{\pi}{\sigma T^4}\right) \int_0^\infty \kappa_\nu B_\nu(T) d\nu \tag{64}$$

where $\sigma = 5.670374419 \times 10^{-8}$ W m^{-2} K^{-4} is the Stefan-Boltzmann constant. In CO^{5}BOLD, the source function S_ν is subject to normalisation by the frequency-integrated Planck function $B(T)$ such that

$$\sum_\nu S_\nu = B(T) = \frac{\sigma}{\pi} T^4. \tag{65}$$

The second method of defining an average opacity uses a temperature derivative of the Planck distribution

$$u(\nu, T) = \frac{\partial B_\nu(T)}{\partial T} \tag{66}$$

and is the harmonic mean of the opacity κ^{-1}, weighted by $u(\nu, T)$. This is the Rosseland mean opacity, defined as

$$\frac{1}{\kappa_{\text{Rosseland}}} = \frac{\int_0^\infty \kappa_\nu^{-1} u(\nu, T) d\nu}{\int_0^\infty u(\nu, T) d\nu}. \tag{67}$$

The Rosseland mean opacity comes from the diffusion approximation to the radiation transport equation, and is valid in deep, collision-dominant, optically thick atmospheric layers. The Planck mean opacity is preferred in higher, optically thin layers. The stellar photosphere, though, is a transition zone from optically thick to thin regions. The mean opacity to use then needs to combine both the Planck and Rosseland opacities as functions of the optical depth. In CO^{5}BOLD, the form of the overall mean opacity (at a given frequency or band i) takes the form

$$\bar{\kappa} = 2^{\left(-\frac{\tau_i}{\tau_{1/2}}\right)} \kappa_{\text{Planck}} + \left(1 - 2^{\left(-\frac{\tau_i}{\tau_{1/2}}\right)}\right) \kappa_{\text{Rosseland}}, \tag{68}$$

where $\tau_{1/2}$ is the optical depth point where both opacities contribute equally.

For coupling the radiation transfer to the (magneto)hydrodynamics, we will need expressions for the radiative energy flux F_{rad} and the change in energy. The radiative energy flux is given by

$$F_{\text{rad}} = \int_0^{2\pi} \int_0^{\pi} I \cos\theta \sin\theta d\theta d\phi \tag{69}$$

where the integral is over the polar and azimuthal angles. The change in energy is computed from the flux divergence via

$$\frac{\partial (\rho e_i)}{\partial t} + \mathbf{v}\nabla(\rho e) = -\nabla \cdot F_{rad}. \tag{70}$$

1.4.2.1 *Departures from Local Thermodynamic Equilibrium (LTE)*

A common assumption made in the study of stellar atmospheres is that of local thermodynamic equilibrium (LTE). At its core, the assumption is that there is thermodynamic equilibrium between mass particles, but not necessarily between them and the radiation (Maoz, 2016). This comes from the motivation to feasibly be able to model radiation transfer, which is a complex problem due to the various intricacies and couplings between the opacities, radiation field, and level populations, to name a few quantities. The LTE assumption essentially uses the local temperature and density to determine the distributions to use, rather than explicitly solving the complex system of coupled equations. The particles have thermal distributions, while the photon distributions can vary. The level populations of bound energy states for a single-species gas are given by the Boltzmann distribution, while the populations of free (ionised) states is given by the Saha ionisation equation. The particles follow Maxwell-Boltzmann statistics within the "local" region of concern, and this results in a Planck intensity spectrum based on the particle energies.

The Boltzmann distribution for the probability for the system to be in a given energy state i is

$$p_i = \frac{1}{Z} \exp\left(\frac{-E_i}{k_B T}\right), \tag{71}$$

where E_i is the energy of state i, k_B is the Boltzmann constant, T is the local temperature, and $Z = \sum_i^N \exp(\frac{-E_i}{k_B T})$ is the canonical partition function. The Boltzmann factor relates the ratio of probabilities of two states, or equivalently, the populations of those states,

$$\frac{n_j}{n_i} = \frac{g_j}{g_i} \exp\left(-\frac{(E_j - E_i)}{k_B T}\right), \tag{72}$$

where (n_j, n_i), (g_j, g_i), and (E_j, E_i) are the populations, statistical weights, and energies of states j and i, respectively. The Saha ionisation equation for a gas comprised of a single atomic species is commonly given as

$$\frac{n_{i+1} n_e}{n_i} = \frac{2}{\lambda_e} \frac{g_{i+1}}{g_i} \exp\left(-\frac{(E_{i+1} - E_i)}{k_B T}\right), \tag{73}$$

where n_e is the electron density, $(E_{i+1} - E_i)$ is the energy required to remove the $(i+1)^{th}$ electron, and λ_e is the thermal de Broglie wavelength given by

$$\lambda_e = \sqrt{\frac{h^2}{2\pi m_e k_B T}}, \tag{74}$$

where $m_e = 9.109383715 \times 10^{-31}$ kg is the electron mass. The Maxwell-Boltzmann distribution for particle energies is

$$f(E) = 2\sqrt{\frac{E}{\pi (k_B T)^3}} \exp\left(-\frac{E}{k_B T}\right), \tag{75}$$

where E is the kinetic energy of the particles.

The LTE assumption implies that the radiation field is in equilibrium with the local temperature field of the matter, and that the material effectively radiates as a blackbody. The source function of the transport equation (Eq. 22) is the Planck function $B_\nu(T)$ (Eq. 62). LTE holds true in collision-dominated regions, when the mean free path for collisions is small, resulting in Maxwellian velocities, and photons are essentially trapped. The convective zone and optically thick photosphere are examples of such regions. As the material becomes optically thin in higher layers of the atmosphere, it is clear that material properties vary greatly over the course of a photon's mean free path. Hence non-local radiation transport becomes increasingly important to consider, and application of the strict LTE assumption could lead to serious errors in calculations. See Hubeny and Mihalas (2015) for further details for modelling radiation transport in stellar atmospheres.

In optically thin regions, the population statistics can be far from the equilibrium imposed by Saha-Boltzmann statistics, and it becomes necessary to solve kinetic equations alongside radiative transfer to converge to the correct solution. This departure from LTE is known as radiative non-LTE (NLTE), and many works have explored the effects of this on various atomic and even molecular species (Amarsi et al., 2019a; Gerber et al., 2022; Mashonkina, 2020; Popa et al., 2022; Shchukina, Sukhorukov, and Trujillo Bueno, 2012; Steffen et al., 2015). Radiative NLTE calculations have proven to be very useful in determining the correct statistical equilibrium of a species in a given atmosphere. However, most studies still consider a single or a few species since the calculations are computationally expensive – even more so in 3D. Additionally, this is a stationary solution. Another way to analyse the implications of LTE is to perform a time-dependent chemical kinetic analysis alongside the hydrodynamics and radiation transfer. This answers the question: is there sufficient time for molecular species to form to their equilibrium values?

Most studies of stellar photospheres assume that the molecular and atomic species are in a chemical equilibrium, that is, there has been sufficient time for all species to react and for the system to reach the minimum Gibbs free energy state (at constant temperature and pressure (Goodstein, 1985)). Hydrodynamical processes (such as convection) can disrupt this evolution by advecting species or by significantly changing the local thermodynamic conditions such that a new minimum energy state would exist. While the assumption of chemical equilibrium is well established in the solar photosphere (Wedemeyer-Böhm et al., 2005, 2006), this assumption is called into question for metal-poor atmospheres. Reaction rates are highly dependent on the number densities of species, so in an atmosphere with 10^2 times fewer species ($[\mathrm{Fe/H}] = -2$), reaction rates are at least 10^2 times slower. In Chapter 3 these calculations are done for MP and CEMP atmospheres to see the potential implications of the LTE assumption.

By implementing a chemical kinetics solver, we hope to gain practical predictive ability as to the evolution of species within the system. Some key questions are **i)** which reactions proceed to products, **ii)** the timescales of individual reactions and how long reactants / products remain before reacting, and **iii)** which reactions drive the overall system.

The solver should be able to evolve a system of initial species to a certain specified state by considering the reactants, products, and the rates of formations of each. In essence, this becomes a system of reaction equations plus the constraint conditions (such as mass conservation). Due to the vast differences in reaction rates, the system will be stiff, so a solver that handles this property efficiently and stably should be chosen.

In the stellar atmosphere, convective motions can advect parcels of gas before they can reach their equilibrium state. It is therefore necessary to consider the time-dependent

evolution of the chemical system. The steady-state solution of a set of chemical species connected by reaction pathways can be found by calculating the time evolution of the system of equations formed from the reactions. This steady-state solution has the number of reactants and products constant over time. In the case of a closed system, then, this is equivalent to chemical equilibrium, and will yield the same equilibrium abundances as in Gibbs energy minimisation. Note that the complexity of the evolution scales primarily with the number of species, but also with the number of reactions.

Every chemical reaction progresses at a certain rate, specified with a rate constant (rate coefficient). The reaction rate expression relates the concentration of species to the rate of the reaction. Consider a reaction

$$aA + bB \rightarrow cC + dD. \tag{76}$$

This is equivalently

$$0 = -aA - bB + cC + dD. \tag{77}$$

The prefactors a, b, c are stoichiometric coefficients (defined as negative for reactants and positive for products). The evolution of this reaction is governed by

$$\frac{1}{a}\frac{d[A]}{dt} = \frac{1}{b}\frac{d[B]}{dt} = \frac{1}{c}\frac{d[C]}{dt} = \frac{1}{d}\frac{d[D]}{dt} \tag{78}$$

since a moles of species A are used with b moles of species B to form c moles of species C. [X] is the number of moles of species X. If the reaction takes place in a closed system at constant temperature and volume, and there is no buildup of reaction intermediates, its reaction rate v is given by

$$v = \frac{1}{\nu_i}\frac{d[X_i]}{dt}, \tag{79}$$

where ν_i is the stoichiometric coefficient for species X_i. The initial reaction rate (which is specified at the start of a chemical kinetics calculation), has some functional dependence on the concentrations of the reactants, and is typically determined experimentally; for the above reaction

$$v_0 = f([A], [B]). \tag{80}$$

This dependence is termed the *rate equation* or *rate law*, and often takes the form of a power law. For the above reaction, we have

$$v_0 = k(T)[A]^x[B]^y. \tag{81}$$

k is the temperature-dependent rate coefficient and the indices x, y are the partial orders of the reaction: their sum is the overall order of the reaction. Sec. 3.2.1 includes an in-depth discussion on these methodologies in the context of MP and CEMP atmospheres.

1.4.3 *Spectroscopic modelling*

Determining parameters from stellar spectroscopy requires a firm grasp of the physics present within a spectral line profile. In a laboratory setting, a spectral line would appear as a perfect Dirac delta peak, but in the atmospheres of stars, thermal, Doppler and atomic broadening effects shape the line core and the wings. By studying the shape of these spectral lines and analysing the physical effects contributing to its strength and

broadening, we can determine parameters such as stellar abundances, surface gravity and temperature. However, to do so accurately is not a completely objective task. There are many choices to be made during the analysis, such as the choice of observational material as well as which spectral lines to use. Moreoever, the entire process is further complicated by noise and blending lines that obscure the primary feature and make it difficult to extract details.

In Chap. 2, we will present a full end-to-end analysis of the solar silicon abundance determined using the model atmosphere code CO^{5}BOLD and spectral synthesis code LINFOR3D . For now, we will consider the generalised approach of synthesising a realistic stellar spectrum which we can use to analyse observations.

There are many codes for synthesising the formation of a stellar spectrum. Some notable examples include TurboSpectrum (TS) (Gerber et al., 2022; Plez, 2012), LINFOR3D (Gallagher et al., 2017b), and MULTI3D (Amarsi et al., 2018; Leenaarts and Carlsson, 2009). Each of these codes takes a model stellar atmosphere (the quantities describing the structure of the atmosphere) and information about the various absorbing species (atomic and molecular data) as an input, and produce an output spectrum in the desired wavelength or frequency range. These can be compared to observations in an iterative process in order to determine stellar abundances. TS operates on 1D model atmospheric inputs (either the output from a 1D stellar atmospheric model or a 3D model averaged to 1D), while both LINFOR3D and MULTI3D can operate on 3D inputs.

1.4.4 *Machine learning methods*

In recent years, machine learning (ML) and artificial intelligence (AI) methods have taken off in almost every field. Particularly recently, large language models (LLMs) have revolutionised natural language processing tasks, and are quickly making their way into many other domain-specific applications (Bubeck et al., 2023; Taori et al., 2023; Touvron et al., 2023). Though still new compared to conventional modelling techniques, it can be argued that AI had its start with Claude Shannon and his mechanical labyrinth-solving mouse, Theseus [3]. This was the early 1950s, and the ideas of ML and AI were still very much in their infancy – particularly when it came to involving computers. Theseus the mouse was able to solve mazes even when placed in arbitrary locations and in unfamiliar territory by utilising clever search algorithms and a system to add new locations to its memory. This process of developing a system that learns directly from the data it is presented is one of the cornerstones of machine learning and data-driven approaches. Note that other pioneers worked on similar projects at this time – Warren McCulloch and Walter Pitts introduced the artificial neuron in 1943, Alan Turing proposed a "learning machine" in 1950, and Marvin Minsky and Dean Edmonds built the first neural-based learning machine in 1951.

ML refers to the development of algorithms that solve problems by discovering solutions, rather than using prescribed models (Alpaydin, 2020). This is particularly useful when it is cost-prohibitive to create models, and when sufficient relevant data is present. The basic premise is that the data an algorithm is presented ("trained" on) contains sufficient information to form patterns for predicting future behaviour. In astronomy, ML methods have felt the effects of the "AI summer", with advances in detections (Hughes et al., 2022) and modelling (Ho et al., 2016; Ting et al., 2019) in recent years. ML tasks can generally be put into two categories: *classification* finds similarities between inputs and groups them; *regression* finds patterns in the input data in order to make predictions. There are (at least) three distinct approaches for these tasks. Supervised learning

3 https://historyof.ai/shannon/

involves providing the ML algorithm with a set of input-output pairs, from which the algorithm will learn the underlying mapping from input to output (Mohri, Rostamizadeh, and Talwalkar, 2012). Unsupervised learning does not provide the algorithm with an output, and is therefore mainly used in classification tasks such as clustering. Reinforcement learning allows the ML "agent" to interact with an "environment" and receive feedback for the actions it takes (Kaelbling, Littman, and Moore, 1996). For a detailed overview of ML techniques and their development, see Géron (2022).

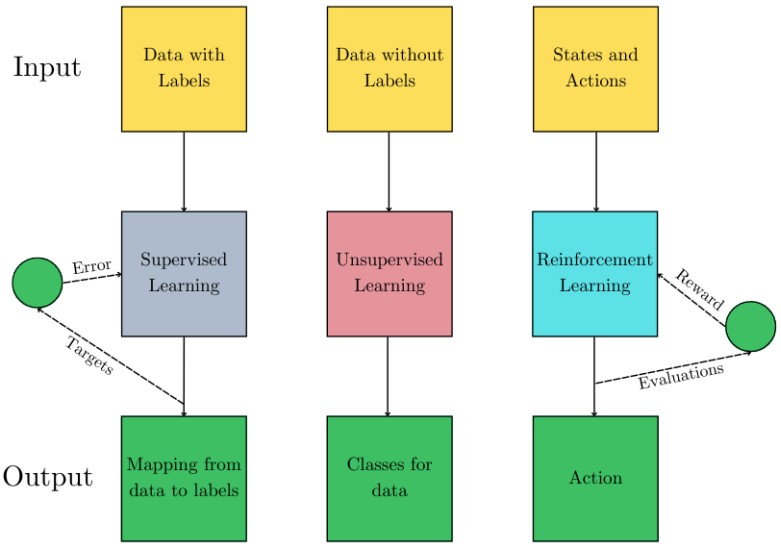

Figure 22: Diagram showing the differences between supervised, unsupervised, and reinforcement learning algorithms. Information flows from the top (input) to the bottom (output).

One class of ML algorithms that deserve their own explanation in the context of this work are artificial neural networks (ANNs), often abbreviated simply to neural networks (NNs). The first NN was the perceptron introduced in 1943 (McCulloch and Pitts, 1943) and built in 1957 by Frank Rosenblatt (Rosenblatt, 1957). The perceptron is an algorithm for supervised learning of a binary classifier, that is, it is a function that maps the inputs $\mathbf{x}$ (real-valued vector) to a single binary output value $f(\mathbf{x})$:

$$f(x) = \begin{cases} 1, & \text{if } \mathbf{w} \cdot \mathbf{x} + b > 0 \\ 0, & \text{otherwise} \end{cases}$$

where $\mathbf{w}$ is a vector of real-valued weights and b is the bias. The weights and bias are learnt through the supervised learning process.

The successor to the perceptron was the multilayer perceptron (MLP) (Rosenblatt, 1962). This was the first ANN to include multiple layers through which a signal was propagated unidirectionally from input to output, in an architecture that has since become known as a feedforward ANN. The MLP introduced by Frank Rosenblatt consisted of an input layer, one hidden layer, and the output layer. Both the hidden and output layers had weights, though the weights in the hidden layer were randomised (and constant), while the weights in the output layer were learnt. Moving forward to 1967, the first MLP incorporating deep learning was introduced (Berners-Lee, 1968). Deep learning simply refers to multiple layers with learning connections; indeed, this new MLP architecture added learning connections to the hidden layer. Fig. 23 shows the architecture of an MLP that accepts multiple inputs to provide a single output.

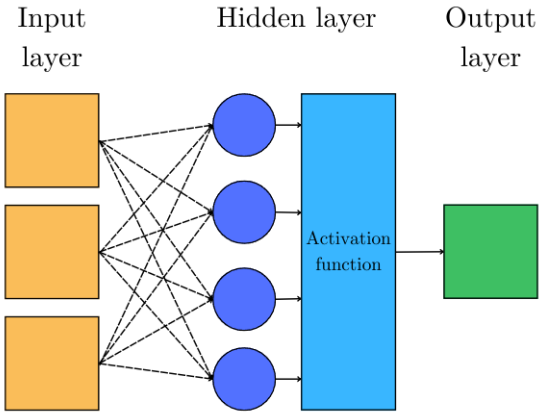

Figure 23: Diagram showing the basic architecture of a multi-layer perceptron with an input layer supporting 3 inputs, a hidden layer with 4 neurons and an arbitrary activation function, and a singular output in the output layer.

The activation function (often denoted σ) defines the output of a given layer. If all the activation functions in an NN are linear, then the NN will only be able to produce linear mappings from input to output. For nonlinear behaviour, then, nonlinear activation functions should be used. For training this new MLP, the backpropagation algorithm was introduced (Griewank, 2012). Put simply, backpropagation is a generalisation of the least-squares algorithm where the error is propagated backwards from output to input, and the learnt weights are updated in a similar fashion. Various techniques exist to actually update the weights, such as gradient descent, and these techniques, as well as their parameters, form a set of hyperparameters that the ML engineer must optimise. Hyperparameters are parameters about the network architecture, such as the number of layers, or number of neurons per layer, that are not learnt by the network itself, but still affect the learning process.

ML has advanced significantly since the invention of the MLP, and it is not uncommon for modern NNs to have millions of trainable parameters. Many sophisticated techniques have been developed to deal with certain kinds of data. Convolutional layers (see Fig. 24) combine patterns and are widely used in image-processing NNs. For astronomical modelling, both simple and complex architectures have been proven to work well. The Payne (Ting et al., 2019) is an N-D interpolator for stellar spectra models, and consists primarily of an MLP. Arévalo, Asensio Ramos, and Esteban Pozuelo (2021) introduce a graph convolutional network, which combines convolutional layers with a graph structure, in order to predict NLTE corrections for Ca II.

In Chap. 5, the goal is to overcome model and observational shortcomings in spectroscopy by training algorithms to remove noise from spectra without removing important information (such as the line shape). In Chap. 6, the goal is to train NNs to predict the steady-state of a system of ordinary differential equations, and validate them with the findings from Chaps. 3 and 4. Relevant details for these specific tasks are provided in the respective chapters, and a useful set of definitions is given in the introduction preceding these two chapters. We are now equipped with the required knowledge to tackle the first problem in this work, the determination of an accurate photospheric solar silicon abundance.

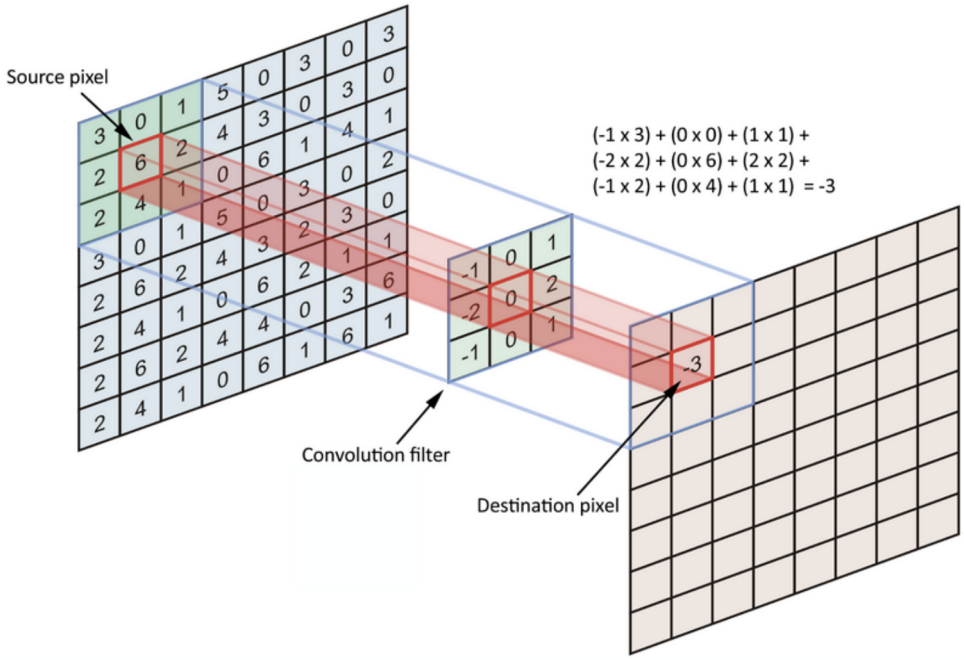

Figure 24: Diagram showing the basic function of a convolutional layer, typical in 2-D convolutional neural networks.

Part II

CONVENTIONAL MODELLING TECHNIQUES

The following three chapters cover conventional modelling techniques for stellar atmospheres. Chap. 2 covers the determination of the photospheric solar silicon abundance, an important element for comparing with primordial meteoritic abundances. The work is also of interest to missions such as PLATO, as a certain set of solar abundances must be used during its operation. I also cover model shortcomings in the chapter, and show that they are not unique to the models used in this work, but are likely general to other 3D codes. Understanding the sources for these shortcomings is a crucial part of further improving them.

Chaps. 3 and 4 explore the time-dependent evolution of molecular species in metal-poor stellar atmospheres. Chemical equilibrium, the notion that chemical species have had sufficient time to react to their equilibrium values, is a widely used assumption in the computation of spectra in stellar atmospheres. These two chapters cover the detailed time-dependent modelling of a chemical reactin network alongside the hydrodynamics and radiative transfer steps in the stellar atmosphere modelling code CO^{5}BOLD. This is the first time these calculations have been performed for (carbon-enhanced) metal-poor dwarf and giant stellar atmospheres, and links to the trend of increasing carbon abundance seen at decreasing metallicity. If the chemical equilibrium assumption is not valid within the relevant line-forming regions, then this trend could be attributed to this bias rather than an actual astrophysical cause. Methods to compute whether a stellar atmosphere is in chemical equilibrium are also discussed.

2

DETERMINING THE SOLAR PHOTOSPHERIC SILICON ABUNDANCE WITH CO^{5}BOLD AND LINFOR3D

This chapter is based on the published work in Deshmukh et al. (2022). I handled the spectroscopic modelling, spectral line fitting, and differential analyses. Computing the model stellar atmospheres, 1D NLTE syntheses, and the `BALDER` line syntheses, as well as determining the de-broadening procedure and kernel were not handled by me. I additionally investigated the new oscillator strengths presented in Pehlivan Rhodin (2018) in order to choose which spectral lines to use for the investigation, however, this was informed by previous work by co-authors who provided a filtered subset of spectral lines shown to provide accurate abundance measurements.

2.1 INTRODUCTION

The chemical composition of the solar photosphere serves as a widely applied yardstick in astronomy, since it is considered largely representative of the chemical make-up of the present-day Universe. The determination of solar abundances has a long history, dating back at least to the 1920s (Payne, 1925; Russell, 1929; Unsöld, 1928). Among the elements which are spectroscopically accessible in the solar photosphere, silicon plays a somewhat special role. Besides being relatively abundant, it is used as a reference to relate the solar photospheric composition to the composition of type-I carbonaceous chondrites which are believed to constitute fairly pristine samples of material from the early Solar System (e.g. Anders and Grevesse, 1989; Lodders, Palme, and Gail, 2009; Lodders, 2003; Palme, Lodders, and Jones, 2014). This important aspect of the silicon abundance led to many investigations trying to establish an ever more precise and accurate solar reference value. Over the years, atomic and observational data have improved, and increasingly sophisticated modelling techniques have been applied, including time-dependent three-dimensional (3D) model atmospheres (e.g. Asplund, 2000; Caffau et al., 2011a; Pereira et al., 2013) and treatment of departures from thermodynamic equilibrium (NLTE) (e.g. Amarsi et al., 2019a; Bergemann et al., 2019; Steffen et al., 2015).

From the above, it is tempting to conclude that the determination of the abundance of a particular element in the solar photosphere is an entirely objective process. Unfortunately, this is not the case, due to several judicious decisions a researcher must make along the way, namely: **i)** which observational material to use, **ii)** where to place the continuum when normalising the spectrum, **iii)** which lines have accurate atomic data (meaning oscillator strengths and broadening constants), and **iv)** which lines are largely unaffected by blends. These aspects influence the final outcome of an analysis, and we list some previous works' results below to illustrate the evolution of the fitted solar silicon abundance with time. Indeed, as we shall later show, statistical uncertainties are of secondary importance here, and it is primarily the line selection that dominates the final outcome (including uncertainties). Moreover, in the present analysis process, we found that more sophisticated model atmospheres do not necessarily give a more coherent picture, since they can bring to light modelling shortcomings which were not recognised before.

Holweger (1973) determined an LTE solar silicon abundance of $\log \varepsilon_{\mathrm{Si}} = 7.65 \pm 0.07$ based on 19 Si I lines whose oscillator strengths were measured by Garz (1973). Wedemeyer (2001) derived a 1D NLTE correction of -0.010 dex for silicon. Together with a cor-

rection of the scale of Garz by Becker, Zimmermann, and Holweger (1980), they arrived at a silicon abundance of $\log \varepsilon_{Si} = 7.550 \pm 0.056$. Some of the first multi-dimensional (multi-D) studies were carried out by Asplund (2000) and Holweger (2001), who arrived at $\log \varepsilon_{Si} = 7.51 \pm 0.04$ and $\log \varepsilon_{Si} = 7.536 \pm 0.049$, respectively. The statistical equilibrium of silicon and collisional processes were investigated by Shi et al. (2008), and an abundance of $\log \varepsilon_{Si} = 7.52 \pm 0.06$ was found, taking an extended line sample into account. They also specified that the NLTE effects on optical silicon lines are weak, but it was later found that near-infrared lines have sizeable NLTE effects (Bergemann et al., 2013; Shi et al., 2012). Shchukina, Sukhorukov, and Trujillo Bueno (2012) conducted an NLTE analysis of 65 Si I lines, and found $\log \varepsilon_{Si} = 7.549 \pm 0.016$. Shaltout et al. (2013) obtained a 3D LTE solar silicon abundance of $\log \varepsilon_{Si} = 7.53 \pm 0.07$ and a 1D NLTE abundance of $\log \varepsilon_{Si} = 7.52 \pm 0.08$, using the aforementioned -0.010 dex correction.

More recently, Scott et al. (2015) conducted a 3D LTE study and found an abundance as low as $\log \varepsilon_{Si} = 7.52 \pm 0.03$. The result was later corroborated by Amarsi and Asplund (2017) who derived a 3D NLTE correction of -0.01 dex to this abundance. This analysis used nine Si I lines and one Si II line in the optical wavelength range. The final abundance was calculated by means of a weighted average. All in all, over the last twenty years, a slight downward trend of the derived solar abundance of silicon has become apparent, but, on a level which is on the edge of being statistically significant.

In the present work, we apply CO^{5}BOLD model atmospheres (Freytag et al., 2012) to derive the photospheric abundance of silicon in the Sun. Primarily, the motivation to do so was the availability of new data for the oscillator strengths of silicon lines (Pehlivan Rhodin, 2018). This enlarged the set of silicon lines that could be potentially useful in an abundance analysis, adding oscillator strengths for near-infrared lines. Additionally, we intended to relate solar abundances so far derived with CO^{5}BOLD models (for a summary, see Caffau et al., 2011a) to the meteoritic abundance scale. This is to unify various solar abundance sets for use in various projects; for example, the PLATO Consortium must decide on a set of solar abundances to compare against for the 2026 PLATO mission (Gent et al., 2022b). Expanding the Si line set and deriving accurate abundances for these solar lines would further help reduce uncertainties in this solar abundance set, particularly when comparing to meteoritic abundances.

The necessary spectral synthesis calculations were performed with the LINFOR3D code[1] in LTE approximation, with only a few exceptions. To compare this with observations, we developed a custom spectral fitting routine that accounts for correlated photometric noise in the observations. Our analysis stands out by using a sizeable number of lines with carefully calculated line broadening constants, new oscillator strengths, and investigating systematic shortcomings of our 3D model atmosphere. The last point became important since we found that our model was predicting systematically overly broadened lines, seen also in Caffau et al. (2015) as a similar finding for oxygen lines.

The rest of the chapter is structured as follows: Section 2.2 discusses the details of the model atmospheres used in this study, the methodology of line selection, and spectral synthesis. It also touches on the role of magnetic field effects pertaining to these topics. Section 2.3 describes the fitting routine and the implemented correlated noise model. Our results, and the differences due to model choice, are shown in Section 2.4 and discussed in Section 2.5. Section 2.6 explains model atmosphere differences in abundance and broadening. Section 2.7 explains differences in regard to NLTE The choice of the broadening kernel, its properties, and its relation to other kernels is presented in Section 2.8 The centre-to-limb variation of the continuum is presented in Section 2.9, and the partition functions used in LINFOR3D are shown in Section 2.10 in further detail.

1 https://www.aip.de/Members/msteffen/linfor3d

2.2.1 *Model atmospheres*

Systematic errors from spectral synthesis and fitting come from the use of 1D hydrostatic model atmospheres, and the assumption of LTE when it is not valid to do so. 1D hydrostatic model atmospheres rely on mixing-length theory (Böhm-Vitense, 1958; Henyey, Vardya, and Bodenheimer, 1965), and introduce additional free parameters such as micro- and macro-turbulence (Gray, 2008). Spectral lines generated from these model atmospheres are too narrow to fit observations, if they do not take macroscopic broadening into account, necessitating the use of free parameters to fit observations. 3D model atmospheres, on the other hand, should in principle be able to reproduce line shapes, shifts and asymmetries, and spectral lines synthesised with these can be directly fit to observations.

The prominent state-of-the-art radiative-convective equilibrium 1D models of solar and stellar atmospheres such as ATLAS (Kurucz, 2005), MARCS (Gustafsson, 1975; Gustafsson et al., 2008), PHOENIX (Allard and Hauschildt, 1995; Allard et al., 2001), and TLUSTY (Hubeny et al., 2021) use classical mixing-length theory, and the efficiency of convective energy transport here is controlled by a free parameter α_{MLT}. This, along with the requirement of fitting the micro- and macro-turbulence free parameters during line synthesis, is a major drawback of 1D models.

3D atmospheres account for the time-dependence and multi-dimensionality of the flow, and a spectral synthesis using these atmospheres reproduces line shapes and asymmetries. Prominent examples include `STAGGER` (Magic et al., 2013),`MuRAM` (Vögler et al., 2005), `Bifrost` (Gudiksen et al., 2011), and `Antares` (Leitner et al., 2017). In this work, we use `CO5BOLD`, a conservative hydrodynamics solver able to model surface convection, waves, shocks and other phenomena in stellar objects (Freytag et al., 2012). As 3D atmospheres are understandably expensive to run, their output can be saved as a sequence where flow properties are recorded, commonly called a sequence of 'snapshots'. These snapshots are then used in spectral synthesis codes, such as `LINFOR3D` (used in this study) or `MULTI3D` (Leenaarts and Carlsson, 2009). The parameters of the `CO5BOLD` model atmospheres used in this work are summarised in Table 7. We use 20 model snapshots to compute line syntheses with `LINFOR3D`. Throughout this work, the 'Model ID' (see Table 7) for each model will be used to refer to it.

The msc600, m595, b000 and b200 models all use a short characteristics scheme with double Gauss-Radau quadrature and 3 μ-angles. The n59 model uses a long characteristics Feautrier scheme with Lobatto quadrature and 4+1 μ-angles. In the current version of `CO5BOLD` the former scheme is given the name "MSCrad" and the latter is given the name "LCFrad" (Freytag et al., 2012; Steffen, 2017).

2.2.2 *Line sample*

Silicon is an interesting element as it is an important electron donor in late-type stars. Though it seems that Si I's ionisation potential of 8.15 eV would mean a significant amount of silicon to be present in the form of Si II, the higher ionisation potential of Si II is unfavourable for the appearance of strong lines in the solar spectrum at wavelengths longer than 3000 Å (Moore, 1970; Russell, 1929). We therefore primarily consider Si I lines and two carefully chosen Si II lines.

The Si I and II line list below (Table 8) was compiled from the line lists used in the solar abundance determination by Holweger (2001), Wedemeyer (2001), Shi et al.

Model ID (d3gt57g44)	Box Size [Mm^3]	Resolution [km^3]	Grid Points $N_x \times N_y \times N_z$	T_{eff} [K]	$< B_z >$ [G]	Rad. Trans. Module
msc600	$8.0 \times 8.0 \times 2.3$	$32 \times 32 \times 10 \ldots 15$	$250 \times 250 \times 207$	5773 ± 9.4	–	MSCrad
n59	$5.6 \times 5.6 \times 2.3$	$40 \times 40 \times 15$	$140 \times 140 \times 150$	5774 ± 16	–	LCFrad
m595	$5.6 \times 5.6 \times 2.3$	$40 \times 40 \times 15$	$140 \times 140 \times 150$	5775 ± 15	–	MSCrad
b000	$5.6 \times 5.6 \times 2.3$	$40 \times 40 \times 15$	$140 \times 140 \times 150$	5750 ± 19	0	MSCrad
b200	$5.6 \times 5.6 \times 2.3$	$40 \times 40 \times 15$	$140 \times 140 \times 150$	5793 ± 17	200	MSCrad

Table 7: "Model ID" lists the name of a 3D model used in this paper (note all models share the prefix "d3gt57g44"), "Box Size" the geometrical size of its computational domain, "Resolution" the applied grid spacing, "Grid Points" the number of mesh points per dimension, "T_{eff}" the effective temperature of the model, "$<B_z>$" the mean magnetic field component in vertical direction, and "Rad. Trans. Module" the name of the radiation transport module used (see Sec. 2.2.1 for an explanation). Different from the other models, the msc600 model uses a variable grid spacing in the vertical direction; for that reason the covered range is provided. We note that '$\pm$' in "T_{eff}" should not be interpreted as an uncertainty: it is the natural dispersion of effective temperature in the time series illustrating fluctuations between snapshots. Each model has $\log(g) = 4.44$ and solar metallicity.

(2008), and Amarsi and Asplund (2017). The initial line selection was performed by synthesising line profiles and comparing to observations, thus checking these for blends.

We solely used the observational data by Neckel and Labs (1984) (hereafter the 'Hamburg spectrum') and have worked with the disc-centre and disc-integrated spectrum. Doerr, Vitas, and Fabbian (2016) show the resolution of the Hamburg spectrum to be up to 520,000 compared to the often-used Liege spectrum (Delbouille, Roland, and Neven, 1973), which practically was shown to have a resolution of ~ 216,000. The higher spectral resolution allows for a more continuous representation of the pixel-to-pixel variations in the spectrum, and we utilise a noise model that represents the covariance between pixels. Additionally, the Liege spectrum covers a range of $3000 - 10000$ Å, while the Hamburg spectrum covers a range of $3290 - 12510$ Å, affording us access to very clean near-infrared lines. Furthermore, it remains unclear whether the Liege spectrum is a true disk-centre spectrum or an integral over a narrow range of angles around disk-centre, and the available documentation does not precisely establish this.

From the original 39 lines, we chose a subset of 11 based on comparisons between disk-centre and disk-integrated spectra, the line shape and the precision of oscillator strength. We focus on lines that do not have strong line blends that can interfere with abundance determination. Each line was weighted on a scale of $1 - 3$ based on these criteria, and the resulting weights were used to compute the mean abundance. This idea of a weighted mean was inspired by the work of Amarsi and Asplund (2017).

There are various sources of error that can enter during the spectroscopic fitting, but the choice of oscillator strength for each spectral line is often the largest one. We use semi-empirical gf-values from Pehlivan Rhodin (2018) (hereafter also PR18) for every line in our chosen sub-sample, which have been updated with respect to previous experimental values measured by Garz (1973) with accurate lifetime renormalisations by O'Brian and Lawler (1991a,b) (hereafter also GOL). The gf-values from PR18 were obtained by combining calculated level lifetimes with experimental branching ratios. Moreover, the calculations were validated against existing measurements of level lifetimes and oscillator strengths. An advantage of the PR18 data is the homogeneity of the extensive set of line transitions, ranging from UV to infrared wavelengths. On average across all lines in Table 8, the new values give a $\Delta \log gf = 0.024$ decrease with

respect to the previous measurements, and lead to a respective increase of the mean abundance by the same value when using all lines. Using the new values of the oscillator strengths lowers the overall scatter in fitted abundance values by 0.07 dex and the formal uncertainty by 0.01 dex.

We investigated the overall performance of the PR18 gf-values on the set of lines used in Scott et al. (2015) and Amarsi and Asplund (2017). Fig. 25 depicts the resulting Si abundances. The use of the PR18 data reduces the overall scatter in the Si abundances from 0.036 dex (applying the data of GOL) to 0.018 dex. In all cases, there is no discernible dependence on line strength or excitation potential. The only Si II line at 6371 Å that we consider sufficiently reliable for abundance analysis may indicate a slight ionisation imbalance. However, this imbalance is of similar magnitude for both sets of oscillator strengths. Moreover, the line has a high excitation potential and is partially blended (see Fig. 27) so that the apparent imbalance could be the result of systematics in the analysis.

In previous studies, strong infrared Si I lines above 10000 Å often lacked reliable experimental oscillator strengths (Borrero et al., 2003; Shchukina, Sukhorukov, and Trujillo Bueno, 2012; Shi et al., 2008). Shi et al. (2012) investigate near-infrared lines in nearby stars with both LTE and NLTE, and find that there is a larger departure from LTE for the infrared lines than optical ones. They point out that weak lines are insensitive to NLTE effects, whereas stronger lines show visible effects. The new oscillator strengths also afford us the use of near-infrared lines in our sample. These lines are not as affected by blends as the optical lines (Shi et al., 2008), but some show strong NLTE cores. We do not include these lines to determine a final abundance. During fitting, we clip points that are more than 0.5% of relative (normalised) flux further from the observations after an initial fit, removing weak line blends and deviating line cores from the abundance determination.

2.2.3 *Spectral synthesis*

In this study, a 3D hydrodynamical solar model atmosphere with an initial silicon abundance of $\log \varepsilon_{\mathrm{Si}} = 7.55$ was used for the line synthesis. Each line is synthesised with the `LINFOR3D` code over 20 atmospheric snapshots. The lines are synthesised in full 3D, including Doppler shifts, and the profile is averaged in time and space (horizontally). We generate a set of syntheses for each spectral line, each with a different $\log \mathrm{gf}\varepsilon_{\odot}$ value. We alter $\log \mathrm{gf}$ in this case, with a distinct stepping around a central value for each line depending on the sensitivity of the lines to oscillator strength changes.

Our investigation of the solar silicon abundance is mostly 3D LTE, but the -0.01 dex correction due to NLTE effects determined by Amarsi and Asplund (2017) was used globally for our calculated abundance. We investigate NLTE effects on broadening and abundance in Sec. 2.7.

2.2.4 *Line broadening*

Aside from the abundance, we also aim to investigate the effects of broadening required to fit synthetic spectra to observations. The broadening we see in the observed lines can be attributed to broadening by macroscopic velocity fields, thermal broadening, and atomic line broadening due to collisions with neutral particles and electrons. For broadening due to macroscopic velocity fields, though a tendency towards less turbulent flow is expected in numerical models due to limited spatial resolution, our 3D syntheses are broader than the observations, even prior to applying instrumental profile broadening.

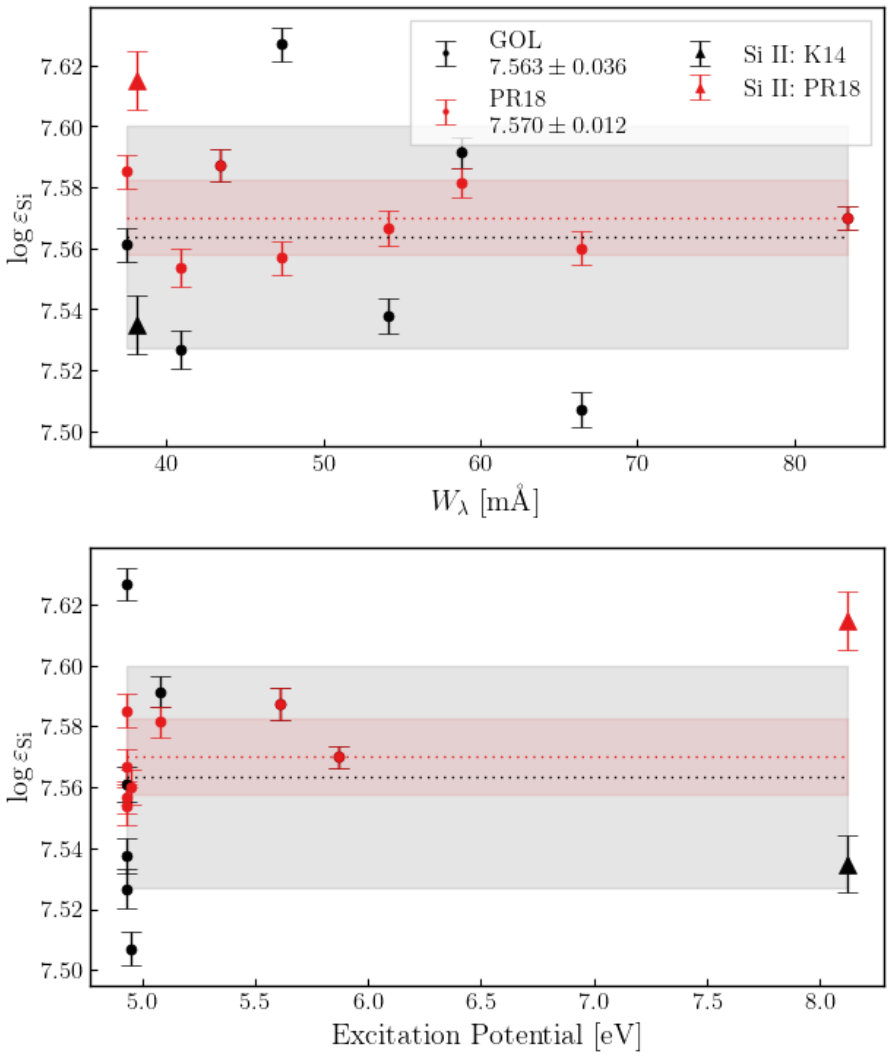

Figure 25: Individual fitted Si abundances for a set of eight Si I lines and one Si II line as a function of equivalent width (**top**) and excitation potential (**bottom**) for eight Si I lines and one Si II line. Only the Si I lines are used to determine the mean and RMSE (see definition in Eq. 90), given in the legend in the left panel. GOL indicates oscillator strengths from Garz (1973) normalised according to the results of O'Brian and Lawler (1991a); the oscillator strength for the Si II line for comparison was taken from Kurucz (2014); PR18 indicates oscillator strengths from Pehlivan Rhodin (2018).

λ [Å]	Transition	log gf old		log gf new	Weight	E_{low} - E_{upp} [cm^{-1}] – [cm^{-1}]	$E_{lim,\,low}$ - $E_{lim,\,upp}$ [cm^{-1}] – [cm^{-1}]	n^*_{low}	n^*_{upp}	σ_0 [a.u.]	α
Si I	–					–	–				
5645.61*	$4s\,^3P^o_1 - 5p\,^3P_2$	− 2.04(3)	GOL	− 2.067	1	39760 – 57468	65748 – 65748	2.054	3.640	1791	0.223
5665.55*	$4s\,^3P^o_0 - 5p\,^3P_1$	− 1.94(3)	GOL	− 2.025	2	39683 – 57329	65748 – 65748	2.051	3.609	1772	0.222
5684.48*	$4s\,^3P^o_2 - 5p\,^3S_1$	− 1.55(3)	GOL	− 1.606	2	39955 – 57542	65748 – 65748	2.062	3.656	1798	0.221
5690.43*	$4s\,^3P^o_1 - 5p\,^3P_1$	− 1.77(3)	GOL	− 1.802	3	39760 – 57328	65748 – 65748	2.054	3.609	1772	0.222
5701.11*	$4s\,^3P^o_1 - 5p\,^3P_0$	− 1.95(3)	GOL	− 1.981	3	39760 – 57296	65748 – 65748	2.054	3.602	1769	0.222
5708.40	$4s\,^3P^o_2 - 5p\,^3P_2$	− 1.37(3)	GOL	− 1.388	0	39955 – 57468	65748 – 65748	2.062	3.640	1788	0.223
5772.15	$4s\,^1P^o_1 - 5p\,^1S_0$	− 1.65(3)	GOL	− 1.643	0	40992 – 58312	65748 – 65748	2.105	3.841	2036	0.208
5780.38	$4s\,^3P^o_0 - 5p\,^3D_1$	− 2.25(3)	GOL	− 2.156	0	39683 – 56978	65748 – 65748	2.051	3.536	1691	0.228
5793.07*	$4s\,^3P^o_1 - 5p\,^3D_2$	− 1.96(3)	GOL	− 1.893	2	39760 – 57017	65748 – 65748	2.054	3.544	1704	0.228
5797.86	$4s\,^3P^o_2 - 5p\,^3D_3$	− 1.95(3)	GOL	− 1.830	0	39955 – 57198	65748 – 65748	2.062	3.582	1755	0.223
5948.54	$4s\,^1P^o_1 - 5p\,^1D_2$	− 1.13(3)	GOL	− 1.179	0	40992 – 57798	65748 – 65748	2.105	3.714	1845	0.222
6125.02	$3p^3\,^3D^o_1 - 5f\,^3D_2$	− 1.465	K07	–	0	45276 – 61598	114716 – 65748	1.257	5.141	3354	0.348
6142.49	$3p\,^3D^o_3 - 5f\,^3D_3$	− 1.296	K07	–	0	45321 – 61597	114716 – 65748	1.257	5.141	3354	0.348
6145.02	$3p\,^3D^o_2 - 5f\,^3G_3$	− 1.311	K07	–	0	45294 – 61562	114716 – 65748	1.257	5.119	3295	0.341
6237.32	$3p\,^3D^o_1 - 5f\,^3F_2$	− 0.975	K07	–	0	45294 – 61304	114716 – 65748	1.257	4.968	3081	0.351
6243.82	$3p\,^3D^o_2 - 5f\,^3F_3$	− 1.244	K07	–	0	45294 – 61305	114716 – 65748	1.257	4.968	3081	0.351
6244.47	$3p\,^3D^o_2 - 5f\,^1D_2$	− 1.091	K07	–	0	45294 – 61305	114716 – 65748	1.257	4.968	3081	0.351
6976.51	$4p\,^3D_1 - 6d\,^3F^o_2$	− 1.07(3)	GOL	–	0	48020 – 62350	65748 – 65748	2.487	5.681	4600	0.530
7003.57	$4p\,^3D_2 - 6d\,^3F^o_3$	− 0.793	GOL	–	0	48102 – 62377	65748 – 65748	2.493	5.704	4700	0.531
7034.91	$3d\,^1D^o_2 - 5f\,^3F_3$	− 0.78(3)	GOL	–	0	47352 – 61562	65748 – 65748	2.442	5.119	3232	0.338
7226.21	$3p\,^3D^o_1 - 4f\,^1D_2$	− 1.41(3)	GOL	–	0	45276 – 59111	114716 – 65748	1.257	4.065	1745	0.307
7405.79	$3p\,^3D^o_1 - 4f\,^3F_2$	− 0.72(3)	GOL	–	0	45276 – 58775	114716 – 65748	1.257	3.966	1585	0.304
7415.36	$3p\,^3D^o_2 - 4f\,^3F_2$	− 0.65(3)	GOL	–	0	45294 – 58774	114716 – 65748	1.257	3.966	1585	0.304
7680.27*	$4p\,^1P_1 - 5d\,^1D^o_2$	− 0.59(3)	GOL	− 0.678	2	47284 – 60301	65748 – 65748	2.437	4.487	2107	0.494
7918.38	$4p\,^3D_1 - 5d\,^3F^o_2$	− 0.51(3)	GOL	− 0.666	0	48020 – 60645	65748 – 65748	2.487	4.636	2934	0.234
7932.35	$4p\,^3D_2 - 5d\,^3F^o_3$	− 0.37(3)	GOL	− 0.472	0	48102 – 60705	65748 – 65748	2.493	4.664	2985	0.234
10288.94*	$4s\,^3P^o_0 - 4p\,^3S_1$	–	–	− 1.622	2	39683 – 49400	65748 – 65748	2.493	4.664	739	0.230
10371.26	$4s\,^3P^o_1 - 4p\,^3S_1$	–	–	− 0.789	0	39760 – 49400	65748 – 65748	2.493	4.664	739	0.230
10603.43	$4s\,^3P^o_1 - 4p\,^3P_2$	–	–	− 0.394	0	39760 – 49188	65748 – 65748	2.493	4.664	727	0.231
10689.72	$4p\,^3D_1 - 4d\,^3F^o_2$	–	–	− 0.017	0	48020 – 57372	65748 – 65748	2.493	4.664	1418	0.234
10694.25	$4p\,^3D_2 - 4d\,^3F^o_3$	–	–	+ 0.155	0	48102 – 57450	65748 – 65748	2.493	4.664	1445	0.750
10749.37	$4s\,^3P^o_1 - 4p\,^3P_1$	–	–	− 0.268	0	39760 – 49061	65748 – 65748	2.493	4.664	721	0.231
10784.56	$4p\,^3D_2 - 4d\,^3F^o_2$	–	–	− 0.746	0	48102 – 57372	65748 – 65748	2.493	4.664	1417	0.296
10786.85	$4s\,^3P^o_1 - 4p\,^3P_0$	–	–	− 0.380	0	39760 – 49028	65748 – 65748	2.493	4.664	719	0.231
10827.09	$4s\,^3P^o_2 - 4p\,^3P_2$	–	–	+ 0.227	0	39955 – 49188	65748 – 65748	2.493	4.664	728	0.231
12390.15*	$4s\,^1P^o_1 - 4p\,^3P_1$	–	–	− 1.805	2	40992 – 49061	65748 – 65748	2.493	4.664	730	0.234
12395.83*	$4s\,^3P^o_2 - 4p\,^3D_1$	–	–	− 1.723	2	39955 – 48020	65748 – 65748	2.493	4.664	675	0.231
Si II	–					–	–				
6347.10	$4s\,^2S_{1/2} - 4p\,^2P^o_{3/2}$	+ 0.170	K14	+ 0.182	0	65500 – 81299	131838 – 131838	2.572	2.943	390	0.190
6371.36*	$4s\,^2S_{1/2} - 4p\,^2P^o_{1/2}$	− 0.040	K14	− 0.120	1	65500 – 81299	131838 – 131838	2.572	2.943	390	0.190

Table 8: Atomic data for spectral lines of Si I and Si II. An asterisk next to the wavelength signifies the line was in the chosen subsample. References to the "old" gf-values are GOL: Garz (1973), renormalised by +0.097 dex according to O'Brian and Lawler (1991a), K07: Kurucz (2007), and K14: Kurucz (2014). "new" log gf values come from Pehlivan Rhodin (2018). The "Weight" column specifies our weighting for each line. The right portion of the table shows ABO theory parameters. "E_{low}" & "E_{upp}" show the lower and upper energy levels of the transitions in cm^{-1}, and "E_{lim}" shows the series limit energy for that level (see e.g. Heiter et al. (2021) for details). "n^*_{low}" & "n^*_{upp}", are the effective quantum numbers associated with the states of the transitions. "σ_0" is the line broadening cross section in atomic units and "α" describes the power law velocity dependence.

The result is not unique to our work (see, e.g. Caffau et al., 2015), nor is it unique to CO5BOLD models (see Sec. 2.6 for details).

2.2.4.1 *Collisional broadening*

Solar spectral lines are subject to broadening from atomic effects. These are pressure broadening effects arising from van der Waals and other interatomic forces. It turns out that the 7680 Å line shows sizeable Stark broadening, meaning the Stark effect is non-negligible for some solar silicon lines and illustrating the importance of accurately modelling these effects. We use the theory by Anstee, Barklem and O'Mara (Anstee and O'Mara, 1991, 1995; Barklem, Anstee, and O'Mara, 1998) to describe the line broadening effects of neutral particles, predominantly neutral hydrogen (hereafter ABO theory). Note that the broadening constants were specifically calculated using existing tables from the above papers or through extended calculations, and are shown in Table 8. `LINFOR3D` additionally takes the Stark broadening of lines into account, employing line widths from from the Vienna Atomic Line Database (VALD) (Kupka et al., 2000; Kupka et al., 1999; Ryabchikova et al., 2015) and assuming temperature dependence from the Unsöld theory (Unsöld, 1955).

The theory of collisional line broadening for neutral species (Anstee and O'Mara, 1991, 1995) was extended to singly ionised atoms in Barklem and O'Mara (1998). For the lines corresponding to ionised Si in this study, we performed specific calculations assuming $E_p = -4/9$ atomic units (the average value of the energy denominator of the second-order contribution to the interaction energy), which is expected to give reasonable estimates, though this assumption is less secure for ions than for neutrals (see Barklem and Aspelund-Johansson, 2005; Roederer and Barklem, 2018). Equation 1 of Anstee and O'Mara (1995) describes the line broadening cross section σ (in atomic units) as a function of the relative collision velocity v, with respect to a reference value of $v_0 = 10^4$ m s^{-1}, with the parameter α giving the power law velocity dependence:

$$\sigma(v) = \sigma_0 \left(\frac{v}{v_0} \right)^{-\alpha} . \tag{82}$$

The line width at a given temperature can then be obtained from this relation by analytic integration over the Maxwellian velocity distribution (see Equation 3 of Anstee and O'Mara (1995)).

2.2.4.2 *Rotational broadening*

For disk-integrated spectra, we consider fixed solid body rotation assuming a synodic $v \sin i = 1.8$ km s^{-1} is present in the observations from the Hamburg spectrum (Bartels, 1934; Gray, 2008). In total, 1 vertical 16 inclined rays were used (4 μ-angles and 4 ϕ-angles) with Lobatto quadrature (Abramowitz and Stegun, 1965). Rotational broadening is not included for disk-centre spectra.

2.2.5 *Magnetic fields*

2.2.5.1 *Effects on model atmospheres*

It is known that weak magnetic fields are present in the solar surface layers and there is evidence that the mean magnetic flux density for these is of the order of 10^2 G (Bueno, Shchukina, and Ramos, 2004; Nordlund, Stein, and Asplund, 2009). Numerical 3D convection models predict that the granulation pattern is profoundly affected in regions with high flux density (Cattaneo, Emonet, and Weiss, 2003; Cheung et al., 2008; Vögler et al., 2005), in agreement with observations. Additionally, photospheric material becomes more transparent in magnetic concentrations due to their lower density, allowing

one to see into deeper, hence hotter, layers of the solar atmosphere (Stein and Nordlund, 2000). In these regions, where flux tubes are also heated through heat influx from the surrounding material (Spruit, 1976), weak spectral lines will experience a brightening of their core, meaning magnetic fields can act on temperature-sensitive lines not only directly through the Zeeman effect, but also indirectly due to temperature stratification in line-forming regions (Fabbian et al., 2012).

2.2.5.2 *Effects on spectral synthesis*

In 1D model atmospheres, Borrero (2008) showed that magnetic fields have non-negligible effects on spectral line synthesis, and Fabbian et al. (2010) expanded this to 3D atmospheres, finding an abundance correction for Fe of the order of $\sim +0.01$ dex when using magneto-convection models. Fabbian et al. (2012) used 28 iron lines and found the average solar iron abundance to be $\sim 0.03 - 0.11$ dex higher when using a magneto-convection model with $\langle B_{vert} \rangle = 200\,G$ and investigated models with average magnetic flux densities of $\langle B_{vert} \rangle = 0, 50, 100, 200\,G$. They also showed that Zeeman broadening gains importance in the infrared, and that the largest contribution to higher abundance is the indirect effect of line-weakening caused by a warmer stratification as seen on an optical depth scale.

Following this, Fabbian and Moreno-Insertis (2015) were able to reproduce the observations of 2 O I spectral lines with blends with the use of a 3D MHD photospheric model with a uniform vertical magnetic field of 200 G. They required an oxygen abundance several centidexes higher than those suggested by Asplund et al. (2009) to fit observations and again showed the need to consider magneto-convection processes when considering problems sensitive to the shape of spectral features, such as spectral synthesis and fitting.

As shown in Table 7, we use two magnetic model atmospheres to investigate the effects of the magnetic field strength on the fitted abundance and broadening values. Zeeman broadening is not taken into account in the spectral synthesis. Note that Shchukina, Sukhorukov, and Trujillo Bueno (2015) and Shchukina, Sukhorukov, and Trujillo Bueno, 2016 also show that such vertical fields as in Fabbian et al. (2012) overestimate the effects when compared with a 3D MHD model with a self-consistent small-scale dynamo and more realistic magnetic fields. With this in mind, and with the fact that the magnetic models used here are not of a high enough resolution to quantitatively investigate the effects of magnetic fields, we consider only differential effects. Section 2.4 shows these differences and concludes that the extra broadening present in the msc600 model syntheses could be partly attributed to the lack of magnetic fields.

2.3 SPECTRAL FITTING ROUTINE

The synthesised lines are fitted to the observations from the Hamburg spectrum via χ^2 minimisation, where we define χ^2 as

$$\chi^2 = \Delta \mathbf{x}^T \mathbf{C}^{-1} \Delta \mathbf{x}, \tag{83}$$

where $\Delta \mathbf{x} = \mathbf{F}_{observed} - \mathbf{F}_{model}$ is the vector of flux residuals and $\mathbf{C}$ is the covariance matrix of the data. We use maximum likelihood estimation using χ^2 rather than the conventional least-squares minimisation in order to incorporate the errors due to covariance in the spectrum.

In this analysis, we fit disk-centre intensities for abundance determination, but disk-integrated spectra are also used when choosing the line sample. To mask weak blends,

a window is chosen around each line for the fitting procedure. An example is shown in Fig. 26.

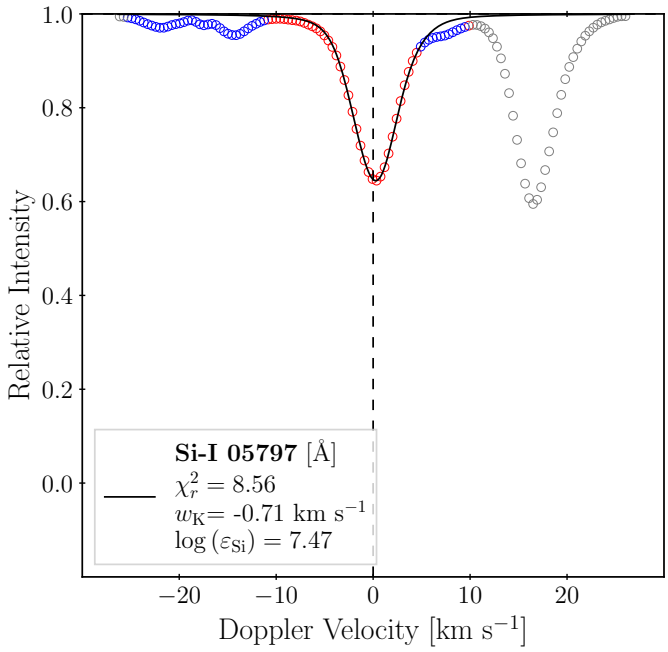

Figure 26: Synthesised fitted line profile (black line) against the observations from the Hamburg atlas (points). Grey points were cut from the initial fit; blue points show areas where the deviation between initial fit and data is too high, and so the subsequent fits do not use the offending points; red points are used for computing all fitted quantities. Removing the points on right hand side removes the strong blend, and sigma-clipping handles weaker ones during fitting. w_K is the width of the broadening kernel used. Note that this line is *not* used in the final determination of the silicon abundance because of the large line blends.

The routine involves first loading the observations and determining the covariance between pixels for a given line (see Section 2.3.2 for details). Then, during the fitting, instrumental profile broadening and rotational broadening (for disk-integrated spectra) are applied to the syntheses. A monotonic cubic interpolation across abundance is used to find the closest synthesis matching the observations, now also fitting the wavelength shift, to create an array of syntheses. Finally, for the nine abundances in steps of 0.05 dex that were synthesised, the abundance is fit by interpolating through the array of syntheses and constructing a spectrum from the overall best fitting points. Sigma-clipping is employed to improve subsequent fits. The tight window is necessary with our particular combination of syntheses and observations to minimise the effects that weak line blends have on fitting. The continuum placement is the same as that in the Hamburg atlas. Originally, the continuum was fitted as a $y-$shift, however, it is degenerate with the other fitting parameters and led to systematically lower abundances. As such, we use the continuum normalisation of the Hamburg atlas and do not fit for it separately.

Some infrared lines exhibited strong NLTE cores, and we do not include these lines in our final sample used to determine abundance. However, we did attempt to fit these lines by masking the core and fitting the line up to 70% residual intensity, inspired by the work of Shi et al. (2008). Their work revolves around accurately treating NLTE effects, and we noticed that infrared lines shown in this work could be fit in LTE up to this 70% intensity. In the end, clipping points at the 0.5% level was more versatile and useful than simply masking the line cores. This choice of 0.5% eliminates stronger offending blends

while still retaining important characteristics in the line profile. We fitted some infrared lines with strong NLTE cores with this method, but ultimately chose to leave them out of the subsample used to derive an abundance since they require excess negative broadening (see Sec. 2.3.1) to fit, which could be indicative of smaller NLTE effects present in the fitted parts of the line profile.

2.3.1 *Profile (de)broadening*

In the present investigation, we found that in many cases the synthetic line profiles were already broader than the observations, even prior to the application of instrumental broadening. Such a problem is specific to spectral synthesis calculations based on 3D model atmospheres (Caffau et al., 2015), as broadening effects of the stellar velocity field in 1D hydrostatic models are added in an ad-hoc fashion via fitting micro- and macro-turbulent broadening to the observations. Hence, mismatches of the overall broadening between model and observations cannot occur.

In our case, we could either broaden the observations or de-broaden the syntheses. Unsurprisingly, broadening the observations a priori by 2.5 km s^{-1} (the value that allowed our syntheses to fit the observations well) resulted in better statistical fits, as the lines appeared more Gaussian-like. However, this removes information about the line, such as weak blends and the overall shape. Instead, we chose to implement the capability to de-broaden our syntheses, rendering them narrower to better fit the observations as opposed to broadening observations instead. This is stated as equivalent to a negative broadening, or broadening with a kernel that has a negative full width at half-maximum (FWHM). We hoped to maintain the ability of 3D line profiles that allows one to identify weak blends that can degrade fits without being immediately recognised. This provides us a fully invertible method when it comes to fitting the broadening value of syntheses. Note that the broadening value we fit is still much smaller than the values of micro- and macro-turbulence fitted in 1D models, and our 3D model still reproduces line shapes and asymmetries.

We formally associate broadening with convolution, and de-broadening (negative broadening) as deconvolution and use a kernel inspired by Dorfi and Drury (1987). This kernel is composed of a double exponential decay centred on zero (see Appendix 2.8 for details of the implementation), and is referred to throughout this work as the G_n kernel, where n is an integer representing the order of the kernel. We can convolve the G_1 kernel (Equation 84) with itself to produce more Gaussian-like kernels, but note that this brings back the issues we faced with using Gaussian kernels (the amplification of noise in the far wings of the lines) that we aimed to mitigate with the use of the G_1 kernel:

$$g_1(x, x') = G_1(x - x') = \frac{\alpha}{2} \exp(-\alpha \left| x - x' \right|). \tag{84}$$

Here, x is position (in velocity space) and α controls the width of the kernel.

Gaussian and sinc functions were both considered as instrumental profile broadening kernels, but these do not allow for efficient and optimal computation of a de-broadened profile, since as the Fourier transform of these kernel functions rapidly goes to zero precluding a deconvolution, small disturbances cause large spikes in the wings of de-broadened spectra. Across all lines (and across the downsample), the choice between the G_1 and G_3 kernels does not affect the fitted abundance. The G_1 kernel does result in slightly better statistical fits, and so we favour it in this study.

2.3.2 *Photometric noise model*

Often, the pixel-to-pixel correlation of the signal in the spectrum is ignored, despite being rather commonly present due to instrumental imperfections during detection as well as steps during data reduction. The Hamburg atlas was rebinned at steps of 3.8 mÅ. This rebinning introduced a correlation between pixels. We implement a photometric noise model that considers the relation between neighbouring pixels in the observations, whose correlated signal introduces correlation in the noise values in each pixel (given by the root mean-squared error (RMSE) of a window). In order to model this, we require a representation of the covariance matrix of the noise. This covariance matrix, or correlated noise matrix, can then be applied to the set of observations in the fitting routine to describe the pixel-to-pixel correlation of the noise in the spectrum. Due to the nature of the covariance matrix, it must be positive semi-definite. To accurately estimate the matrix of correlated noise, we fit the autocorrelation function of continuum regions of the spectrum with an exponential decay.

Our line sample spans both the optical and near-infrared, and across a considerable range of signal-to-noise ratios. In order to properly determine the effects of noise, it was necessary to split the spectrum into several wavelength ranges. This is not a simple task, since one could define many separate ranges based on signal-to-noise thresholds, but we restrict our study to three representative regimes. The regimes themselves span the ranges $5500 - 6500$ Å, $7000 - 8000$ Å, and $10000 - 12500$ Å, for the green, red and near-infrared, respectively. Note that not all wavelengths are included in this, since some pre-sampling was done in order to find ranges that were comparatively clean in regard to continuum intensity. Both the overall RMSE value and the fitted exponential decay constant vary with wavelength range. This means each wavelength range has a distinct correlated noise matrix associated with it. For each of these, a signal-to-noise ratio was computed by examining the RMSE scatter around the best continuum region (i.e. the largest set of wavelength points devoid of any spectral lines and other features) in each range. Then, an exponential decay was fitted to the autocorrelation function of the spectral range where the continuum was computed in each wavelength region, in order to calculate the decay constant chosen to fit the autocorrelation as an exponential decay. The RMSE of this smaller range is then used for the entire regime. Table 9 shows the calculated decay constants β and signal-to-noise ratios in each wavelength range.

Table 9: Signal-to-noise ratios and fitted decay constants β (see Eq. 85) for the three representative wavelength regimes chosen from the Hamburg spectrum.

Wavelength (Å)	SNR	RMSE	β
$5500 - 6500$	1720	5.82×10^{-4}	0.215
$7000 - 8000$	2010	4.98×10^{-4}	0.309
$10000 - 12000$	3760	2.66×10^{-4}	0.797

2.3.2.1 *Applying the model*

The pixel-to-pixel autocorrelated noise is applied independently for each spectral line. For n observed points, an $n \times n$ matrix is constructed with a matrix element N_{ij} given by

$$N_{ij} = \exp(-\beta\,|i-j|) \tag{85}$$

β is the decay constant for the given regime, and $|i-j|$ represents the autocorrelation step. This covariance matrix is then normalised by the square of the noise-to-signal ratio.

Initially, the model was applied via Cholesky decomposition, but we found that including the observed spectrum's covariances as a parameter was a better way to intuitively formulate the problem due to our use of the 'mpfitcovar' routine (Markwardt, 2009) (which uses correlated inputs, but uncorrelates the calculated sum of squared residuals). The correlated noise model decreases the reduced χ^2 values during the fitting routine for all of the infrared lines and some of the optical lines. The uncertainty on fitted parameters hence includes correlations between neighbouring pixels in the spectrum.

Nevertheless, the correlated noise approach presented here is still an approximation. We assume that the noise present in spectral lines behaves the same way in the lines as it does in the continuum near the line. We also assume that the noise is not extremely wavelength-dependent, i.e. considering separate regimes in the spectrum is sufficient, so that the noise determined at one wavelength can be used at a different wavelength within the same regime, namely the wavelength of the line in question. While the correlated noise model does not drastically impact the final fitted abundance, we believe it important to consider these sources of error in the procedure.

2.4 RESULTS

2.4.1 *Line syntheses*

The spectral line syntheses for the chosen 11 lines are shown in Fig. 27. The lines are synthesised with the non-magnetic msc600 model atmosphere and use the G_1 broadening kernel during fitting. We also use a covariance matrix for pixel-correlated noise, which results in an increase in mean abundance of 0.001 dex compared to assuming uncorrelated noise. Our final derived photospheric solar silicon abundance is $\log \varepsilon_{Si} = 7.57 \pm 0.04$, including the -0.01 dex correction from NLTE effects (Amarsi and Asplund, 2017).

We find that simultaneously fitting the continuum for the entire selection of spectral lines systematically lowers the abundance by 0.01 dex. A local fit of the continuum is therefore not representative of the spectrum on a larger scale, and we rely on the normalisation provided by the Hamburg atlas. This comparison is shown for two lines in Fig. 28. Broadening the observations a priori by 2.5 km s^{-1} (to counter the overly broadened syntheses) increases the abundance across all configurations by 0.02 dex as this convolves weak line blends into the primary line shape, rendering the observations more Gaussian-like and removing information (such as the observational line shape) in the process.

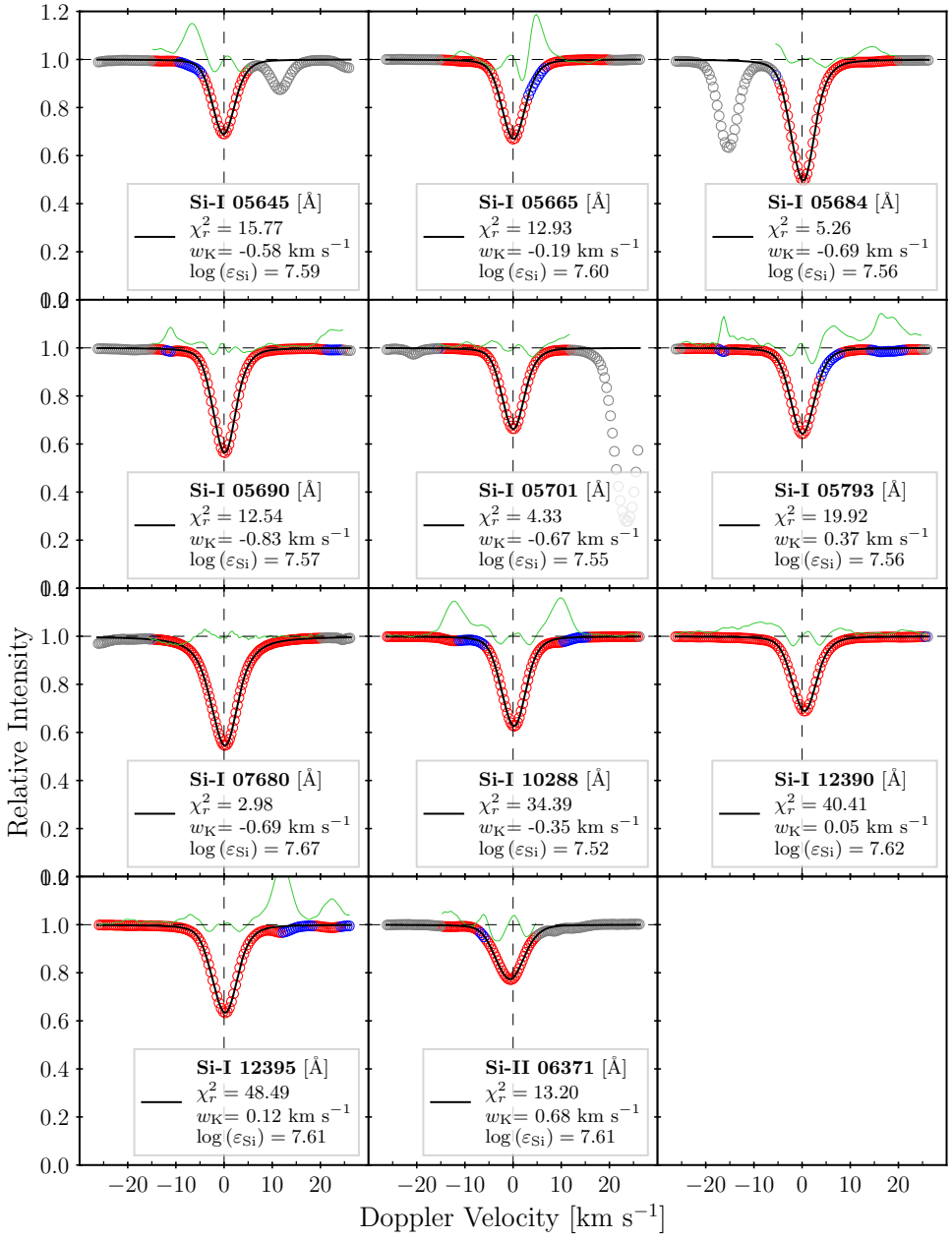

Figure 27: Synthesised fitted line shapes (black solid line) against observations from the Hamburg spectrum (points) for 11 silicon lines for the msc600 model. Grey points were removed before fitting, blue points show areas where sigma-clipping was employed to remove poorly fitting points, and red points were used for determining final fitted quantities. Green lines show the residuals increased by a factor of 10 for readability. In each panel, the name of the line, the reduced χ^2 value, the width of the broadening kernel w_{K}, and the LTE abundance $\log \varepsilon_{\mathrm{Si}}$ are shown. The final weighted mean abundance of 7.57 ± 0.04 includes the -0.01 dex NLTE correction, a fixed continuum, no pre-broadening, and de-broadening.

2.4.2 *Magnetic field effects*

Figure 30 shows the difference in abundance and broadening fitted when comparing different magnetic model atmospheres: one without a magnetic field and one with a magnetic field of 200 G (b200).

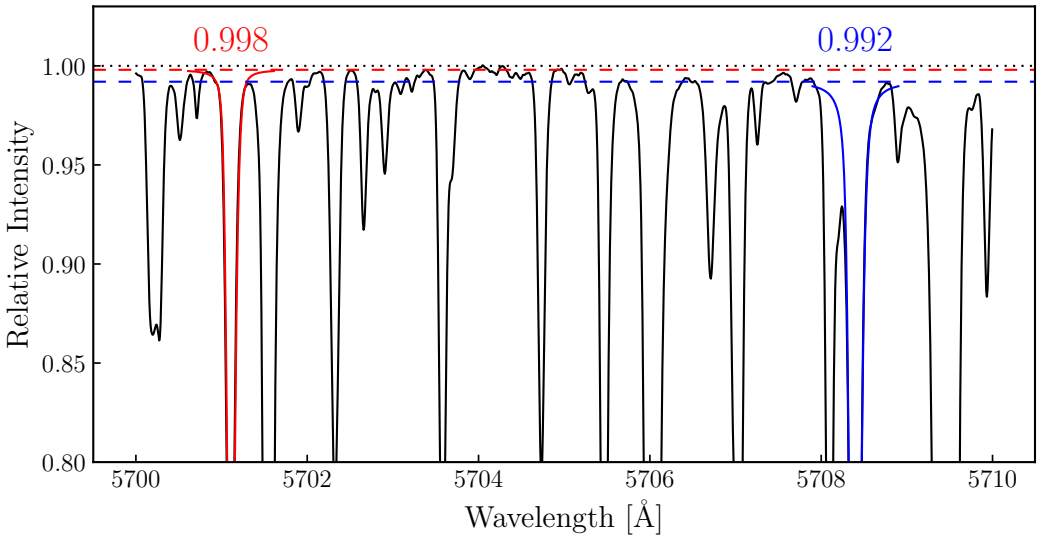

Figure 28: Comparison of two silicon line profiles while locally fitting the continuum. Observations are shown in black and the fitted syntheses at 5701.11 and 5708.40 Å are shown in red and blue, respectively, along with the fitted continuum value. Across a wider wavelength range, the various fitted continua are not consistent with one another.

The fitted results of the magnetic models should not be used on an absolute scale, as the model atmosphere grids are too coarse to resolve the detailed structure of small magnetic flux concentrations. Additionally, as the effective temperatures of these models are further from the nominal $T_{eff} = 5772$ K (Prša et al., 2016), we apply a correction to each line's fitted abundance to account for this change in temperature. The correction was derived from the snapshot-to-snapshot variation of T_{eff} and equivalent width. The highest correction, for the b000 model, was $+0.015$ dex for the Si II lines, while the Si I lines averaged a -0.005 dex correction. Si I and Si II lines show opposite trends in each model. The models are used for differential comparison, noting that increasing the magnetic field strength increases both the fitted abundance and broadening values. A possible implication is that the over-broadening of synthesised lines is caused by a lack of magnetic fields in the model atmosphere, as magnetic field lines constrain the flow of material in the solar atmosphere, reducing turbulence and thereby the line broadening. Fig. 29 illustrates this point for all 4 models alongside 2 models with much higher and lower effective temperatures. Though the b200 model has a higher effective temperature than the other solar-type models, its still has a lower vertical RMS velocity. Comparing to the t63g45mm00 model at 6233 K, the increase in effective temperature in the b200 model to overcome the magnetic field effects would need to be much greater than the current model's value.

Additionally, a magnetic field strength of 200 G still does not give the full amount of de-broadening required to fit the observations and is higher than the value of up to 75 G expected in the majority of the quiet photosphere (Ramírez Vélez, López Ariste, and Semel, 2008). Again, as shown by Shchukina, Sukhorukov, and Trujillo Bueno (2015) & Shchukina, Sukhorukov, and Trujillo Bueno (2016), a vertical field of 200 G would overestimate the effects when compared with a self-consistent 3D MHD model with a small-scale dynamo. The syntheses do not include the 1 km s^{-1} instrumental broadening, meaning the nominal $w_K \approx 1$ km s^{-1} – hence even further de-broadening from magnetic fields would be required. The centre-to-limb variation of the b200 model is also incompatible with observations. Therefore, our results are suggestive but not definitive that the lack of magnetic fields contributes to the over-broadening of spectral lines, and

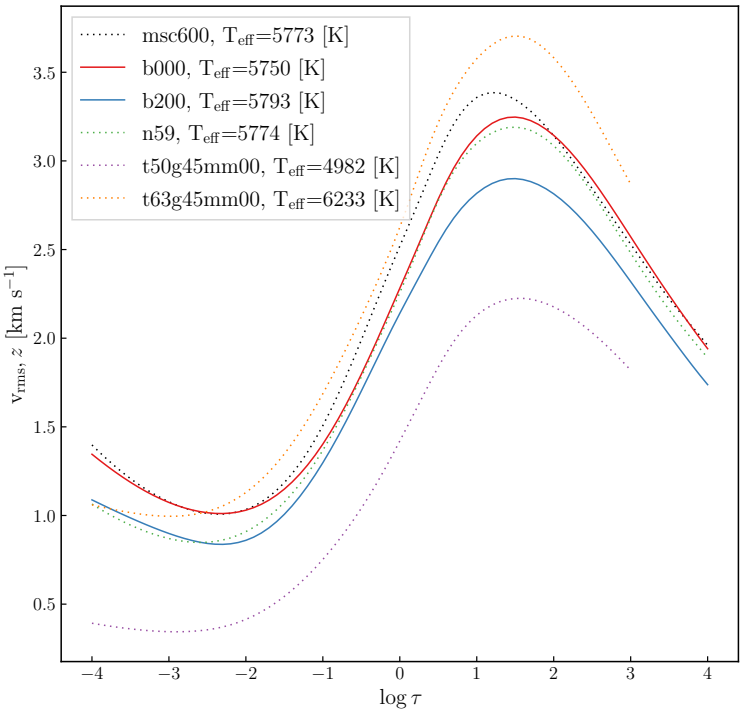

Figure 29: Vertical RMS velocity profiles in and around line-forming regions for the b000, b200 models (solid lines) with the msc600, n59, and 2 other models at much lower and higher effective temperatures shown for comparison (dotted lines). The b200 model clearly has lower RMS velocity than the other solar-type models, even though its effective temperature is higher.

the high magnetic field strengths required to produce the required broadening would not be consistent with 3D MHD models with small-scale dynamos.

2.4.3 *Effects of model differences*

The models presented in this work have different spatial resolutions and utilise different radiation transport (RT) schemes. As a comparison, Fig. 31 shows the difference between the fitted abundance and broadening values in the msc600, m595 and n59 models. We find that using the coarser models predicts a slightly higher abundance, and the lines are not synthesised as broad as when using the finer msc600 model, which is shown in Fig. 32. This is in line with the reduced level of turbulence in the n59 model due to its lower resolution. The n59 model also has a significantly higher extra viscosity relative to the msc600 model, and utilises a long characteristic RT scheme while the msc600 model uses a newer, multiple short characteristic scheme. The m595 model has the same parameters as msc600, except the spatial resolution, which is that of n59. Its fitted broadening lies between n59 and msc600, but is closer to the latter model. This suggests that, rather than the spatial resolution, it is the RT scheme and viscosity parameters that primarily affect the line broadening; though the spatial resolution does have a small effect. All models use the same opacity table and equation of state. With the chosen line sample, generally positive broadening is required for the n59 model; however, when considering all lines, the majority still require negative broadening to fit the observations.

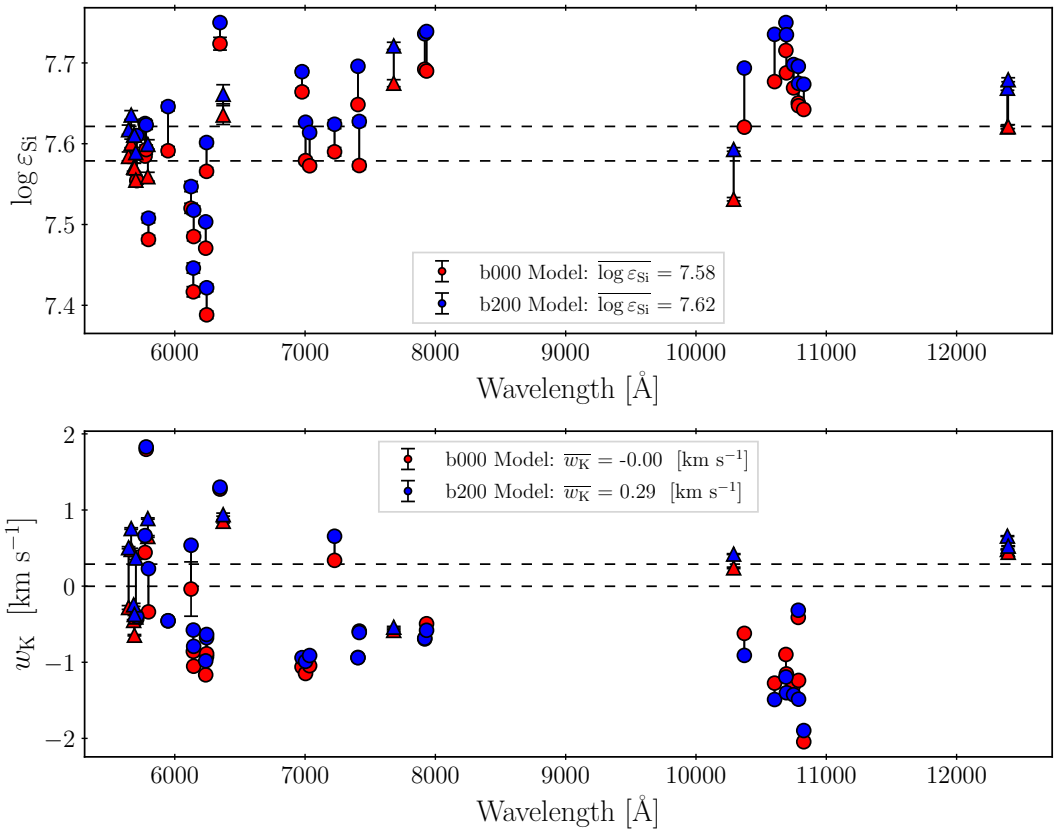

Figure 30: Comparison of abundance and broadening between the b000 (red points), and b200 (blue points) models. The red and blue horizontal dashed lines follow the same colour scheme and show the weighted average values (denoted by $\overline{x}$). Triangles indicate the lines used in the subsample. Increasing the magnetic field strength increases fitted abundance and decreases negative broadening.

2.4.4 *Disk-centre and disk-integrated spectrum differences*

Comparisons between disk-centre and disk-integrated spectra for the msc600 model are shown in Fig. 33. Disk-integrated spectra show a 0.01 dex higher abundance on average, and a broadening 0.03 km s^{-1} more negative than the disk-centre spectra across the full sample of 39 lines. The correspondence between disk-centre and disk-integrated fitted abundance and broadening is hence quite satisfactory. The infrared lines not chosen in the subsample show higher deviation than most optical lines, perhaps due to NLTE core effects that are more prominent in the disk-integrated spectrum. Additionally, the largest deviation is given by the Si II 6347.10 Å line, which is not used in the subsample because of this large deviation. The other Si II at 6371.36 Å line is used in the subsample and shows a large uncertainty in the fitted abundance.

The fitted abundance and broadening values for the disk-centre and disk-integrated syntheses, as well as the old and new oscillator strengths used in this study are given in Table 10. Only the disk-centre spectra and new gf-values are used for determining the final abundance.

2.4.5 *Comparisons with meteoritic abundances*

Type-I carbonaceous chondrites (named after the Ivuna meteorite, usually abbreviated to CI chondrites) constitute a special class of meteorites. Their chemical composition

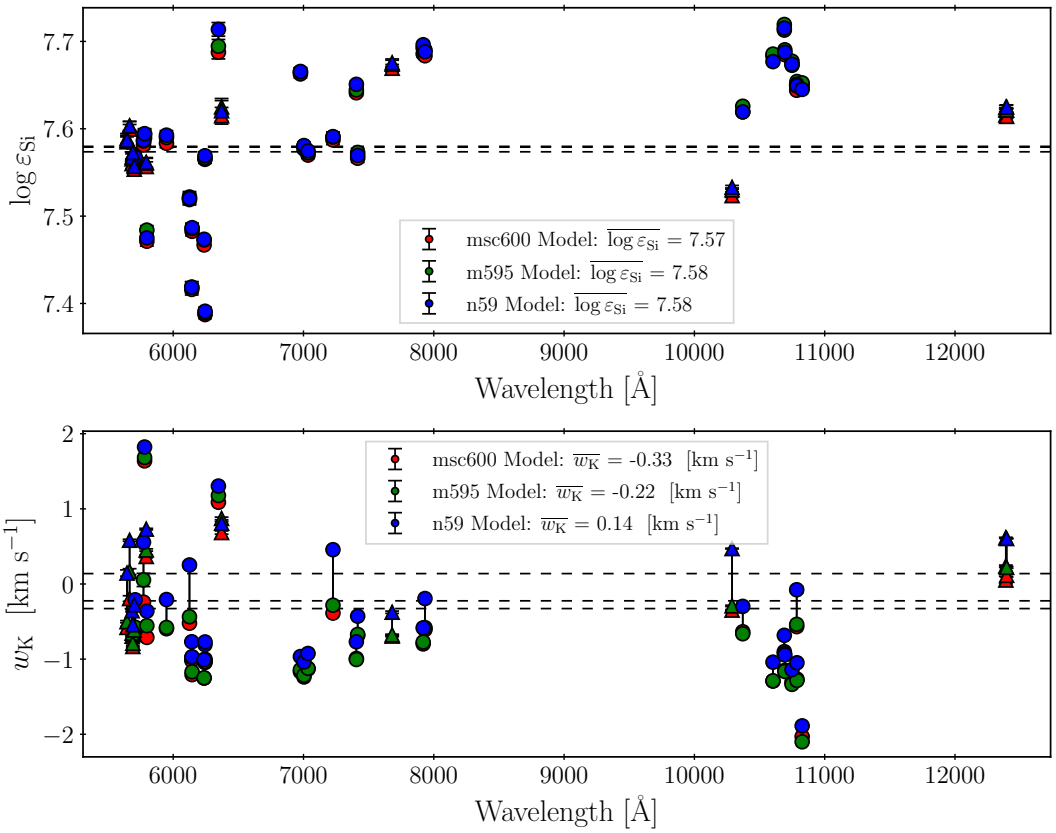

Figure 31: Comparison of abundance and broadening between the msc600 (red points), m595 (green points) and n59 (blue points) models. Triangles indicate the lines used in the subsample. The red, green and blue horizontal dashed lines follow the same colour scheme and show the weighted average values (denoted by $\overline{x}$).

of refractory elements is believed to reflect the composition of the early solar system (e.g., Lodders, Palme, and Gail, 2009). Conventionally, meteoritic abundances are given relative to silicon on the so-called cosmochemical scale, here for an element X written as

$$\mu_X \equiv 10^6 \times \frac{n_X}{n_{Si}}, \tag{86}$$

where n_X denotes the number density per volume of element X. In this paper, we gave abundances on the astronomical scale defined by

$$\varepsilon_X \equiv 10^{12} \times \frac{n_X}{n_H}. \tag{87}$$

With these definitions we have[2] $\lg \mu_{Si} = 6$, and $\lg \varepsilon_H = 12$. Conversion from the abundance of an element X from the astronomical to the cosmochemical scale reads

$$\lg \mu_X = \lg \varepsilon_X - \lg \varepsilon_{Si} + 6 \tag{88}$$

which necessitates the knowledge of the silicon abundance on the astronomical scale. Equation (88) shows that an increase of the silicon abundance – as found in this work in comparison to earlier results – leads to a corresponding decrease of an abundance given on the cosmochemical scale. Since the abundance on the cosmochemical scale

2 $\lg \equiv \log_{10}$

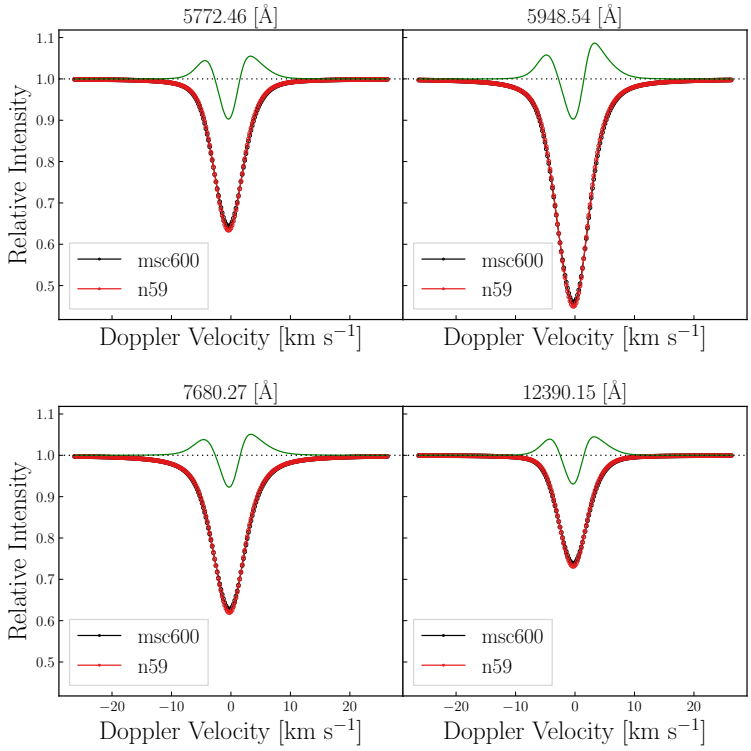

Figure 32: Line profiles from msc600 (black) and n59 (red) models with the residuals magnified by a factor of 10 in green. The difference in the line profiles is greatest in the line core.

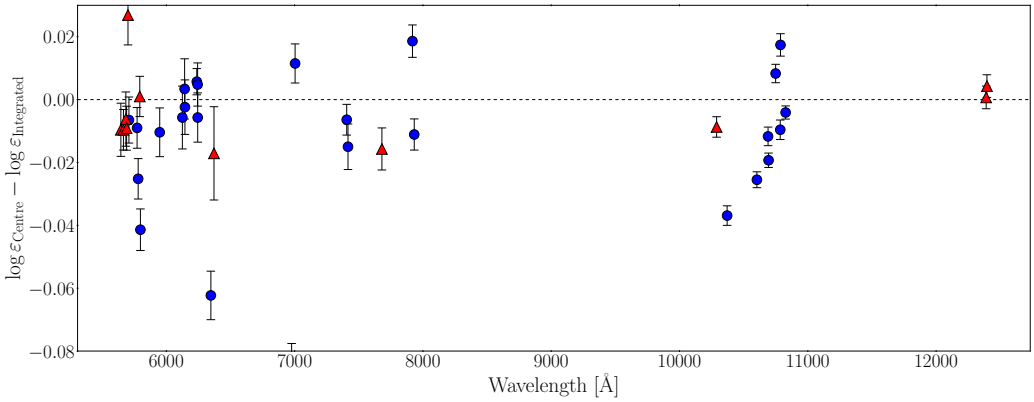

Figure 33: Differences between disk-centre and disk-integrated fitted abundances for the msc600 model. Red triangles indicate the lines in the subsample used for the final abundance calculation.

involves two abundances on the astronomical scale the conversion generally leads to an increase of the resulting uncertainty for an abundance – assuming that there are no significant correlations among the individual input uncertainties. Dealing with a ratio of two metal abundances here has the advantage that settling effects over the lifetime of the Sun should cancel out to first order (Lodders, Palme, and Gail, 2009), and we can directly compare to the corresponding meteoritic ratios. In Fig. 34 we compare these abundance ratios on the cosmochemical scale in ascending order of the 50% condensation temperatures of the elements. All condensation temperatures are from Palme, Lodders, and Jones (2014) and meteoritic abundances are taken from Lodders (2021, here Tab. 3, present solar system). We use the solar photospheric abundances of non-volatile elements based on CO^{5}BOLD models presented in Caffau et al. (2011a). The uncertainties

Wavelength [Å]	W_λ (DC) [mÅ]	W_λ (DI) [mÅ]	$\log \varepsilon_{Si}$ (DC)	$\log \varepsilon_{Si}$ (DI)	w_K (DC) [km s^{-1}]	w_K (DI) [km s^{-1}]
Si I						
5645.6128*	37.285 ± 0.004	38.465 ± 0.004	7.583 ± 0.005	7.590 ± 0.006	-0.62 ± 0.01	-0.60 ± 0.02
5665.5545*	40.850 ± 0.003	42.100 ± 0.003	7.589 ± 0.004	7.600 ± 0.005	-0.36 ± 0.02	-0.40 ± 0.04
5684.4840*	66.447 ± 0.003	65.793 ± 0.003	7.560 ± 0.006	7.566 ± 0.007	-0.70 ± 0.01	-0.89 ± 0.01
5690.4250*	54.123 ± 0.003	54.875 ± 0.003	7.566 ± 0.006	7.581 ± 0.005	-0.83 ± 0.01	-1.12 ± 0.01
5701.1040*	40.941 ± 0.004	41.240 ± 0.005	7.554 ± 0.006	7.554 ± 0.007	-0.67 ± 0.01	-0.81 ± 0.02
5708.3995	83.932 ± 0.001	81.971 ± 0.002	7.547 ± 0.003	7.557 ± 0.004	-0.61 ± 0.01	-0.79 ± 0.01
5772.1460	58.461 ± 0.003	58.254 ± 0.003	7.578 ± 0.005	7.590 ± 0.004	-0.31 ± 0.02	-0.26 ± 0.25
5780.3838	34.914 ± 0.004	38.252 ± 0.005	7.618 ± 0.007	7.664 ± 0.007	$+1.94 \pm 0.02$	$+2.49 \pm 0.00$
5793.0726*	47.079 ± 0.003	47.932 ± 0.004	7.553 ± 0.005	7.565 ± 0.006	$+0.27 \pm 0.02$	$+0.49 \pm 0.02$
5797.8559	44.799 ± 0.003	46.259 ± 0.002	7.476 ± 0.005	7.497 ± 0.003	-0.67 ± 0.01	-0.48 ± 0.03
5948.5410	97.658 ± 0.002	94.248 ± 0.003	7.581 ± 0.005	7.598 ± 0.006	-0.60 ± 0.01	-0.82 ± 0.01
6125.0209	34.496 ± 0.005	34.737 ± 0.006	7.517 ± 0.006	7.529 ± 0.007	-0.58 ± 0.02	-0.53 ± 0.03
6142.4832	39.323 ± 0.004	38.765 ± 0.006	7.408 ± 0.006	7.413 ± 0.007	-1.10 ± 0.01	-1.12 ± 0.02
6145.0159	44.040 ± 0.004	42.187 ± 0.005	7.487 ± 0.006	7.479 ± 0.006	-1.17 ± 0.01	-1.36 ± 0.01
6237.3191	81.782 ± 0.002	76.779 ± 0.003	7.468 ± 0.003	7.462 ± 0.003	-1.23 ± 0.01	-1.39 ± 0.01
6243.8146	57.363 ± 0.003	54.134 ± 0.004	7.574 ± 0.004	7.567 ± 0.005	-0.96 ± 0.01	-1.13 ± 0.01
6244.4655	54.674 ± 0.003	52.042 ± 0.004	7.390 ± 0.005	7.388 ± 0.005	-0.98 ± 0.01	-1.15 ± 0.01
6976.5129	56.438 ± 0.003	52.806 ± 0.003	7.654 ± 0.003	7.648 ± 0.004	-1.22 ± 0.01	-1.22 ± 0.01
7003.5690	75.507 ± 0.002	68.469 ± 0.003	7.583 ± 0.003	7.569 ± 0.005	-1.43 ± 0.01	-1.39 ± 0.01
7034.9006	83.976 ± 0.002	76.443 ± 0.003	7.575 ± 0.003	7.565 ± 0.004	-1.13 ± 0.01	-1.28 ± 0.01
7226.2079	43.345 ± 0.004	42.227 ± 0.004	7.587 ± 0.005	7.597 ± 0.006	-0.24 ± 0.02	-1.47 ± 0.05
7405.7718	110.020 ± 0.002	101.650 ± 0.002	7.634 ± 0.004	7.655 ± 0.004	-1.31 ± 0.00	-1.27 ± 0.01
7415.9480	105.090 ± 0.002	99.125 ± 0.002	7.558 ± 0.004	7.590 ± 0.005	-0.83 ± 0.01	-0.87 ± 0.01
7680.2660*	102.790 ± 0.002	95.068 ± 0.002	7.669 ± 0.004	7.698 ± 0.005	-0.93 ± 0.01	-0.92 ± 0.01
7918.3835	103.440 ± 0.002	97.816 ± 0.002	7.690 ± 0.003	7.723 ± 0.004	-0.82 ± 0.01	-0.85 ± 0.01
7932.3479	127.030 ± 0.002	117.070 ± 0.002	7.689 ± 0.004	7.706 ± 0.004	-0.61 ± 0.01	-0.81 ± 0.01
10288.9440*	88.692 ± 0.001	85.213 ± 0.001	7.522 ± 0.002	7.538 ± 0.003	-0.37 ± 0.01	-0.39 ± 0.01
10371.2630	199.010 ± 0.001	189.420 ± 0.001	7.621 ± 0.002	7.668 ± 0.003	-0.63 ± 0.00	-1.08 ± 0.00
10603.4250	295.370 ± 0.001	281.120 ± 0.001	7.686 ± 0.002	7.742 ± 0.002	-1.24 ± 0.00	-1.88 ± 0.00
10689.7160	228.360 ± 0.001	205.700 ± 0.001	7.712 ± 0.003	7.741 ± 0.002	-0.91 ± 0.00	-1.28 ± 0.00
10694.2510	251.900 ± 0.001	230.870 ± 0.001	7.679 ± 0.002	7.727 ± 0.002	-1.15 ± 0.00	-1.51 ± 0.00
10749.3780	330.400 ± 0.000	308.620 ± 0.001	7.677 ± 0.001	7.713 ± 0.002	-1.44 ± 0.00	-2.08 ± 0.03
10784.5620	106.910 ± 0.001	98.584 ± 0.001	7.645 ± 0.002	7.664 ± 0.002	-0.54 ± 0.01	-0.72 ± 0.01
10786.8490	296.440 ± 0.001	278.200 ± 0.001	7.651 ± 0.001	7.687 ± 0.002	-1.29 ± 0.00	-1.98 ± 0.03
10827.0880	473.350 ± 0.000	433.190 ± 0.001	7.662 ± 0.001	7.678 ± 0.002	-2.32 ± 0.01	-1.97 ± 0.02
12390.1540*	89.770 ± 0.001	87.503 ± 0.001	7.615 ± 0.002	7.613 ± 0.003	-0.11 ± 0.03	-0.29 ± 0.83
12395.8320*	111.000 ± 0.001	106.810 ± 0.001	7.613 ± 0.002	7.609 ± 0.003	$+0.08 \pm 0.03$	-0.38 ± 0.02
Si II						
6347.1087	55.354 ± 0.002	48.835 ± 0.002	7.675 ± 0.005	7.547 ± 0.005	$+0.91 \pm 0.01$	$+1.43 \pm 0.01$
6371.3714*	37.936 ± 0.004	32.226 ± 0.006	7.610 ± 0.010	7.469 ± 0.011	$+0.59 \pm 0.02$	$+1.25 \pm 0.03$

Table 10: Fitted 3D LTE abundance and broadening values for disk-centre (DC) and disk-integrated (DI) spectra with their formal statistical uncertainties. w_K is the width of the broadening kernel. The old and new $\log gf$ values are also provided. An asterisk next to the wavelength signifies the line was in the chosen subsample.

indicated in Fig. 34 are dominated by the uncertainties of the spectroscopically determined photospheric abundances. The uncertainty of the silicon abundance noticeably contributes here. The error bars are perhaps over-estimated since some compensatory

effects due to error correlations might be present. With the exception of hafnium (a well-known problem case) meteoritic and photospheric abundances are consistent with each other on the $1\,\sigma$ level. However, for being able to identify possible differences a reduction of the uncertainties appears desirable.

2.4.6 *Mass fractions of hydrogen, helium, and metals*

In this section we calculate the mass fractions of hydrogen X, helium Y, and metals Z which are of particular interest for stellar structure. Our intention is not so much to provide the absolute numbers but rather to demonstrate the involved uncertainties. Serenelli et al. (2016) and Vinyoles et al. (2017) both advocate the use of meteoritic abundances for elements heavier than C, N, O in the Sun. We follow this idea, and augment the 12 photospheric abundances from Caffau et al. (2011a) (Li, C, N, O, P, S, K, Fe, Eu, Os, Hf, Th) and the newly derived silicon abundance by the meteoritic abundances given by Lodders (2021). To this end, we need to bring photospheric and meteoritic abundances onto the same scale. For relating the abundances we use the abundance of *silicon only*. Using Eq. (87) we obtain

$$\lg \varepsilon_{\mathrm{X}}^{\diamond} = \lg \mu_{\mathrm{X}}^{\diamond} + \lg \varepsilon_{\mathrm{Si}}^{\odot} - 6 \qquad \text{or} \qquad \varepsilon_{\mathrm{X}}^{\diamond} = \frac{n_{\mathrm{X}}^{\diamond}}{n_{\mathrm{Si}}^{\diamond}}\, \varepsilon_{\mathrm{Si}}^{\odot}, \tag{89}$$

where diamonds ($\diamond$) indicate meteoritic values, the Sun symbol ($\odot$) solar photospheric values. The basic assumption underlying Eq. (89) is that $\varepsilon_{\mathrm{Si}}^{\diamond} = \varepsilon_{\mathrm{Si}}^{\odot}$, that is to say, silicon is not subject to differentiation effects, neither in the solar photosphere, nor in the meteorites.

Equation (89) shows that in the conversion of the meteoritic abundances we have to take into account the uncertainties of the individual species including the silicon abundance as measured in meteorites. The normalisation puts the meteoritic silicon abundance on a value of 10^6, however, with an uncertainty of 3.4 %. The uncertainty of the solar silicon abundance contributes to the meteoritic uncertainties in the conversion to the astronomical scale. An input neither directly obtained from meteorites nor from photospheric spectroscopy is the helium abundance. Here, we assume a ratio $n_{\mathrm{He}}^{\odot}/n_{\mathrm{H}}^{\odot} = (8.38 \pm 0.39) \times 10^{-2}$ as given by Lodders (2021) for the present Sun which is motivated from helioseismic measurements. With these ingredients and atomic weights assumed to be precisely known we ran Monte-Carlo error propagations and obtained $\mathrm{X} = 0.7382 \pm 0.0084$, $\mathrm{Y} = 0.2456 \pm 0.0086$, $\mathrm{Z} = 0.0162 \pm 0.0015$, and $\mathrm{Z/X} = 0.0220 \pm 0.0020$ (independent of the abundance of helium). The uncertainties of X and Y are dominated by the uncertainty of the helium abundance. In order to further quantify the uncertainties of Z we present the build-up of the overall uncertainty of Z by sequentially adding sources of uncertainty. We obtain the sequence $\sigma_{\mathrm{Z}} = (65, 77, 79, 148) \times 10^{-5}$ when adding the uncertainties of the meteoritic abundances, of the photospheric abundance of silicon, of all photospheric abundances except CNO, and of all contributions including from CNO, respectively. This perhaps odd-appearing procedure is motivated by the fact that the individual sources of uncertainty are not simply additive (rather additive in quadrature), and there is some coupling emergent from the presence of the photospheric silicon abundance in the conversion given by Eq. (89). Keeping this limitation in mind, we see that the contribution to the overall uncertainty by the meteorites is not insignificant, and noticeably increased by the uncertainty of the photospheric silicon abundance. We emphasise that the "meteoritic" abundances include the noble gases (particularly neon). Their assumed values are coming from measurements other than those in meteorites. The photospheric abundances other than of CNO contribute

little to the overall uncertainty, the most important contribution stems – perhaps unsurprisingly – from CNO. We conclude that the procedure of using the average of several refractory elements (e.g., Lodders, Palme, and Gail, 2009) is a good way to reduce the overall uncertainty on the mass fraction of metals. The precision to which the CNO elements are measured in the solar photosphere is most important. Beyond that, any reduction of the uncertainty of photospheric or meteoritic abundances is helpful.

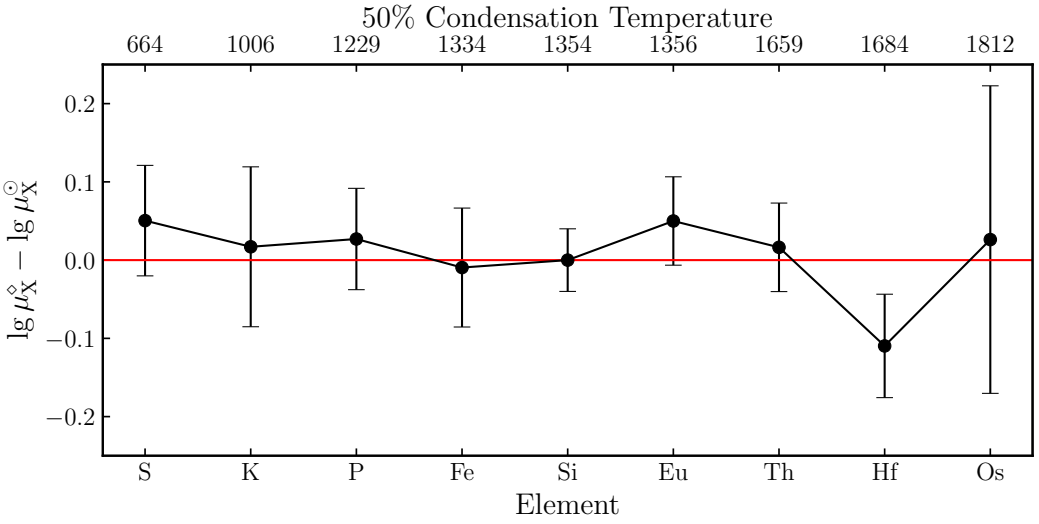

Figure 34: Elemental abundance differences between CI chondrites ($\mu_X^\diamond$) and solar photospheric composition ($\mu_X^\odot$) according to CO5BOLD in ascending order of the condensation temperatures of the elements. The silicon abundance difference is zero by definition, but shown to illustrate the scale of the error.

2.5 DISCUSSION

2.5.1 *Comparisons between models and line samples*

Both the choice of model atmosphere and the line sample affect the final abundance (and the level of broadening or debroadening required). Across all configurations, prior broadening of the observations increases the fitted abundance. Moreover, there is a spread of fitted abundances for even a single model based on the chosen line sample and fitting method. Overall, it is the combination of more or less judicious decisions taken during the fitting process that ultimately determines the final fitted abundance value.

2.5.2 *Comparisons with previous works*

Our derived abundance of 7.57 ± 0.04 is 0.06 dex higher than the abundance recently presented in Asplund, Amarsi, and Grevesse (2021). As a comparison to their work, we calculated a mean abundance using the line sample they presented (leaving out the 6741.61 Å line) alongside their weights, and find an abundance of 7.55 ± 0.02, which is 0.04 dex higher than that presented in their work. Part of the difference in fitted abundance stems from the new oscillator strength data used; when using the same oscillator strength data, we find an abundance of 7.54 ± 0.03. This is consistent with the average difference of the oscillator strength data used for these lines. The equivalent

widths obtained by our line profile fitting for all models are higher than those given in Amarsi and Asplund (2017), and are shown in Table 11. The corresponding differences in abundance are shown in Fig. 35. Altogether, the dominant difference comes from the new oscillator strength data (0.04 dex) and equivalent widths (0.02 dex), while line selection, weighting and 3D model are of secondary importance (0.01 dex).

Wavelength [Å]	msc600 [mÅ]	b000 [mÅ]	b200 [mÅ]	n59 [mÅ]	m595 [mÅ]	AA17
Si I						
5645.6128	37.4	37.4	37.5	37.4	37.4	35.0
5684.4840	66.5	67.0	67.0	66.5	66.5	63.7
5690.4250	54.2	54.2	54.6	54.2	54.1	52.6
5701.1040	40.9	40.9	41.1	40.9	40.9	39.5
5772.1460	58.8	58.8	59.4	58.8	58.8	56.0
5793.0726	47.4	47.4	47.9	47.4	47.4	45.8
7034.9006	83.4	83.4	84.6	83.5	83.2	74.0
7226.2079	43.4	43.4	43.7	43.4	43.4	38.7
Si II						
6371.3714	38.1	37.6	37.6	37.6	38.3	36.6

Table 11: Equivalent widths for the four models presented in this study alongside those given in Amarsi and Asplund (2017) (AA17). Our higher equivalent widths lead to a +0.02 dex increase in abundance across all cases (using the weighting of AA17).

2.5.3 *Uncertainties*

We use the root-mean-squared error (RMSE) of the selected sample to capture the final uncertainty on the fitted abundance. This uncertainty represents the uncertainties through the entire fitting procedure, including uncertainties in oscillator strengths as well as statistical uncertainties. The RMSE is given by

$$\mathrm{RMSE} = \sqrt{\frac{1}{N}\sum_{i}^{L}(y_i - \hat{y})^2}, \tag{90}$$

where $\hat{y}$ is the weighted mean abundance, y_i is the weighted abundance calculated for a single line, L is the number of lines used to determine the weighted mean and N is the sum of the weights. We chose this estimator since each line yields a different fitted abundance, and the RMSE naturally incorporates this scatter. Additionally, since we compute the RMSE on the final fitted abundances, the uncertainties in fitting and in the oscillator strengths are already represented in the scatter. On average, the oscillator strength uncertainty is 8.57%, which is compatible with our RMSE uncertainty in abundance. For other fitted quantities, we use the statistical uncertainties from the fitting procedure and other relevant sources of error, such as uncertainties in ABO theory parameters for broadening.

Despite careful line selection, new oscillator strength values and an improved broadening theory, there is still a substantial scatter in individual fitted abundance values.

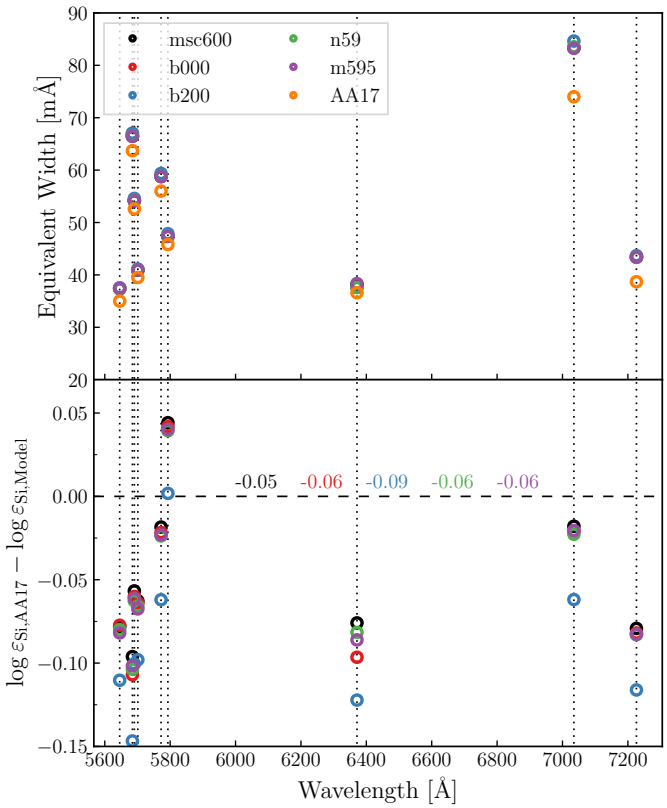

Figure 35: Differences in equivalent width (top) and fitted abundance (bottom) in comparison to the values in Amarsi and Asplund (2017). The numbers in the bottom panel give the mean abundance difference using the weighting scheme of Amarsi and Asplund (2017). The difference in abundance includes all sources, not just the difference in equivalent width.

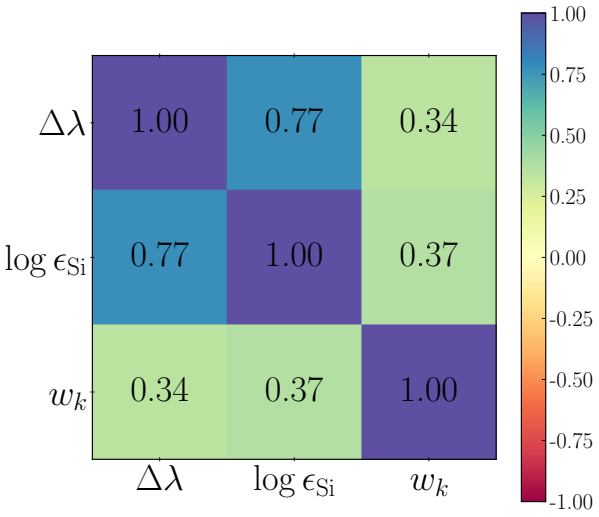

Figure 36: Correlation coefficient between fitted parameters for the msc600 model. $\Delta\lambda$ is the wavelength shift, $\log \varepsilon_{Si}$ is the abundance and w_K is the width of the broadening kernel.

The scatter is included in the uncertainties by means of the RMSE. The (maximum - minimum) scatter in abundance values is 0.15 dex for our main configuration, with an RMSE of 0.04. Using the line list of Amarsi and Asplund (2017) decreases the scatter to 0.06 dex and the RMSE to 0.02. Again, this shows that the choice of lines to use has a non-negligible impact on the final derived abundance.

We make use of the 'mpfitcovar' routine (Markwardt, 2009) which takes in the spectrum and correlated noise model and fits the free parameters of our routine (normally abundance, broadening and wavelength shift). We use χ^2 statistics to find the best fitting parameter as well as the errors on those parameters. There is some correlation between the quantities themselves, shown in Fig. 36 for the msc600 model.

2.6 COMPARISONS BETWEEN LINFOR3D/CO5BOLD AND BALDER/STAGGER

There was motivation to investigate whether the extra broadening present in the syntheses produced by `LINFOR3D` using the `CO5BOLD` model atmospheres was unique to these codes. To test this, we compared six LTE Si I line syntheses using our models against those produced by `BALDER` (Amarsi et al., 2018), a custom version of `Multi3D` (Leenaarts and Carlsson, 2009) (data provided by A. Amarsi, priv. comm.). These data were calculated on a 3D hydrodynamic `STAGGER` model solar atmosphere (Collet, Magic, and Asplund, 2011). These lines were: 5690, 5780, 5793, 6244, 6976 and 7680 Å.

We use the same log gf values, ABO parameters and central wavelengths for the lines in both sets of syntheses. After fitting for the abundance ($\log \varepsilon_{Si} = 7.51$ was assumed in the `BALDER` syntheses), the results are near-identical, and the fits shown in Figs. 37 & 38 using the n59 and 600 models are excellent. We are able to refit the abundance and broadening of the `BALDER` syntheses. The black points represent the `BALDER` synthesis, and the red lines are the `LINFOR3D` syntheses after fitting the lines synthesised with `BALDER`.

Two `CO5BOLD` model atmospheres were used for the analysis. The msc600 solar model is a newer model that has a higher spatial resolution and larger box size than the older n59 model (see Table 7 for details). The n59 model requires positive broadening to fit the `BALDER` syntheses, while the msc600 requires negative broadening. Broadening-wise,

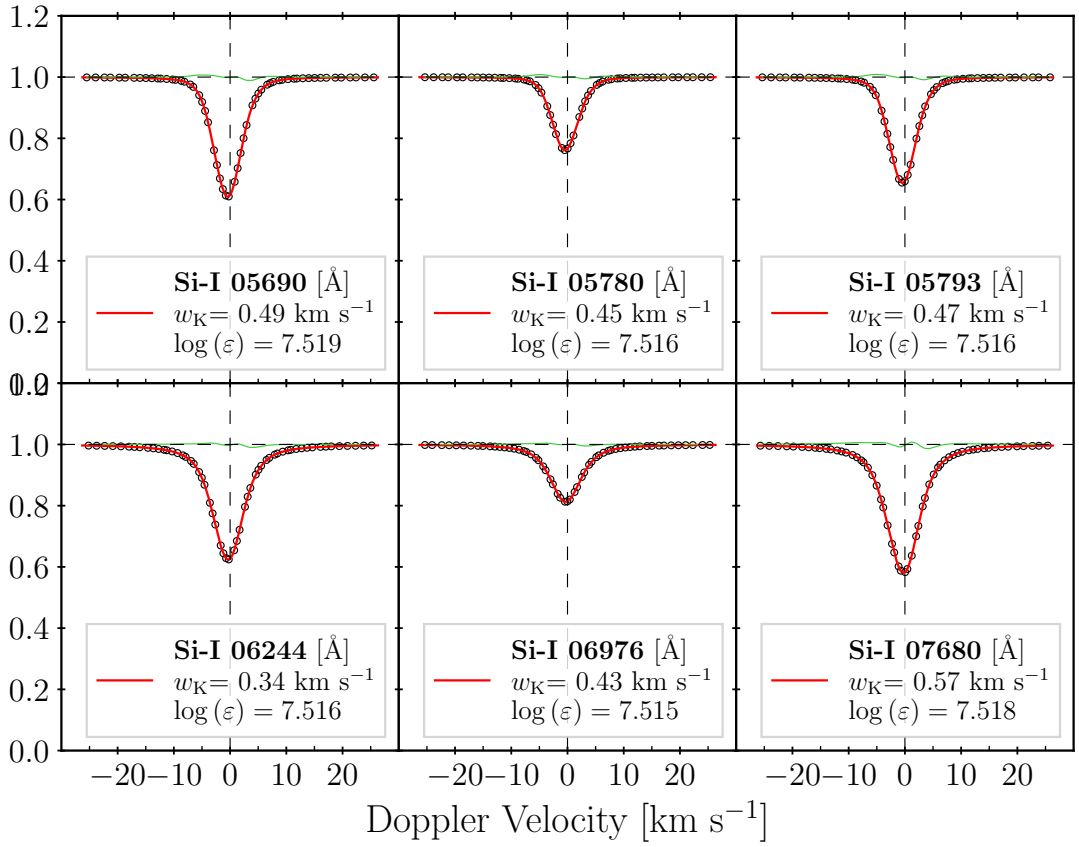

Figure 37: LINFOR3D + CO^{5}BOLD n59 model syntheses (red lines) fit to BALDER + STAGGER (black points). Green lines show residuals increased by a factor of 10. The mean abundance as derived by the CO^{5}BOLD fit is 7.52 ± 0.01.

then, the BALDER syntheses lie somewhere between our two chosen models - they are broader than the n59 model, but not as broad as the msc600 model. Table 12 shows the broadening values required by our models to reproduce the STAGGER syntheses and the observations from the Hamburg atlas. While the n59 model is less broad than the STAGGER model in all cases and the msc600 model is broader, both of these models still generally require negative broadening to fit a majority of the lines. Again, no instrumental broadening (typically $\sim$ 1 km s^{-1} FWHM) was applied to the synthetic spectra, as should be possible without the presence of over-broadening. This shows the issue of the syntheses being over-broadened is not unique to CO^{5}BOLD + LINFOR3D but is also present in the syntheses produced by BALDER + STAGGER.

2.7 1D LTE versus NLTE comparisons in LINFOR3D

Following the comparison between model atmospheres and spectral synthesis routines, four lines were synthesised in both 1D LTE and 1D NLTE as an additional investigation into the potential extra broadening seen in LINFOR3D. These lines were 5772.46, 5948.54, 7680.27 and 12288.15 Å. We fit the 1D NLTE line profiles with the 1D LTE syntheses for nine different abundance values to investigate whether the consequent fitted broadening is strongly affected. The abundance corrections generally remain within the predicted -0.01 dex; the 12288.28 Å requires slightly higher corrections at higher abundances. The employed model atom is the same as that in Wedemeyer (2001) with 115 energy levels for Si I and Si II with 84 transitions. Moreover, the collisional cross-sections for neutral

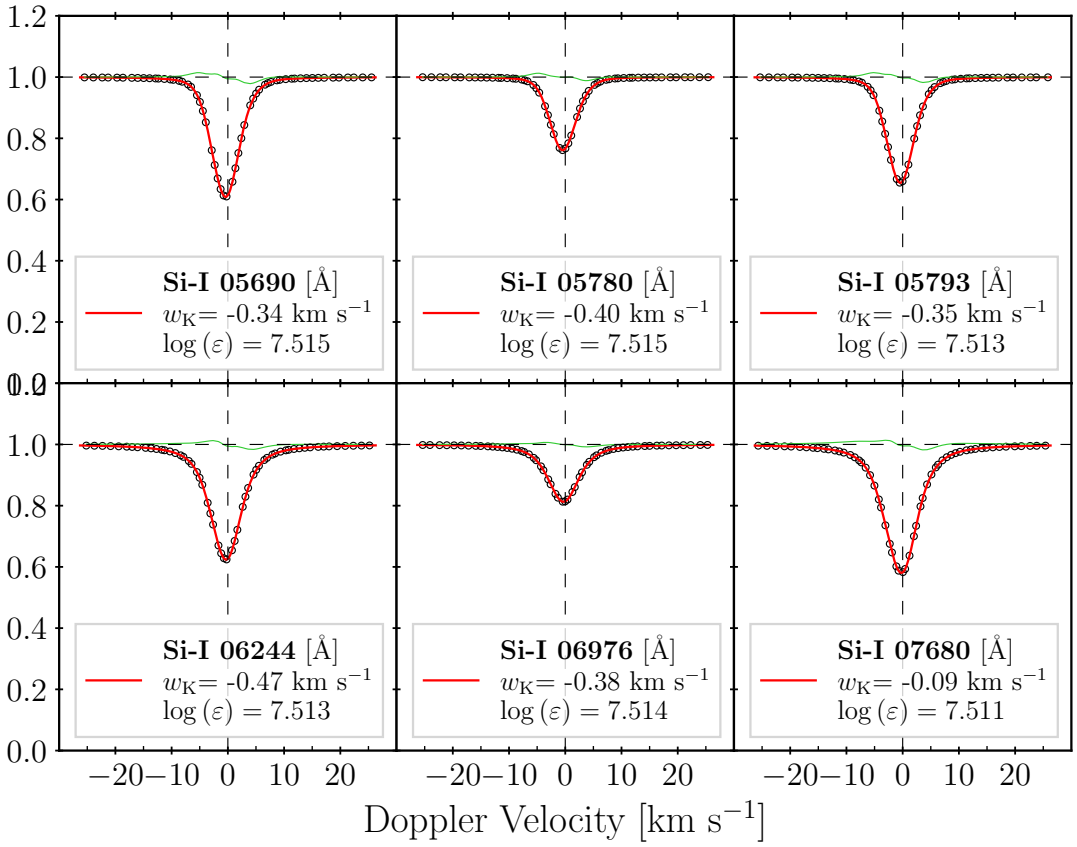

Figure 38: LINFOR3D + CO^{5}BOLD msc600 model model syntheses (red lines) fit to BALDER + STAGGER (black points). Green lines show residuals increased by a factor of 10. The mean abundance as derived by the CO^{5}BOLD fit is 7.51 ± 0.01.

particles follow Drawin (1967) and Steenbock and Holweger (1984) using a correction factor of $S_H = 0.1$.

Fig. 39 shows the fitted broadening at each abundance point for each line, and Fig. 40 shows the LTE versus NLTE line profiles. In this small sample, NLTE effects become stronger with increasing abundance resulting in stronger negative broadening for the 5772.46 Å, 5948.54 Å and 12288.15 Å lines, and less positive broadening for the 7680.27 Å line. It should be noted that the trends are reversed if we fit NLTE to LTE profiles, i.e. lines that showed negative broadening would instead show positive broadening. The three lines with a negative NLTE correction also require negative broadening, suggesting that part of the overly broadened line profiles could be attributed to NLTE effects. We also found that removing the core of the line (within ±3 km s^{-1}) removes the necessity for negative broadening, illustrating that the NLTE effects are concentrated in the cores of these lines.

2.8 DE-BROADENING OF SPECTRAL LINES

Mathematically, the effect of broadening is described as convolution and de-broadening as deconvolution. It is well-known that deconvolution is an ill-posed problem. A robust solution to a deconvolution problem can only be obtained by suitable regularisation. The problem becomes immediately apparent when considering a Gaussian (the "kernel") with which a spectrum is to be de-convolved. In Fourier space, deconvolution corresponds to a division with the Fourier transform of the kernel, which is again a

	n59 – Stagger	msc600 – Stagger	n59 – Hamburg	msc600 – Hamburg
λ	w_K	w_K	w_K	w_K
[Å]	[km s^{-1}]	[km s^{-1}]	[km s^{-1}]	[km s^{-1}]
5690.4250	0.49	−0.33	−0.54	−0.83
5780.3838	0.45	−0.40	1.47	1.40
5793.0726	0.47	−0.36	0.72	0.27
6244.4655	0.34	−0.47	−0.79	−0.98
6976.5129	0.43	−0.38	−1.05	−1.23
7680.2660	0.57	−0.08	−0.38	−0.69

Table 12: Fitted broadening values for six lines chosen as a comparison to STAGGER. The values come from fitting the n59 and msc600 models fitting to the STAGGER models (first two columns) and to the Hamburg atlas observations (last two columns). In all cases, the n59 model is less broad than the STAGGER model syntheses while the msc600 model is broader. However, since the n59 model generally also requires significant negative broadening to fit the observations, the STAGGER models must also yield too broad lines compared to the observations.

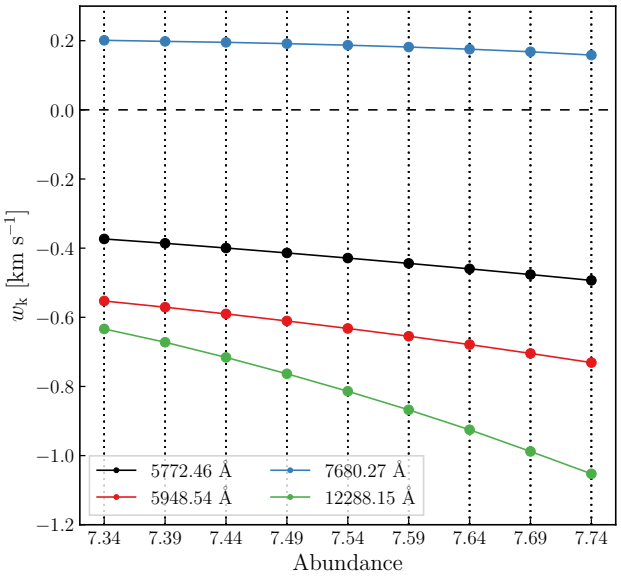

Figure 39: Fitted broadening values for four lines, fitting 1D LTE to 1D NLTE profiles. Larger NLTE effects are present in 5948.65 Å and 12228.15 Å lines than the 5772.46 Å and 7680.27 Å lines.

Gaussian in this case. The rapid decline of the wings of a Gaussian leads to a division by almost zero at distances of a few widths of the Gaussian away from its centre. Any numerical or physical imprecision leads to large disturbance under such circumstances. This means even noise-free synthetic line profiles cannot be de-convolved by a naive division of the raw spectrum by the Fourier transform of a Gaussian kernel.

The key question is now whether one can suitably regularise the problem or reduce the level of noise amplification. We followed the latter approach by seeking a different

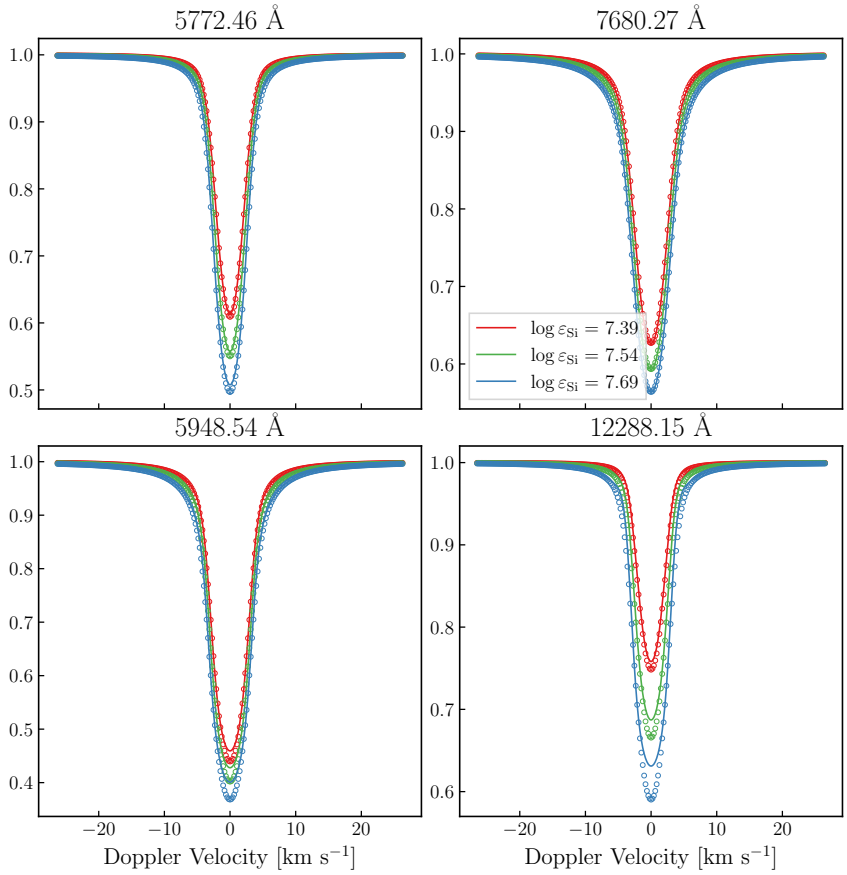

Figure 40: LTE (points) versus NLTE (solid lines) profiles for three representative abundance values. The 5948.54 Å and 12288.15 Å show visible NLTE effects in the core that become stronger with increasing abundance.

kernel with less steeply falling wings than a Gaussian. As starting point we chose the kernel function

$$G_1(x) = \frac{\alpha}{2} e^{-\alpha |x|}, \tag{91}$$

normalised to one according to

$$\int_{-\infty}^{\infty} dx \; G_1(x) = 1 \,. \tag{92}$$

The parameter α controls the width of the kernel. The kernel is symmetric, and has a peaked shape at the origin. Later, we shall discuss higher powers in terms of convolutions of the kernel with itself. We index the resulting kernels by the number of convolutions, which in the present case is one. Convolving a function f with kernel G_1 results in a function g according to

$$g(x) = \int_{-\infty}^{\infty} dx' \, G_1(x' - x) \, f(x') \,. \tag{93}$$

Our choice of the kernel function was inspired by work of Dorfi and Drury (1987). The authors pointed out that the above kernel is the Green's function associated with the differential operator

$$1 - \frac{1}{\alpha^2} \frac{d^2}{dx^2} \,, \tag{94}$$

where $\mathbf{1}$ indicates the identity operator. This allows one to formulate the convolution expressed by Eq. 93 as solution of a ordinary differential equation of second order. Discretising the differential operator, as well as the functions f and g (simplest on an equidistant x-grid), results in a set of linear equations of the form

$$\mathbf{A}\, g = f \tag{95}$$

where $\mathbf{A}$ is a tri-diagonal matrix which can be inverted efficiently. Remarkably, in this formulation a deconvolution appears even simpler than convolution: if g is given, a simple matrix multiplication with matrix $\mathbf{A}$ yields the de-convolved function f. It was this feature that made us choose G_1 as kernel for deconvolution, and for consistency, also for convolution. Using the same kernel when convolving a line profile has the advantage that during fitting there is a continuous transition from convolution to deconvolution and vice versa. This improves the stability of the fitting operation when having to deal with a situation where the broadening or de-broadening is around zero. It should be noted that the G kernels are in fact the Matérn functions with half-numbered indices (Genton, 2002).

One may question the suitability of the function G_1 for describing broadening or de-broadening effects, and might prefer a more Gaussian-shaped kernel. The Central Limit Theorem states that repeated convolution of a function with itself (subject to certain regularity conditions) approaches a Gaussian. We used this property to construct further kernel functions by convolving G_1 with itself. We obtained the following sequence of functions

$$G_2(x) \equiv G_1^2(x) = \frac{\alpha}{4} e^{-\alpha|x|}(1 + \alpha|x|), \tag{96}$$

$$G_3(x) \equiv G_1^3(x) = \frac{\alpha}{16} e^{-\alpha|x|}\left[3(1 + \alpha|x|) + \alpha^2|x|^2\right], \tag{97}$$

$$G_4(x) \equiv G_1^4(x) = \frac{\alpha}{96} e^{-\alpha|x|}\left[15(1 + \alpha|x|) + \alpha^2|x|^2(6 + \alpha|x|)\right]. \tag{98}$$

All functions are normalised to one according to Eq. 92. The possibility of formulating the convolution operation in Fourier space let it appear desirable to have the Fourier transforms of the G_n function at hand. Defining the Fourier transform via

$$\widehat{G}(k) \equiv \frac{1}{\sqrt{2\pi}} \int_{-\infty}^{\infty} G(x)\, \exp(ikx)\, dx \tag{99}$$

we obtained for the (purely real) transforms of the kernel functions

$$\widehat{G}_n(k) = \frac{\alpha^{2n}}{\sqrt{2\pi}(\alpha^2 + k^2)^n} \qquad n \in \{1, 2, 3, 4\}. \tag{100}$$

Figure 41 illustrates the shapes of kernels G_1 and G_3. G_3 already resembles a Gaussian quite well, having a smooth maximum at the origin and wings that are moderately wider than in the case of a Gaussian. One should keep in mind that approaching a Gaussian brings back in the problems that we intended to mitigate, namely significant amplification of noise. Hence, one should limit the number of repeated convolutions. A last point concerns the choice of the broadening parameter α. While the formulae take a simple form by using α, physically one likes to specify the width of the kernel more directly. Fortunately, except for the pre-factor, all kernels are functions of the product $\alpha|x|$

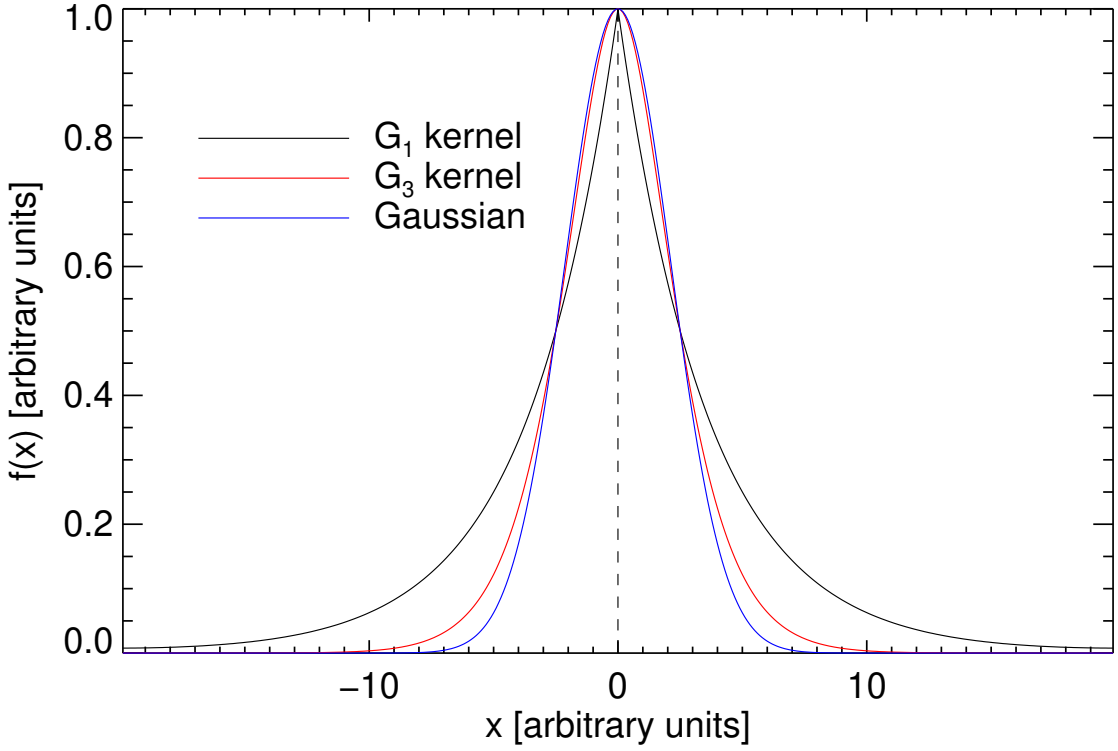

Figure 41: Shapes of the kernels G_1 and G_3 in comparison with a Gaussian. For display purposes all functions were normalised to $G_i(0) = 1$. All share the same FWHM.

alone, resulting in a simple (inverse) relation between the full width at half maximum (FWHM) of a kernel and α. For kernel G_1, the relation reads $\alpha = 2\sqrt{\ln 2}/\mathrm{FWHM}$. The other kernels can be obtained from G_1 by two-, three-, and four-fold application of G_1 with a FWHM of 0.42243, 0.29746, and 0.24325 times the targeted FWHM, respectively. The numbers were obtained by solving numerically the transcendent equations for the widths of the three kernels in question, and the approach was applied when creating Figure 41.

Figure 42 illustrates the impact of convolving and de-convolving a Gaussian-shaped line profile with kernels G_1 and G_3. The FWHM of the line and the levels of broadening or de-broadening were roughly tailored after the silicon lines we observe in solar disk-centre spectra. G_3 has a milder effect on the line shape than G_1 at the same FWHM. While not clear from the plot, it turns out that one can largely mimic the effect of G_1 by using G_3 with a greater width. For the given parameters the "peaky" shape of G_1 leaves no imprint in the line shape. So far, the kernels described above worked in practice, but deconvolution can be handled only for kernels significantly narrower than the spectral line to be de-broadened.

2.9 Centre-to-limb variation of the continuum and line shapes predicted by the 3D models

Here we report on the performance of our 3D models in combination with our spectral synthesis codes (`LINFOR3D` for line syntheses, `NLTE3D` for spectral energy distributions) when representing the solar centre-to-limb variation (CLV) of its continuum radiation and the shape of lines. We start with the CLV, and later point to investigations in the literature which use features of line shapes that were calculated with the help of `CO5BOLD` models.

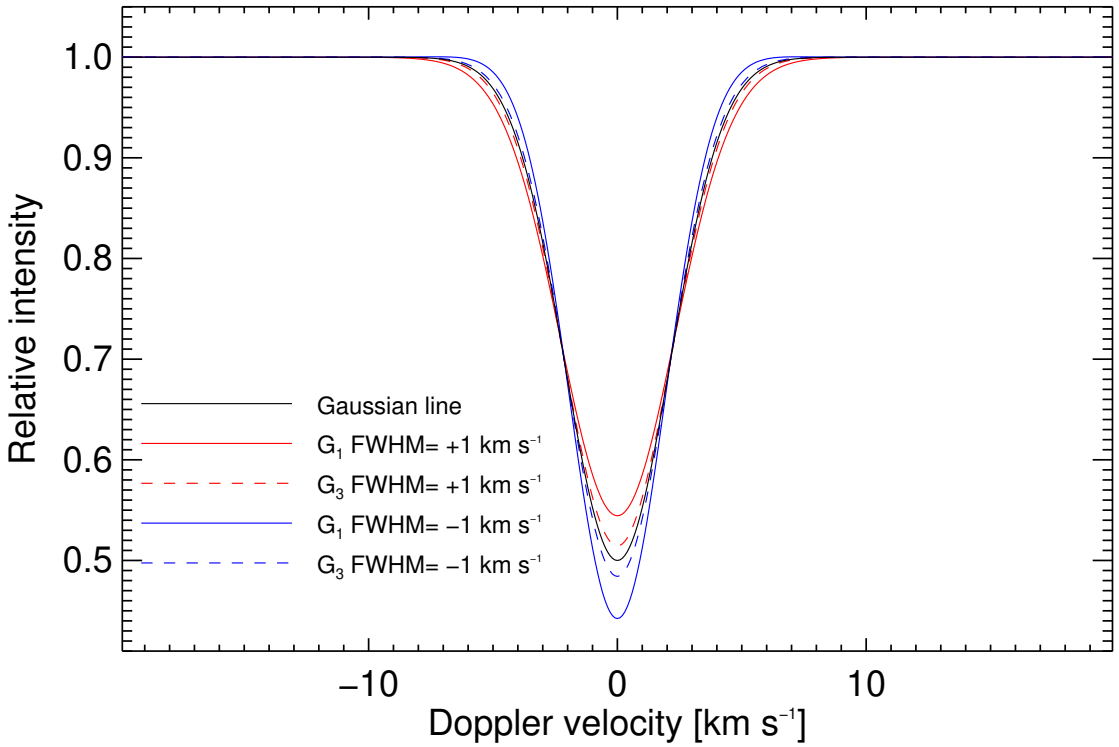

Figure 42: Broadening and de-broadening effects of kernels G_1 and G_3: a Gaussian-shaped line with FWHM of $5\,\mathrm{km\,s^{-1}}$ was convolved and de-convolved with kernels having an absolute width of $1\,\mathrm{km\,s^{-1}}$. Negative broadening values indicate a deconvolution.

Figure 45 shows a comparison between prediction of our 3D models with observations by Neckel and Labs (1994, hereafter NL). NL provide 30 wavelengths from the near-UV to the near-IR for which they measured relative intensities over narrow bandwidths (in equivalent Doppler velocity between 1.4 to 1.9 km s^{-1}). The wavelength points were chosen to be largely free of absorption lines. We ran pure continuum syntheses for the NL wavelengths for our four 3D models, and for further comparison for three 1D model atmospheres. The lower panels (left panels in rotated view) depict the result. For the non-magnetic models msc600 and n59 the correspondence between observation and model prediction is very good for $\lambda > 0.6\,\mu\mathrm{m}$. We note that the results for models msc600 and n59 are almost identical so that they are difficult to distinguish on the scale of the plot. 1D models are added for setting the scale for a "very good" correspondence: a standard `ATLAS9` (Kurucz, 1979; Kurucz, 2005; Sbordone et al., 2004) model shows a significantly steeper CLV than found in the observations. Similarly, an `LHD` model (`LHD` is a home-grown 1D stellar atmosphere code that uses the same microphysics as applied in our 3D models) shows a similar behaviour. Remarkably, our msc600 model performs even slightly better than the well-known Holweger-Müller solar model (Holweger, 1967; Holweger and Mueller, 1974) despite the fact that this semi-empirical model was constructed to match the CLV.

At $\lambda < 0.6\,\mu\mathrm{m}$ the good correspondence deteriorates. However, as NL point out themselves the notion of observing pure continuum over the bandwidth used in the measurements becomes questionable. At wavelengths shorter than $0.6\,\mu\mathrm{m}$ the previously negligible contribution of line absorption to the observed intensity becomes non-zero but otherwise undefined. To address this issue we took an extreme stand and calculated the intensity over 20 Å wide intervals including *all* line absorption with the help of opacity distribution functions (ODFs). We combined line ODFs from Kurucz' `ATLAS`

suite (Kurucz, 2017) with continuous opacities from our own opacity package. In each ODF interval the distribution of the line opacity was represented by a step-function of 12 steps. For each step, the emergent intensity was calculated and finally integrated over the whole ODF interval so that we obtained the intensity emerging in the 20 Å wide ODF interval. From the construction is is clear that one obtains the average effect on the intensity of the absorbers present in the ODF interval. The upper panels (right panels in rotated view) of Fig. 45 illustrate that the correspondence between model predictions and observations clearly improves for wavelengths $\lambda < 0.6\,\mu$m, strongly suggesting that indeed missing line absorption is the reason for the mismatch at these shorter wavelength in the pure continuum calculations. In fact, the good correspondence in the near-UV is striking. One has to admit that this is certainly in part fortuitous since the true contribution of lines to the observations is unclear, and also whether the line lists going into the construction of the ODFs are sufficiently complete in the near-UV. To illuminate the influence of line absorption a bit further we write the intensity ratio between a location μ and and disk centre $\mu = 1$ as

$$\frac{I_\mu}{I_1} = \frac{c_\mu - l_\mu}{c_1 - l_1} \approx \frac{c_\mu}{c_1}\left(1 - \frac{l_\mu}{c_\mu} + \frac{l_1}{c_1}\right) \tag{101}$$

where c_μ is the continuum intensity at location μ and l_μ the intensity reduction by line absorption at this point. The approximate equality holds for weak line absorption. Equation (101) shows that there is a compensatory effect by considering intensity ratios. Moreover, since there is typically a reduction of the intensity ratio with respect to pure continuum calculations the contribution of line absorption must become larger towards the stellar limb. It is not straight forward to see why this is: the silicon lines synthesised for this investigation generally show a mild decrease in strength towards the limb – particularly the medium to strong lines. However, we conjecture that in fact molecular lines are a major player here which significantly increase in strength due to the lower temperatures at which line formation takes place towards the limb.

Since the contribution of lines is observationally not well-defined we have also plotted intensity ratios considering ODF sub-intervals only. We expected that especially the sub-interval with the smallest line contribution would result in a closer match to the observations which was, however, not immediately apparent (not shown). We finally remark that the findings discussed here coincide with results on the CLV based on a CO^{5}BOLD model of an earlier generation (Ludwig et al., 2010).

For completeness we also investigated the CLV of the magnetic models b000 and b200. Figure 45 illustrates that the field-free model provides a reasonable match to the observations while the 200 G model is clearly off. For the given (somewhat artificial) field configuration one may conclude that the observed CLV does not permit a mean field strength $\gtrsim 50$ G on the Sun. Pereira et al. (2013) already arrived at a similar conclusion by comparing a 100 G model with a field-free case.

All spectral synthesis calculations for the 3D models underlying Fig. 45 approximate scattering in the continuum as well as lines as true absorption. We investigated the effect of this approximation on the CLV in the continuum by comparing the cases of isotropic coherent scattering and true absorption in a 1D stratification obtained when averaging (over optical depth surfaces and time) the msc600 model. As a first step, Fig. 43 illustrates that scattering generally leads to an increase of the emergent intensity for wavelength $\lesssim 0.65\,\mu$m, and that effects becomes more pronounced towards the solar limb. However, quantitatively the changes of the intensity are modest ($\lesssim 4.5\,\%$). Figure 44 shows that this translates into small differences ($\lesssim 0.01$) in the CLV, again, mostly at short wavelengths and close to the limb. The overall limb darkening reduces the effect apparent in the intensity ratios directly. To see this, we denote by S the inten-

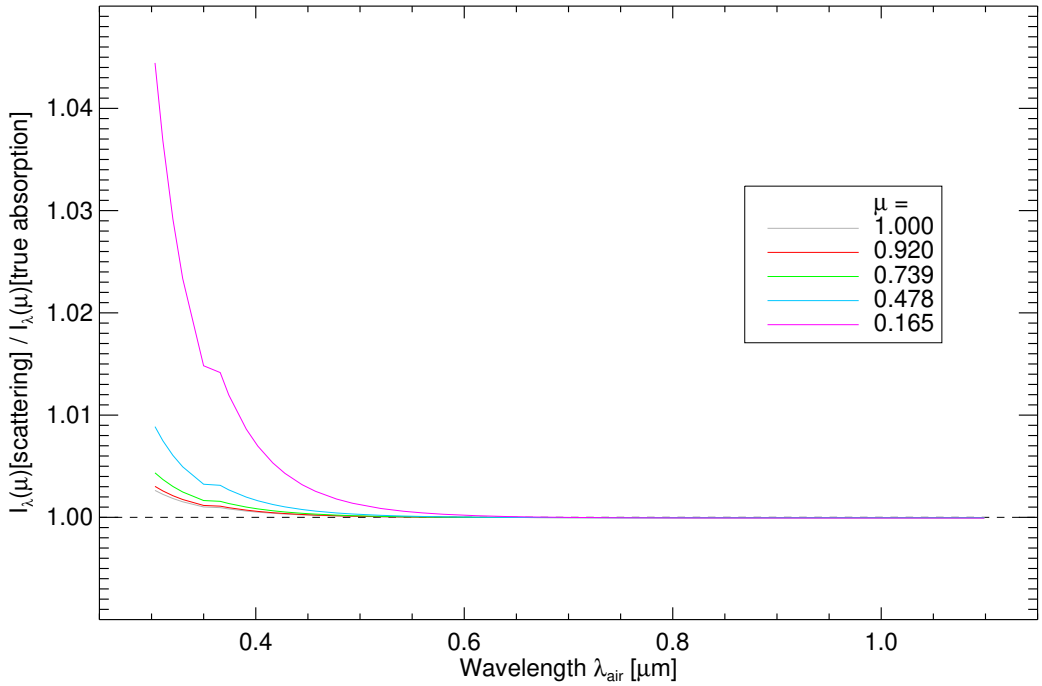

Figure 43: Ratio of the emergent intensities as function of wavelength and limb angle cosine μ between cases when continuum scattering is treated exactly or as true absorption. The average vertical profile of model msc600 was used as structure in the spectral synthesis calculations.

sity when scattering is treated exactly, by A the intensity when scattering is treated as true absorption. The difference in the CLV can then be written as

$$\frac{S(\mu)}{S(1)} - \frac{A(\mu)}{A(1)} \approx \frac{S(\mu) - A(\mu)}{A(1)} = \frac{A(\mu)}{A(1)} \left(\frac{S(\mu)}{A(\mu)} - 1 \right) . \tag{102}$$

The approximate equality comes from the observation that $S(1) \approx A(1)$. All this means that the very good correspondence between models and observations shown in Fig. 45 gets only very slightly worse when scattering is treated correctly but remains very satisfactory.

We now briefly turn to line shapes, particularly line shifts, as predicted by model n59. As a first example we point to González Hernández et al. (2020, Fig. 6) where absolute core shifts of 144 Fe I lines are compared to observations. In their work a very accurate wavelength calibration of the observed spectra was achieved by utilising a laser frequency comb. Lines with an equivalent width less than 60 mÅ show a good correspondence with their observed shifts. One has to keep in mind here that a comparison on an absolute scale also relies on accurately known laboratory wavelengths. The reason for the mismatch of lines with equivalent widths greater than 60 mÅ is not clear but not necessarily related to shortcomings in the model structure. Moreover, it was also seen in LTE line syntheses based on STAGGER models (see González Hernández et al., 2020, for further discussion). As second example, in Löhner-Böttcher et al. (2019, Fig. 19) the observed shape of the Fe I 6173 Å line is compared to synthetic line profiles computed with a CO^{5}BOLD model as a function of limb angle. While not all details are matched the overall correspondence is satisfactory.

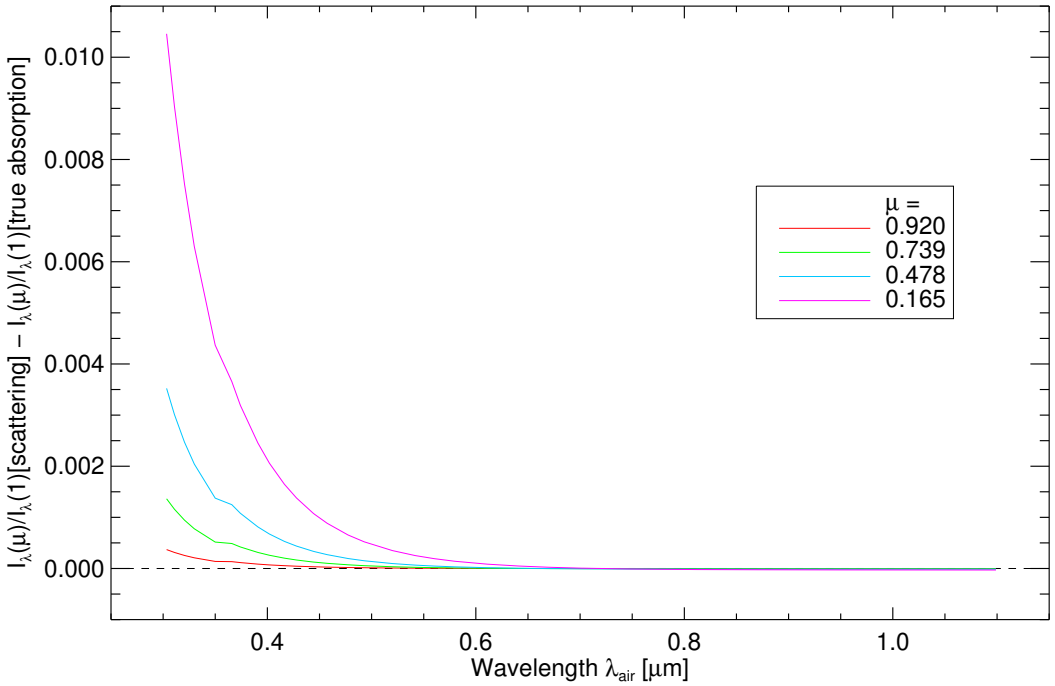

Figure 44: Difference of the centre-to-limb variation when continuum scattering is treated exactly or as true absorption. Note the reduction of the impact of scattering in comparison to Fig. 43.

2.10 THE PARTITION FUNCTIONS OF SILICON AS IMPLEMENTED `linfor3d`

We compared the partition functions of the first three ionisation stages of silicon as implemented in our spectral synthesis code to data given in the recent compilation of Barklem and Collet (2016). We find a close to perfect agreement in the temperature range relevant for the formation of silicon lines in the solar photosphere, as seen in Fig. 46.

2.11 CONCLUSIONS

We have presented a 3D LTE analysis of 39 silicon lines using `CO5BOLD` model atmospheres and the `LINFOR3D` spectral synthesis code. Of these, a total of 11 were selected for the abundance analysis, comprising of 7 optical Si I lines, 3 near-infrared Si I lines and 1 Si II line. New oscillator strengths from Pehlivan Rhodin (2018) were used, enabling the use of infrared lines alongside optical ones and providing smaller uncertainties for oscillator strengths. Compared to the previous experimental strengths from Garz (1973), the new $\log(gf)$ values and weighting scheme decrease the formal statistical uncertainty across the relevant lines from 0.07 dex to 0.04 dex. An improved broadening theory also helped to constrain statistical uncertainties further.

Our main conclusions are as follows:

- We find a photospheric solar silicon abundance of $\log \varepsilon_{\mathrm{Si}} = 7.57 \pm 0.04$, including the -0.01 dex correction from NLTE effects investigated in Amarsi and Asplund (2017). The 0.06 dex increase with respect to the recent studies by Asplund, Amarsi,

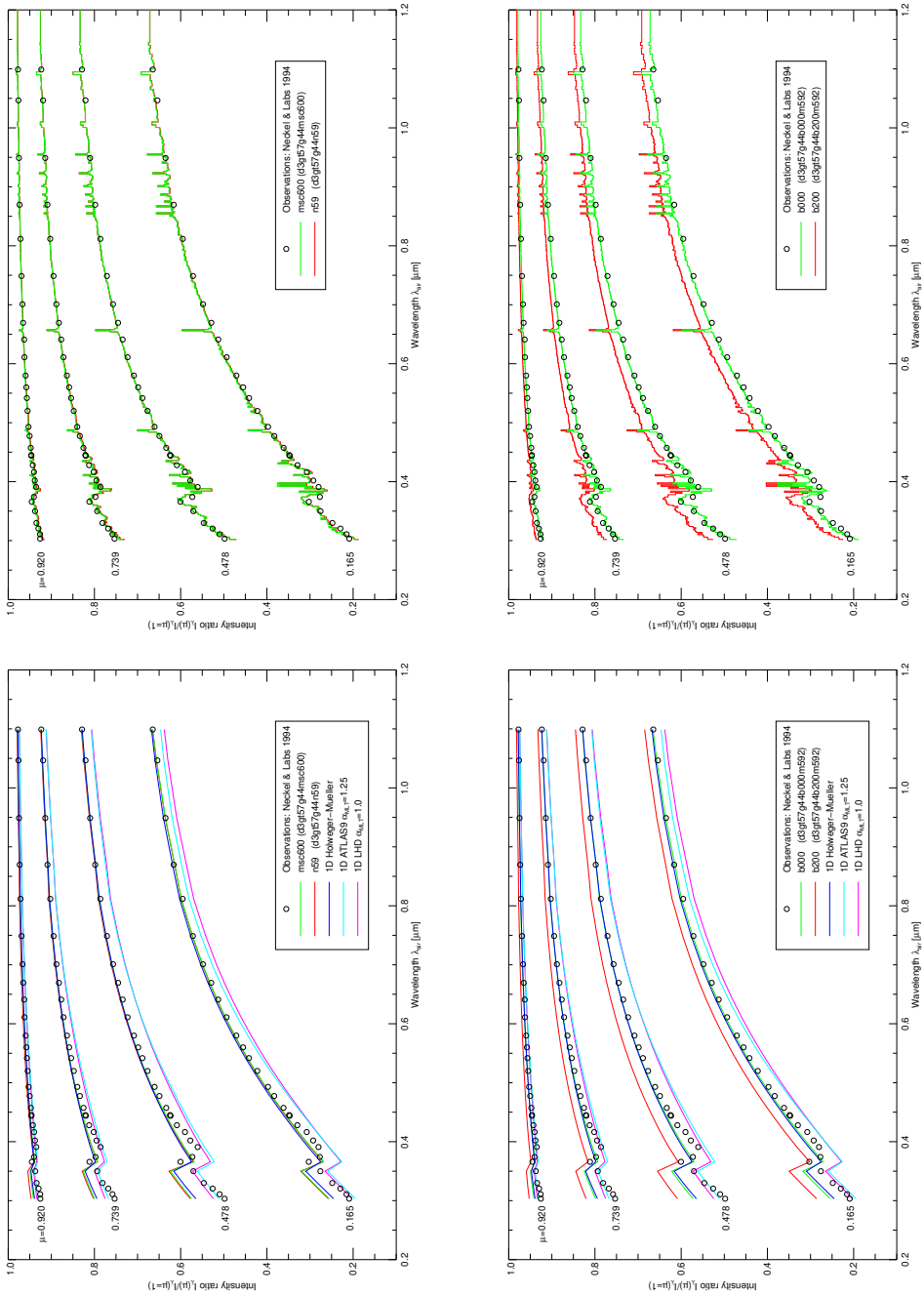

Figure 45: Centre-to-limb variation as predicted by our 3D models in comparison to observations and 1D results. Syntheses excluding (bottom) and including (top) line absorption are shown. Left panels: models msc600 and n59. Right panels: models b000 and b200.

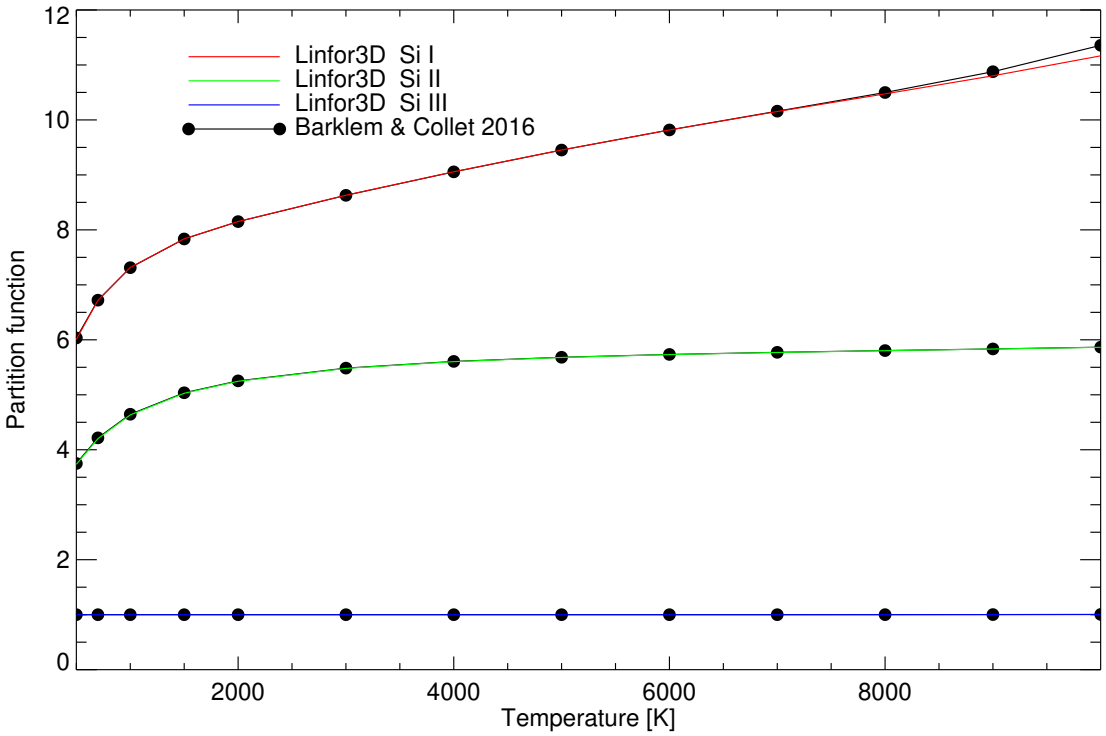

Figure 46: Partition functions implemented in `LINFOR3D` compared to data of Barklem and Collet (2016).

and Grevesse (2021), Amarsi and Asplund (2017) suggests that the determination of the solar silicon abundance is not yet a firmly solved problem. Our advocated configuration uses the G_1 broadening kernel, the higher resolution msc600 model and our chosen subsample of lines.

- Several factors affect the fitted abundance and broadening, but the line selection plays the primary role. We focus on lines that are devoid of major blends, have updated oscillator strengths, and also where syntheses match well with observed line shapes. Notably, the near-infrared lines give higher abundances than optical lines on average.

- The over-broadened line syntheses we see in this work are not specific to the `CO5BOLD` atmospheres. Comparisons were made with `STAGGER` + `BALDER` and we are able to refit their abundances and broadening values using both the msc600 and n59 models. Broadening-wise, their syntheses lie between the msc600 and n59 models described here. Additionally, the overly broadened line syntheses are caused by the combination of various effects, including velocity fields, atomic broadening and neglect of magnetic field effects – we did not find a single definite cause for over-broadening.

- Using a magnetic model with a magnetic field strength of 200 G increases the fitted abundance and reduces the Doppler broadening when compared to the same model with a magnetic field strength of 0 G. These differential results could point towards over-broadened syntheses resulting from a lack of consideration of magnetic field effects, particularly that strong magnetic fields impede turbulent flow in the atmosphere (Cattaneo, Emonet, and Weiss, 2003), resulting in narrower lines.

However, the vertical magnetic fields that would be required to offset the negative broadening are much too large to be consistent with 3D MHD models with small-scale dynamos (Shchukina, Sukhorukov, and Trujillo Bueno, 2016; Shchukina, Sukhorukov, and Trujillo Bueno, 2015), meaning magnetic field effects likely do not play a major role in the overbroadening of the line syntheses.

- The atomic broadening cross-sections for the silicon lines presented in this work are remarkably large, which subsequently increases the effect of collisional broadening. Alongside the effects of magnetic fields, the collisional broadening may then also contribute to the over-broadening in the line syntheses.

- Meteoritic abundances when transformed onto the astronomical scale are increased with respect to the previous study by Palme, Lodders, and Jones (2014) due to the increase in our photospheric silicon abundance. The differences of the non-volatile elements available from CO^{5}BOLD-based analyses are – except for hafnium – consistent with zero, however, with significant uncertainties. Serenelli et al. (2016) and Vinyoles et al. (2017) both advocate the use of meteoritic abundances for elements heavier than C, N, O in the Sun, but using only the silicon abundance for the conversion between cosmochemical and astronomical scale (e.g., Asplund, Grevesse, and Sauval, 2005) would give a 0.05 dex increase for non-volatile metals. The sizeable uncertainty of the silicon abundance found in this study lets the use of multiple elements for referencing meteoritic and photospheric abundances appear attractive, such as done in Lodders, Palme, and Gail (2009).

- A local fit of the continuum level is clearly at odds when looking at the spectrum on a large scale. Performing such a fit results in an artificial lowering of the equivalent width, and systematically lowers the abundance by 0.01 dex.

- We find no strong evidence of NLTE effects severely affecting abundance calculations in optical lines and the chosen infrared lines beyond the -0.01 dex correction included, though the negative broadening required could be indicative of minor NLTE effects being present.

- The non-magnetic CO^{5}BOLD models used for abundance determination show good correspondence with observed centre-to-limb variations (CLV). The magnetic model "b200" has CLV that are incompatible with observations, so though a lack of magnetic fields could account for the overly broadened syntheses, a field strength of 200 G would be observationally inconsistent.

- An NLTE solar silicon abundance of 7.57 ± 0.04 could improve the differences for solar neutrino fluxes, sound speed profiles and the surface helium fraction. Vinyoles et al. (2017) show that a solar model with the composition proposed in Grevesse and Sauval (1998) statistically performs better in regard to the solar sound speed profile than a model with a solar composition proposed in (Asplund et al., 2009). The former composition uses $\log \varepsilon_{\mathrm{Si}} = 7.56 \pm 0.01$, while the latter uses $\log \varepsilon_{\mathrm{Si}} = 7.51 \pm 0.01$. Serenelli et al. (2016) show that the silicon abundance of $\log \varepsilon_{\mathrm{Si}} = 7.82$ from von Steiger and Zurbuchen (2016) gives worse fits overall for solar neutrino fluxes, sound speed profiles, and the surface helium fraction, so a silicon abundance of 7.57 ± 0.04, closer to the abundance derived from the Grevesse and Sauval (1998) composition, clearly results in an improvement relative to (Asplund et al., 2009).

All in all, our analysis suggests that the photospheric solar Si abundance is not yet a definitively solved problem. The use of state-of-the-art 3D model atmospheres and

an improved broadening theory is essentially a requirement to accurately reproduce line shapes. Even with these improvements, our synthetic line profiles were generally overbroadened with respect to the observations, and it is unlikely that this feature is unique to CO^{5}BOLD model atmospheres or to Si lines.

3

TIME-DEPENDENT MOLECULAR CHEMISTRY IN CARBON-ENHANCED METAL-POOR DWARF STELLAR ATMOSPHERES

3.1 INTRODUCTION

Stellar atmospheres are generally assumed to preserve the makeup of their birth environment. The abundance of elements heavier than helium (known as metals) in a star's atmosphere is an indication of a star's age, with older stars being deficient in metals. Spectroscopy is one of the foremost tools in determining the abundances of various elements in stellar atmospheres. Since the first studies on solar abundances in the 1920s (Payne, 1925; Russell, 1929; Unsöld, 1928) to modern large-scale surveys such as the Gaia-ESO survey (Gilmore et al., 2012), the *Gaia* survey (Gaia Collaboration et al., 2022), GALAH (Bland-Hawthorn and Sharma, 2016), and *Pristine* (Starkenburg et al., 2017), to name a few, spectroscopically determined stellar parameters have been a key tool in understanding the composition of stellar atmospheres. Instrumentation and modelling have been refined in tandem, with improvements such as the treatment of departure from local thermodynamic equilibrium (LTE) and advancements in one-dimensional (1D) and three-dimensional (3D) model atmospheres. These directly lead to improvements in the determination of solar and stellar abundances, since the methods to do so often rely on model atmospheres and the assumptions therein. As a core component of Galactic archaeology, abundance determinations of stellar photospheres from spectroscopy often assume the presence of a chemical equilibrium (implicitly assumed within the LTE assumption). While LTE studies have been used historically to determine stellar abundances (Asplund, 2000; Caffau et al., 2011a; Holweger, 2001), the accurate treatment of the departure from LTE of level populations (known as radiative NLTE treatment) has been shown to provide more accurate abundances in both solar and stellar photospheres (Amarsi et al., 2019b; Bergemann et al., 2013; Magg et al., 2022; Mashonkina, 2020; Wedemeyer, 2001).

Molecular features are important in metal-poor (MP) stars as atomic lines are comparatively weak (Aoki et al., 2013; Beers, Preston, and Shectman, 1992; Koch, Grebel, and Martell, 2019; Yong et al., 2013). In recent years, increasingly metal-poor stars have been discovered (Aoki et al., 2013; Beers, Preston, and Shectman, 1992; Beveridge and Sneden, 1994; Hughes et al., 2022) with a tendency of an enhancement of carbon in their atmospheres (Beers and Christlieb, 2005; Carollo et al., 2014; Cohen et al., 2005; Hansen et al., 2016; Lucey et al., 2022; Sivarani et al., 2006). These carbon-enhanced metal-poor (CEMP) stars comprise a large fraction of the low-metallicity tail of the metallicity distribution function in the Galactic halo (Norris et al., 2007; Susmitha et al., 2020). Though NLTE treatment of spectral lines is becoming more prominent (Bergemann et al., 2013, 2019; Mashonkina, 2020), most of the work concerning these abundance determinations is still done under the assumption of chemical equilibrium, i.e. that all chemical species are in equilibrium with one another. Most NLTE studies consider radiative NLTE, meaning that the radiation field is not in equilibrium with the local background temperature. This changes the population of energy levels in an atom or molecule. Radiative NLTE is still considered in a time-independent fashion. We instead model the time-dependent chemical processes for a variety of species to investigate the effects of hydrodynamics on molecular formation & dissociation to study whether the carbon enhancement seen at

very low metallicities is a real effect or due to a lack of consideration for time-dependent chemistry.

Chemical species will react with one another in such a manner as to approach thermodynamic equilibrium, given enough time. However, as the rates of these reactions depend strongly on temperature and density (Horn and Jackson, 1972), there may be regions in the star where chemical equilibrium conditions are not met. In the deeper, hotter, collision-dominated photospheric layers, chemical species evolve to equilibrium on timescales much faster than other physical timescales in the system. The assumption of chemical equilibrium therefore implies that the chemistry evolves to its equilibrium state faster than other processes can significantly perturb it. In this work, the other physical processes are hydrodynamical, and the key question is whether the chemistry reaches its local thermodynamic equilibrium before the species are advected. Convection in a stellar atmosphere can also lead to compression shocks which quickly heat material. When coupling chemical kinetics to these processes, the chemistry evolves on a finite timescale, and a prevalence of such hydrodynamical effects can push the overall chemistry out of its local equilibrium state.

Metallicity also has a large impact on both the overall structure of the atmosphere and the number densities of the species. At a cursory glance, reducing the metallicity by a factor of 100 immediately results in a 100x reduction in the number densities, which naturally results in slower mass-action reaction rates. Relative abundances (especially of C and O) also play a large role in determining the final yield as well as the chemical timescales of different species (Hubeny and Mihalas, 2015). Simply due to the mass-action rates, then, one can see that the sharp reduction in chemical timescales may result in the chemistry being out of equilibrium in higher, cooler layers.

Currently, many different codes exist to model stellar atmospheres. While one-dimensional (1D) atmospheres have been used to great effect (Allard and Hauschildt, 1995; Gustafsson et al., 2008), three-dimensional (3D) time-dependent modelling is essential for accurately modelling hydrodynamical effects within an atmosphere (Pereira et al., 2013). Codes such as CO^{5}BOLD (Freytag et al., 2012), Stagger (Magic et al., 2013), Bifrost (Gudiksen et al., 2011), MuRAM (Vögler et al., 2005) and Mancha (Khomenko et al., 2017) are prominent examples. In this work we use CO^{5}BOLD model atmospheres to model hydrodynamics, radiation transfer and time-dependent chemistry together.

We investigate two distinct methods to treat the chemical evolution in a stellar atmosphere. The first is to evolve the chemistry as a postprocessing step, utilising outputs from model atmospheres (known as snapshots) in order to determine the chemical evolution of various species. This method yields accurate results in regimes where the density-temperature profile is conducive to fast-evolving chemistry (in comparison to advection). The second is to evolve the chemistry alongside the hydrodynamics, usually done after advecting the species. While this is much more computationally expensive, it will yield accurate results even in regimes where the timescales of the chemistry are comparable to that of advection. In principle, both approaches are equivalent given a fine enough cadence, since the chemical species are treated as passive scalars. In other words, given a fine enough sampling of snapshots, the postprocessing method would tend towards the full time-dependent treatment. We will utilise the postprocessing method to evolve chemical species into equilibrium in order to contrast the time-dependent case.

Wedemeyer-Böhm et al. (2005) investigated CO in the solar photosphere and chromosphere in 2D, employing a chemical network with 7 species and 27 reactions. Wedemeyer-Böhm et al. (2006) then expanded this into a 3D analysis, showing the formation of CO "clouds" at higher layers. We build on this further to include an extended chemical network involving 14 species and 83 reactions, and focus on the photospheres of main-

sequence turn-off dwarf stars. We investigate CO, CH, C_2, CN, OH in detail, since these 5 species are spectroscopically interesting for abundance determinations in MP stars.

The numerical methods and chemical network setup are described in Sec. 3.2. The results of the three-dimensional simulations for the time-dependent and steady-state calculations are presented in Sec. 3.3 and discussed in Sec. 3.4; additional results are presented in Sec. 3.5. The effect of carbon enhancement and metallicity is further explored in Sec. 3.6.

3.2 METHODOLOGY

3.2.1 *Chemical kinetics and the reaction network*

The time-dependent chemistry for a species n_i takes the form

$$\frac{\partial n_i}{\partial t} + \nabla \cdot (n_i \vec{v}) = S, \tag{103}$$

where $\vec{v}$ is the velocity field and S is a source term. The source term is given by the rate of formation and destruction of each species characterised by the reactions in the network.

Each chemical reaction can be written as a differential equation describing the destruction and formation of species, and together the reactions form an ordinary differential equation (ODE) system. We consider all reactions in this work to follow mass-action kinetics. A reaction's rate is then given by

$$w_r = k \prod_j n_j \tag{104}$$

where k is the rate coefficient and the product over n_j includes the stoichiometry of either the reactants (forward reaction) or products (reverse reaction).

The rate coefficient for mass-action kinetics is often given by the Arrehenius equation (Arrhenius, 1889a,b)

$$k(T) = A \exp\left(\frac{E_a}{RT}\right), \tag{105}$$

where A is a constant of proportionality, E_a is the activation energy, $R = 8.314\ \mathrm{J\ K^{-1}\ mol^{-1}}$ is the gas constant and T is the temperature. By making the temperature-dependence of the prefactor explicit and defining $\gamma = \frac{E_a}{R}$, we arrive at the so-called modified Arrhenius equation

$$k(T) = \alpha\ T_{300}^{\beta}\ \exp\left(\frac{\gamma}{T}\right), \tag{106}$$

with α as a constant of proportionality independent of temperature, $T_{300} = \frac{T}{300\ \mathrm{K}}$ and β being the explicit power on the temperature. With this formulation, we have α as a temperature-independent prefactor and T_{300}^{β} as a temperature-dependent prefactor. The parameters α, β and γ vary based on the reaction, and are again typically experimentally determined.

Some of the reactions presented in this work are unfortunately defined outside of their temperature limits simply due to the lack of studies of chemical reactions in high-temperature regions such as stellar photospheric layers. There is also an uncertainty associated with the rate coefficients themselves. Despite these shortcomings, we believe the chosen reaction rates describe the evolution of our species reasonably well. The

reaction rates are all Arrhenius-like, given in modified Arrhenius form (Eq. 106). For a reversible reaction, the forward and reverse coefficients are related to the dimensional equilibrium constant K'_{eq} by

$$K'_{eq} = \frac{k_1}{k_2}, \tag{107}$$

where k_1 and k_2 are the forward and reverse rate coefficients, respectively. This equilibrium constant can be used to determine the chemical equilibrium of a given composition, defined when all forward and reverse processes are balanced (Blecic, Harrington, and Bowman, 2016; Stock et al., 2018). As our reaction network contains irreversible reactions in the thermodynamic domain under study, equilibrium constants cannot be determined for each chemical pathway. Hence, we study the "equilibrium" chemistry by solving the chemical kinetics until the chemistry reaches a steady-state. In the absence of processes such as advection, this steady-state should correspond to chemical equilibrium. For a generic reaction r with forward rate coefficient k_1 and reverse rate coefficient k_2

$$aA + bB \rightleftharpoons^{k_1}_{k_2} cC + dD, \tag{108}$$

the rates of change of the generic species A, B, C and D in the reaction r are related via

$$-\frac{1}{a}\left(\frac{\partial n_A}{\partial t}\right)_r = -\frac{1}{b}\left(\frac{\partial n_B}{\partial t}\right)_r = \frac{1}{c}\left(\frac{\partial n_C}{\partial t}\right)_r = \frac{1}{d}\left(\frac{\partial n_D}{\partial t}\right)_r. \tag{109}$$

Eq. (104) then gives the forward and reverse reaction rates w_1 and w_2, respectively, as

$$w_1 = k_1 n_A^a n_B^b, \quad w_2 = k_2 n_C^c n_D^d$$

We can then construct the differential $\left(\frac{\partial n_i}{\partial t}\right)_r$ for a species n_i and reaction r. The full time-dependent chemical evolution of species n_i is then given by the sum over the reactions r:

$$\frac{\partial n_i}{\partial t} = \sum_r \left(\frac{\partial n_i}{\partial t}\right)_r. \tag{110}$$

The chemical reaction network (CRN) (which is described by a system of differential equations) builds on the one presented in Wedemeyer-Böhm et al. (2005), extending it to 14 species and 76 reactions. It also includes the catalytic "metal" species "M", as in Wedemeyer-Böhm et al. (2005). Table 13 describes these reactions along with the parameters of the rate coefficients. The present network is focused on the evolution of CO, CH, C_2, CN and OH through reactions with neutral atomic and bimolecular species. Radiative association, species exchange, two- & three-body reactions, and collisional dissociation are included. Each reaction is given in the modified Arrhenius form, parametrised by the pre-exponential factor α, an explicit temperature dependence β and a characterisation of the activation energy γ. Some reactions with CO are catalysed reactions and include a characteristic metal M.

A discussion on the choice of reactions follows below. Generally, the CRN was built to analyse the species CO, CH, CN, $C_2$and OH. As the network presented in Wedemeyer-Böhm et al. (2005) already includes a good treatment of CO, CH and OH, we supplement this network with reactions taken from the UMIST Astrochemistry Database (McElroy et al., 2013) to model the other molecular species. Only neutral atomic and bimolecular species are considered due to their prevalence compared to other trace

molecules, and the storage limitations imposed by considering a full 3D, time-dependent treatment. We neglect photodissociation in this network, though accept that the effects may not be negligible in very optically thin layers. Additionally, as the reactions used here often come from studies in planetary atmospheres and combustion chemistry, the reactions presented are sometimes defined outside of their temperature limits, especially when considering deep photospheric regions. We choose to focus on higher, cooler layers for this reason.

Reaction 58. We choose to use the rate that includes only α, instead of the rate that includes explicit temperature dependence. This is because the temperature limits of this reaction are $10 - 300$ K, and including the temperature-dependent rate would lead to a much greater extrapolation due to the comparatively high temperatures in the model atmospheres.

Reaction 116, 133, 198. For each of these reactions, two rates are presented in the database for temperature limits of $10 - 300$ K, and $300 - 3000$ K. We opt to use the latter rate as the temperature limits are closer to our use case.

Reaction 206. The reaction is defined for the temperature limits $298 - 3300$ K and $295 - 4000$ K. We opt to use the latter rate that includes a higher upper-temperature limit.

Reaction 236. The reaction is defined for the temperature limits $10 - 500$ K and $158 - 5000$ K. We opt to use the latter rate that includes a higher upper-temperature limit.

Reaction 244. The reaction is defined for the temperature limits $10 - 294$ K and $295 - 4500$ K. We opt to use the latter rate that includes a higher upper-temperature limit.

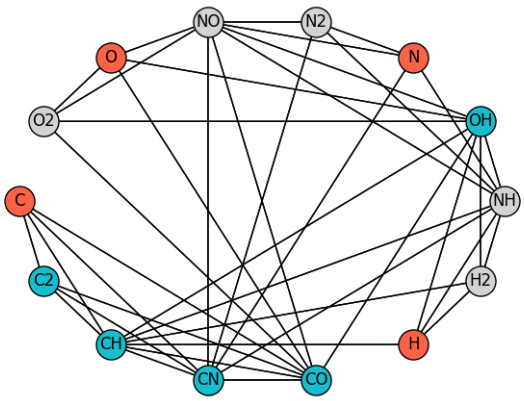

Figure 47: Graph of the chemical reaction network with atoms (red), key molecular species (blue) and remaining molecular species (grey). Connections qualitatively describe reaction pathways.

A visualisation of the reaction network is shown in Fig. 47. Atomic species are shown in red, key molecular species are shown in blue, and all other molecular species are shown in grey. The full network with all reactions is too complex to show in full detail, so we choose to highlight the important reactions as edges between nodes. It is clearly seen that the network is connected, meaning one can reach any node starting from any other node, but not fully-connected, since every node does not share an edge with every other node. These properties allow us to find reaction pathways in the reaction network (see Sec. 3.4.4).

Index	Reactants		Products	α	β	γ	Reference
		Radiative Association					
3681	C + H	$\Longrightarrow$	CH + γ	1.00e-17	0.00	0.0	UMIST
3683	H + O	$\Longrightarrow$	OH + γ	9.90e-19	-0.38	0.0	UMIST
3703	C + C	$\Longrightarrow$	C_2 + γ	4.36e-18	0.35	161.3	UMIST
3705	C + N	$\Longrightarrow$	CN + γ	5.72e-19	0.37	51.0	UMIST
3707	C + O	$\Longrightarrow$	CO + γ	1.58e-17	0.34	1297.0	UMIST
3730	O + O	$\Longrightarrow$	O_2 + γ	4.90e-20	1.58	0.0	UMIST
		3-body association					
4079	H + M + O	$\Longrightarrow$	M + OH	4.33e-32	-1.00	0.0	UMIST
4097	C + M + O	$\Longrightarrow$	CO + M	2.14e-29	-3.08	-2114.0	BDDG76
5000	H + H + M	$\Longrightarrow$	H_2 + M	6.43e-33	-1.00	0.0	KCD
5001	H + H + H_2	$\Longrightarrow$	H_2 + H_2	9.00e-33	-0.60	0.0	KCD
5002	H + H + H	$\Longrightarrow$	H + H_2	4.43e-28	-4.00	0.0	BDHL72
7000	H + H + O	$\Longrightarrow$	H + OH	1.00e-32	0.00	0.0	BDHL72
7001	C + H + O	$\Longrightarrow$	CO + H	2.14e-29	-3.08	-2114.0	BDDG76
		Species Exchange					
1	CH + H	$\Longrightarrow$	C + H_2	2.70e-11	0.38	0.0	UMIST
3	H + NH	$\Longrightarrow$	H_2 + N	1.73e-11	0.50	2400.0	UMIST
8	H + OH	$\Longrightarrow$	H_2 + O	6.99e-14	2.80	1950.0	UMIST
11	C_2 + H	$\Longrightarrow$	C + CH	4.67e-10	0.50	30450.0	UMIST
14	CO + H	$\Longrightarrow$	C + OH	5.75e-10	0.50	77755.0	W80
18	H + NO	$\Longrightarrow$	NH + O	9.29e-10	-0.10	35220.0	UMIST
19	H + NO	$\Longrightarrow$	N + OH	3.60e-10	0.00	24910.0	UMIST
24	H + O_2	$\Longrightarrow$	O + OH	2.61e-10	0.00	8156.0	UMIST
42	C + H_2	$\Longrightarrow$	CH + H	6.64e-10	0.00	11700.0	UMIST
44	H_2 + N	$\Longrightarrow$	H + NH	1.69e-09	0.00	18095.0	UMIST
48	H_2 + O	$\Longrightarrow$	H + OH	3.14e-13	2.70	3150.0	UMIST
52	H_2 + O_2	$\Longrightarrow$	OH + OH	3.16e-10	0.00	21890.0	UMIST
58	C + CH	$\Longrightarrow$	C_2 + H	6.59e-11	0.00	0.0	UMIST
61	C + NH	$\Longrightarrow$	CH + N	1.73e-11	0.50	4000.0	UMIST
62	C + NH	$\Longrightarrow$	CN + H	1.20e-10	0.00	0.0	UMIST
66	C + OH	$\Longrightarrow$	CH + O	2.25e-11	0.50	14800.0	UMIST
67	C + OH	$\Longrightarrow$	CO + H	1.81e-11	0.50	0.0	W80
68	C + CN	$\Longrightarrow$	C_2 + N	4.98e-10	0.00	18116.0	UMIST
70	C + CO	$\Longrightarrow$	C_2 + O	2.94e-11	0.50	58025.0	UMIST
71	C + N_2	$\Longrightarrow$	CN + N	8.69e-11	0.00	22600.0	UMIST
75	C + NO	$\Longrightarrow$	CN + O	6.00e-11	-0.16	0.0	UMIST
76	C + NO	$\Longrightarrow$	CO + N	9.00e-11	-0.16	0.0	UMIST
80	C + O_2	$\Longrightarrow$	CO + O	5.56e-11	0.41	-26.9	UMIST
100	CH + N	$\Longrightarrow$	C + NH	3.03e-11	0.65	1207.0	UMIST
102	CH + O	$\Longrightarrow$	C + OH	2.52e-11	0.00	2381.0	UMIST
104	CH + O	$\Longrightarrow$	CO + H	1.02e-10	0.00	914.0	UMIST
116	CH + O_2	$\Longrightarrow$	CO + OH	7.60e-12	0.00	0.0	UMIST
126	N + NH	$\Longrightarrow$	H + N_2	4.98e-11	0.00	0.0	UMIST

130	N + OH	$\Longrightarrow$	NH + O	1.88e-11	0.10	10700.0	UMIST
131	N + OH	$\Longrightarrow$	H + NO	6.05e-11	-0.23	14.9	UMIST
132	C_2 + N	$\Longrightarrow$	C + CN	5.00e-11	0.00	0.0	UMIST
133	CN + N	$\Longrightarrow$	C + N_2	1.00e-10	0.40	0.0	UMIST
138	N + NO	$\Longrightarrow$	N_2 + O	3.38e-11	-0.17	-2.8	UMIST
144	N + O_2	$\Longrightarrow$	NO + O	2.26e-12	0.86	3134.0	UMIST
195	NH + NH	$\Longrightarrow$	H_2 + N_2	1.70e-11	0.00	0.0	UMIST
197	NH + O	$\Longrightarrow$	N + OH	1.16e-11	0.00	0.0	UMIST
198	NH + O	$\Longrightarrow$	H + NO	1.80e-10	0.00	300.0	UMIST
206	NH + NO	$\Longrightarrow$	N_2 + OH	1.46e-11	-0.58	37.0	UMIST
236	O + OH	$\Longrightarrow$	H + O_2	1.77e-11	0.00	-178.0	UMIST
240	C_2 + O	$\Longrightarrow$	C + CO	2.00e-10	-0.12	0.0	UMIST
243	CN + O	$\Longrightarrow$	C + NO	5.37e-11	0.00	13800.0	UMIST
244	CN + O	$\Longrightarrow$	CO + N	5.00e-11	0.00	200.0	UMIST
251	N_2 + O	$\Longrightarrow$	N + NO	2.51e-10	0.00	38602.0	UMIST
261	NO + O	$\Longrightarrow$	N + O_2	1.18e-11	0.00	20413.0	UMIST
377	C_2 + O_2	$\Longrightarrow$	CO + CO	1.50e-11	0.00	4300.0	UMIST
382	CN + CN	$\Longrightarrow$	C_2 + N_2	2.66e-09	0.00	21638.0	UMIST
387	CN + NO	$\Longrightarrow$	CO + N_2	1.60e-13	0.00	0.0	UMIST
392	CN + O_2	$\Longrightarrow$	CO + NO	5.12e-12	-0.49	-5.2	UMIST
416	NO + NO	$\Longrightarrow$	N_2 + O_2	2.51e-11	0.00	30653.0	UMIST
7601	NH + O_2	$\Longrightarrow$	NO + OH	2.54e-14	1.18	312.0	UMIST
		Collisional Dissociation					
194	NH + NH	$\Longrightarrow$	H + H + N_2	1.16e-09	0.00	0.0	UMIST
205	NH + NO	$\Longrightarrow$	H + N_2 + O	7.40e-10	0.00	10540.0	UMIST
4060	H + H_2	$\Longrightarrow$	H + H + H	4.67e-07	-1.00	55000.0	UMIST
4061	CH + H	$\Longrightarrow$	C + H + H	6.00e-09	0.00	40200.0	UMIST
4062	H + OH	$\Longrightarrow$	H + H + O	6.00e-09	0.00	50900.0	UMIST
4067	H + O_2	$\Longrightarrow$	H + O + O	6.00e-09	0.00	52300.0	UMIST
4069	H_2 + H_2	$\Longrightarrow$	H + H + H_2	1.00e-08	0.00	84100.0	UMIST
4070	CH + H_2	$\Longrightarrow$	C + H + H_2	6.00e-09	0.00	40200.0	UMIST
4071	H_2 + OH	$\Longrightarrow$	H + H_2 + O	6.00e-09	0.00	50900.0	UMIST
4074	H_2 + O_2	$\Longrightarrow$	H_2 + O + O	6.00e-09	0.00	52300.0	UMIST
4076	CO + M	$\Longrightarrow$	C + M + O	2.79e-03	-3.52	128700.0	BDDG76
7002	CO + H	$\Longrightarrow$	C + H + O	2.79e-03	-3.52	128700.0	BDDG76
7585	CH + O_2	$\Longrightarrow$	CO + H + O	1.14e-11	0.00	0.0	UMIST

Table 13: Reactions used in this work. "Index" refers to the index in the UMIST astrochemistry database. All reactions are of modified-Arrhenius form with rate coefficient $k(T) = \alpha \left(\frac{T}{300}\right)^{\beta} \exp\left(\frac{-\gamma}{T}\right)$. References are: "UMIST" McElroy et al. (2013) "BDHL72" Baulch et al. (1972), "KCD" Konnov (2000), "BDDG76" Baulch et al. (1976), "W80" Westley (1980)

The carbon enhancement phenomenon is represented by a number of molecular carbon features, including the strong CH G-band feature at 4300 Å (Gray and Corbally, 2009), the C_2 feature at 5636 Å (Green, 2013), the Swan bands (C_2) at 5635 Å and 5585 Å, and the 3883 Å CN

band (Harmer and Pagel, 1973). Koch, Grebel, and Martell (2019) also used CN features to identify CN-strong and CN-weak stars in globular clusters. Overall, spectral synthesis in cool carbon stars from $4000 - 10000$ Å shows that the region harbours many CH, CN and C_2 lines.

CO, having a very high bond-dissociation energy of 11.08 eV (March and Smith, 2001), is the key stable state within the chemical network. In the regions where molecular features form it is energetically favourable to form CO over, e.g. CH and OH. As such, CO dictates the relative yield of other carbon- and oxygen-bearing molecules. Generally, C and O will be largely consumed to form CO, and any excess then forms other molecular species. With a C/O ratio less than 1 (e.g. for solar composition), and at temperatures that allow for molecular formation, most of the carbon is locked into CO leaving very little to form other carbonic molecules. With a C/O ratio greater than 1 (e.g. certain carbon-enhanced stars), it is instead oxygen that is used up first and more carbonic molecules form (see Fig. 55b).

We include OH to investigate the effect of the C/O ratio on molecular species. OH provides an important symmetry to CH when considering the evolution of C, O, CH, OH and CO (Gallagher et al., 2017a, 2016). As the amount of non-CO carbon-bearing molecules heavily depends on the C/O ratio, so too does the evolution of OH.

3.2.2 *Numerical Method*

We use CO5BOLD, a conservative finite-volume hydrodynamics solver capable of modelling surface convection, waves, shocks and other phenomena in stellar objects (Freytag et al., 2012). The hydrodynamics, radiation transfer and chemistry are treated via operator splitting and solved on a Cartesian grid in a time-dependent manner. The chemistry is solved after the hydrodynamics and radiative transfer time steps. Standard directional splitting along the directions of the 1D operators is used. A Roe solver computes all updates in a single step, where higher order terms in time are provided based on the applied reconstruction scheme.

Radiative transfer is solved frequency-dependently (non-grey) under the assumption of local thermodynamic equilibrium (LTE) using a multiple short-scale characteristic scheme (Steffen, 2017). The opacity tables use 12 frequency bins and are consistent with the atomic abundances used for the chemistry input. The model does not treat frequency-dependent photodissociation of chemical species, nor heating and cooling via reactions. The equation-of-state is also consistent with the abundances used in the chemistry input and assumes the formation of molecules in instantaneous equilibrium.

All models used in this work were created by taking a thermally relaxed CO5BOLD model output and adding "quantity centred" (QUC) cell-centred quantities. These QUC quantities allow the user to arbitrarily add cell-centred quantities to the simulation, such as passive scalars. Here, each QUC quantity stores the number densities of a single chemical species across all grid cells. The QUC quantities can be advected as prescribed by the velocity field. Periodic boundary conditions are implemented on the lateral edges of the computational domain. The lower boundary layer is open with inflowing entropy and pressure adjustment, while the top layer is transmitting. Number densities in ghost cells are copied from the nearest cells in the computational domain, but scaled to the mass density of those cells. In this way, the chemistry is still consistent across the boundary and the number densities of the elements are almost perfectly conserved. We only present 3D models in this work as we focus on the stellar photosphere and it was shown that 1D models are more insensitive to a change in CNO abundances (Gustafsson et al., 2008; Masseron, 2008; Plez and Cohen, 2005)

CO5BOLD includes a time-dependent chemical kinetics solver (Freytag et al., 2012; Wedemeyer-Böhm et al., 2005) that has so far been used to investigate the solar photosphere and chromosphere in two- and three-dimensions. The code includes modules to advect passive tracers and to solve a chemical reaction network using these passive tracers. Once the model has been initialised with chemical species (QUC quantities), CO5BOLD then solves the chemistry for each cell at each time step (alongside the equations of hydrodynamics and radiation transfer), and the species are advected as prescribed by the velocity field.

The output of the model atmosphere is stored in a sequence of recorded flow properties, commonly called a sequence of "snapshots." Each snapshot also functions as a start model to restart a simulation, or as a template to start a new simulation. A total of 20 independent snapshots are chosen for the analysis. This is a large enough number to investigate interesting

phenemena such as shocks without biasing the sample far from the expected ambient conditions. To contrast the time-dependent chemistry, the same reaction network is solved on a background static snapshot (i.e. a single snapshot without taking advection into account) until the chemistry reaches a steady-state. This is similar to the treatment of chemistry in equilibrium, but in this case we still solve the kinetic system instead of relying on equilibrium constants. The method for solving the chemistry independently of the hydrodynamics in postprocessing is described in Sec. 3.2.3. The models in this study do not utilise the MHD module, and hence represent only quiet stellar atmospheres without magnetic fields.

Due to the high computational expense of computing time-dependent chemistry across a large grid, parallelisation is highly recommended. This, along with the increased memory load of storing the number densities of QUC species, limits the size of the network that can be treated time-dependently. Even with these steps, solving the chemistry is still the most time-intensive step, taking upwards of 75% of the total runtime.

The DVODE solver (Hindmarsh et al., 2005) is used to solve the system of chemical kinetic equations, making use of the implicit backward differentiation formula (BDF). The solver uses an internally adjusted adaptive time step – a requirement when considering that the system of equations is often very stiff. The solution of the final number densities is provided after the full hydrodynamics time step.

For stability, we utilise first-order reconstruction schemes for both the hydrodynamics and advection of QUC quantities. Higher order schemes were found to cause some grid cells to extrapolate beyond the equation-of-state tables or low number densities to become negative. This was not a consistently reproducible effect for a given grid cell, meaning its source could lie in single-precision numerical errors.

Model ID	[Fe/H]	A(C)	A(O)	log C / O	Internal ID
					(d3t63g40)
AM1	+0.00	8.41	8.66	−0.25	mm00
AM2	−2.00	6.41	7.06	−0.65	mm20
AM3	−3.00	5.41	6.06	−0.65	mm30
AC1	−3.00	7.39	7.66	−0.27	mm30C20N20O20
AC2	−3.00	7.39	6.06	+1.33	mm30C20N20O04

Table 14: Model atmosphere parameters for the five models used in the study. Each model has $T_{eff} = 6250$ K and $\log g = 4.00$, a resolution of $140 \times 140 \times 150$ cells and an extent of $26 \times 26 \times 12.7$ Mm ($x \times y \times z$). The abundances for each model are consistent with those in the respective opacity tables, and we use the "Internal ID" to refer to each model uniquely within this work.

We use standard solar abundances from the CIFIST grid as the basis for our abundance values (Caffau et al., 2011a), and initialise the molecular species to a number density of 10^{-20} g cm^{-3}.

3.2.3 *Steady-State Chemistry*

The treatment of steady-state chemistry is handled via the solution of the chemical kinetic system on a background model atmosphere (a single, static snapshot), neglecting advection. The chemistry is evolved long enough to reach a steady-state where processes are balanced for each grid cell. The formulation of the final system of equations is the same as that in Eq 110. In this way, we are able to evaluate the time-dependent effects of advection when compared to the statically postprocessed chemistry in steady-state.

To solve the chemistry on a background CO^{5}BOLD model snapshot, we present the Graph Chemical Reaction Network (GCRN) code[1]. GCRN handles strictly a chemical kinetics problem and is able to evaluate the solution at arbitrary times, provided the chemical network, initial

1 https://github.com/SiddhantDeshmukh/graphCRNs

number densities and temperature. The chemistry is solved isothermally in each cell. GCRN is able to read and write chemical network files in the format required by `CO`^{5}`BOLD` as well as that of KROME (Grassi et al., 2014). The code is written in Python and Julia and relies primarily on the numpy, scipy, and networkx Python libraries, and the DifferentialEquations.jl and Catalyst.jl Julia libraries.

The numerical solver is the same as that used in the time-dependent case, namely DVODE with the BDF method. By default the absolute tolerance is set to 10^{-30} and the relative tolerance to 10^{-4}. The Jacobian is computed and evaluated within the DVODE solver itself, but GCRN supports a user-supplied Jacobian matrix. GCRN can also automatically compute an analytical Jacobian based on the equation system and pass this to the solver. Supplying a Jacobian to the solver can help improve stability, but it was not necessary in this work.

To understand the motivation for writing an in-house chemical kinetics solver, let us first consider the nature of a CRN. A CRN consists of a set of chemical species that are connected to one another via reaction pathways. A CRN can therefore be represented as a weighted, directed graph. The vertices of this graph are the chemical species involved, and the edges represent the reactions between them. The weights and directions of the edges describe the rates of the reactions, often defined using the mass-action law (Érdi and Tóth, 1989). For single-species reaction networks, where every reaction is of the form

$$A \rightarrow B, \tag{111}$$

the CRN graph and its incidence and adjacency matrices can be easily represented. However, when multiple reactants and products are involved in a reaction, it becomes necessary to introduce the notion of a chemical "complex", defined as the left or right-hand side of a reaction equation. Expressing the system of reactions in terms of its complexes corresponds to a translation from the space of species $\mathbb{R}^s$ to the space of complexes $\mathbb{R}^c$.

GCRN first represents the system of chemical reactions as a weighted, directed graph (see e.g. Horn (1972) and van der Schaft, Rao, and Jayawardhana (2015)). The vertices of the graph are the left- and right-hand chemical complexes, while the edges represent the reactions themselves. The weights of the edges are the reaction rates, evaluated for the provided temperature and initial number densities. For a reaction network with c complexes and r reactions, its directed (multi)graph[2] G can be characterised by its $c \times r$ incidence matrix $\mathbf{D}$, which represents the connection between vertices and edges i.e. which edges connect which vertices. Each column of $\mathbf{D}$ corresponds to an edge (a reaction) of G. The (i, j)-th element of $\mathbf{D}$ represents the reaction j containing complex i. It is $+1$ if i is a product, and -1 if i is a reactant. For s species, the $s \times c$ complex composition matrix $\mathbf{Z}$ describes the mapping from the space of complexes to that of species, i.e. it describes which species make up which complexes. Multiplying $\mathbf{Z}$ and $\mathbf{D}$ yields the $s \times r$ stoichiometric matrix $\mathbf{S} = \mathbf{Z}\,\mathbf{D}$. Finally, to include the mass-action kinetics, we require a vector of reaction rates $\mathbf{v}(\mathbf{x})$ as a function of the species vector x. In general, for a single reaction with reactant complex C specified by its corresponding column $z_C = [z_{C,1} \dots z_{C,s}]^T$ of $\mathbf{Z}$, the mass action kinetic rate with rate coefficient k is given by

$$k\, x_1^{z_{C,1}} x_2^{z_{C,2}} \dots x_m^{z_{C,s}}, \tag{112}$$

or more concisely

$$k\, \exp(\mathbf{z}_C^T \mathrm{Ln}(\mathbf{x})), \tag{113}$$

where $\mathrm{Ln}(\mathbf{x})$ is defined as an element-wise operation producing the vector $[\ln(x_1) \dots \ln(x_s)]^T$. Similarly, the element-wise operation $\mathrm{Exp}(\mathbf{y})$ produces the vector $[\exp(y_1) \dots \exp(y_s)]^T$. With this, the mass-action reaction rates for the total network are given by evaluating the expression

$$v_j(\mathbf{x}) = k_j\, \mathrm{Exp}\left(\mathbf{z}_j^T \mathrm{Ln}(\mathbf{x})\right) \tag{114}$$

for the $j = 1, \dots, r$ reactions. This can be written compactly in matrix form. We define the $r \times c$ matrix $\mathbf{K}$ as the matrix whose (j, σ)-th element is the rate coefficient k_j if the σ-th complex is the reactant complex of the j-th reaction, and zero otherwise. Then,

$$\mathbf{v}(\mathbf{x}) = \mathbf{K}\, \mathrm{Exp}\left(\mathbf{Z}^T \mathrm{Ln}(\mathbf{x})\right) \tag{115}$$

2 allows for multiple edges between vertices

and the mass-action reaction kinetic system can be written as

$$\dot{\mathbf{x}} = \mathbf{Z}\,\mathbf{D}\,\mathbf{K}\,\mathrm{Exp}\left(\mathbf{Z}^{\mathrm{T}}\mathrm{Ln}(\mathbf{x})\right) \tag{116}$$

The formulation is equivalent to that in Eq. (110), with the stoichiometric matrix $\mathbf{S} = \mathbf{Z}\,\mathbf{D}$ supplying the stoichiometric coefficients and the rates vector $\mathbf{v}(\mathbf{x}) = \mathbf{K}\,\mathrm{Exp}\left(\mathbf{Z}^{\mathrm{T}}\mathrm{Ln}(\mathbf{x})\right)$ supplying the mass-action kinetic rates. A detailed explanation on the graph theoretical formulation and further analyses can be found in van der Schaft, Rao, and Jayawardhana (2016).

To illustrate this, let us consider a simple two-reaction model of CO formation put forward by Wedemeyer et al. (2003) based on the reactions from Ayres and Rabin (1996). There is one reaction for formation (through radiative association), and one for destruction (through collision with atomic hydrogen). The CO formation reaction is

$$\mathrm{C} + \mathrm{O} \rightarrow \mathrm{CO} + \hbar\nu, \tag{117}$$

where $\hbar\nu$ represents the energy released, and is omitted in further notation since we are primarily interested in the chemical species themselves. The CO destruction reaction is

$$\mathrm{CO} + \mathrm{H} \rightarrow \mathrm{C} + \mathrm{O} + \mathrm{H}. \tag{118}$$

This network comprises of 4 species, C, O, CO, and H. The two reactions yield four complexes: (C + O), (CO), (CO + H), and (C + O + H). The vectors of number densities for species ($\mathbf{x} \in \mathbb{R}^{s}_{+}$) and complexes ($\mathbf{y} \in \mathbb{R}^{c}_{+}$) are

$$\mathbf{x} = \begin{pmatrix} n_{\mathrm{C}} \\ n_{\mathrm{O}} \\ n_{\mathrm{CO}} \\ n_{\mathrm{H}} \end{pmatrix}, \mathbf{y} = \begin{pmatrix} n_{(\mathrm{C+O})} \\ n_{(\mathrm{CO})} \\ n_{(\mathrm{CO+H})} \\ n_{(\mathrm{C+O+H})} \end{pmatrix}$$

where n_X represents the number density of the quantity X. The form of the ODE system is given by Eq. 116. Our matrices of interest are: the complex composition matrix

$$\mathbf{Z}_{(4_{\mathrm{species}} \times 4_{\mathrm{complexes}})} = \begin{bmatrix} 1 & 0 & 0 & 1 \\ 1 & 0 & 0 & 1 \\ 0 & 1 & 1 & 0 \\ 0 & 0 & 1 & 1 \end{bmatrix}$$

showing which species (rows) belong to which complexes (columns); the complex incidence matrix

$$\mathbf{D}_{(4_{\mathrm{complexes}} \times 2_{\mathrm{reactions}})} = \begin{bmatrix} -1 & 0 \\ +1 & 0 \\ 0 & -1 \\ 0 & +1 \end{bmatrix}$$

, describing which complexes (rows) are reactants or products (-1 or $+1$) of reactions (columns); and the complex kinetics matrix

$$\mathbf{K}_{(2_{\mathrm{reactions}} \times 4_{\mathrm{complexes}})} = \begin{bmatrix} k_1 & 0 & 0 & 0 \\ 0 & 0 & k_2 & 0 \end{bmatrix}$$

which describes the rate coeffients corresponding to the reaction (row) where the complex (column) is a reactant. The stoichiometric matrix $\mathbf{S}$ is found through $\mathbf{S} = \mathbf{ZD}$:

$$\mathbf{D}_{(4_{\mathrm{species}} \times 2_{\mathrm{reactions}})} = \begin{bmatrix} -1 & +1 \\ -1 & +1 \\ 1 & -1 \\ 0 & 0 \end{bmatrix}$$

and describes the stoichiometry of each species (row) for each reaction (column). The first two rows describe C and O, the third row describes CO, and the fourth describes H. Since our reaction system is closed, and there are an equal number of sources and sinks for each species, the rows sum to zero. Note that as H is a catalytic species here (in that it is always present on both sides of the reaction equation), its stoichiometry is zero.

The rest of the right-hand side, involving the mass-action dependence of the rates, is given by Eq. 115. Note that this represents the rate of change of the complexes, not the species themselves. Left-multiplying by the stoichiometric matrix $\mathbf{S}$ completes the full equation representing the rates of change of species.

A graph theoretical approach allows one to investigate certain behaviours across chemical pathways, such as the timescales of processes and the importance of certain species. Note that these graph representations are only created and accessed upon request and are not used when solving the kinetic system. The graph representations then allow for the analysis of the network in more depth before and after solving the system, such as finding reaction pathways and determining symmetries. In solving the actual kinetic system, only the rates vector $\mathbf{v}(\mathbf{x})$ changes based on the change in number densities. Sec 3.4.4 explores a novel pathfinding approach to find the most important reaction pathways in a network that is achieved by representing the system in this form.

A drawback of the Python version of GCRN is its low efficiency compared to compiled languages. Though we have implemented a few optimisations, computing the chemical evolution for many snapshots in 3D is still computationally challenging. As such, we utilise the Julia library Catalyst.jl [3] for steady-state calculations across many 3D snapshots. The Python side of GCRN is used primarily to evaluate 2D slices, 1D averages and timescales, and investigate reaction pathways, while large, 3D steady-state calculations are performed in Julia. The results are identical between the two.

3.3 RESULTS

3.3.1 *Time-Dependent vs Steady-State Chemistry*

We investigated the results of time-dependent (TD) chemistry compared to equilibrium (Eqm) chemistry in 3D. For all models, chemical equilibrium is generally held below $\log\tau = 1$. In order to consider relative differences, we introduce the mixing ratio

$$r = \frac{n_i}{n_{\text{total}}}, \tag{119}$$

where n_i is the number density of species i and n_{total} is the number density of all species excluding H, H_2 and M. In this way, the mixing ratio describes the relative abundances of important atomic and molecular species in a given volume. H, H_2 and M are much more abundant than other species, and including these species simply scales the relevant quantities down. We characterise deviations by considering the ratio of TD to CE mixing ratios, which is equivalent to considering the ratio of TD to CE number densities. Large deviations between TD and CE species might not be spectroscopically relevant if the species is anyways present at very low abundances, since these deviations will not be observable. Considering both the total number density and the mixing ratio of a species therefore allows the inspection of relative and absolute deviations from equilibrium in order to understand whether the deviations are significant. Fig. 48 shows the absolute number densities and mixing ratios of species across the photosphere for both the time-dependent and steady-state chemistry as horizontal averages on optical depth ($\log\tau$) surfaces, as a function of optical depth.

Molecular chemistry is clearly in equilibrium in the deeper photospheric layers, generally below $\log\tau = 1$. This is expected, as the high temperatures in this collision-dominated regime result in very short timescales (much shorter than characteristic hydrodynamical timescales). In essence, the assumption of chemical equilibrium holds in these regimes. Significant deviations are not present in the AM1 model, but appear above $\log\tau \approx -2$ in model AM2, and above $\log\tau \approx -1$ in model AM3. In all cases where deviations are non-zero, time-dependent chem-

3 https://catalyst.sciml.ai/dev/

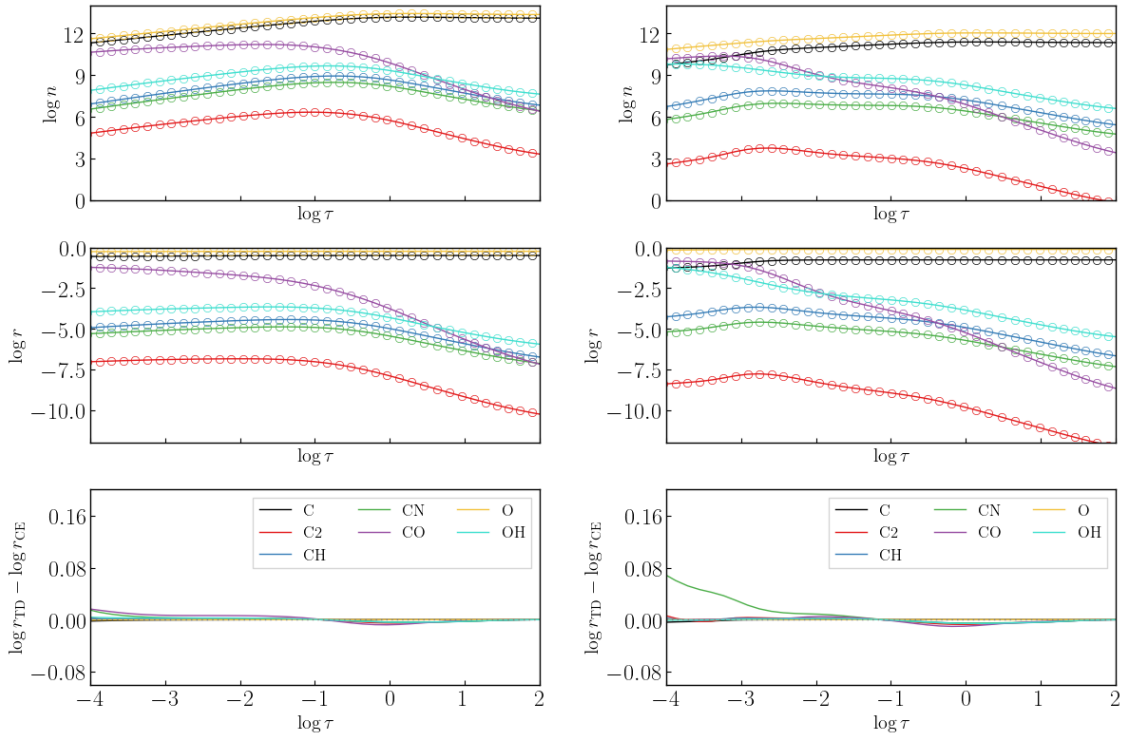

(a)

(b)

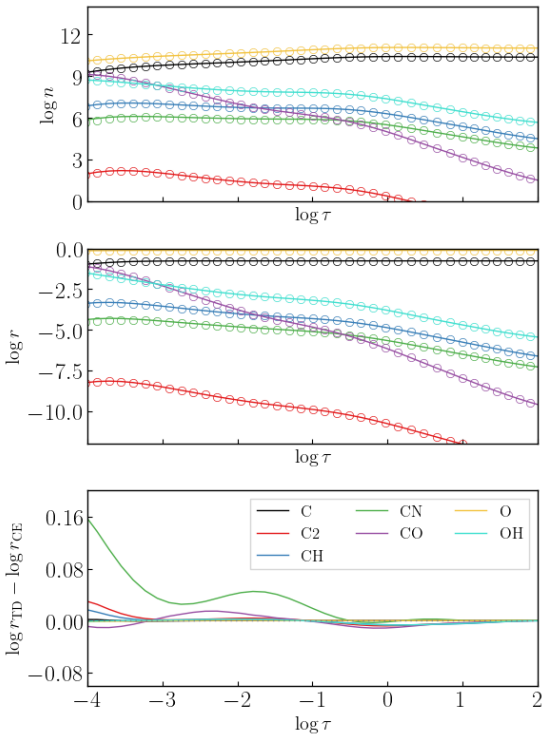

(c)

Figure 48: Mixing ratios and deviations from chemical equilibrium for the AM1, AM2 and AM3 models. **(a)** [Fe/H] = 0.0. **(b)** [Fe/H] = −2.0. **(c)** [Fe/H] = −3.0.

istry is affected by hydrodynamics such that there is insufficient time to reach a local chemical equilibrium.

As expected, decreasing metallicity decreases the amount of molecular species that can be formed. Deviations from equilibrium molecular number densities increase with decreasing metallicity due to slower chemical timescales. The largest deviations are seen in C_2 and CN in the AM3 model, reaching up to 0.15 dex at $\log \tau = -4$. The deviations for other molecules similarly increase with increasing height. These positive deviations are balanced by (smaller) negative deviations in CO. Essentially, there is insufficient time to form the equilibrium yield of CO in these thermodynamic conditions, and hence the yield of species that would react to form CO is higher.

Often, differences present around local features such as shocks can be lost when viewing the global picture (averaging over space and time). Even though the chemistry is mostly in equilibrium throughout the atmosphere, investigating cases where it is out of equilibrium can lead to an understanding of the hydrodynamical effects as well as insights into where approximations of chemical equilibrium break down. Figs. 49 & 50 show the time-dependent mixing ratios in a horizontal and vertical slice through the AM3 model atmosphere, respectively.

In Fig. 49, deviations from CE are seen in CN in and around cool features. Mass-action rates increase with temperature, hence cooler cells lead to longer chemical timescales. The instantaneous CE therefore predicts dissociation that is inconsistent with the time-dependent scheme, and higher amounts of these molecular species are seen in the time-dependent scheme since there is insufficient time for them to be dissociated to their equilibrium values. In higher layers, the same reasoning applies generally, leading to a positive deviations in CN, CH and C_2 , offset by negative deviations in CO, as seen in Fig. 48.

The vertical slice in Fig. 50 shows the evolution of chemistry in various layers, and highlights a shock in the upper photosphere. Deviations from CE are seen in all species in higher layers, with the shock being the most prominent example. In CE, all molecular species are immediately dissociated, while the time-dependent shows that, even in these higher-temperature regions, CO is not so quickly depleted. While it may seem counterintuitive that CO then shows a small negative deviation from CE, the mean amount of CO in the time-dependent case is less than that in CE. This is reflected in the positive deviations from CE seen in CH and CN, which, due to mass conservation, are offset by the negative deviation in CO. Additionally, the reverse trend is also true, in that the formation of CO after a shock passes is slower than predicted in CE.

3.3.2 *Carbon Enhancement*

For the models presented thus far, oxygen has been more abundant than carbon. CO, being extremely stable, often dominates the molecular species when it can form. It is possible, though, that this preference towards CO formation is influenced by the enhancement of oxygen relative to carbon present in the atmosphere. We investigated two cases of carbon enhancement in a model atmosphere with metallicity [Fe/H] = −3.0. The first increases both C and O by 2.0 dex (AC1), while the second increases only C by 2.0 dex (AC2). Nitrogen was also increased by 2.0 dex. The increase for all elements includes the 0.4 dex enhancement for alpha elements.

Fig. 51 shows the mixing ratios and deviations from equilibrium for the two CEMP model atmospheres presented in this work. In model AC1 ($\log (C/O) = -0.26$), more CO and CH is formed compared to the standard metal-poor case, but OH is still more abundant than CH. Almost all C is locked up into CO, hence the next most-abundant molecular species is OH. This is analagoues to models AM2 and AM3, as O is still more abundant than C. Carbon-bearing molecules are more abundant than in AM3, but it is clear when looking at the mixing ratios of, e.g. CH to OH, that the carbon enhancement does not necessarily lead to a large increase in all carbon-bearing molecular abundances. In model AC2 ($C/O = +1.33$), CO is still the most abundant species, while CH is more abundant than OH. We observe the opposite effect compared to models AM2, AM3 and AC1 where it is instead O that is locked up into CO. This results in a significant depletion of OH compared to model AM3, as there is relatively little O left to form OH due to the overabundance of C. The depletion of O hinders the formation of further CO, and the chemical equilibrium is such that atomic C is the most abundant species. All models hence reinforce the notion of CO being the most stable molecular state in the chemical network.

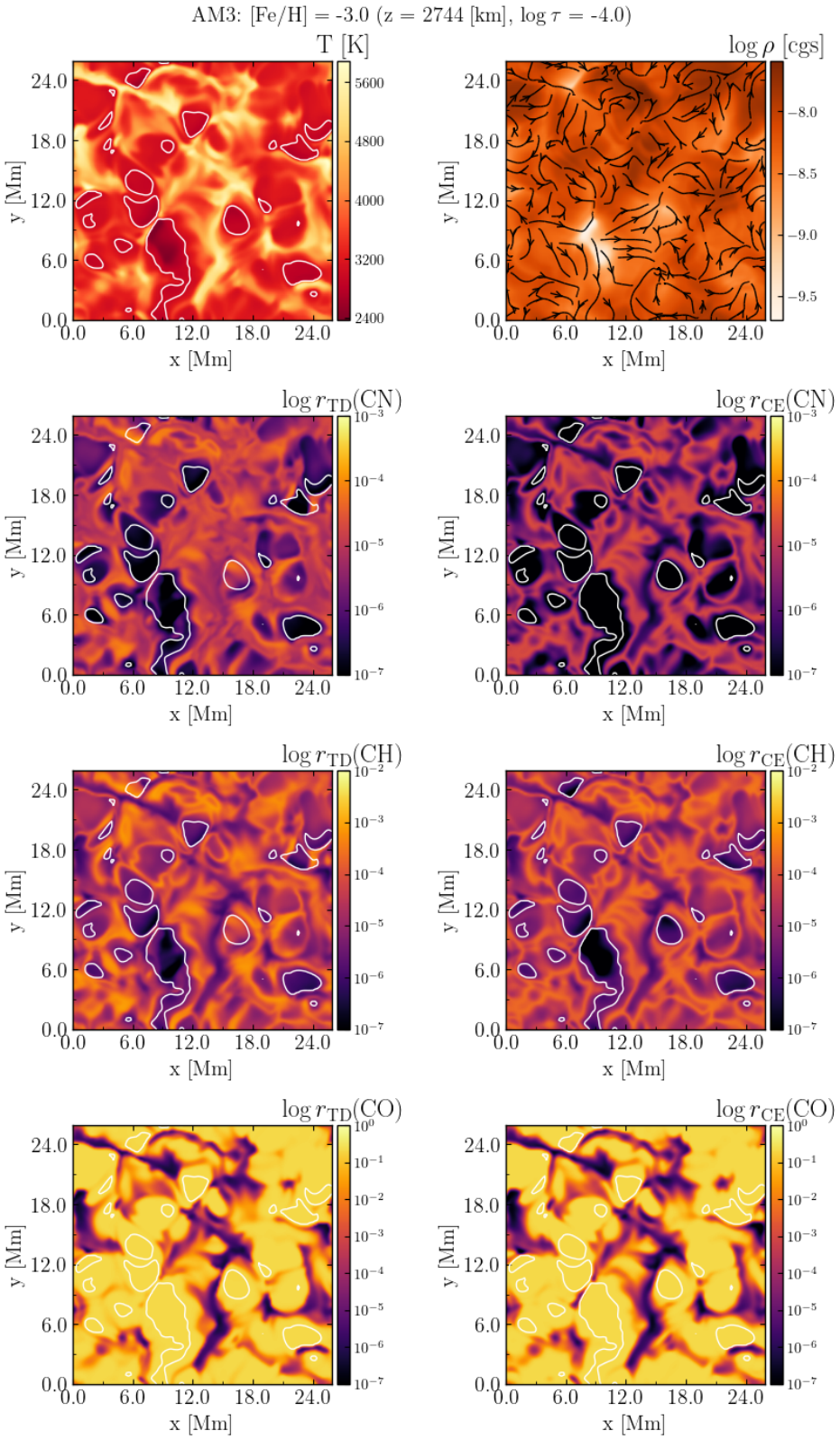

Figure 49: Mixing ratios of molecular species in a horizontal slice through the photosphere in the AM3 model. **Left.** Time-dependent. **Right.** Equilibrium. Molecular formation follows a reversed granulation pattern. The effect of finite chemical timescales is most prominent when contrasting warm and cool regions in CN and CH; CO is seen to be relatively close to CE, as confirmed by Fig. 48c at $\log\tau = -4$. The white contour traces a temperature of 4500 K.

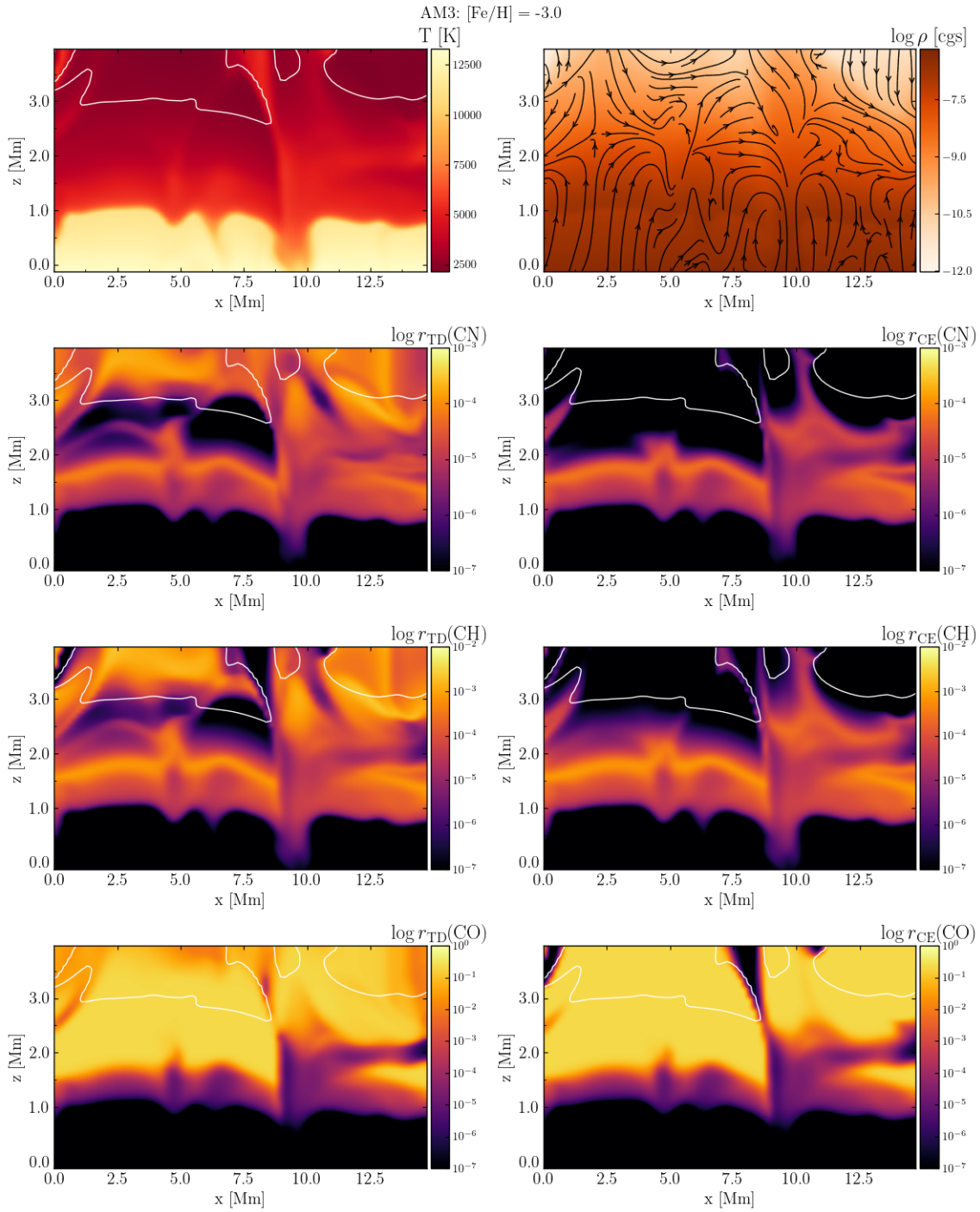

Figure 50: Time-dependent mixing ratios of molecular species in a vertical slice through the photosphere above $\log \tau = 1$ in the AM3 model atmosphere. The white contour traces a temperature of 4500 K. The colour scale is the same for all molecular species.

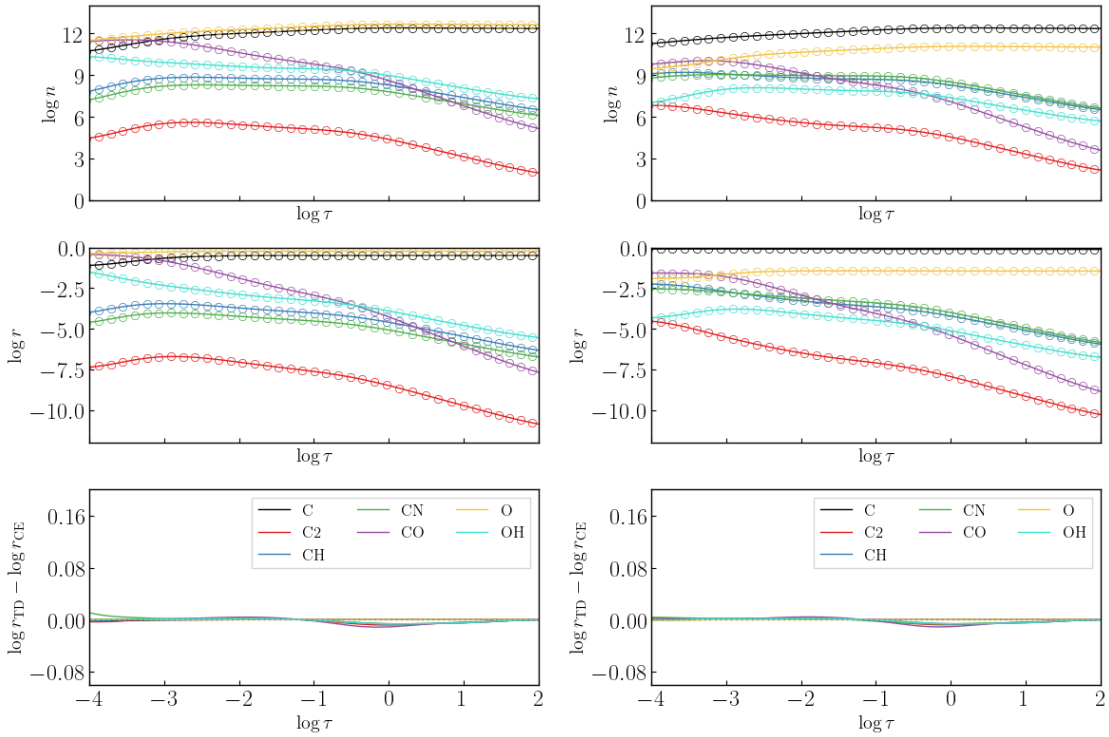

(a) (b)

Figure 51: Mixing ratios and deviations from chemical equilibrium at [Fe/H] = −3.0 and a carbon enhancement of +2.0 dex for two atmospheres with different C/O ratios. **(a)** Model AC1, C/O = −0.26. **(b)** Model AC2, C/O = +1.33.

Oxygen-bearing species seem to be further out of equilibrium in model AC1, while carbon-bearing species are further out of equilibrium in model AC2. Interestingly, deviations from equilibrium decrease in model AC2 where the C/O ratio of +1.33 means carbon is more abundant than oxygen. While this favours formation of carbon-bearing species such as C_2 and CH, the formation of CO is hindered compared to model AC1 due to the lack of OH formation, reinforcing the idea that the pathway for CO formation involving OH is an important one. The significantly smaller deviations in model AC2 may suggest that oxygen-bearing molecules may show larger deviations from chemical equilibrium due to hydrodynamical effects. All in all, CEMP atmospheres do not seem to be largely out of chemical equilibrium for the species presented in this work.

3.4 DISCUSSION

3.4.1 *Effects of Convection*

As material is transported from hotter, deeper photospheric layers to cooler, higher ones, the conditions for chemistry to equilibriate change. It is feasible, then, that material from a lower layer can be carried upwards, reach a new equilibrium state, and later return to a deeper layer. In this process, molecular species will be present in greater amounts in cooler regions compared to hotter regions. If chemistry does not equilibriate faster than advection occurs, we will observe deviations from chemical equilibrium throughout convection cells. This effect is seen in Fig. 49 for CN and CH, where features are traced much more sharply in the equilibrium case than in the time-dependent one. We see that the finite chemical timescales are responsible for differences in formation in cool regions, and dissociation in hot ones. At this layer, the chemical equilibrium approximation still holds well for CO.

3.4.2 *Behaviour around Shocks*

While the overall differences in time-dependent and steady-state chemistry are small when averaged over time and space (horizontally), there can be significant differences when looking at individual instances in time. In addition to the shock seen in Fig. 50, Fig. 52 shows the deviations from equilibrium molecular chemistry in the photospheres of the AM3, AC1 and AC2 models. This histogram shows deviations from CE binned in gas density and temperature across the 20 snapshots used in this work. The top panel gives the bin counts, showing the difference between background material (high density of points) and transient states (low density of points).

Though the background material is generally in equilibrium, three interesting regimes emerge where the molecular chemistry is clearly out of equilibrium, labelled as R_1, R_2 and R_3. R_1 is the regime of convection taking place in the upper photosphere and chromosphere, where hot material is advected upwards to a new layer faster than the molecular chemistry can reach equilibrium. When this material cools and falls, it can sometimes reach very high velocities (around 10 km s^{-1}) exceeding the local sound speed. This supersonic material of the shock front is captured in the regime R_2. Equilibrium chemistry predicts an almost-instantaneous dissociation of molecular species, while the time-dependent case models this over a finite timescale. Thus an excess of molecular species is present in the time-dependent case. Finally, the regime R_3 is the wake of the shock, where material has cooled and is subsonic. The slower chemical timescales in this regime lead to a depletion of molecular species in the time-dependent case. CO is an outlier here; it is still present in slight excess in R_3 as it does not dissociate as quickly as the other molecular species in the shock.

Models AC1 and AC2 show opposite trends in regimes R_1 when considering CH, CN, C_2 and OH. In model AC1 ($\log C/O = -0.26$), the carbon-bearing molecules are more abundant in the time-dependent case, and OH is in depletion. Model AC2 ($\log C/O = +1.33$) instead has the carbon-bearing molecules in depletion while OH is more abundant. This is due to the relative abundances of C and O. Chemical timescales depend on the abundances of C and O, so the oxygen-rich atmosphere AC1 has slower dissociation rates for carbon-bearing molecules while having higher yield due to faster formation rates for OH (and vice versa for the carbon-rich atmosphere AC2). Since CO is a stable end-product of most reaction pathways, it is not as strongly affected by this phenomenon.

Overall, the differences between the time-dependent and steady-state treatments in the photosphere are small, meaning the chemistry in convection cells is likely not far from its equilibrium state. This is especially evident when averaging over space and time. However, it is possible that the effects would become larger in stars on the red giant branch (RGB stars) due to larger scale flows and M-type dwarfs due to cooler temperatures – though the latter have smaller velocity fields, meaning the effects of advection on the evolution of chemical species are reduced. Wedemeyer-Böhm et al. (2005) showed that the need for time-dependent chemistry becomes increasingly important in the solar chromosphere due to the higher frequency of shock waves alongside longer chemical timescales, but that the photosphere of the Sun was generally in chemical equilibrium for CO. We find the same trend when considering metal-poor dwarf stars: that chemical equilibrium does generally hold for the photospheres of these stars when averaging over space and time, and that deviations are largely present in their chromospheres. This further shows the need to include accurate time-dependent molecular chemistry when modelling stellar chromospheres.

3.4.3 *1D Analysis*

Considering a 1D horizontal cut through the atmosphere shows the instantaneous variations in parameters and can help identify patterns. Due to mass-action kinetics, chemical timescales depend on gas density and temperature. Fig. 53 shows profiles of these quantities alongside the time-dependent and equilibrium number densities of CO across a prototypical downflow feature in the chromosphere of the AM3 model.

The equilibrium CO number density changes much more sharply across the feature than in the time-dependent case, showcasing the finite chemical timescales in play. The number densities are also more sensitive to fluctuations in temperature, as seen towards the end, where the gas density is changing but temperature is constant. In the equilibrium number densities, there are

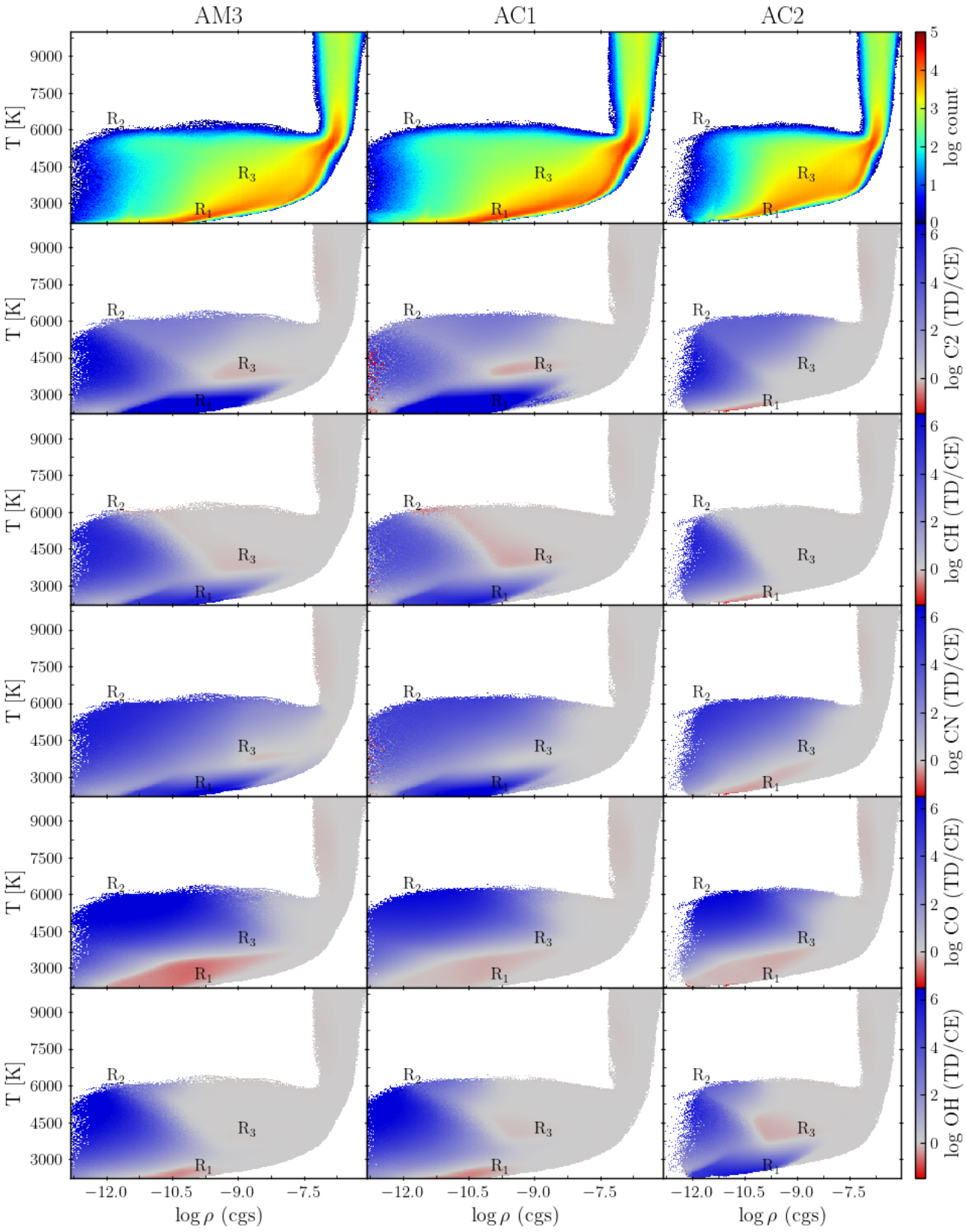

Figure 52: Heatmaps of binned quantities for the AM3, AC1 and AC2 models. Each quantity was binned using 20 snapshots of each 3D model. Deviations from equilibrium are seen in three distinct regions, labelled R_1 (convective cells in the upper photosphere), R_2 (shock fronts in the chromosphere), and R_3 (wake of the shock).

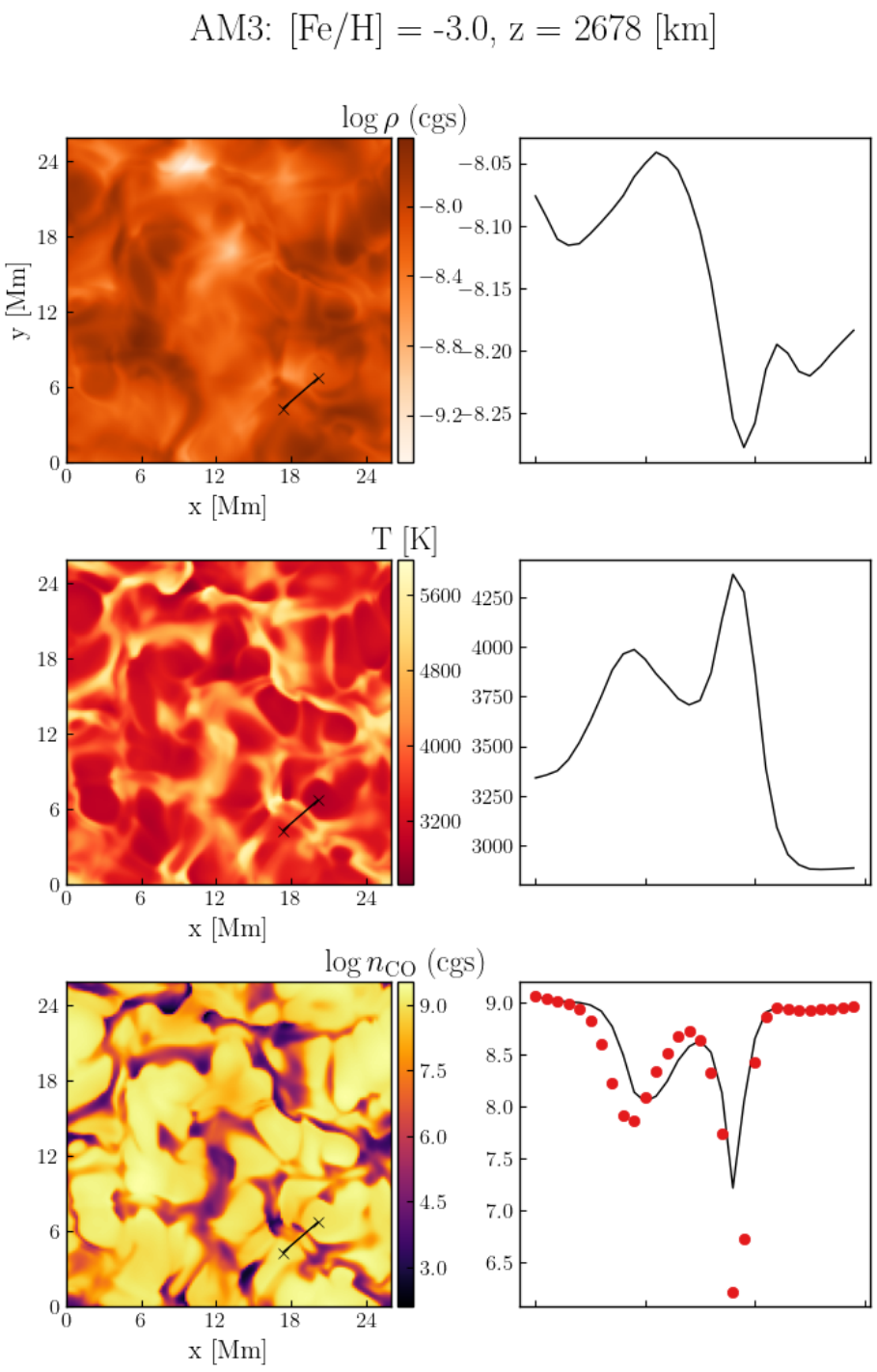

Figure 53: Gas density, temperature and the number density of CO molecules in a slice across the AM3 atmosphere. The left panels show the 2D heatmaps of these quantities, while the right panels show a 1D cut across a prototypical downflow feature, depicted by the black solid line in the top panels. The bottom right panel shows the time-dependent number density as a black solid line and the equilibrium number density as red points.

sharp discontinuities due to the vastly different chemical timescales around the shock front. While these are implausible, the average number densities are very similar (as shown in Fig. 48), showing that the shock here is not disruptive enough to CO chemistry to have a profound impact overall.

3.4.4 *Timescales and Pathways*

It is perceivable that a metallicity reduction by 2.0 dex leads to timescales that are slower by at least a factor of $\sim 10^2 - 10^4$ due to the mass-action law for single-species and two-species reactions. Additionally, relative abundances have a strong effect and the overall yield is lower at lower metallicities. Fig. 55a shows the evolution and equilibrium times for 3 metallicities, and Fig. 55b shows this for the two CEMP models. The equilibrium times for each model and species of interest are given in Table 15. Note that due to the time-stepping of the solver, these times are not necessarily exact, but they should give a clear picture of how the species interact. The equilibrium times here are generally given as the point at which the relative difference in the number densities falls below a threshold ϵ, i.e. t_{eqm} is reached when $\frac{n_{i+1}}{n_i} \leqslant \epsilon$. We adopt $\epsilon = 10^{-6}$ for this network. Again, since this definition relies on the solver's time-stepping to find n_i, n_{i+1}, the times are only exact to the times where the solution is evaluated.

Model	$t_{eqm}(C_2)$ [s]	$t_{eqm}(CH)$ [s]	$t_{eqm}(CN)$ [s]	$t_{eqm}(CO)$ [s]	$t_{eqm}(OH)$ [s]
AM1	4.5×10^2	1.0×10^3	2.4×10^3	1.7×10^2	1.7×10^2
AM2	5.7×10^3	5.1×10^3	6.3×10^4	3.9×10^3	3.2×10^3
AM3	4.9×10^4	2.4×10^4	2.4×10^5	4.0×10^4	1.3×10^4
AC1	9.0×10^3	7.7×10^3	1.6×10^4	1.6×10^3	1.6×10^3
AC2	2.2×10^3	1.2×10^3	2.4×10^3	1.8×10^3	2.4×10^3

Table 15: Time-to-equilibrium for all models and key molecular species at a temperature of 3500 K and a gas density of 10^{-9} g cm^{-3}, corresponding to the upper photospheric layers. Due to the time-stepping of the solver, these times are not exact, but they provide a useful picture of how quickly various species set into equilibrium at varying chemical compositions.

We find that the time for each species to reach equilibrium increases with decreasing metallicity. This is a direct consequence of the mass-action kinetics used to determine reaction rates. The carbon-enhanced models show faster timescales for the same reason.

Another interesting investigation involves the pathways that molecular species are formed (and disassociated) by, and how these change throughout the atmosphere. To pursue this, we represent the reaction network as a weighted, directed graph, as shown in Sec. 3.2.3. The nodes are the left- and right-hand sides of the reactions, (hereafter complexes) while the edges represent the reactions themselves, weighted by their corresponding inverse rate. As this graph is often disconnected, and it is the species we are interested in, we add nodes for each individual chemical species. To connect the graph fully, the individual species nodes have an unweighted edge to each complex that contains it. In this way, we can represent the evolution of one species into another by means of the reaction pathways.

We can now utilise pathfinding algorithms to move from a source species to a target species, identifying the chemical pathway and its corresponding timescale (simply the sum of the edge weights). These change not only with the temperature, but also with the number densities of the reactants, meaning the most-frequented pathways for a given source-target pair can change during the chemical evolution.

The custom pathfinding algorithm (based on Dijkstra's shortest-path algorithm (Dijkstra, 1959) and taking inspiration from A* pathfinding (Foead et al., 2021)) is described in the following steps:

Figure 54: Chemical evolution for 5 chemical mixtures at differing metallicities at T = 3500 K, $\rho = 10^{-9}$ g cm^{-3} (corresponding to upper photospheric layers). Vertical dashed/dotted lines show the time a species has set into equilibrium.

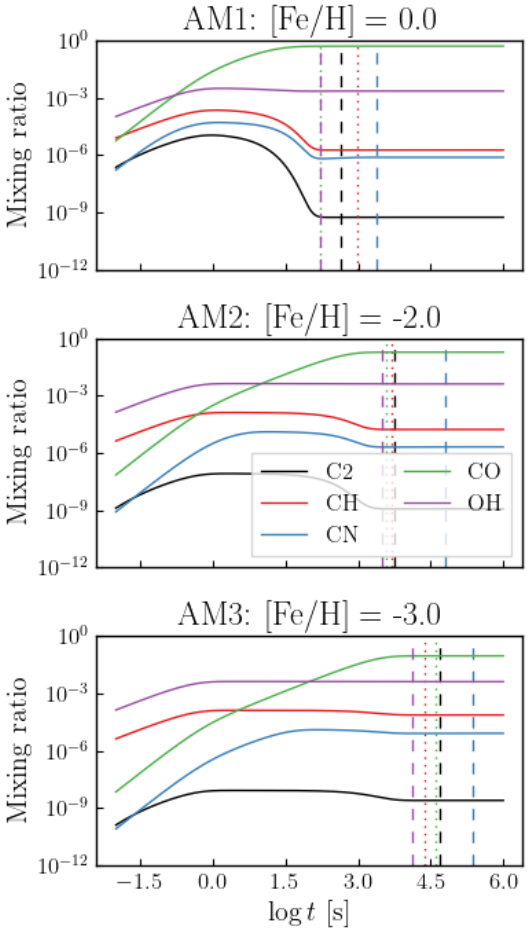

(a) A reduction in metallicity leads to a corresponding reduction in time-to-equilibrium and overall yield.

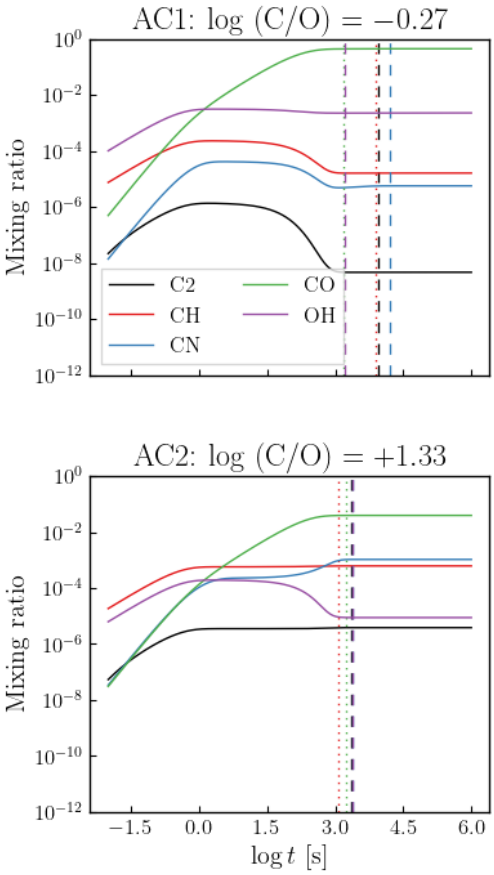

(b) In the oxygen-dominated atmosphere, CH is depleted compared to OH, while the opposite is true in the carbon-dominated atmosphere.

1. Start on a species source node.
2. If the current node is the target node, return the path.
3. Otherwise, find all nodes connected to the current node.
4. If the last travelled edge had a weight of zero, omit all edges with weights of zero from the next choice of edges.
5. Pick an edge at random and repeat from 2.
6. Pathfinding will converge once all possible paths from source to target have been explored.

Step 4 is necessary to prevent "species-species" jumps that are included as a side-effect of adding chemical species to the graph. These unweighted edges are represented with a weight of 0, and traversing two of these consecutively is unphysical (e.g. moving from CO -> CO + H -> H) as it represents a species transforming into another (often completely unrelated) species without a reaction occurring. However, these connections are still necessary to fully connect the graph; we remove the ability to travel along these connections consecutively, effectively altering the graph during pathfinding.

In our network, we investigate key pathways from C and O to CO, as well as the reverse. In all cases, reducing the metallicity results in longer timescales for reactions. Additionally, most pathways have a single reaction that dominates the pathway, often referred to as the "rate-limiting step" (Tsai et al., 2018, 2017). Table 16 shows the main reactions involved in the formation and dissociation of CO for the AM3 atmosphere. We qualitatively reproduce the same effects as those explored in (Wedemeyer-Böhm et al., 2005), and find that of the three reactions that dissociate CO to C and O, the reaction CO $\rightarrow$ CO + H is by far the most efficient, even in this extremely metal-poor atmosphere. Additionally, formation via species exchange (especially by OH) is the most preferable set of pathways.

We can examine the preferred pathways in the network for OH for 3 abundance mixtures: AM3, AC1 and AC2. AM3 and AC2 are qualititively similar, where radiative association of OH via H is a leading timescale. Species exchange with CH and CO is not as preferable. AC2 shows exactly the opposite trend, with species exchange routes being significantly better-travelled than direct radiative association. Again, this is because in both AM3 and AC2, more free O is available after CO has been formed, while in AC1, very little O is present and OH formation relies on carbonic species.

3.4.5 *Treatment of Photochemistry*

Our network does not include the effects of photodissociation of species, due to the greatly increased complexity required to treat this process properly. In the collision-dominated layers, photochemistry is unlikely to be important, but the situation may be different in higher, optically thin layers, where radiation-driven processes become important. The importance of photochemistry is perhaps traced better by the prominence of radiative NLTE effects. The treatment of neutral C in the Sun (Amarsi et al., 2019a) and O in the Sun (Steffen et al., 2015) shows that the abundances are affected up to 0.1 dex in relevant line-forming regions. It is feasible that photochemistry is then an important consideration in higher layers, but the treatment of all atomic and molecular species' photochemical reactions is a considerably difficult and time-consuming endeavour. We welcome any further advancements in this direction.

3.4.6 *Complexity Reduction*

Ideally, one would like to include as many species and reactions as possible into the network to model it as precisely as possible. Unfortunately, due to the large memory cost of storing 3D arrays as well as the steep scaling of the solution time with the size of the kinetic system, methods to reduce complexity are often required. In this work, we have presented a heavily reduced network that is focused on the formation and disassociation of a few key molecular species. However, the existence and addition of other species into the network can alter evolution, pathways and timescales. It is often the case that only a small subset of reactions control the vast majority of the evolution. Identifying these reactions can prove challenging, but a few methods

Pathway	Step	Reactants		Products	Timescale [s]
C → CO					
Pathway 1	1.	C + OH	→	CO + H	$\mathbf{7.43 \times 10^{-5}}$
				Total:	7.43×10^{-5}
Pathway 2	1.	C + OH	→	CH + O	$\mathbf{4.10 \times 10^{-3}}$
	2.	CH + O	→	CO + H	4.27×10^{-4}
				Total:	4.53×10^{-3}
Pathway 3	1.	C + NO	→	CN + O	$\mathbf{1.44 \times 10^{1}}$
	2.	CN + O	→	CO + N	6.46×10^{-3}
				Total:	1.44×10^{1}
O → CO					
Pathway 1	1.	CH + O	→	CO + H	$\mathbf{4.27 \times 10^{-4}}$
				Total:	4.27×10^{-4}
Pathway 2	1.	CH + O	→	C + OH	$\mathbf{2.63 \times 10^{-3}}$
	2.	C + OH	→	CO + H	7.43×10^{-5}
				Total:	2.70×10^{-3}
Pathway 3	1.	O + C2	→	C + CO	$\mathbf{6.72 \times 10^{0}}$
				Total:	6.72×10^{0}
CO → C					
Pathway 1	1.	CO + H	→	C + OH	$\mathbf{6.26 \times 10^{-5}}$
				Total:	6.26×10^{-5}
Pathway 2	1.	CO + H	→	C + O + H	$\mathbf{5.27 \times 10^{-1}}$
				Total:	5.27×10^{-1}
Pathway 3	1.	CO + M	→	C + O + M	$\mathbf{5.24 \times 10^{0}}$
				Total:	5.24×10^{0}
CO → O					
Pathway 1	1.	CO + H	→	C + OH	6.26×10^{-5}
	2.	C + OH	→	CH + H	$\mathbf{4.10 \times 10^{-3}}$
				Total:	4.16×10^{-3}
Pathway 2	1.	CO + H	→	C + O + H	$\mathbf{5.27 \times 10^{-1}}$
				Total:	5.27×10^{-1}
Pathway 3					
	1.	CO + C	→	C2 + O	$\mathbf{3.24 \times 10^{1}}$
				Total:	3.24×10^{1}

Table 16: Step-by-step reactions and rate-limiting steps for the AM3 model atmosphere at a temperature of 3500 [K] and a gas density of 10^{-9} [g cm^{-3}]. The rate-limiting step (longest step in a pathway), is highlighted in bold.

exist to reduce the complexity of the kinetics problem (Grassi et al., 2012; Pope, 1997). In our case, the network was already heavily reduced to the key reactions, and chemical pathways were investigated by Wedemeyer-Böhm et al. (2005) which in part verify this. In the future, we aim to investigate chemical pathways found via a graph theoretical analysis to reduce the number of reactions and species to only those necessary to model significant trends in the regions of interest.

The following figures show horizontal and vertical slices through the photospheres of all models, analogous to Figs. 49 and 50. The slices in the xy direction are all taken at an optical depth of $\log \tau = -4$. In all cases, the differences in the xy slices are minor, seen primarily around hot shock fronts where equilibrium chemistry predicts near-instantaneous dissociation of molecular species, while in the time-dependent case, this proceeds on a finite timescale. As such, time-dependent molecular species are seen in excess.

In the xz slices, differences are seen in the uppermost layers of the atmosphere (generally only in chromospheric layers). These layers are frequented by shock waves that disrupt molecular formation, and when considering equilibrium chemistry, we once again see the effects of molecular dissociation occurring too quickly in the hot shock fronts, and formation of CO occurring too quickly in the cooler regions. As shown in Figs. 55a and 55b, molecular formation is very slow (on the order of hours to days), and most molecular species first show an excess in their yield profile before this decreases as they form CO.

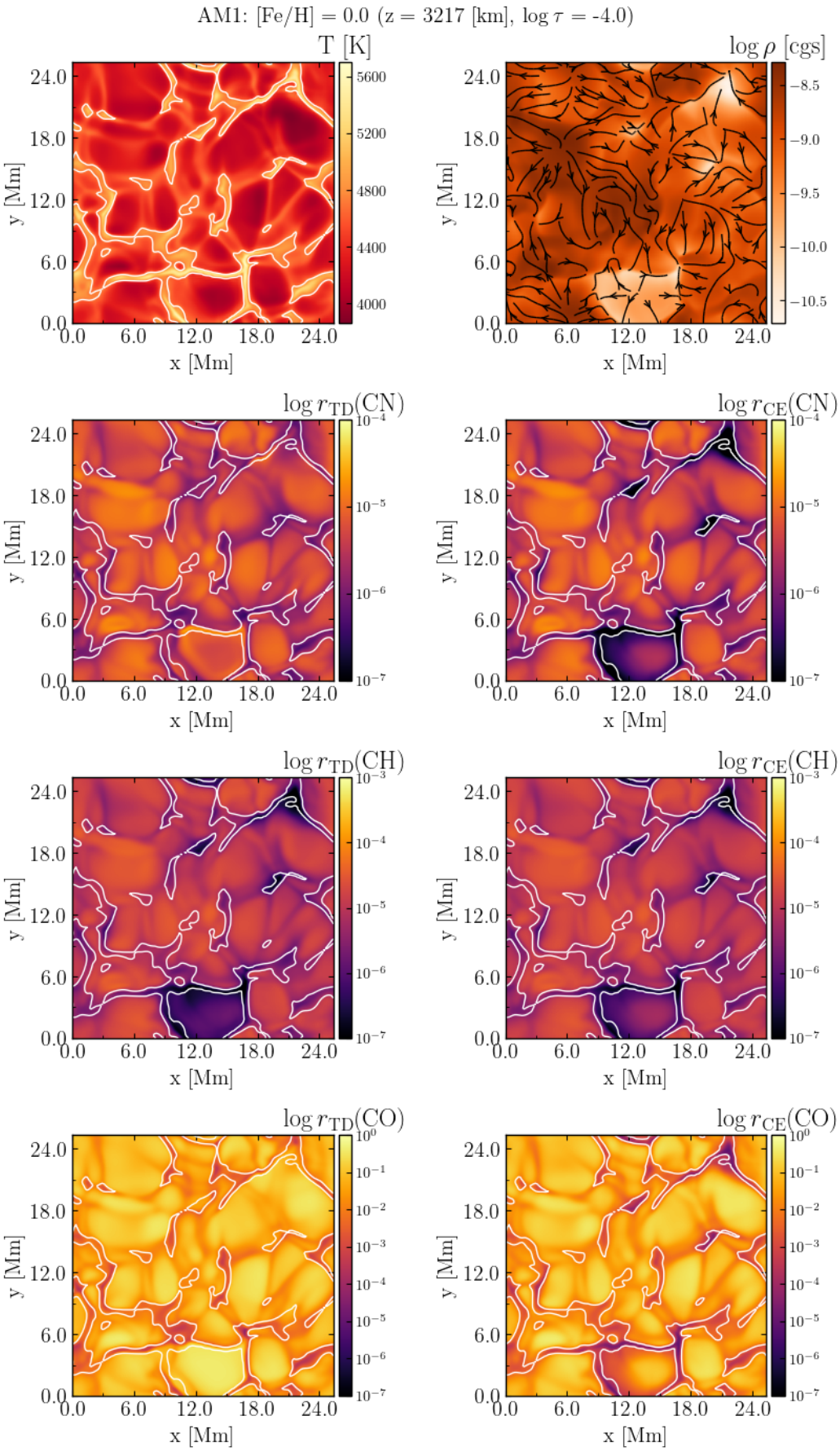

Figure 56: As Fig. 49, but with [Fe/H] = +0.0. The contour line traces a temperature of 5000 K and highlights areas where deviations may be present (seen primarily in CN and CO).

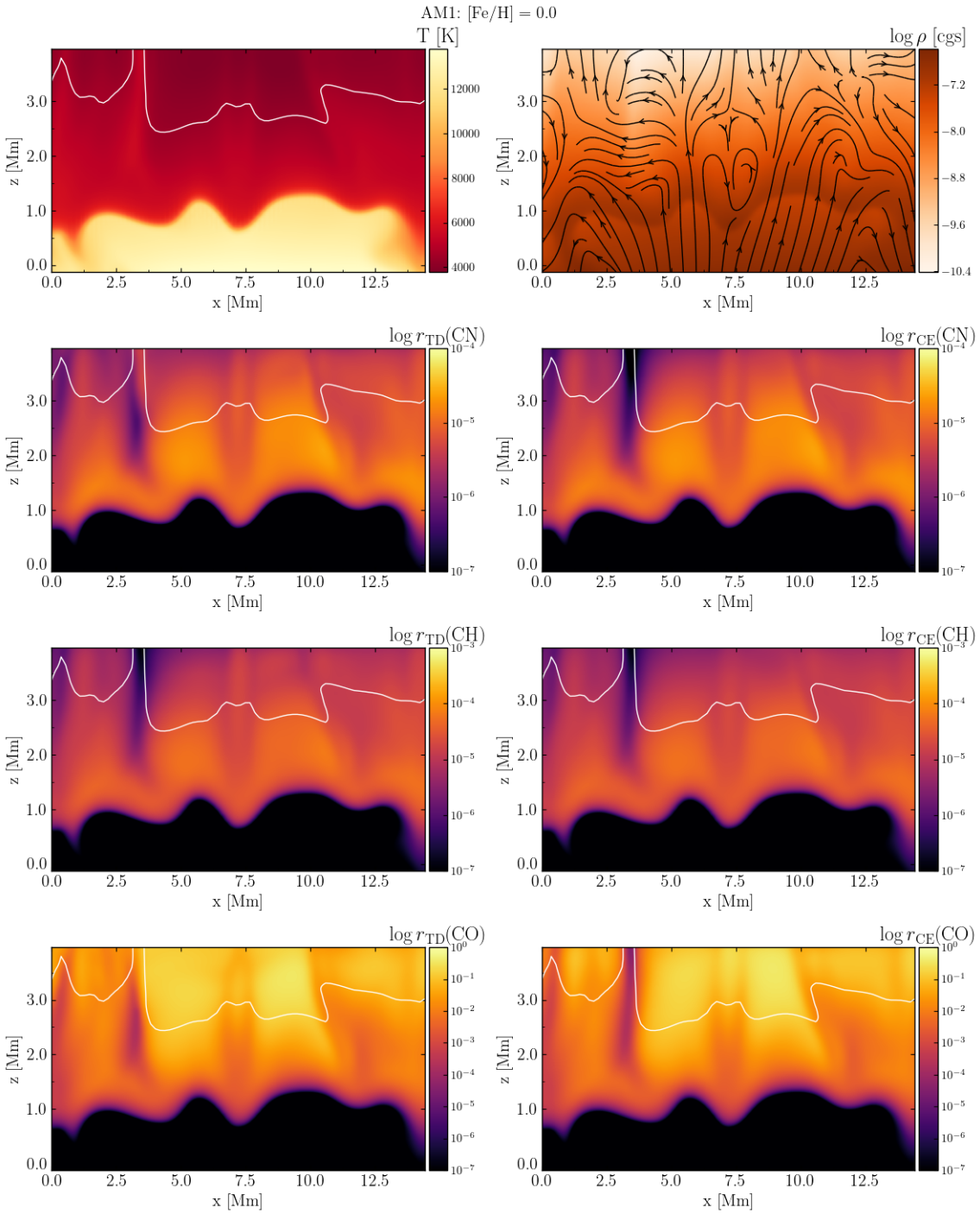

Figure 57: As Fig. 50, but with [Fe/H] = +0.0. The contour line traces a temperature of 4550 K. Minor deviations are present in the uppermost layers of the atmosphere for CN and CO.

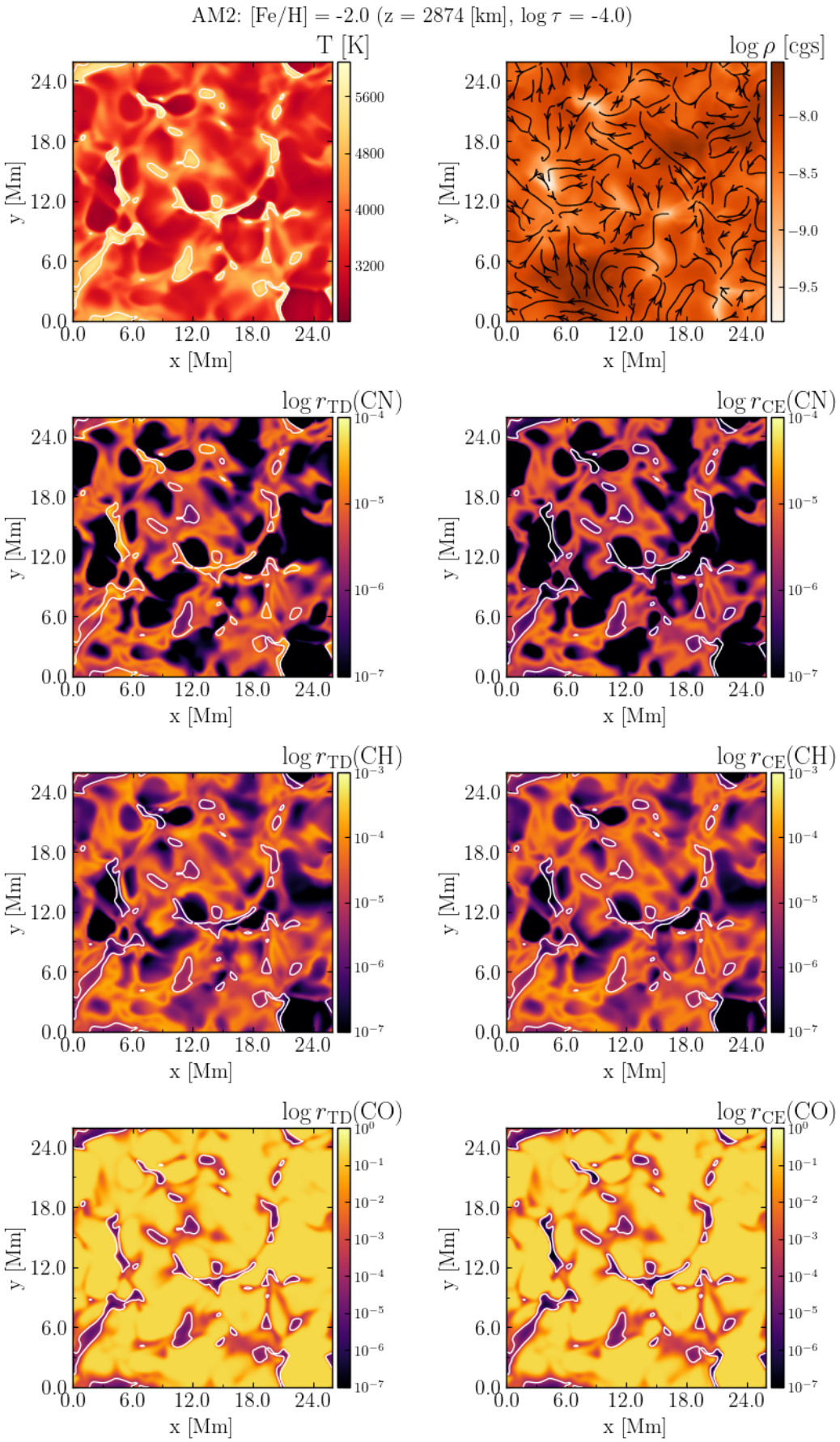

Figure 58: As Fig. 49, but with [Fe/H] = −2.0. The contour line traces a temperature of 5000 K, highlighting areas where CN chemistry is out of equilibrium. CH and CO are generally formed under equilibrium conditions.

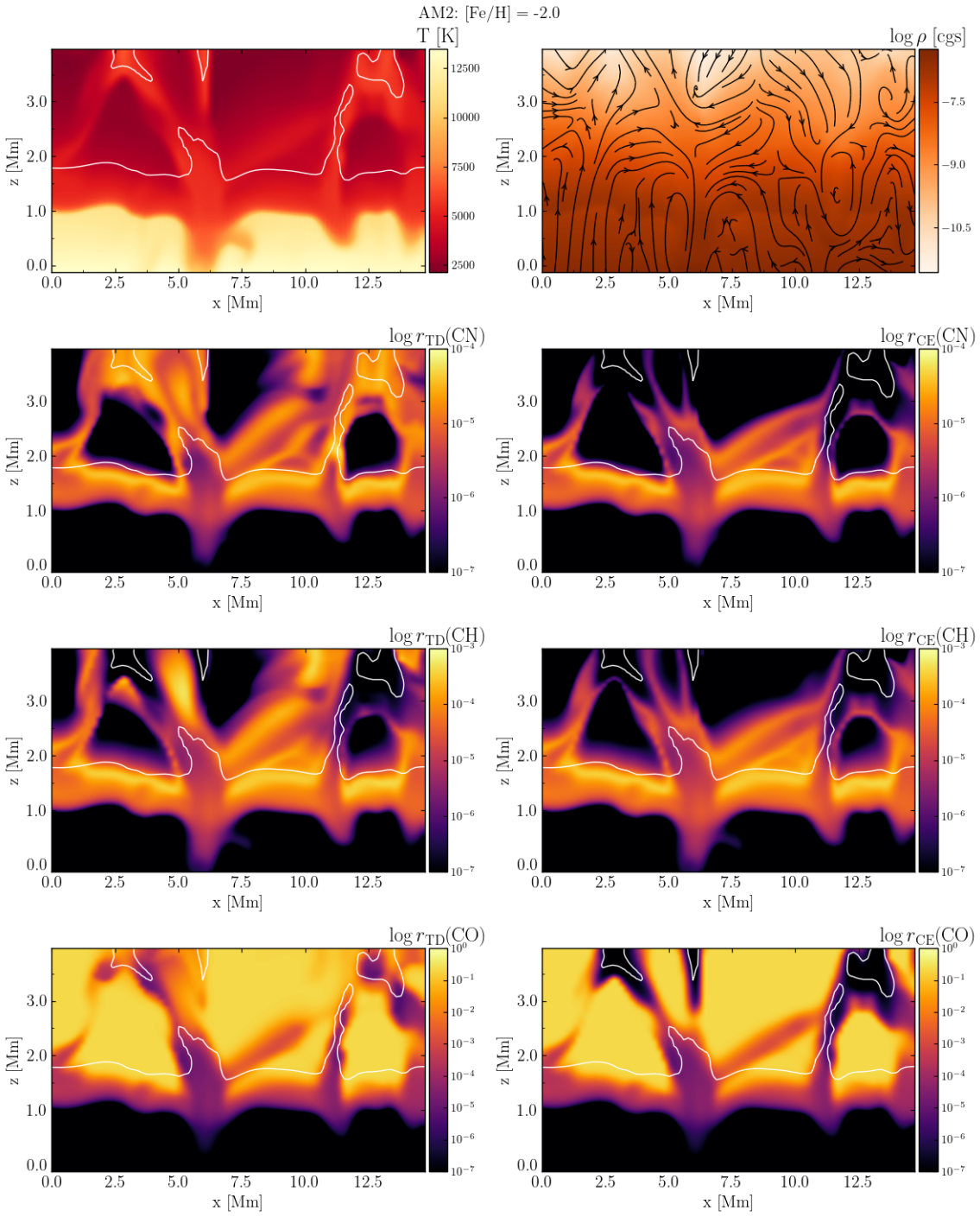

Figure 59: As Fig. 50, but with [Fe/H] = −2.0. The contour line traces a temperature of 5400 K and highlight hydrodynamical features such as an updraft colliding with a downdraft around x = 6.0 Mm, $z = 2.5$ Mm. All molecular species are out of equilibrium around this feature as they do not dissociate as quickly as predicted by the equilibrium chemistry.

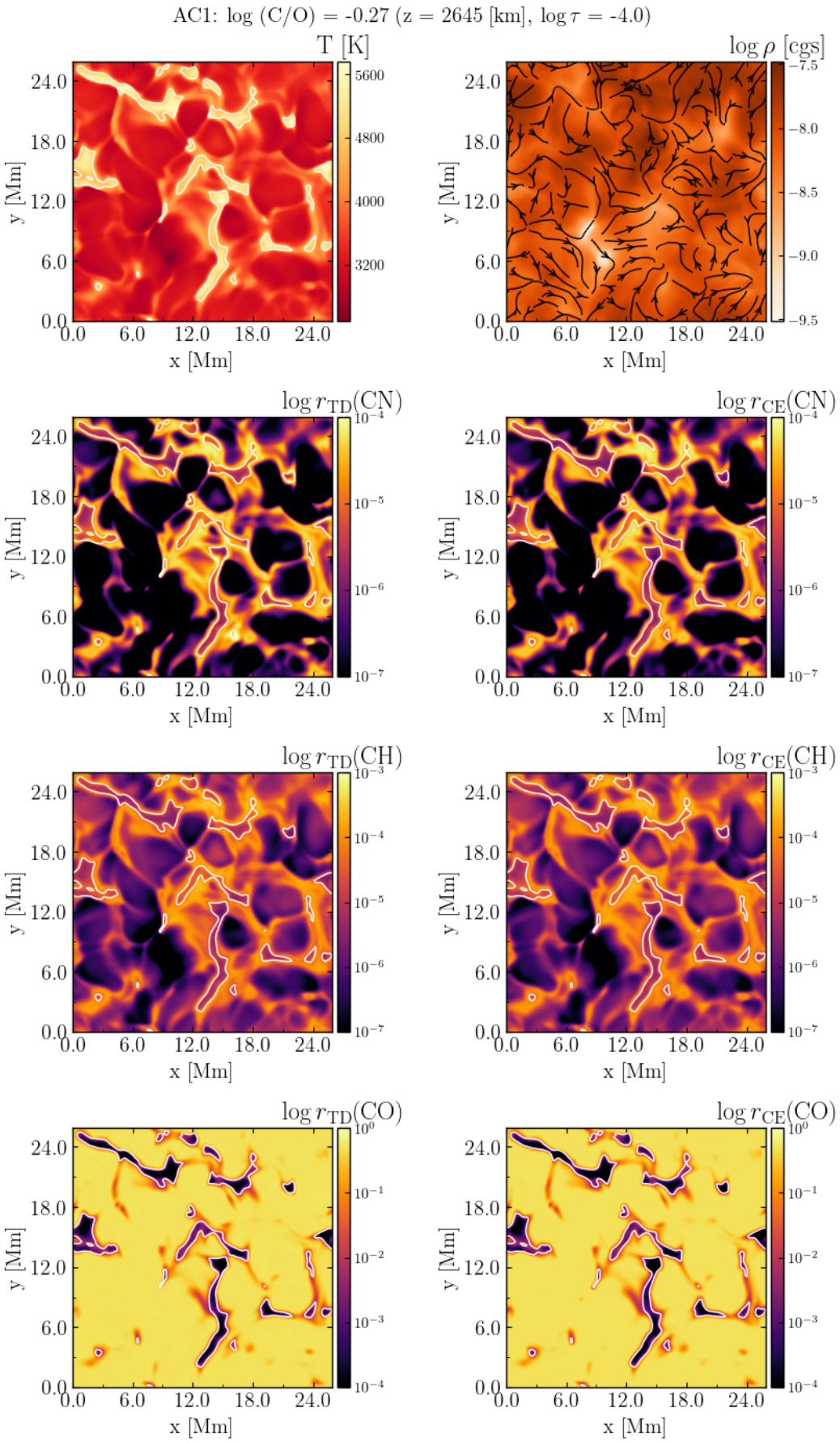

Figure 60: As Fig. 49, but with a C & O enhancement of +2.0 dex and C/O = −0.27 The contour line traces a temperature of 4900 K. The chemistry is almost entirely in equilibrium in this layer of the atmosphere (due to the enhanced C & O abundances), and minor deviations are visible only for CN around the hotter regions.

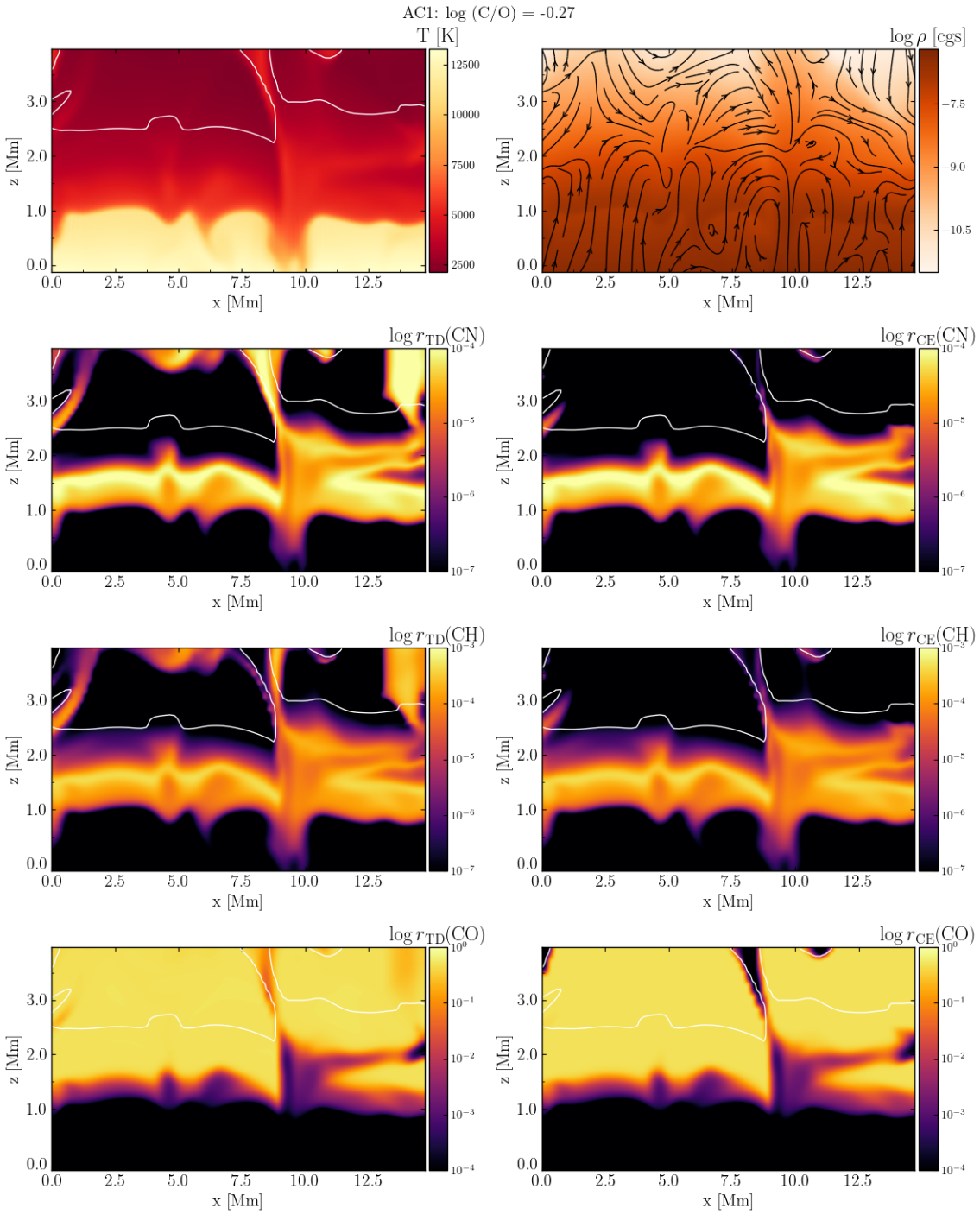

Figure 61: As Fig. 50, but with a C & O enhancement of +2.0 dex and C/O = −0.27. The contour line traces a temperature of 5150 K and highlights a hot updraft near x = 9.0 Mm where primarily CN and CO molecular dissociation is out of equilibrium.

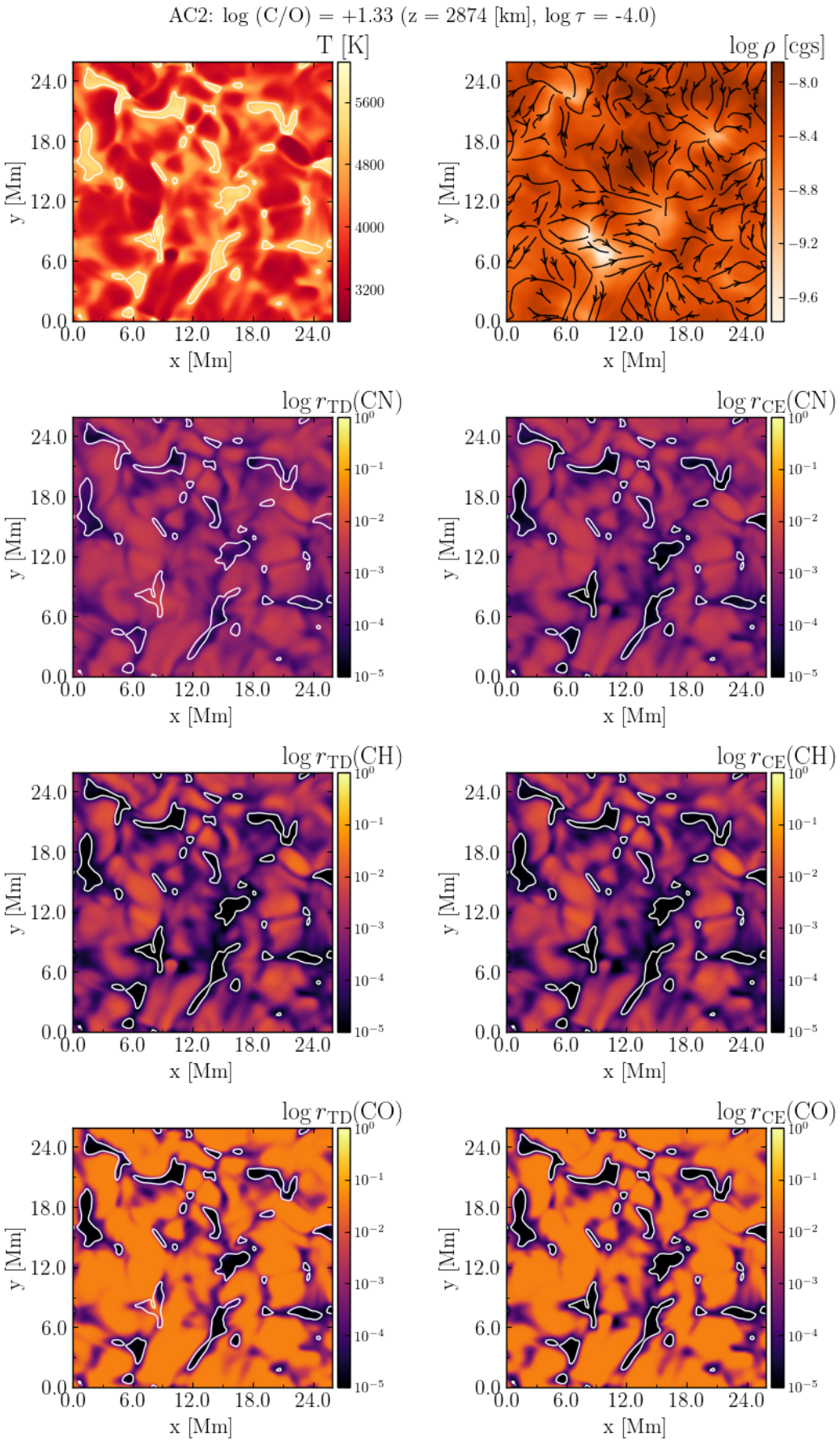

Figure 62: As Fig. 49, but with a C enhancement of +2.0 dex and C/O = +1.33. The contour line traces a temperature of 5000 K, showcasing minor deviations present only in CN. The relatively high carbon abundance results in the molecular chemistry being very close to equilibrium conditions.

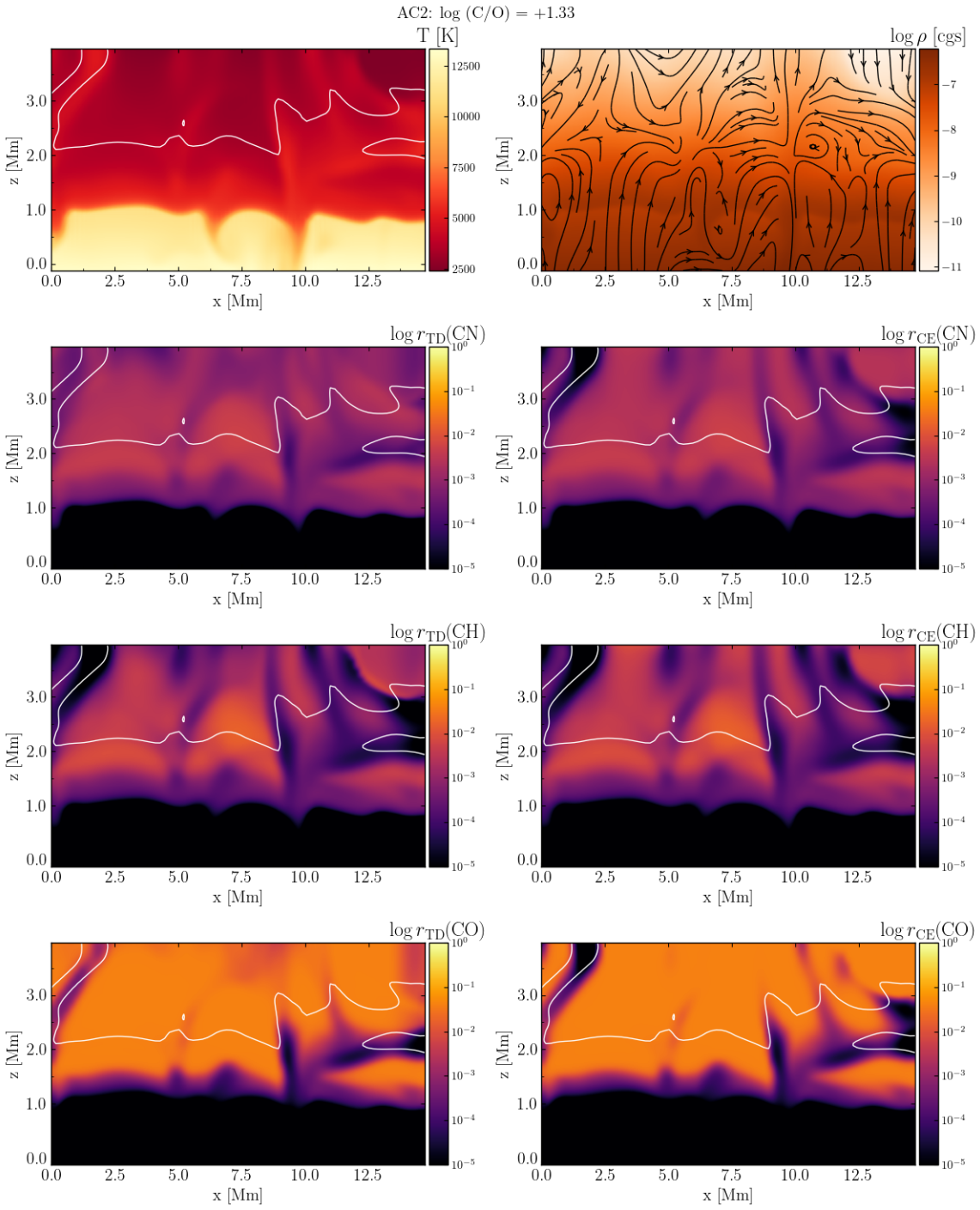

Figure 63: As Fig. 50, but with a C enhancement of +2.0 dex and C/O = +1.33. The contour line traces a temperature of 4950 K, and the largest deviations are seen in a hot updraft near $x = 6.0$ Mm, $z = 3.0$ Mm. The relatively high carbon abundances result in these molecular species being formed very close to equilibrium conditions, though differences are present in these very dilute regions.

The effect of the C/O ratio can be visualised by investigating reaction pathways between the species C, O, CH, OH and CO. A simplified reaction network with 8 reactions was used in this study with temperature-dependence removed from the rate coefficients to investigate the effects of mass-action kinetics. This simplified network takes a subset of reactions from the original network used in this work that characterise the formation and dissociation of CO via CH & OH. In this network, there are 2 pathways from C and O to CO (and back), shown and labelled in Fig. 64. The pathway involving C-CH-CO is labelled P_1 and O-OH-CO is labelled P_2. Additionally, the pathways are constructed such that pathways P_1 and P_2 have the same rates when the amount of C and O is equal. This symmetry allows us to investigate purely the effect of the C/O ratio on the mass-action kinetics. The reaction rates are constant in temperature, but are otherwise constructed to qualitatively match those of the larger network (apart from the symmetry).

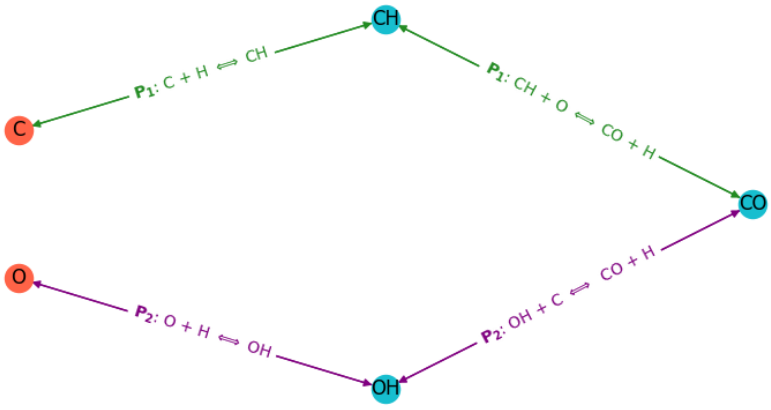

Figure 64: Diagram of the simplified reaction network showing pathways P_1 and P_2.

Fig. 65 shows the evolution of these species for three cases. In Case 1, there is more oxygen than carbon; in Case 2, the amount of carbon and oxygen is equal; in Case 3 there is more carbon than oxygen. As expected, the overall yield of the number densities reflects that of the input abundances.

We adopt abundances similar to the AM2 model for the 3 cases. The total timescale is calculated by summing the individual timescales of the reactions along the pathway. The total timescales and abundances considered for each case are shown in Table 17, with the smallest timescales highlighted in bold. Note that these are not the same timescales as shown in Table 15; the timescales shown there represent the times various species evolve to chemical equilibrium, while the timescales here are inverse reaction rates scaled by number densities. In this sense, they are essentially e-folding timescales.

Case	A(C)	A(O)	log C/O	P_1 [s]	P_2 [s]
1	6.41	7.06	−0.65	36.8	**1.6**
2	7.06	7.06	0.00	3.6	3.6
3	7.06	6.41	+0.65	**1.6**	36.8

Table 17: Total timescales for the C-CH-CO pathway P_1 and the O-OH-CO pathway P_2 (towards formation of CO) for three different log C/O ratios.

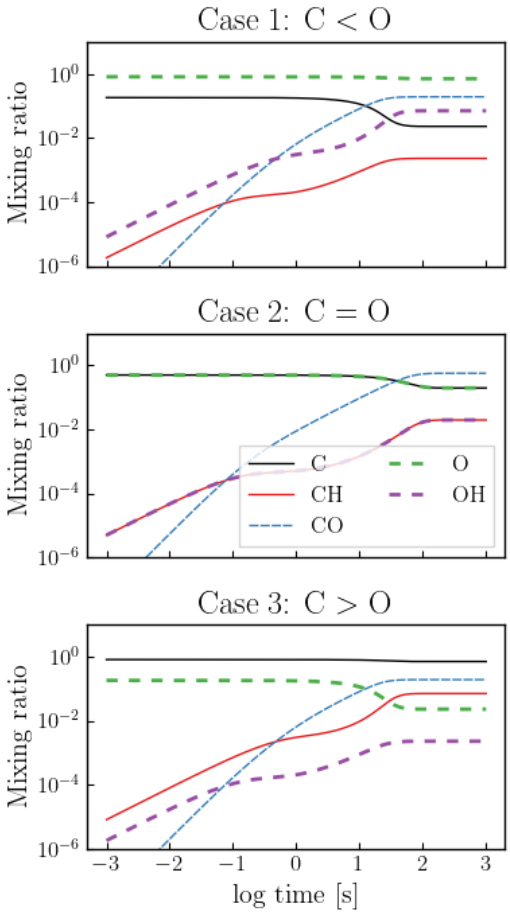

Figure 65: Evolution of C, CH, CO, O and OH for a simplified reaction network used to illustrate the effect of the C/O ratio on equilibrium timescales.

In case 1, where O is more abundant than C, pathway P_2 is faster since forming OH is favourable to forming CH. This results in C and CH being considerably depleted compared to the other species, and is the same effect as in model AM2. In case 2, where O and C are equally abundant, CH and OH form equally quickly due to the symmetry in the simplified network. In case 3, where C is more abundant than O, the exact opposite behaviour to case 1 is observed (again due to the symmetry), however this is qualitatively similar to model AC2. All in all, the current method allows us to investigate favourable pathways in a given network, validating which chemical species are especially important when considering the evolution of another. The longer pathways seen here in the simplified network are indicative of similar trends in the full network, reinforcing the notion that as chemical timescales grow longer, approaching dynamical timescales, it becomes increasingly likely that chemical species lie further from their equilibrium values. However, due to the inclusion of more species and many more pathways between them, the dynamics of the full network are significantly more complicated and it is not immediately clear from the timescales alone how far species will be out of equilibrium, nor whether they would be present in excess or in depletion. Nevertheless, an analysis of favourable reaction pathways could lead to improvements such as complexity reduction.

3.7 CONCLUSION

We have presented a study of 3D time-dependent molecular formation and dissociation in one solar metallicity and four metal-poor atmospheres. The chemistry is modelled through mass-action kinetics with 76 reactions and 14 species which are advected by the velocity field during the hydrodynamics step. We additionally present a comparison to the equilibrium abundances, computed with a Python/Julia chemical kinetics code. Deviations from equilibrium are seen pri-

marily in higher photospheric layers, around shocks and in the temperature differences throughout convection cells.

- Across all models presented in this work, molecular species are generally in chemical equilibrium throughout the model photospheres. Molecular species show mean deviations from equilibrium reaching 0.15 in the lower chromosphere, and these deviations increase with decreasing metallicity and increasing height. The largest deviations are in CN, C_2 and CH when $\log(C/O) < 1$, and in OH when $\log(C/O) > 1$. Above $\log\tau \approx -2$, the less abundant of C or O becomes locked into CO, inhibiting the formation of other molecular species involving that species. This results in comparatively low amounts of CH, CN & C_2 in all models except AC2, and comparatively low OH in model AC2.
- The deviations from equilibrium can also be attributed to behaviour around chromospheric shock waves. In the equilibrium case, the hot shock front contains very low number densities of molecular species, while the time-dependent treatment has greater number densities as the evolution proceeds with a finite timescale. In the uppermost, coolest layers ($T \lesssim 3500$ [K]), slow chemical timescales result in a depletion of CO as there is insufficient time to form it before material is advected to a significantly different thermodynamic state.
- These deviations are unlikely to contribute significantly to spectroscopic measurements for metal-poor dwarfs, as the line cores of key molecular species are generally formed in deeper layers (Gallagher et al., 2017a). The largest deviations are mostly outside of the range of the contribution functions for the CH G-band and OH-band, but these deviations could still affect spectral line shapes, which can only be properly reproduced in 3D models. The perceived trend of increased carbon enhancement with decreasing stellar metallicity is therefore not due to an improper treatment of time-dependent chemistry. An investigation including spectrum synthesis using the time-dependent number densities is however warranted in light of these deviations.
- Relative deviations increase with decreasing metallicity due to slower mass-action reaction rates. The change in metallicity does not lead to a strictly linear increase in chemical timescale or decrease in yield in all layers, but generally, lower metallicities result in larger chemical timescales and lower yields.
- The C/O ratio plays a key role in determining which molecular species are further out of equilibrium. Both CH and OH are formed along reaction pathways to form CO. In the majority of atmospheres presented, oxygen is present in excess compared to carbon, making OH formation more viable than CH. This leads to faster chemical timescales for reaction pathways involving OH. Changing this ratio so carbon is in excess likewise changes pathways to make the formation of carbon-bearing species preferential.

4

TIME-DEPENDENT MOLECULAR CHEMISTRY IN THE PHOTOSPHERES OF GIANT STARS

4.1 INTRODUCTION

Stars on the red giant branch (RGB) contain a wealth of information about stellar evolution, much of which is accessible through their spectra. The spectra of late-type giants show a plethora of molecular lines, as the cooler temperatures favour molecular formation of species such as CO, CH and CN. These observations of the vast amount of molecular lines continues towards lower metallicities, as atomic lines become comparatively weaker, and so the proper treatment of these molecular lines becomes increasingly important. The most metal-poor stars show a trend of increasing carbon enhancement with decreasing metallicity. In Chap. 3, we found that, in dwarf stars, this effect does not come from an improper treatment of molecular chemistry, as the layers in which molecular formation and dissociation is severely disrupted by hydrodynamic effects lies outside the formation regions of key molecular species such as CH, OH, CO and CN. In this work, we perform a similar analysis for red giant atmospheres.

RGB stars are important in the study of the evolution of low-mass stars. As the Milky Way Halo contains a larger fraction of older, metal-poor Population II stars, the study of metal-poor giants gives direct insights into the evolution of some of the oldest stars in the Galaxy. The models we consider extend across the RGB, from $T_{\rm eff} = 5000$ K, $\log g = 2.5$ to $T_{\rm eff} = 3600$ K, $\log g = 1.0$. We also cover metallicities down to $[Fe/H] = -3$, approaching the tail of the metallicity distribution function.

The extended atmospheres of RGB stars, along with the cooler temperatures we consider here lead to environments where molecular chemistry (often described with mass-action kinetics) slows down. In other words, there may not be sufficient time for species to react and form their equilibrium yields before effects such as convection cause the local thermodynamic state to change. We hence treat this as a departure from local thermodynamic equilibrium (LTE). In contrast to radiative NLTE, we model the evolution of chemical species in a time-dependent fashion, taking into account the advection of species as well as chemical reactions occurring on a finite timescale.

In this work, we present three-dimensional model atmospheres with self-consistent molecular formation and dissociation for 7 stars computed with the radiation (magneto)hydrodynamics code CO^{5}BOLD. We use the same chemical network as the one presented in Table 13 to model the evolution of molecular species such as CO, CH, CN and OH. In addition to the study of hydrodynamical effects and direct comparisons between equilibrium and non-equilibrium molecular chemistry, we investigate the interplay between hydrodynamical and chemical timescales quantitatively to determine whether the question of whether chemical equilibri um holds for a given chemical network can be precisely answered with a simpler methodology.

The methods are described in Sec. 4.2. The results and implications of the three-dimensional simulations for the time-dependent and steady-state calculations are presented in Sec. 4.3. Chemical and hydrodynamical timescales are discussed in Sec. 4.4.

4.2 METHODOLOGY

4.2.1 *Model Atmospheres*

Our models have been computed with the CO^{5}BOLD model atmosphere code. CO^{5}BOLD is a conservative finite-volume hydrodynamics solver capable of modelling surface convection, waves, shocks and other phenomena in stellar objects (Freytag et al., 2012). We treat hydrodynamics, radiation transfer and molecular chemistry by means of operator splitting. Each model is solved on a Cartesian grid in a time-dependent manner. For consistency, the chemistry is solved as the last step in each iteration, meaning the final number densities are representative of the fluid state in the moment. We employ standard directional splitting along the directions of 1D opera-

tors, and a Roe solver is used to compute updates in a single time step. Higher order terms in time are provided based on the applied reconstruction scheme, which, for the passive tracers, is chosen such that number densities are strictly non-negative.

The properties of the model atmospheres used in this work are summarised in Table 18. For each model, the passive tracers representing the chemical species were added to an already thermally relaxed model. Each model was then evolved long enough to be chemically relaxed.

Model ID	T_{eff}	log g	[Fe/H]	Internal ID
A1	4000	1.50	+0.00	d3t40g15mm00
A2	4000	1.50	-2.00	d3t40g15mm20
A3	4000	1.50	-3.00	d3t40g16mm30
B1	5000	2.50	+0.00	d3t50g16mm00
B2	5000	2.50	-2.00	d3t50g16mm20
B3	5000	2.50	-3.00	d3t50g16mm30
C1	3600	1.00	0.00	d3t36g10mm00*

Table 18: Model atmosphere parameters for the seven models used in the study. The C1 model uses the smaller reaction network presented in Wedemeyer-Böhm et al. (2005).

The chemical network used in the time-dependent evolution is the same as that described in Deshmukh and Ludwig (2023). The initial abundances for the molecular chemistry are scaled by metallicity and alpha enhancement. Each model's molecular chemistry input is consistent with its equation-of-state and opacity table.

4.2.2 *Equilibrium Chemistry*

We use the GCRN code[1] to compute the equilibrium number densities for the given chemical network, provided the gas density, temperature and abundances. The GCRN code is capable of solving chemical kinetics problems provided a chemical reaction network, and also includes the ability to analyse reaction pathways in a graph theoretical manner. We directly compare the equilibrium number densities to those obtained from the time-dependent evolution using `CO5BOLD`. The assumption made in equilibrium chemistry is that chemical timescales are much shorter than any other timescale in the system, meaning that chemical reactions proceed until the material is in chemical equilibrium.

4.3 RESULTS

Figs. 66-68 show the mean number densities, mixing ratios and deviations for the models we consider in this work in the range $-4 \leqslant \log \tau \leqslant 2$ for the different kinds of giants' atmospheres in this work.

Deviations increase with height in the atmosphere as the temperature and gas density decrease, leading to slower chemical kinetic rates. The largest deviations are seen in CN, C_2 and atomic C, though in all cases where deviations grow, the overall number densities and mixing ratios of these species shrink. Therefore, convective flows advect these species into higher layers and there is insufficient time for them to form more stable species due to the cooler, less dense environment.

Somewhat surprisingly, average deviations in the A-series of models decrease with decreasing metallicity, while normally, the lower metallicity would lead to slower chemical timescales and increasing deviations. Instead, since the deviations seen here are due to upward flows advecting material from lower layers (where they are present in excess) to higher ones, lower yields in general lead to lower deviations in higher layers. All in all, the largest deviations coincide with

1 https://github.com/SiddhantDeshmukh/graphCRNs

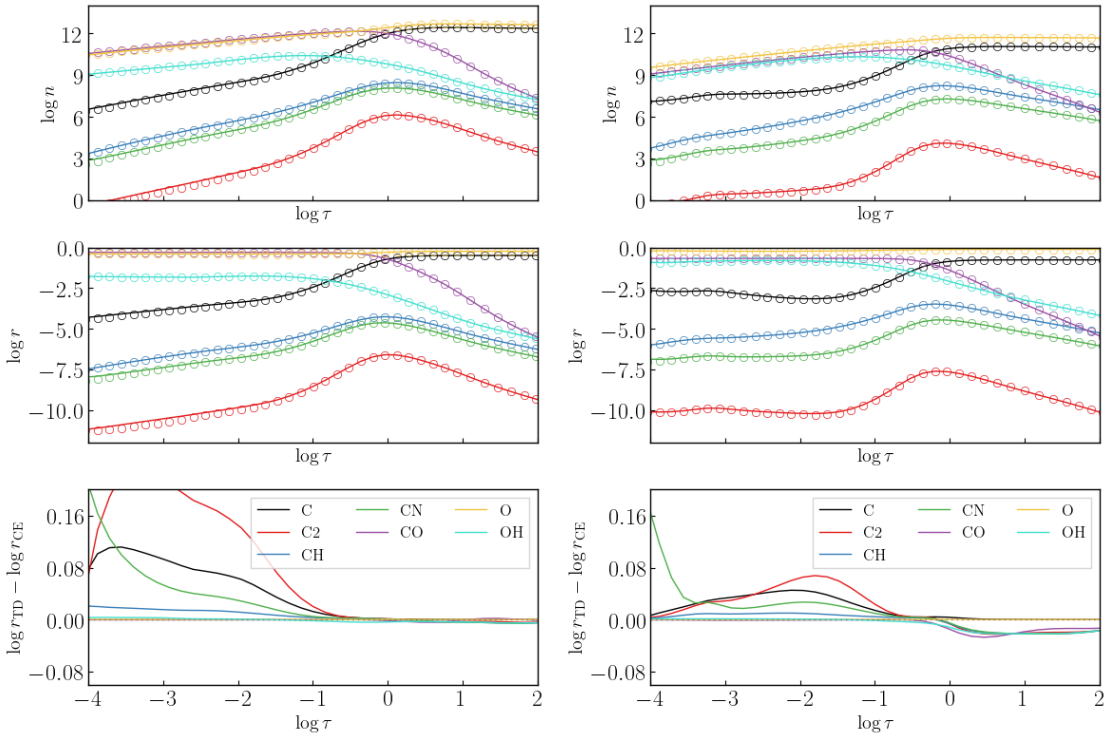

(a) [Fe/H] = 0.0

(b) [Fe/H] = −2.0

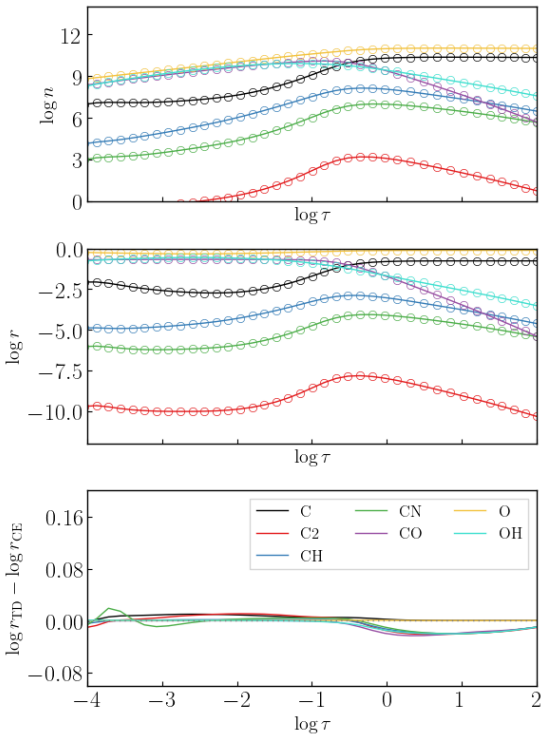

(c) [Fe/H] = −3.0

Figure 66: Mixing ratios and deviations from chemical equilibrium for the A1, A2 and A3 models. In the first and second panels, solid lines show the time-dependent quantities while the hollow points show the equilibrium quantities.

decreasing number densities, meaning it is unlikely that these deviations will result in significant NLTE corrections to abundances. Additionally, the cores of the spectroscopically accessible lines are formed in the deeper layers, where the deviations are extremely minor.

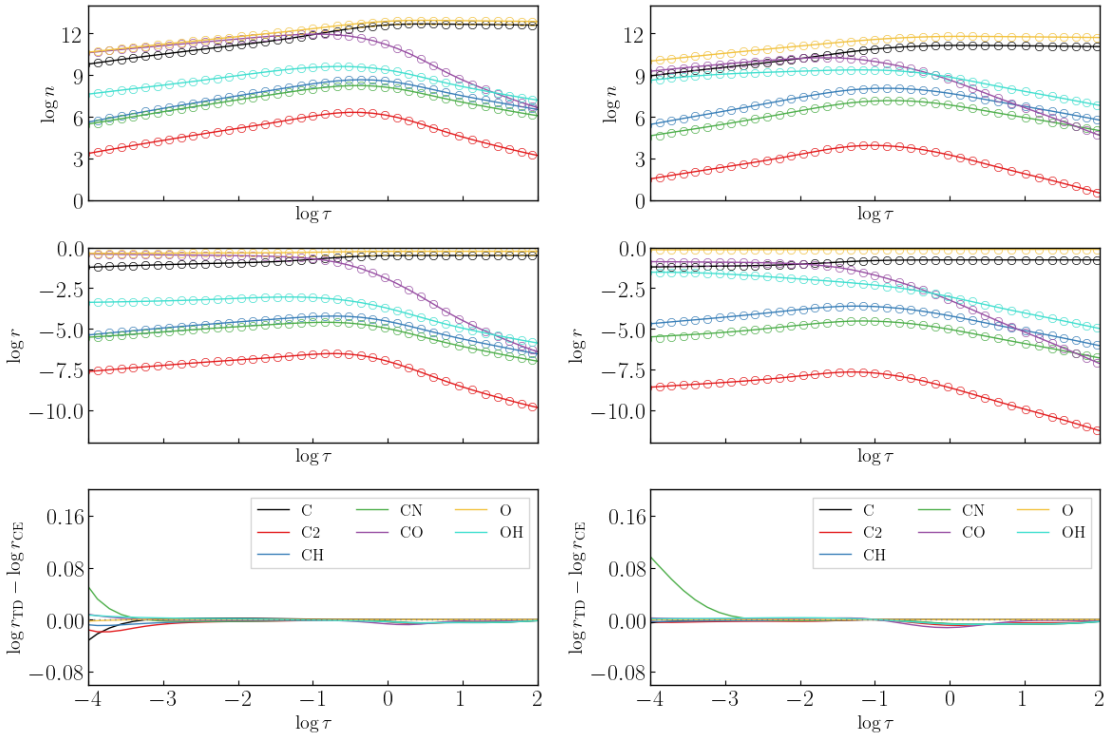

(a) [Fe/H] = 0.0

(b) [Fe/H] = −2.0

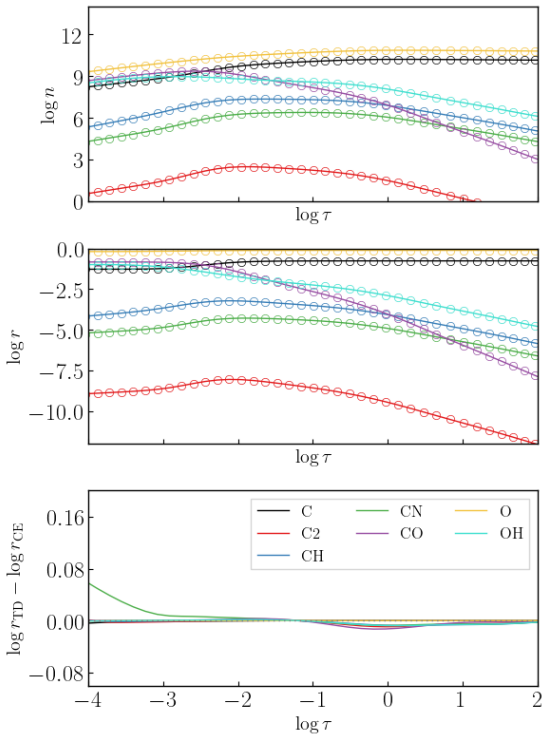

(c) [Fe/H] = −3.0

Figure 67: Mixing ratios and deviations from chemical equilibrium for the B1, B2 and B3 models. In the first and second panels, solid lines show the time-dependent quantities while the hollow points show the equilibrium quantities.

To see the effects of time-dependent chemical evolution in more detail, we can observe the instantaneous differences that exist between the two treatments.

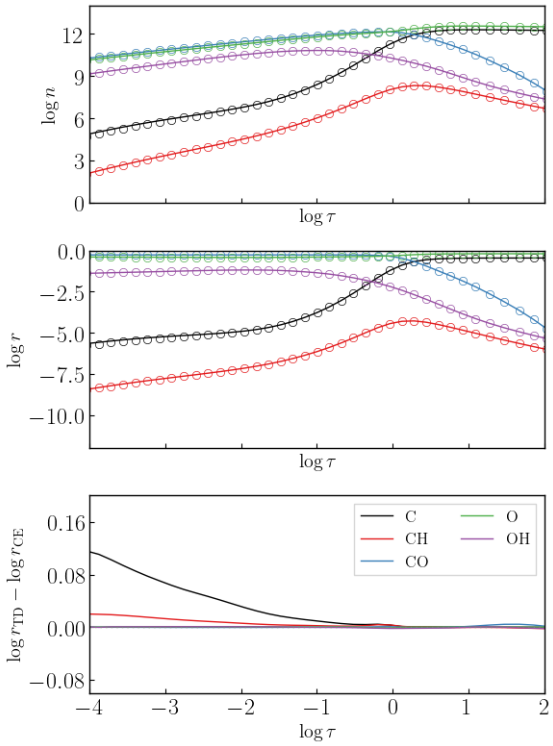

Figure 68: Mixing ratios and deviations from chemical equilibrium for the C1 model. In the first and second panels, solid lines show the time-dependent quantities while the hollow points show the equilibrium quantities.

Fig. 69 shows a typical flow pattern in the atmosphere. Molecular formation is once again seen to correlate with cool temperatures and large densities. A convective cell is visible in the lower left corner (see top-right panel), and molecular chemistry is generally in equilibrium here. The largest deviations from equilibrium are seen in the higher levels around the contour line, particularly in the top-left part of the plots, where hydrodynamical flows advect molecular species to higher levels where they exist in excess of their equilibrium values. While the overall effect is small (see Fig. 67c), this effect is the most likely contributor to the excess CN number density observed in the time-dependent case.

Fig. 70 shows the binned heatmaps of differences in time-dependent and steady-state chemistry. In the majority of the atmosphere, deviations are very small, and the deviations are only seen in the uppermost, cooler layers. Many molecular species are present in excess in the time-dependent case owing to the slow timescales of formation. Notably, the cool, diffuse region around $T \approx 3000$ K, $\log \rho \approx -11$ shows a depletion of CO and OH but an excess in other molecular species. This is due to the formation pathways of CO and OH via the other molecular species being inhibited due to the thermodynamic conditions. Overall, while significant deviations are present at times, these are not reflected when considering the relevant line formation regions.

Fig. 71 shows the 3D representation of the gas density, temperature and number density of CO (time-dependent) in a portion of the higher layers. The formation of CO clouds can clearly be seen in the cooler, denser regions of the atmosphere.

4.4 DISCUSSION

In order to better understand the regimes in which molecular chemistry is out of equilibrium, we compute representative timescales for the two competing processes, namely chemical evolution and hydrodynamical mixing. The timescale of chemical evolution is derived by analysing the system of ordinary differential equations (ODEs) that describe the change in the number densities of the species, while the timescale of hydrodynamical mixing is obtained by analysing

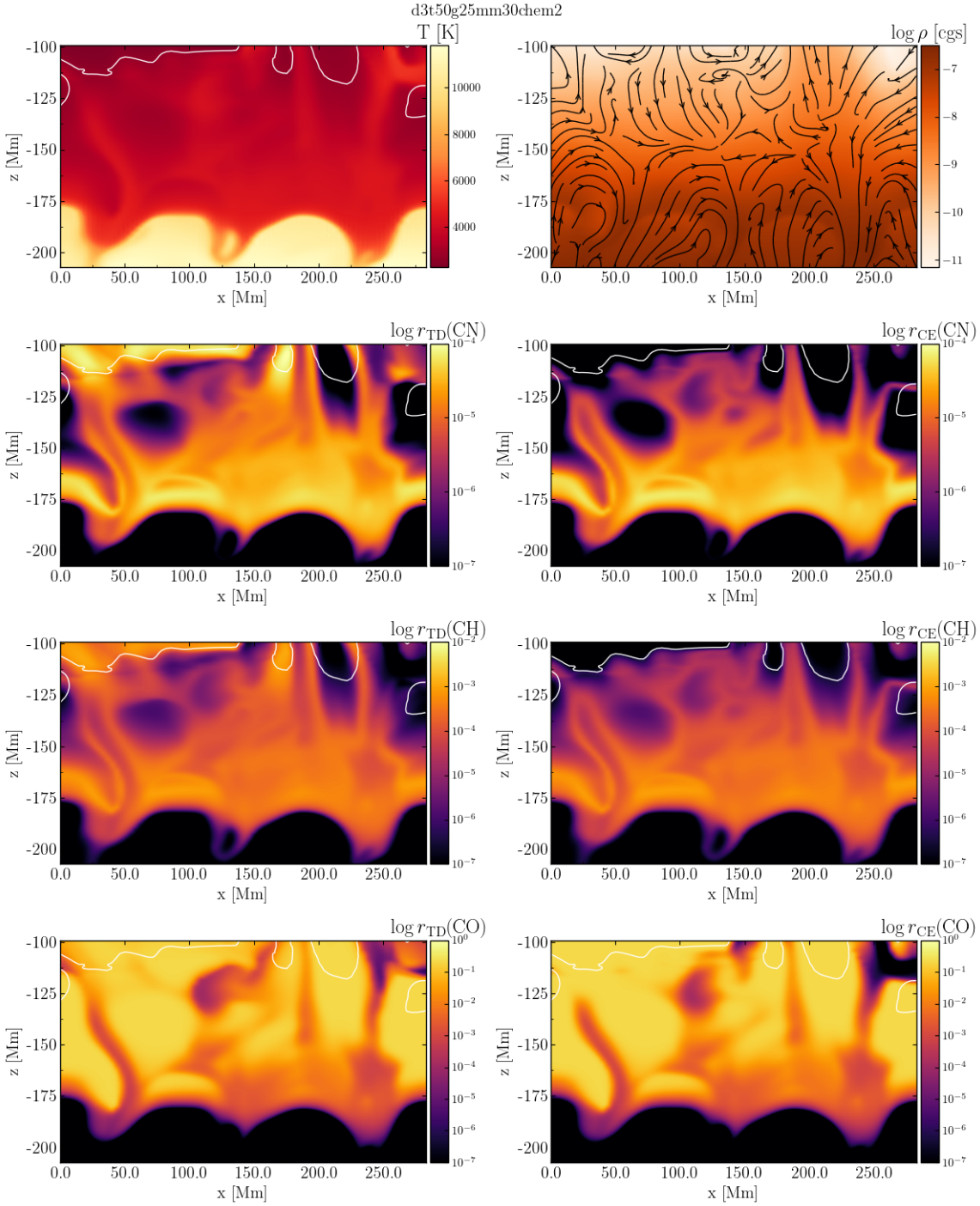

Figure 69: Time-dependent mixing ratios of molecular species in a vertical slice through the photosphere above $\log \tau = 2$ in the B3 model atmosphere. The white contour traces a temperature of 2850 K.

the velocity field of the 3D model atmosphere. While this analysis was done using 3D model atmospheres, the process involves the spatial and temporal averaging of flow quantities, meaning the actual timescale comparison can be done in 1D.

Many different methods exist for determining the chemical timescale of a reaction system (Caudal et al., 2013; Wartha, Bösenhofer, and Harasek, 2021) with varying levels of complexity. We compared the use of the inverse reaction rate (Ayres and Rabin, 1996; Wedemeyer-Böhm et al., 2005), Evans timescale (Evans et al., 2019) and inverse eigenvalue timescales.

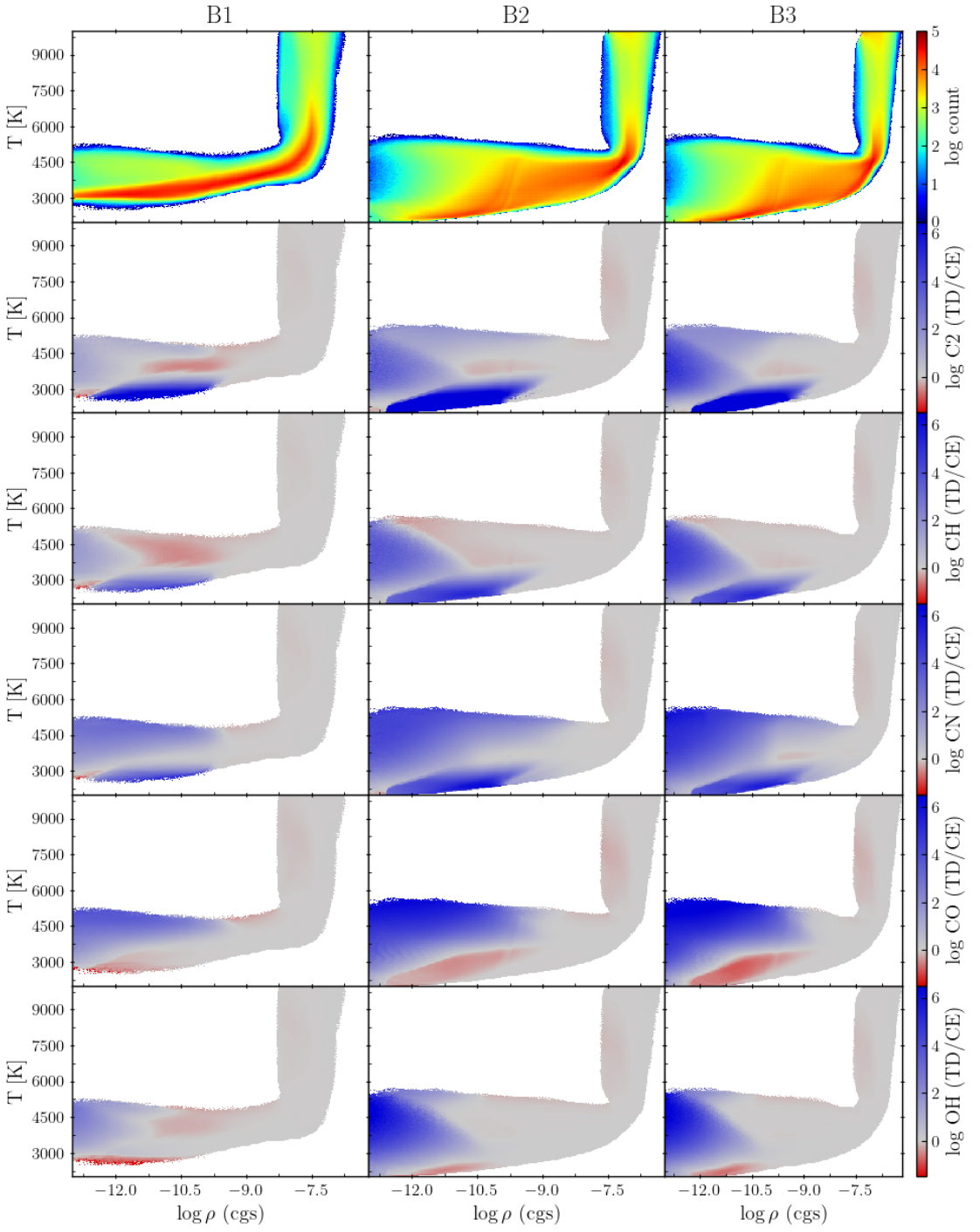

Figure 70: Heatmaps of binned quantities for the B-series of models. Each quantity was binned using 20 snapshots of the relevant 3D model. Deviations from equilibrium are seen primarily in regions with low counts that correspond to hydrodynamical features found in the upper photosphere including the tops of convective cells, shock fronts, and wakes.

The inverse reaction rate timescale involves simply inverting the reaction rate of a chemical reaction and scaling by the number density of the chemical species in question. For example, the evolution of CO via the reaction

$$C + O \rightarrow^{k} CO \tag{120}$$

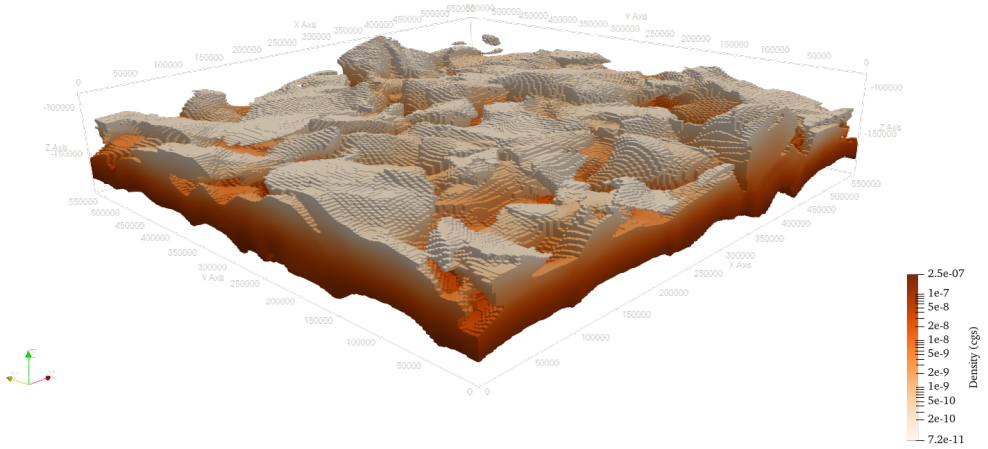

(a) Gas density.

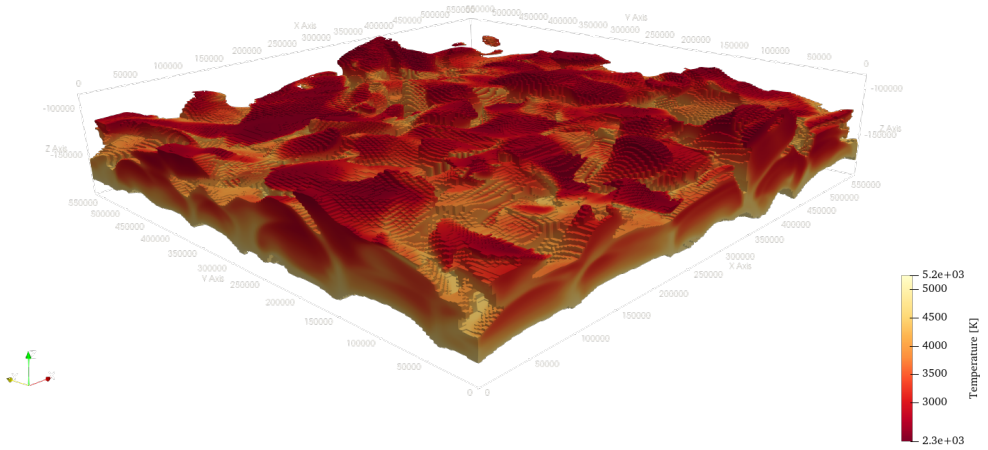

(b) Temperature.

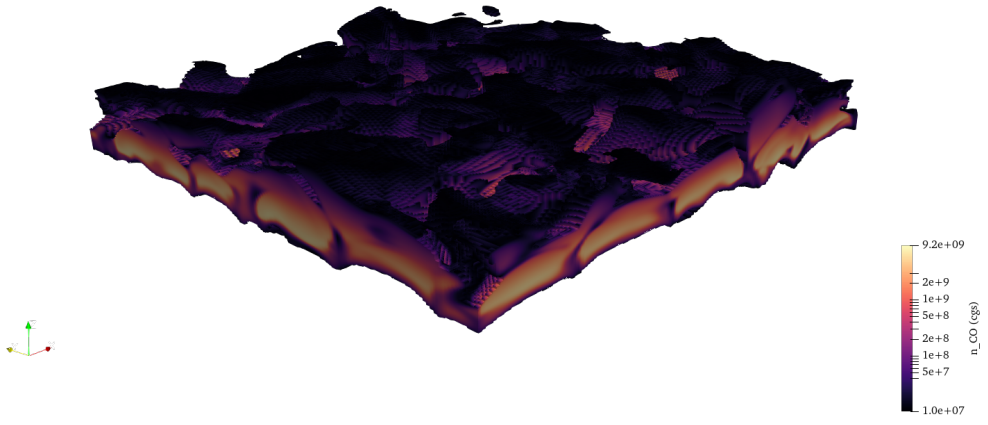

(c) Number density of CO (time-dependent).

Figure 71

with rate coefficient k can be represented by the ODE

$$\frac{dn_{CO}}{dt} = k n_C n_O. \tag{121}$$

From dimensional analysis, we can compute the relevant timescale by dividing both sides by [CO] and inverting the right-hand side:

$$t_{\text{chem,rate}} = \frac{n_{CO}}{k n_C n_O} \tag{122}$$

In a reaction network with many different reactions, we then compute a different timescale for each reaction. To find the relevant timescale in this analysis, it is necessary to first identify the most important reactions, and to then take the fastest timescale, since this corresponds to the reaction with the highest yield.

The Evans timescale is defined as

$$t_{\text{chem,Evans}} = \max_{i \varepsilon N_{\text{major}}} \left[\frac{n_i}{|\omega_i|} \right] \tag{123}$$

where n_i is the number density of species i and ω_i is the net reaction rate of species i (i.e., the summed contribution of all reactions involving species i). Evans et al. (2019) suggest to use the N_{maj} major reacting species for this calculation.

Yet another method involves computing the inverse of the eigenvalues of the Jacobian matrix. The inverse of the smallest (absolute) eigenvalue is then taken to be the dominant timescale:

$$t_{\text{chem,Jacobian}} = \min \left[\frac{1}{\lambda_i} \right] \tag{124}$$

where λ_i is the ith eigenvalue of the Jacobian matrix $\mathbf{J}$. In certain cases, the diagonal elements of $\mathbf{J}$ can be taken as approximations of the eigenvalues (Wartha, Bösenhofer, and Harasek, 2021), though in systems where off-diagonal elements are important, oscillating behaviour covered by complex eigenvalues will be neglected.

In the end, we chose to use the inverse reaction rate timescale as it performed the best across the atmospheric domain. We found that the inverse eigenvalue method gave extremely small timescales that were not consistent with the deviations we observed, and the Evans method did not provide sufficient detail as to the reaction mechanisms involved. However, we did take inspiration from their filtering method and only considered the evolution reactions of C, O, N, CO, OH, C_2 and CN to compute relevant timescales, as these are the prominent reacting species that are relevant. To compute a single timescale, we further consider only CO-relevant timescales, as CO is the main molecular species in the network. Additionally, we sorted the contributing terms to a given species evolution equation based on the rate (a proxy for the yield), and removed all reactions that contribute less than 10%.

The hydrodynamical timescale should characterise the level of mixing in the atmosphere, as it is this process that disrupts the chemical evolution process by changing the local temperature and gas density. Freytag et al. (2012) determine a convective turnover timescale using the pressure scale height H_P and characteristic convective velocity v_c according to classical mixing length theory:

$$t_{\text{turnover}} = \frac{H_P}{v_c} \tag{125}$$

We adopt a similar method, but use the root-mean-squared (RMS) velocity in the z-direction instead of the characteristic convective velocity, since it is the quantity that characterises the amount of mixing in the z-direction:

$$v_{\text{RMS}} = \sqrt{|\langle v_z^2 \rangle - \langle v_z \rangle^2|}. \tag{126}$$

The pressure scale height H_P is given by

$$H_P = \frac{P}{\rho g} \tag{127}$$

where P is the gas pressure, ρ is the gas density, and g is the surface gravity of the star. In full, the hydrodynamical mixing timescale is hence given by

$$t_{\text{hydro}} = \frac{H_P}{v_{\text{RMS}}} = \frac{P}{\rho g \sqrt{|\langle v_z^2 \rangle - \langle v_z \rangle^2|}}. \tag{128}$$

We can now compute a measure of chemical disequilibrium by means of the Damköhler number (Schaschke, 2014) Da:

$$\mathtt{Da} = \frac{t_{\mathrm{hydro}}}{t_{\mathrm{chem}}}. \tag{129}$$

Da can be used to identify which timescales are dominant in a regime. Large values of Da (greater than 10) imply that hydrodynamical timescales are dominant, and hence the chemistry is not largely affected by mixing. Conversely, small values of Da (less than 1) imply that chemical timescales are dominant, and that there is insufficient time for chemistry to equilibriate before hydrodynamical effects change the local state.

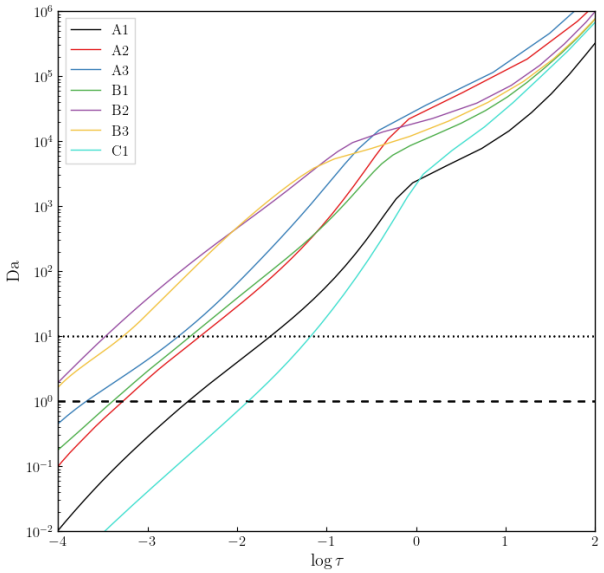

Figure 72: Da as a function of optical depth for all 7 atmospheres presented in this work. The dotted and dashed lines mark Da = 10 and Da = 1, respectively.

Fig. 72 shows Da as a function of optical depth for all 7 atmospheres presented in this work. This analysis shows that all molecular chemistry is in equilibrium below $\log\tau = -1$. The approach correctly predicts that models C1 and A1 show the largest deviations above $\log\tau = -2$, and that the B-series of models show relatively minor deviations overall. However, the A1 and A2 models both show deviations beginning above $\log\tau = -1$, yet the Da analysis predicts deviations to become significant closer to $\log\tau = -2$ for both of these models. While insightful, other factors will likely need to be taken into account to utilise this as a means of determining exactly where deviations from chemical equilibrium will occur. Overall, though, the Da analysis provides a good first insight into where the assumption of chemical equilibrium may not be valid.

4.5 CONCLUSION

We have presented an analysis of time-dependent molecular formation and dissociation in 7 red-giant atmospheres focusing on the evolution of CO, CH, CN, OH and C_2. The models considered here extend across a range of temperatures, surface gravities, and metallicities, and serve to illustrate the validity of the approximation of chemical equilibrium in the spectroscopically accessible regions.

- Deviations from chemical equilibrium are largest in the highest layers of the model atmospheres, as expected with the decrease in temperature and gas density leading to slower mass-action kinetic rates. In all atmospheres, the deviations do not exceed 0.2 dex in the region $-4 \leqslant \log\tau \leqslant 2$, and rarely exceed 0.1 dex. These deviations are on-par with the deviations seen in dwarf stellar models (Deshmukh and Ludwig, 2023). The assumption

of chemical equilibrium is largely valid when performing abundance analyses within this range.

- The largest average deviations are seen in CN and C_2 which are also the least abundant molecular species considered here. This is due to the structure of the chemical network, which has many formation pathways towards CO, the most stable molecule. As the other molecular species are generally formed along the path to CO, they are naturally less abundant since the majority of potential carbon is locked into the CO molecule at these cool temperatures.
- Molecular formation generally traces the reversed granulation pattern, though CH and CN are more abundant in the time-dependent case while CO is depleted. This effect is due to the long chemical timescales that model the species exchange of CH and CN to form CO, which are not reached in the time-dependent case. As such, chemical equilibrium will overestimate the abundance of CH and CN while underestimating the abundance of CO. However, this effect is only seen clearly past the spectroscopically accessible region (above $\log \tau = -4$) and is therefore unlikely to contribute significantly to abundance analyses.
- We present an analysis of various chemical timescales including the inverse-rate, Evans and inverse-Jacobian timescales. The inverse-rate timescale, despite being the simplest, yields the most plausible result when computed near chemical equilibrium. We filter the reactions to use only those that give significant contribution to the formation or destruction of the species CO, CH, CN, OH and C_2 .
- The Damköhler number `Da` can be used to find regions wher chemistry is likely to be out of equilibrium. Da considers a ratio between the hydrodynamical mixing and chemical timescales, and therefore provides a simple evaluation to check if molecular chemistry is significantly affected by hydrodynamical effects. The Da analysis generally predicts trends where chemistry is out of equilibrium correctly, under the assumption that chemical timescales are significantly slower than hydrodynamical timescales in these regimes.

Part III

MACHINE LEARNING METHODS

So far, we have explored conventional modelling techniques for analysing stellar atmospheres. In this penultimate part, the focus is on machine learning (ML) techniques. Chap. 5 explores the problems encountered during spectroscopic analysis (such as line blends) seen throughout Chap. 2, and describes ML techniques designed to remedy them. Chap. 6 considers the time-consuming problem of solving stiff chemical ODE systems to their equilibrium point (encountered in Chaps. 3 & 4) and introduces novel neural network techniques to address it.

The use of ML techniques has increased drastically in recent years, and this increase also applies to fields within astrophysics. While there is a large focus on the improvement of data reduction and analysis for large surveys, there have similarly been developments in astrophysical modelling. The main ideas throughout the following chapters seek to further develop ML techniques that complement conventional ones. Both the chapters presented in this section introduce many operational defintions that are common in machine learning, but may have slightly different meanings when used in an astrophysical context. For convenience, many of the operational definitions are given below in alphabetical order:

- **Activation function**: a function that collects the outputs of a layer and combines them into a value to be passed to the next layer. Activation functions for hidden layers are usually non-linear to enable the neural network to learn non-linear behaviour, while the activation function of the output layer depends on the output to be predicted, e.g., for strictly non-negative outputs, a suitable function such as the Rectified Linear Unit will be chosen.
- **Batch size (mini-batches)**: The dataset is divided into "batch size"-length samples, and one such sample is a mini-batch. The batch size is a hyperparameter chosen such that training converges quickly while allowing for sufficient robustness to be learnt.
- **Bias**: a constant added to the weights vector in a layer, often denoted as b, with the full bias vector (across all layers) denoted as $\mathbf{b}$.
- **Convolutional kernel**: a matrix used for convolutional operations in convolutional layers. For image processing, these kernels often take the role of blurring, sharpening, edge detection, and more.
- **Early stopping**: a method for preventing overfitting that halts the training process if a certain metric (usually validation loss) ceases to improve for a given number of training iterations.
- **Epoch**: one cycle through the entire training dataset. Neural network training often requires more than one epoch, and the number of epochs is a hyperparameter.
- **Feature**: an input to the ML algorithm, with a set of features often denoted as the vector $\mathbf{X}$.
- **Hyperparameters**: parts of the ML algorithm that are determined by the user and are not updated during the process. These include the learning rate, number of epochs, and the batch size. As the hyperparameters affect the training process, it is often necessary to optimise over the set of hyperparameters to find the best combination for a given algorithm and dataset.
- **Label**: an output from a ML algorithm, with a set of labels often denoted as the vector $\mathbf{y}$.
- **Layer**: a set of neurons that are usually not connected, but contribute to the same output. Distinctions are often made between the input layer, hidden layers, and output layers. Generally, weights are learnt in hidden layers and output layers. Each layer is followed by an activation function.
- **Learning rate**: the step size at each iteration during the optimisation process that determines how far towards a minimum to move when applying a loss function. The learning rate is a hyperparameter that can be altered during training; throughout the training process, the learning rate is often altered depending on how close the current solution is to a minimum.

- **Loss function**: a function used in ML tasks to determine how close the ML solution is to the ground truth solution.
- **L_1/L_2 norm**: distance functions corresponding to linear and squared distance, respectively. These are common loss functions.
- **Neuron**: one "node" inside a layer in a neural network. A set of neurons makes up a layer, and each neuron has a weight that it is often learnt.
- **Optimiser**: the optimisation method used to reach a satisfactory solution, such as gradient descent. The choice of optimiser depends on the kind of ML task, and it is a hyperparameter that is often a function of other hyperparameters, such as the learning rate.
- **Parameters**: parts of the ML algorithm that are usually updated during the training process. For neural networks, these are the weights and biases of the layers.
- **Regularisation**: a process that removes needless complexity from the network, reducing the likelihood of overfitting. Regularisation is an umbrella term and many methods fall under it. Applying constraints is an example of explicit regularisation, while early stopping is an example of implicit regularisation.
- **Training/validation/testing datasets**: the three commonly used splits from the entire dataset. The training dataset contains data that the ML algorithm is trained on (used to update parameters); the validation dataset contains data used to compute validation metrics at the end of each epoch; the testing dataset is used to evaluate the performance of the algorithm. As a general rule, the validation and testing datasets are never seen by the network, and hence represent datasets that the algorithm would encounter after real-world deployment.
- **Weights**: the vector of learnt quantities from a layer of neurons, often denoted as the vector $\mathbf{w}$, and the full matrix of weights is often denoted as the matrix $\mathbf{W}$.

5

SPECTROSCOPIC APPLICATIONS OF MACHINE LEARNING AND NEURAL NETWORK METHODS

5.1 INTRODUCTION

Fitting synthetic spectra to observations is a commonly used tool in stellar spectroscopy (Amarsi and Asplund, 2017; Asplund et al., 2009; Caffau et al., 2015). The technique involves computing synthetic spectral lines from a model atmosphere (such as Freytag et al. (2012), Gudiksen et al. (2011), Gustafsson et al. (2008), and Magic et al. (2013)) which often involves physically motivated radiative transfer calculations (Leenaarts and Carlsson, 2009). These synthetic line profiles are then fit to observations in order to determine quantities such as elemental abundances. The choice of observations varies for different sources; we primarily consider stellar sources, and within that subset, we focus on the Sun. In particular, we use the data from Neckel and Labs (1984) (hereafter the Hamburg atlas) for our fitting routine.

However, regardless of their astrophysical source, observations contain noise. This can make some data unusable, but it is often possible to take this into account statistically, and fit the spectrum regardless. A larger issue in spectroscopy comes from the presence of line blends. These are obscuring lines that mask the line of interest (e.g. neutral hydrogen lines in galactic observations or magnesium absorption lines in stellar atmospheres), with an example of such a blend obscuring a solar silicon line shown in Fig. 73.

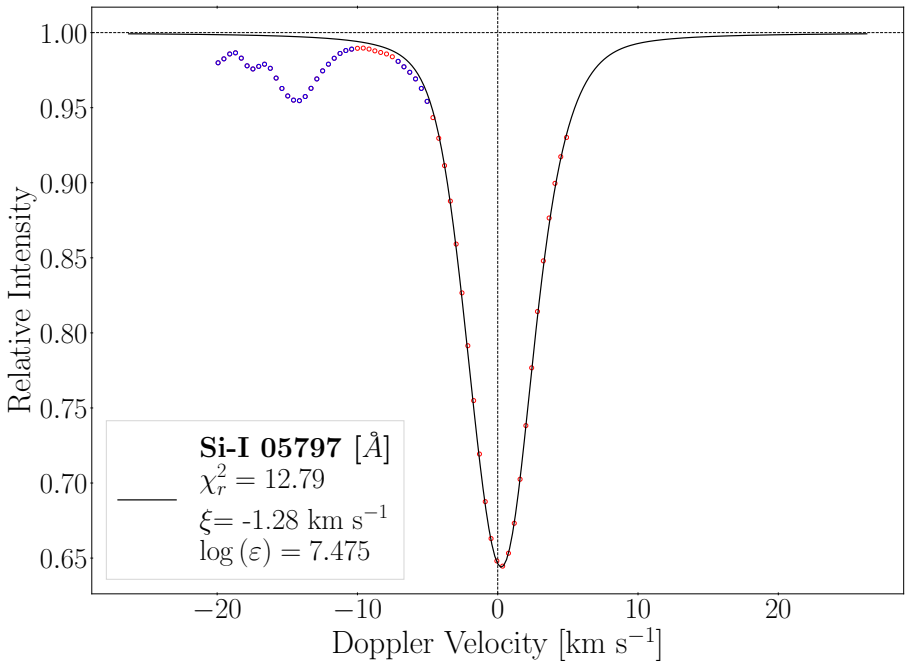

Figure 73: A synthesised fitted line profile (black line) against the observations from the Hamburg atlas (red and blue points). Strong blends have been removed from the line on the right hand side. The blue points signify weak blends, and are not used for the final fit.

In order to fit the observed silicon line profile, strong blends are masked from the observations. This involves visually assessing each spectral line and choosing the window to use for line profile fitting. One then has to make certain that small changes of the window size do not drastically alter the fitted parameters; or if they do, that it is indeed due to the presence of these blends, and the large changes are not representative of the primary line profile in question.

The line profile shown in Figure 73 shows a single, isolated spectral line with a window carefully chosen to allow for accurate fitting. It is often however the case that one wishes to use larger parts of a spectrum, especially in the case of distant astronomical objects. Such a spectrum is shown in Figure 74.

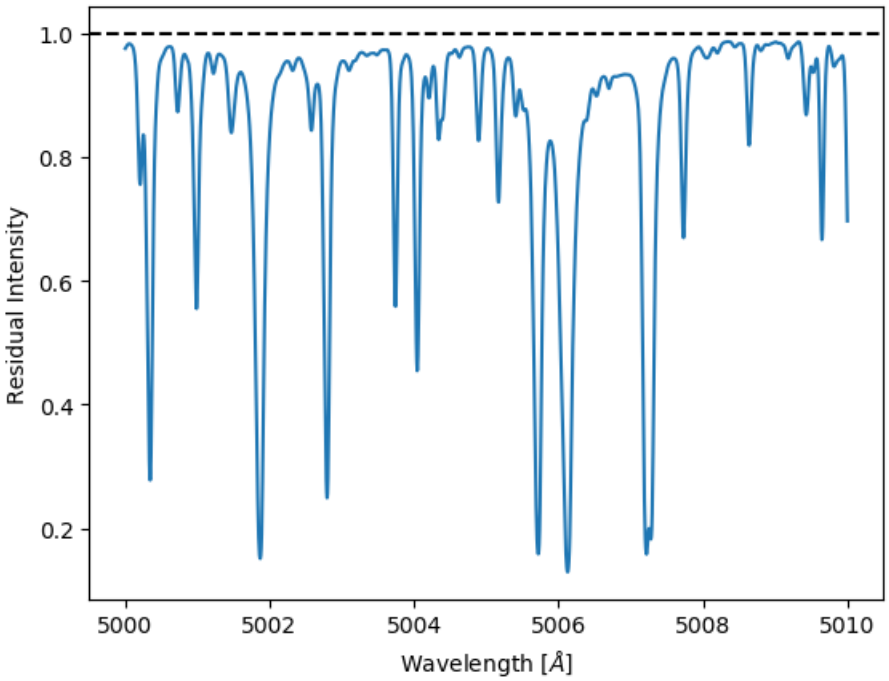

Figure 74: Hamburg atlas intensities from $5000 - 5010$ Å.

Here, then, simply isolating line profiles and masking blends by hand is a very tedious task. Though the principle remains the same, there are now many more lines to consider and the process is much more complicated as a result. In fact, it is not immediately clear which lines should be removed in such a spectrum, as works often use such data to determine multiple elemental abundances (Holweger, 2001). Instrumental defects and mistakes can also lead to spikes in the data which may also obscure crucial data points.

Work has been done to reproduce synthetic spectra using machine learning techniques (Ho et al., 2016; Ting et al., 2019) which encompass the spectral fitting to determine parameter estimates for astrophysical quantities. Though they do not necessarily directly use the observations, they are trained with observed spectra, and so any issues can permeate through, leading to higher errors and incorrect predictions.

With all this in mind, there is definitely motivation to improve the quality of observations for spectral line fitting by implementing methods that handle root-mean-squared (RMS) fluctuations (noise) and line blends. This was primarily motivated by the problems encountered in Chap. 2, where strong and weak blends made many lines inaccessible for spectroscopic analysis. Ideally, we would like to use as many clean spectral lines as possible for abundance analysis in order to increase the precision of the final fitted abundance value. Three distinct methods are presented to improve the quality of the data here: Section 5.2 details fitting Gaussian line shapes to fit residuals, Section 5.3 discusses the use of Autonomous Gaussian Decomposition to acquire the Gaussian components in a spectrum, and Section 5.4 investigates the use of an autoencoder neural network to denoise spectra and extract the main features of a spectral line profile.

5.2 Gaussian line shape fitting

An initial approach to fitting line blends was to consider the blends to be Gaussian line shapes and to fit these accordingly. Initially, attempts were made to fit Gaussian line profiles to the spectral lines in the spectral fitting routine itself. However, the issue with this method is the fitting routine has no way of knowing which of the fitting parameters it should prioritise, and

often the physical parameters such as elemental abundance were compromised. In addition, when performing this simultaneous fitting, the number of Gaussians and the initial parameters for each Gaussian must be supplied. In fact, the initial parameters needed to be supplied so close to the actual optimum parameters that one was perhaps better off manually adding the Gaussians to each blend. Indeed, the results of this simultaneous fitting were not significantly better than simply removing the areas of the spectrum where line blends existed.

Instead, Gaussian profiles were fit to the residuals from the original fitting routine. Here, the fitting routine was run normally, but with very wide windows (in a few cases, the windows were still truncated as larger blends can badly skew the fitting routine), and the residuals were used to identify blends. As the fitting routine employs sigma-clipping and hence ignores poorly-fitting points, the line blends stand out. However, there is also a small amount of scatter (not unlike noise in a signal) since the fit will not be perfect. The sigma-clipping can also introduce discontinuities in the residuals. Figure 75 shows one such line profile's residuals after an initial run of the fitting routine.

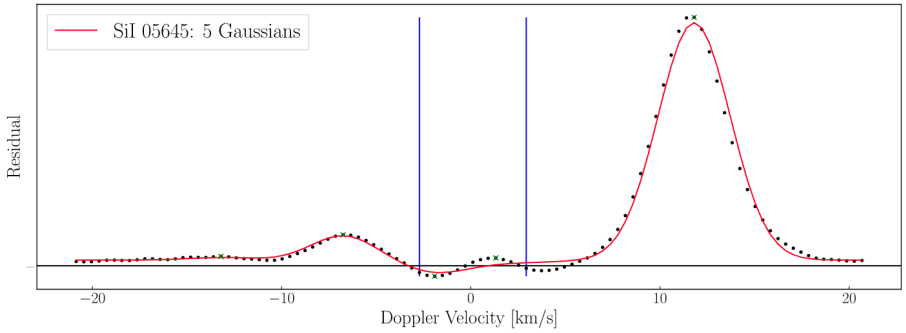

Figure 75: Residuals of spectral fitting routine for a single line.

The line blends in the residuals appear as Gaussian-like line shapes. Initially, Gaussians were fit to these by manually specifying the number of Gaussian components and the initial parameter guesses for them (i.e., initial values for the amplitude, position and width of each Gaussian). When this was seen to work in practice, steps were taken to automate this process. To do this, a peak-finding algorithm was applied to the spectrum in order to detect the Gaussian line shapes. However, it became necessary to determine a signal-to-noise threshold below which a peak should not be detected, as well as a peak prominence threshold. The prominence of a peak is its relative height compared to other peaks, rather than its absolute height above the baseline, and is detailed in Figure 76.

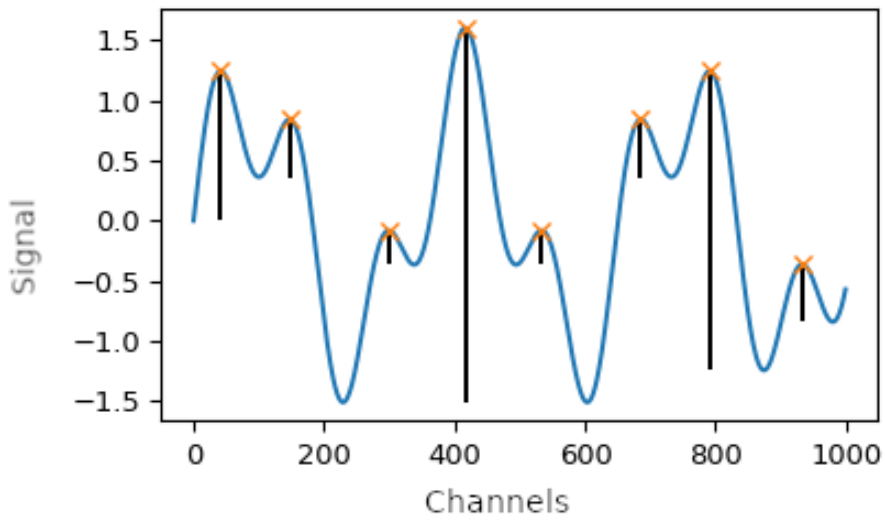

Figure 76: Prominence of peaks.

This takes into account that blended lines are close to one another, and so the relative intensity does not reach the baseline in between the blended line profiles. Specifying the peak prominence and the signal-to-noise threshold for peaks is sufficient to find Gaussian components in the spectrum. In its current implementation, the user chooses the n most prominent peaks in the spectrum to be fitted with Gaussian components, with $n \in \mathbb{Z}^+$.

The fitting routine works on a spectrum-by-spectrum basis, meaning the value of n can vary between datasets. The reasoning behind this choice is that for single-line observations, as in Figure 77, it is often very useful to visually identify the number of Gaussian components in the spectrum first to prevent overfitting. By default, $n = 5$ for the dataset we are using (Neckel and Labs, 1984) since this value was found to work well for all lines.

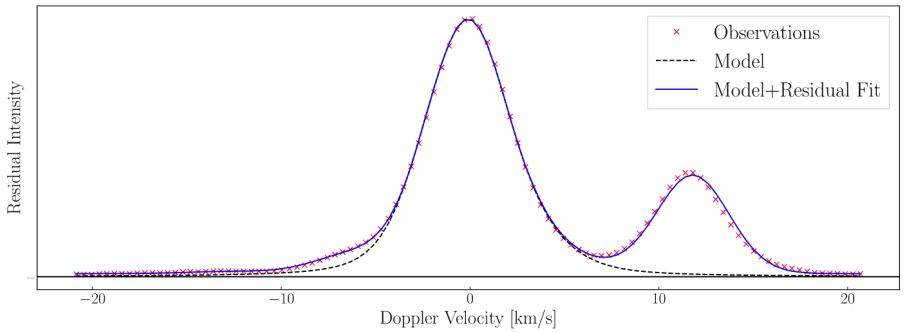

Figure 77: Single line profile with blends.

Once the Gaussian components have been identified and fitted, they are added to the original fitted model (or subtracted from the original observations, depending on user preference) and plotted for comparison. In this way, the independently fitted Gaussian components correctly contribute to the overall spectrum and are on the same scale. The user can also choose to ignore the line core, and though a Gaussian component is still fitted, it is not added as a contribution in the final model. A few examples are shown in Figures 78-80, showing varying degrees of success depending on the data. The core is ignored between $-3 - 3$ km s^{-1} in each.

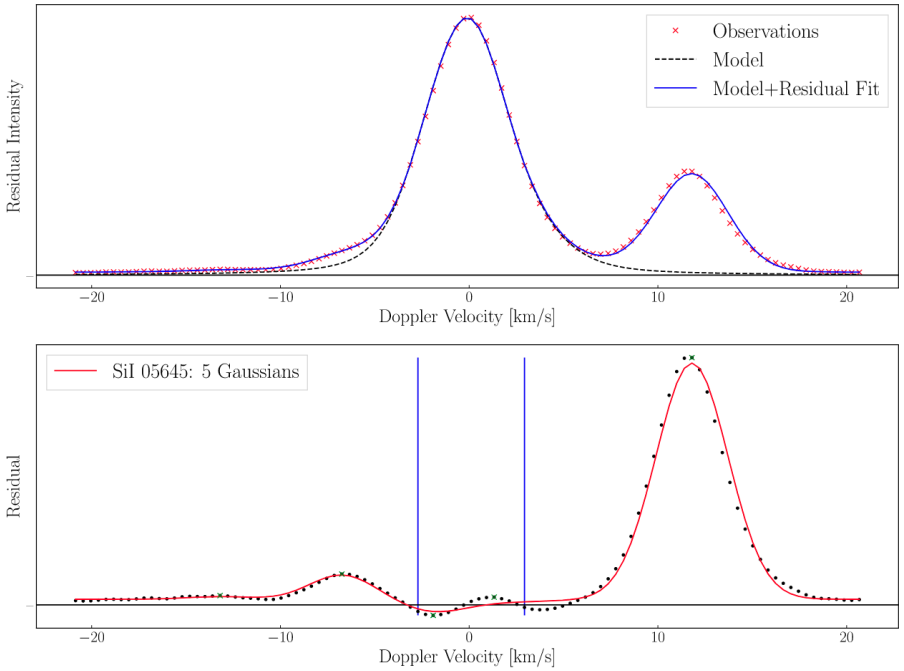

Figure 78: Single optical line profile with blends.

In Figure 78, the peak-finding algorithm and Gaussian fitting routine works well, adding the fitted components to the residuals. It correctly identifies the Gaussian components, though

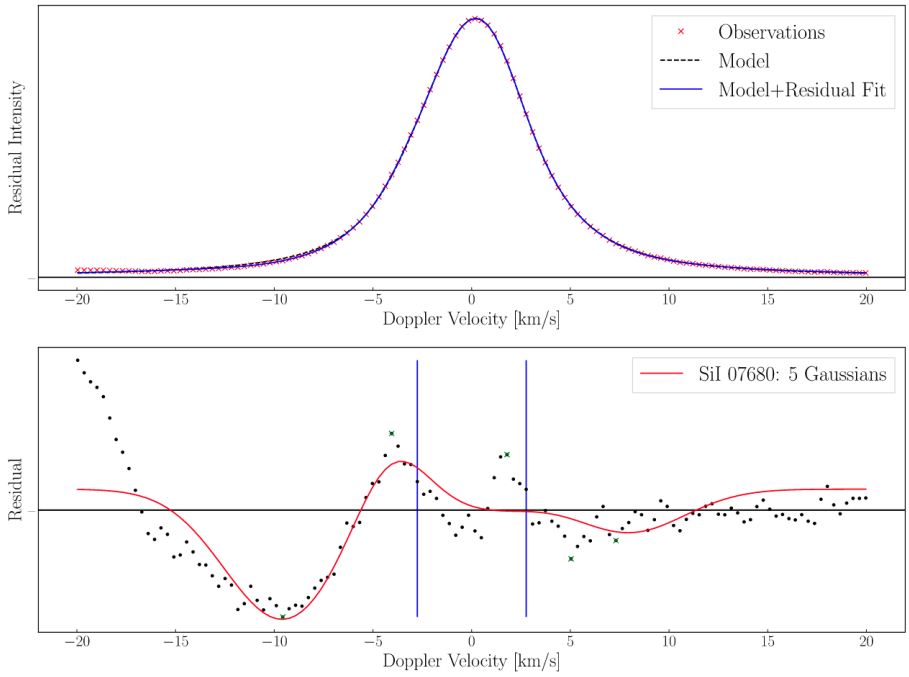

Figure 79: Single optical line profile without strong blends.

they are perhaps shifted. This could be due to the discreteness of the x-axis, though, since the true centre of the Gaussian is likely slightly to the left of the detected peak. Figure 79 shows a seemingly large scatter, but this is actually a very well-behaved line in that the residuals are very small. Here, though, the routine still fits Gaussians as the combination of peak prominences with a signal-to-noise threshold is not sufficient to completely ignore the scatter.

Figure 80 shows the reasoning behind ignoring line cores. In a few lines from our sample (primarily infrared lines), the line cores demonstrate departures from local thermodynamic equilibrium (LTE), meaning they are deeper. As our synthetic lines assume LTE, we are unable to fit the non-LTE (NLTE) part of the line. Since this is a physical process that should be properly modelled rather than simply fitted based on residuals, we opt to mask the line core such that these effects are not fitted for with Gaussian components. Unfortunately, this does lead to discontinuities appearing in the final fitted model. Here, the discontinuity is only present on the positive side of the line due to a combination of the x-axis discretisation's effect on the peak-finding algorithm as well as an inherent shift present in the line centre.

Figure 80 also shows an edge effect resulting from an older artefact in the spectral fitting routine. Though the artefact is no longer present in the current version, it was enlightening to find that the Gaussian fitting routine does not try to fit this as a peak, meaning it correctly identifies spikes in the data as a form of noise.

5.2.1 *Quality Control Options*

The user has a few options to control the process. As stated above, the number of prominent peaks to fit for (n) can be specified beforehand, and this is often used to prevent overfitting. Since the peak-finding algorithm does not know anything about the scale of the dataset, this is quite an important parameter to specify. When using this Gaussian fitting routine for our single-line measurements of solar absorption spectra, $n = 5$ is a value that works well for every line. It does allow for different scales of residuals to be fit, but this is simply due to the peak-finding algorithm's capabilities, not through any scale parameters present in the Gaussian fitting routine. Due to the signal-to-noise threshold in place, the peak-finding algorithm does not detect every instance of negative curvature as a peak, and many smaller bumps are indeed ignored. Ideally, the value of n should not be much lower than the number of peaks the algorithm will find naturally. But, n is also used for regularisation so that if this is the case, there will still be a reasonable amount of Gaussian components.

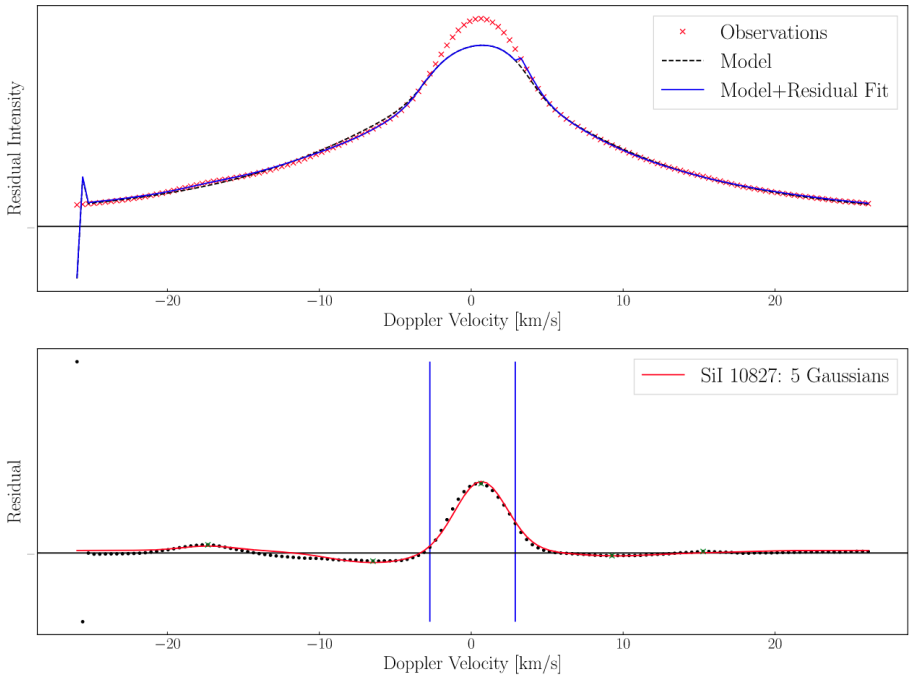

Figure 80: Single infrared line profile with strong NLTE line core.

Due to the nature of fitting residuals, it was also necessary to let the amplitude of the Gaussian be negative. This is required when the model overestimates the observations and a negative correction is needed. However, if the user adds the Gaussian fit contributions to the observations rather than the model, the fit components are not allowed to take the fitted model below the observations. This is simply because the purpose of this routine is to detect line blends, and removing information about the observations does not lend itself to that task. Additionally, though the routine is capable of adding the Gaussian fit components to the observations, using those new data as new observations in our spectral fitting routine did not result in a better result, suggesting that there are minute precision differences that become apparent only when fitting synthetic spectra to the new observations.

To ensure the fits are of a good quality, the user should tweak options regarding the number of peak prominences n as well as the choice of line profile function. Though originally intended to be used with Gaussian line profiles, the fitting routine can be changed to use any single-peaked line profile function, such as a Lorentzian or Voigt profile. However, the success of convergence in these cases has not been rigorously tested, as using purely Gaussian line shapes offered a sufficient analysis in our case.

5.2.2 *Limitations and Possible Improvements*

There are a few limitations of the described procedure, and quite a few possible improvements. Firstly, there is no way to specify the length scales present in the data aside from tweaking the number of prominent peaks n, which in turn actually depends on a peak threshold value. A more elegant way of formulating the problem would remove this degeneracy and characterise this as a length scale parameter to be specified by the user. However, this does remove some intuition from the fitting routine. Currently, the "number of Gaussians to fit" is a simple quantity to envision from a dataset, whereas a "length scale parameter for peak prominence" is rather less so. Nevertheless, in the idea of specifying a length scale, it would be useful for the user to be able to specify multiple length scales to describe smaller and larger peaks in the dataset. This would further help in reducing noise being detected as a peak while still allowing for small line blends to be fit. At the moment, all of this nuance is singly controlled by the parameter n.

Figure 80 showed a dataset with edge effects present. Though these were not fit for, it does bring to light the potential of such edge effects negatively affecting fit performance. Here, we are again trusting the peak-finding algorithm to correctly determine peak prominences.

There is currently no implementation to re-fit Gaussian components (or the entire model) if the comparison is poor. Originally, this was because the data we use for this analysis are residuals themselves, and we did not want to alter these to the point where we could not use the result as a physical analysis. An improvement that would also add regularisation would be to check the distance between peaks and compare that to the widths of the said peaks. It is perhaps possible to reduce the number of Gaussian components present in the model this way while also improving the statistical fit. In this sense, both the individual fit components and the resulting model should be re-fit to ensure that the improvement of one does not lead to the detriment of the other.

Finally, the most important improvement would be to extract physical understanding of the line blends from the fit Gaussian components. Each one has a specified width and height, but these do not necessarily correspond to physical quantities such as broadening (due to macroscopic velocity flows in a stellar atmosphere, affecting the width) or an elemental abundance (which would affect the amplitude). Unfortunately, this drawback means this particular method is not well suited for our particular task of removing line blends from stellar spectra, since we cannot be sure that the method does not also remove vital information about the primary line profile. The described procedure is still a useful tool to analyse spectra, though, and shows that the blended line components are indeed present in the residuals as Gaussian line shapes.

5.3 AUTONOMOUS GAUSSIAN DECOMPOSITION

Removing blended lines and noise is a difficult task and often done by hand. It is, however, possible to use Autonomous Gaussian Decomposition (AGD) to decompose a spectrum into its Gaussian components. Unlike other methods, one does not have to specify the number of Gaussians beforehand, and the method is also flexible enough to handle lines of different prominences in the spectrum. AGD combines derivative spectroscopy with machine learning in order to provide optimised guesses for the locations, widths and amplitudes of the Gaussian components in the signal (Lindner et al., 2015).

AGD has been tested in an astronomical context, namely on 21 cm absorption spectra from the 21 cm SPectral line Observations of Neutral Gas with the EVLA (21-SPONGE) survey (Lindner et al., 2015). Here, the method produces results comparable to human-derived solutions. AGD was used in conjunction with Monte Carlo methods to derive the H I line completeness as a function of peak optical depth and velocity width for the observations. The authors also who that the results of AGD are stable against observational noise intensity, meaning the method generalises well to observations with higher or lower signal-to-noise ratios as well. Lindner et al. (2015) have released their algorithm as a Python package GaussPy (`github/gausspy?`).

Riener et al. (2019) recently released GaussPy+ (), which builds upon GaussPy specifically for emission spectra. They use this package to study detailed velocity structure of emission line observations. In particular, they focus on a test field from the Galactic Ring Survey. Indeed, though the GaussPy package works very well on isolated line profiles and smaller spectra, the lack of full automation for training the algorithm means it does not scale well to large scale surveys. GaussPy+ handles this by fully automating creation of the training set for the algorithm adding preprocessing steps, and building in quality control and spatial coherence measures for the fit results. The final point involves adding spatial coherence to the decomposition results by refitting based on neighbouring solutions; a point that becomes increasingly important with spectra where neighbouring lines are often not independent. GaussPy+ is able to handle cases of complex emission and low signal-to-noise values.

Both GaussPy and GaussPy+ are extremely efficient, especially when compared to manual masking blends in line profiles. They also significantly improve upon noise estimates and are able to use quality control measures to ensure the algorithm is not overfitting the number of Gaussian components and also that the errors are statistically accurate when spatial coherence is taken into account.

In essence, AGD approaches Gaussian decomposition through least-squares minimisation and focuses on automating the choice of parameters' initial guesses. Accurately performing this

allows the fit to quickly converge to a global optimum. For an example spectrum, let x be the frequency grid of flux density values $f(x)$. The algorithm then aims to decompose the spectrum into Gaussian components, where the Gaussian function G is given by

$$G(x; a, \mu, \sigma) = ae^{(x-\mu)^2/2\sigma^2} \tag{130}$$

where a, μ, σ represent the amplitude, position and width (standard deviation) of the Gaussian function. Note that, even with the empirical assumption of a Gaussian profile for the final least-squares fit, the initial guesses are only weakly dependent on the specific Gaussian shape. In fact, AGD can be used to provide reasonable initial guesses for the amplitude, position and width of any well-behaved single-peaked profile, such as Lorentzian or Voigt profiles. This generalisation is important in regards to stellar spectroscopy, where the spectral line profiles often show a resultant Voigt profile due to a combination of Doppler broadening (Gaussian) and pressure broadening in the line wings (Lorentzian). However, this is more of a limitation in GaussPy+.

AGD initially smooths the spectrum to remove noise and to better identify individual components. This smoothing is controlled by a parameter α. A preliminary result for a single Gaussian is shown in Figure 81 and the effect of the smoothing parameter α for multiple Gaussian components is shown in Figure 82.

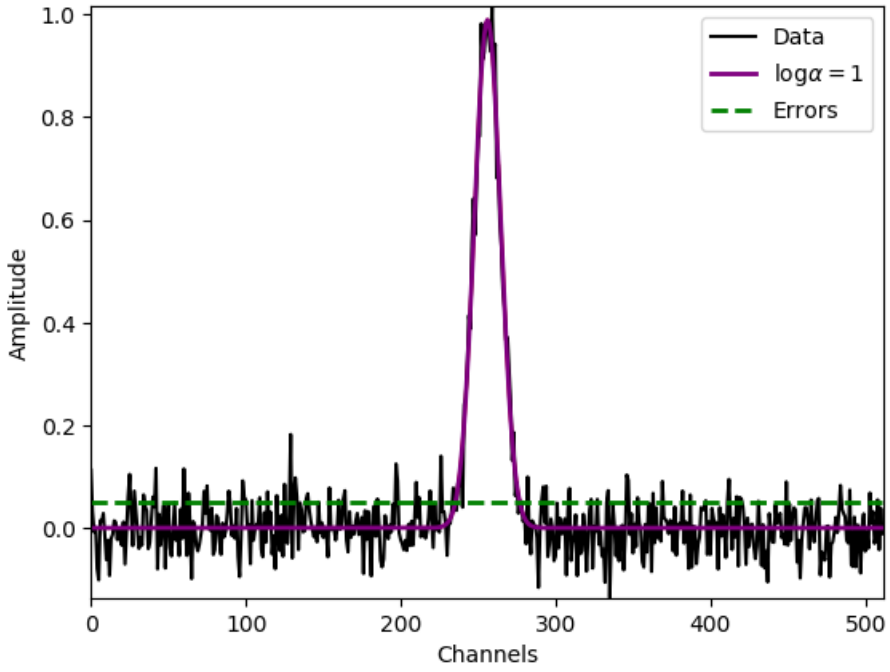

Figure 81: A single Gaussian component identified by AGD. The black line shows the data, the purple line shows the final fitted model, and the green dashed lines are the errors.

5.3.1 *Optimising the Smoothing Parameter through Supervised Machine Learning*

Though one can tune the regularisation parameter α manually, it is much more efficient to train the AGD algorithm using supervised machine learning techniques to optimise it. In supervised machine learning, a collection of input/output pairs known as a training set is provided to the algorithm in order for it to learn a general rule for mapping inputs to outputs. Here, it is used to train AGD to optimise the value of α such that the accuracy of component guesses on a training set of spectra is maximised.

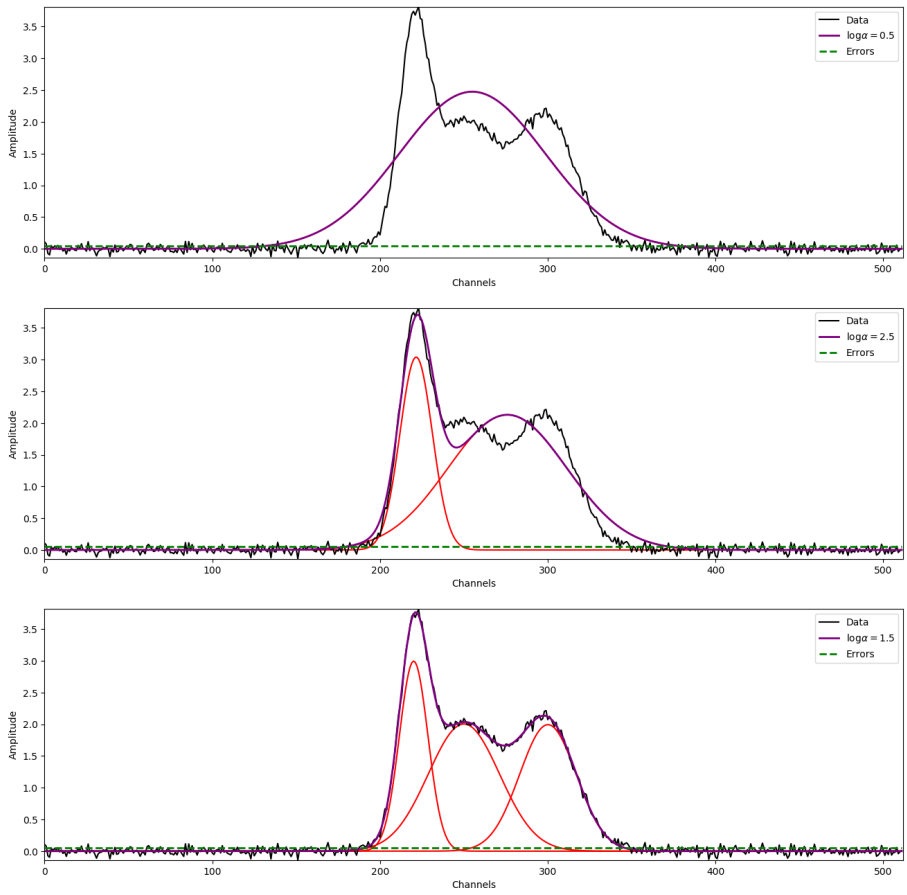

Figure 82: Multiple Gaussian components decomposed with different values of α. The black lines show the original data, the purple lines show final fitted model, and the green dashed lines give the errors. The red lines plot the individual Gaussian components. In this example, the three components are only found with a smoothing parameter $\log \alpha = 1.5$, as the other values both underestimate the number of Gaussian components present in the dataset.

5.3.1.1 *Creating a Training Dataset*

Supervised machine learning techniques require training datasets to learn input-output mappings using nonlinear functions. A training set is a collection of data where the underlying properties the machine learning algorithm is fitting for are already known. In this case, a training set can be constructed with data for which the underlying Gaussian decomposition is already known, i.e. the number of Gaussian components and their centres, heights and widths of each are known. The training set can contain real Gaussian samples or synthetically constructed ones, so long as the underlying decomposition is known. This prior information is used to maximise the accuracy of the AGD algorithm by optimising the regularisation parameter α.

Creating a synthetic training dataset is very straightforward. Firstly, one should specify the number of training spectra to create. Then, it is best to randomise the number of Gaussian components in a reasonable range based on the number of channels for each training spectrum (i.e. the length of the x-axis). For each Gaussian component, the amplitude, position and width (specifically the full-width at half-maximum (FWHM)) should be randomised in given ranges. We choose these three parameters since they are the same parameters that will be fit by the AGD algorithm. The goal is to produce a versatile and varied dataset that also reflects the state of the actual data one wants to use. Taking the example of 21-SPONGE data, the training dataset should resemble the style of emission spectra seen in those observations. Randomising the Gaussian components ensures that the trained model will also generalise well, at least within

the randomisation boundaries. These boundaries, then, should also reflect the state of the data. Representative RMS noise should be added to each spectrum as well.

The number of training spectra will affect the accuracy and precision of the optimisation for α. In general, a high number of varied training spectra will result in better optimisation, as the model will generalise to many different potential spectra. However, using too many training spectra without proper validation can result in the model overfitting. The number of training instances to use depends on the machine learning problem at hand, but in general, more training instances will result in faster and better convergence.

Though the methods described above work well for creating training data, real data may still be rather different. For example, many spikes of noise could make a certain spectrum unusable if the AGD algorithm cannot suitably smooth it, or a Gaussian component may be located past the edge of the spectrum, but its tail could affect the signal in the observed spectrum. In these cases, it may be useful to provide a few training instances where these previously unforseen effects are taken into account. This will allow the algorithm to generalise further, resulting in a more optimal value of α.

5.3.1.2 *Training the Algorithm*

GaussPy naturally incorporates methods to train the algorithm on a training dataset. The idea behind training the algorithm is to apply GaussPy to the training dataset and compare the results with the known underlying Gaussian decomposition. From this, the optimal value of the regularisation parameter α can be found. Within GaussPy, an initial estimate for α as well as a signal-to-noise threshold below which components should not be fit need to be provided. The signal-to-noise threshold is simply the RMS noise present in the training dataset, and since this can often also be measured for observations, it should be provided as accurately as possible. The initial choice for α can heavily influence the optimal value (depending, of course, on the complexity of the data), and so this should also be an accurate estimate.

From Figure 82, it is seen that slight deviations can cause mismatches in the number of detected components, but the training algorithm is often versatile enough to handle this. So, for example, if the correct value was $\log \alpha = 1.45$ for a given set of spectra, an initial choice of $\log \alpha = 1.0$ would be sufficient to have the algorithm converge. As always, more accurate initial guesses will result in faster and better convergence, though. Because of this potential uncertainty in the best possible convergence, it is useful to rerun the training algorithm with multiple initial choices for α.

The training process is iterative, starting with the initial choice of α and changing this while comparing the GaussPy decomposition with the known decomposition. The accuracy of the algorithm is associated with how well it recovers the true underlying composition. Note that while accuracy could be high, the accuracy on the actual data is often lower. To know whether or not the algorithm is overfitting, a validation dataset can be used to assess model performance. The validation dataset is simply a subsample of the training dataset (e.g. the last 20%) that is used at the end of each training iteration to gauge the model's performance on data it has not trained on. While the model updates the value of α after new training instances, it does not update that value after validation instances, meaning the validation accuracy is a better indicator on how the model will perform on new data. If validation accuracy remains stagnant while model accuracy increases, the model is likely overfitting and will therefore not generalise well to new instances.

5.3.1.3 *Performance After Training*

The algorithm was trained using a synthetic training dataset of 200 instances, with each spectrum containing three Gaussian components with reasonably randomised amplitudes, widths and centres. This was to replicate the data seen in Figure 82. A small amount of RMS noise was added, equivalent to the RMS noise present in the actual data. Using an initial value of $\log \alpha = 1$, the algorithm converged to $\log \alpha = 0.77$.

5.3.2 *Two-Phase Regularisation*

So far, α has been used as a regularisation parameter for the AGD algorithm. GaussPy extends the AGD algorithm to search for Gaussian components at multiple different scales in the dataset (Lindner et al., 2015). While α is used to smooth the derivatives in the so-called "one-phase" mode, GaussPy offers a "two-phase" mode where the parameters α_1 and α_2 can be specified. It is then possible to train the algorithm with the aforementioned supervised machine learning approach to determine the optimal values of α_1 and α_2. Generally, the $\log \alpha$ values between one- and two-phase decompositions follow the trend $\log \alpha_1^{\text{twophase}} < \log \alpha^{\text{onephase}} < \log \alpha_2^{\text{twophase}}$.

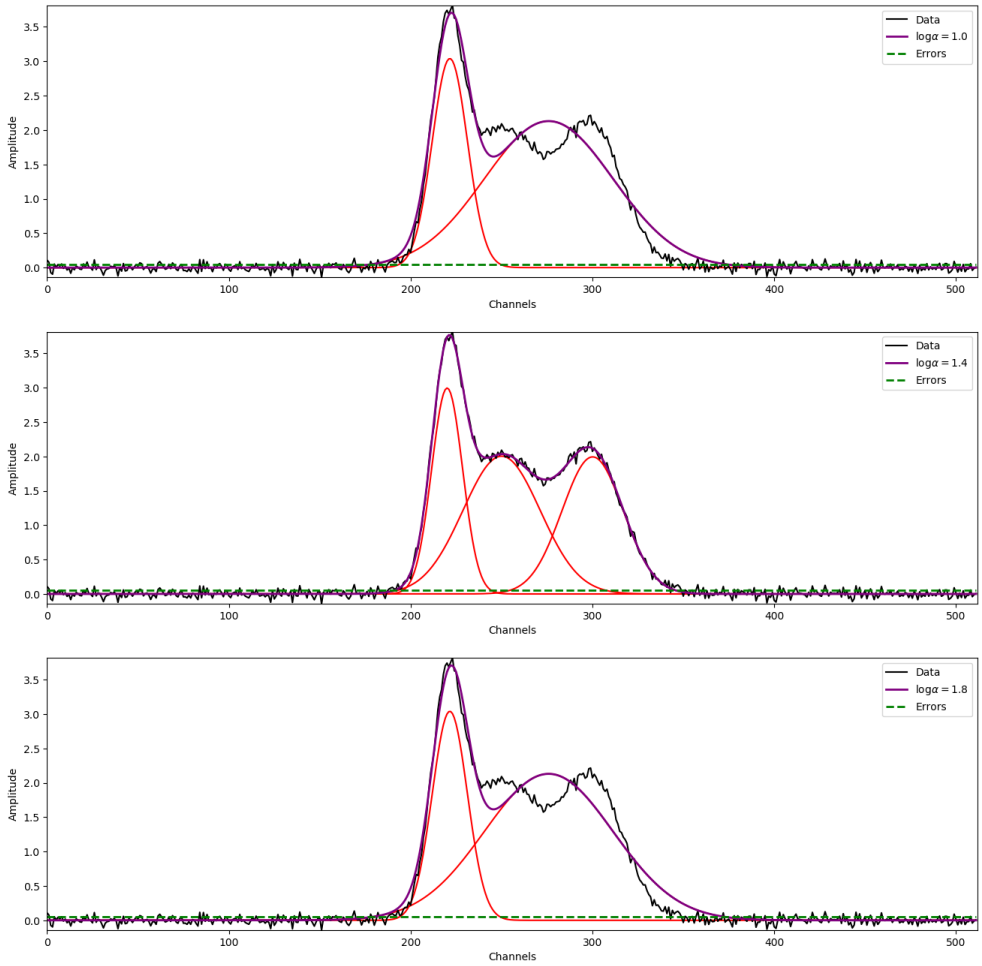

Figure 83: Multiple Gaussian components decomposed with different values of α. The black lines show the original data, the purple lines show final fitted model, and the green dashed lines give the errors. The red lines plot the individual Gaussian components. The three components are only found with the choice $\log \alpha = 1.4$.

The reasoning behind the two-phase approach is to separate narrow and broad components present in the spectrum. When using a single α value for regularisation, it must be tuned extremely carefully to avoid smoothing away narrow components. This can be seen in Figure 83, where small deviations in α result in Gaussian components being ignored by the AGD algorithm. Here, then, it would be useful to incorporate separate smoothing parameters for narrow and broad Gaussian components. This can also be done by training the algorithm on a training dataset. In fact, the same training dataset can be used, though it is perhaps better to include training data that include both narrow and broad components (and in the same spectrum). Now, initial estimates for both α_1 and α_2 must be provided, with the same caveats as discussed previously. The training routine is exactly the same, but GaussPy will now optimise both regularisation parameters.

In general, two-phase decomposition will improve the accuracy of the algorithm since it is introducing another free parameter. However, this could also lead to overfitting, and the training algorithm should be monitored for this. One should also justify whether the use of two-phase decomposition significantly improves the accuracy and quality of the decomposition compared to one-phase decomposition. In the above examples, both one- and two-phase decompositions successfully reproduce the spectrum. The choice between one- and two-phase decomposition is also affected by the data. If the data contain signals from multiple types of components (such as different physical sources) two-phase decomposition is likely to perform significantly better.

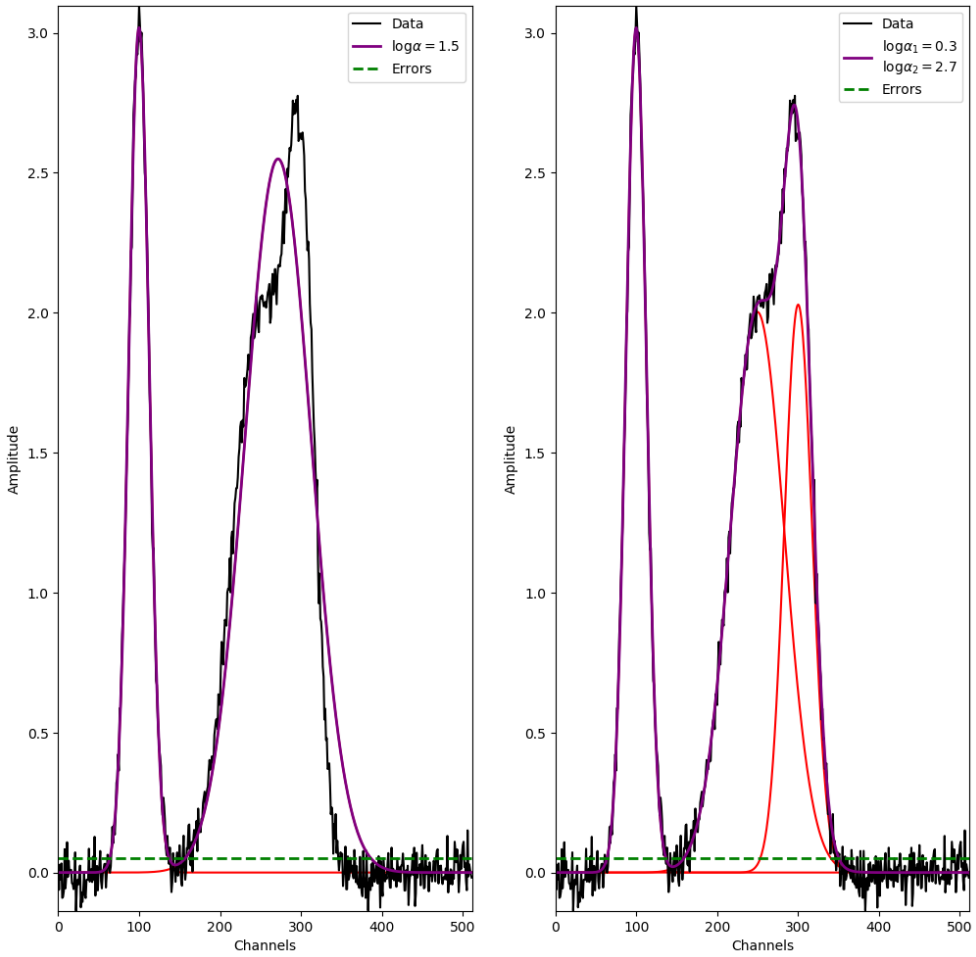

Figure 84: Spectra decomposed with best-fitting values in one-phase decomposition (left panel) and two-phase decomposition (right panel). The black lines show the original data, the purple lines show final fitted model, and the green dashed lines give the errors. The red lines plot the individual Gaussian components. One-phase decomposition is unable to retrieve the correct number of Gaussian components.

Figure 84 directly compares one- and two-phase decomposition for a dataset containing narrow and broad Gaussian components. Here, the combination of narrow and broad Gaussian components shows the drawbacks of one-phase decomposition, which is unable to fit both types. In this case, the one-phase decomposition is tuned to fit the narrow peak, but in doing so is unable to fit the blended components that are broader; in fact it is not even able to correctly identify the three components. On the other hand, two-phase decomposition both identifies the three components and provides good estimates for the Gaussian parameters to reproduce the signal.

In real astrophysical data, it is imperative to be able to separate spikes from noise from narrow lines. For these cases, then, it is perhaps too great a risk to use a single regularisation parameter α for smoothing the derivatives of the spectrum. For observational data, Lindner et al. (2015) find that two-phase decomposition performs better than one-phase decomposition on the

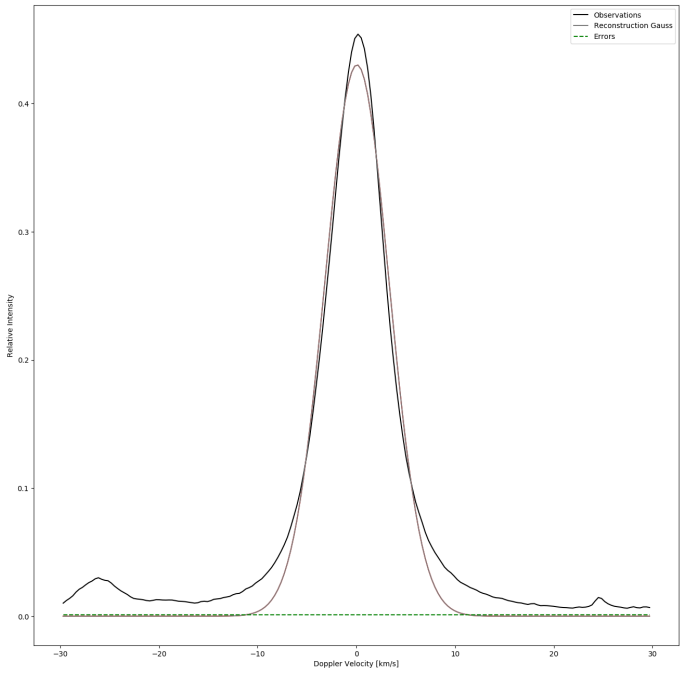

Figure 85: Silicon line at 7680 Å. The black line shows the observations, the red lines show the individual Gaussian components, the grey line shows the total reconstruction and the green dashed line shows the errors.

21-SPONGE data. Two-phase AGD resulted in lower residual errors when compared to human-decomposed spectra as well as slightly more accurate estimates of the number of Gaussian components.

5.3.3 *Performance on the Hamburg Atlas*

For the Hamburg atlas, we opt to use two-phase AGD with the parameters $\alpha_1 = 0.3$, $\alpha_2 = 2.7$. These are the parameters obtained after training the algorithm on similar blended Gaussian line profiles. Note that these estimates are not perfect since the line shapes in the Hamburg atlas are not perfect Gaussians and there are many more weak blends. We show four decomposed spectra that represent the different lines used for our determination of solar silicon abundance from the Hamburg atlas in Figures 85 - 88. These show a clean optical line, a blended optical line, a clean infrared line, and an infrared line with strong NLTE core effects, respectively.

Generally, the algorithm is able to correctly identify strong Gaussian signals and ignore scatter from noise. However, despite using two-phase AGD, it is not able to pick up on very weak blends present in the data, seen in Figure 86. Also, the decomposed Gaussians consistenly underpredict the height of the spectral line, which is determined by both the amplitude and the width. This is because the spectral line profiles are not pure Gaussians, but rather Voigt-like profiles. The difference is exceedingly clear in the decomposition of an infrared line with strong NLTE core effects, as in Figure 88, where a Gaussian is not at all able to reproduce the line shape.

In such cases, it would be useful to decompose the spectral lines with different single-peaked functions. Unfortunately, this is not currently possible with the AGD algorithm, but will be investigated in the future, along with GaussPy+. Despite these differences, though, the algorithm performs well for autonomously identifying spectral lines within a spectrum. Though very weak spectral lines are still ignored, this can be remedied through training the algorithm on a more representative dataset. Overall, AGD works extremely well for decomposing Gaussians and can additionally be used to successfully identify single-peaked functions in a dataset.

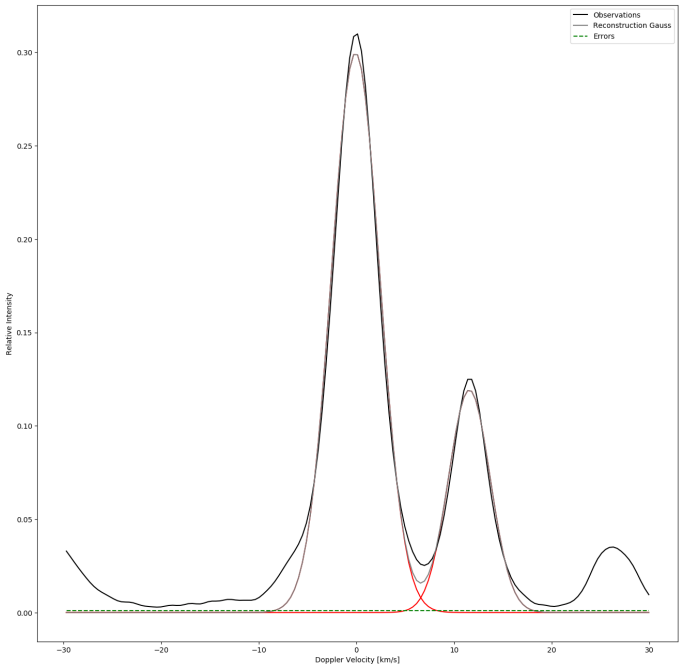

Figure 86: Silicon line at 5645 Å. The black line shows the observations, the red lines show the individual Gaussian components, the grey line shows the total reconstruction and the green dashed line shows the errors.

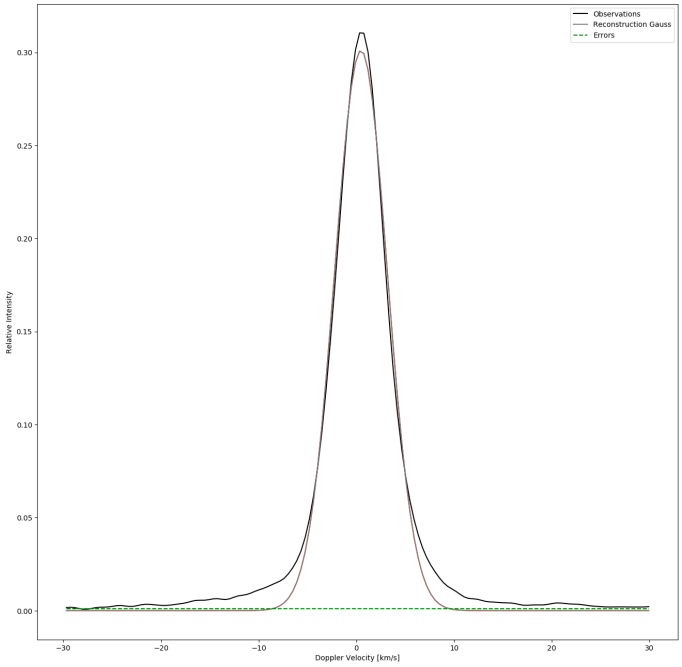

Figure 87: Silicon line at 12390 Å. The black line shows the observations, the red lines show the individual Gaussian components, the grey line shows the total reconstruction and the green dashed line shows the errors.

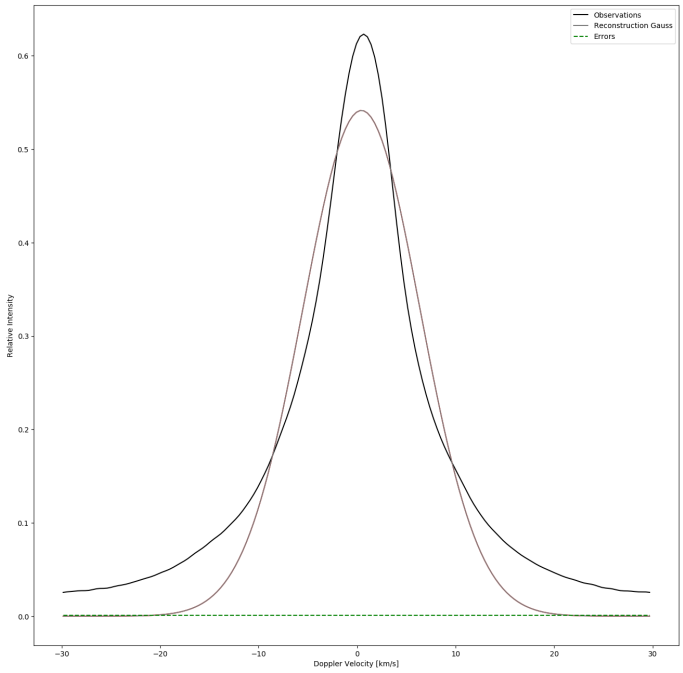

Figure 88: Silicon line at 10749 Å. The black line shows the observations, the red lines show the individual Gaussian components, the grey line shows the total reconstruction and the green dashed line shows the errors.

5.4 AUTOENCODERS FOR SPECTRAL LINE FITTING

Autoencoders are a type of neural network that attempt to reproduce the input data they are given. Suitable regularisation is required to avoid overfitting, such as constraining the number of layers and number of neurons per layer. In spectroscopy, neural networks have been shown to be successful in the past (Ho et al., 2016; Ting et al., 2019). In this study, we aim to use a neural network to extract the key features from a spectrum (namely the individual lines) and remove noise from these components. We investigated a few different machine learning methods for the task, but ultimately settled on using autoencoders.

5.4.1 *Overview of Machine Learning methods*

Many machine learning methods exist and are used for data analysis. In our present situation, we seek a method that is capable of identifying spectral line profiles and extracting the details of these. The method should also be robust against small fluctuations in the signal (i.e. noise), and be able to handle various input shapes of the data (e.g. single line profiles with blends or larger pieces of a spectrum). With this in mind, two conventional methods come to mind: Principal Component Analysis (PCA) (F.R.S, 1901) and Independent Component Analysis (ICA) (Hyvärinen, 2013). PCA is often used for dimensionality reduction (Pudil and Novovičová, 1998) and it can identify the components of a dataset that exhibit the greatest variance. ICA attempts to decompose a multivariate signal into its individual constituent components, providing the details of each. Additionally, two neural network architectures seem well suited for this task, namely autoencoders (Kramer, 1991) and Generative Adversarial Networks (GANs) (Goodfellow et al., 2014). Autoencoders simply attempt to reproduce their input data, while GANs are made up of two networks (a generative network and an adversarial network) which compete against one another. But, while PCA, ICA and GANs are useful in their own right, there are some drawbacks to each that render them fairly unusable in the current context of fitting spectral line profiles.

5.4.1.1 *Drawbacks of Principal Component Analysis (PCA)*

PCA is a dimensionality reduction technique that utilises projection (Samet, 2006). It computes principal components, which are axes of a hyperplane that retain the maximum variance. The first axis $\vec{c_1}$ is chosen such that it accounts for the largest variance in the original dataset. Further orthogonal axes $\vec{c_i}$ are then found which maximise the variance in the dataset after the previous axis has been considered. The first d components can then be used to project the n-dimensional dataset to d dimensions.

While PCA is a powerful tool with many useful additions, using maximum variance is a roundabout way of approaching the current problem. With a blended spectral line profile, it is possible that each line component can be identified as its own axis, but there is no way of specifying this to the algorithm. Kernel PCA (Schölkopf, Smola, and Müller, 1998) offers more control, but in general this method seems unpredictable when used to fit spectral line profiles. Especially in spectra with low signal-to-noise ratios, it could be that PCA falsely identifies multiple noise components as principal axes and ignores weak line blends.

5.4.1.2 *Drawbacks of Independent Component Analysis (ICA)*

ICA attempts to decompse an incoming multivariate signal into independent signals; the caveat is that these independent signals must be non-Gaussian. This is because the descriptions of independence involve **i)** minimisation of mutual information (similar to maximum variance in PCA) and **ii)** maximisation of non-Gaussianity. These conditions are tailored to find independent signals whose values do not come from Gaussian distributions. Though spectral lines are not purely Gaussian, this property of ICA renders it unusable in the current context.

5.4.1.3 *Drawbacks of Generative Adversarial Networks (GANs)*

GANs are very powerful neural networks that are often used to produce new samples based on a training dataset. They are rather more advanced in architecture than autoencoders (which will be detailed shortly) as they involve two networks which compete against one another to maximise their individual performance. Though this makes them very powerful, it is also the reason why they are notoriously difficult to train. Doing so in the present study would require a large amount of training data and the outcome may not be worth the effort in producing this training data. Additionally, the problems that GANs solve are slightly different to identifying features, and though they can be used for feature extraction, a more simplified network architecture fits the situation better.

5.4.2 *Autoencoder Architecture*

An autoencoder's architecture appeals to the problem at hand. It consists of an input and an output layer, and like most neural networks, contains hidden layers. The autoencoder is composed of an encoder, which simplifies the input information to a representation or 'code' learnt by the network, and a decoder, which takes the code and attempts to recreate the input data. From this, it is easy to see that overfitting will be an issue if the network is able to simply map every input to an output, effectively just memorising the data instead of finding patterns. To solve this, the size of hidden layers is often decreased in the encoder and increased in the decoder. An example of autoencoder architecture is shown in Figure 89.

Autoencoders with multiple hidden layers are known as stacked autoencoders and have shown to be successful in regression tasks (De et al., 2017). Multiple hidden layers allow the autoencoder to learn more complex mappings, but as always, with the risk of overfitting. Figure 89 is an example of a stacked autoencoder, and these types of networks are often symmetric about their representation.

An autoencoder whose inputs have a dimensionality of n and whose representation has a dimensionality $d < n$ is said to be undercomplete. Undercompleteness results in the autoencoder being unable to simply copy the inputs to the outputs, and must instead learn an efficient representation of the inputs to create the output reconstructions. We aim to use an autoencoder to perform feature extraction and hence make our autoencoder undercomplete.

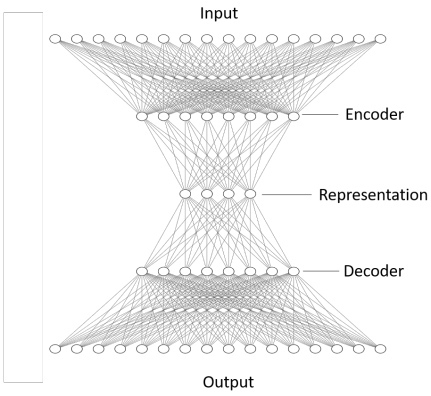

Figure 89: Autoencoder architecture.

The number of hidden layers in the encoder and decoder portions of the network and the number of neurons in each hidden layer should be tuned based on the problem. For this study, we use three layers in both the encoder and decoder portions of the network, with 224, 128 and 32 neurons in the layers. The size of the layers reflects the input data which has a size of 256 pixels.

5.4.2.1 *Hidden Layers*

We make use of convolutional layers (Valueva et al., 2020) for every hidden layer in the encoder and decoder. As the name suggests, convolutional layers perform a convolution on their input using a convolutional kernel created in the layer. Each layer can use a different kernel, but we use the same type of kernel throughout the network. Additionally, we apply a ReLU (Rectified Linear Unit (Hahnloser et al., 2000)) activation function to each layer except the output layer, which uses a sigmoid activation (Han and Moraga, 1995). The choice of activation function, as well as the precautions taken to ensure good performance for each, is detailed in Section 5.4.2.2.

Convolutional layers are used primarily in computer vision applications (Huang, 1996) and their use has met with great success. As a spectrum is essentially a measurement of correlated light intensity, we make use of convolution to identify the strength of underlying correlations as line profiles. Though our spectrum is essentially a 1D array of intensity measurements, we reshape it into a 2D array, since it is currently not possible to effectively use the 1D convolutional layers in Keras[1]. Since it often reverts to converting 1D convolutional layers into 2D ones anyways, the current network simply uses 2D convolutional layers and the input data is reshaped to reflect this: The 256 pixel 1D spectrum is transformed into a 16 x 16 2D 'image'. To consider the image analogy further, convolutional autoencoders are often used for working with images (Karimpouli and Tahmasebi, 2019). The encoder portion of the network typically reduces the spatial dimensionality of the inputs (i.e. width and height) while increasing the number of feature maps (i.e. relations between pixels). The decoder portion then performs the opposite: it upscales the image and lowers the number of feature maps to create a reconstruction of the input. By formulating our spectrum as a 2D array, we are able to utilise these natural features of convolutional autoencoders.

1 https://keras.io/

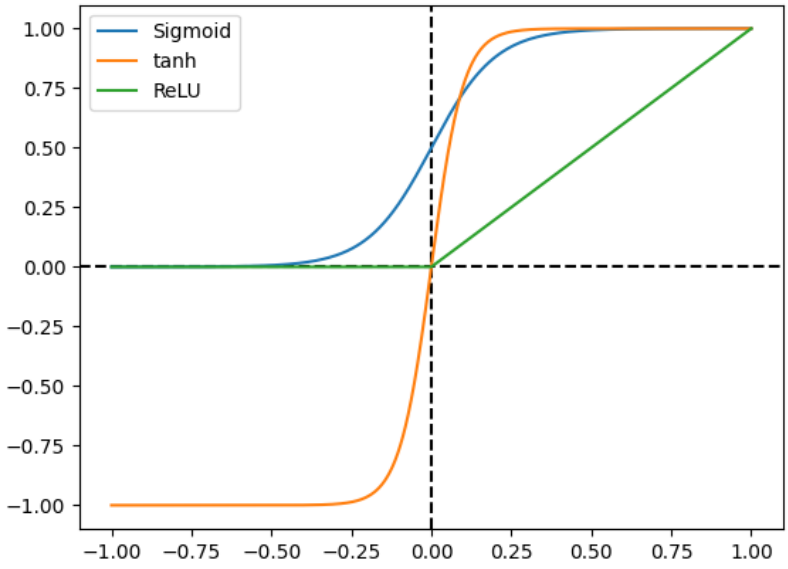

Figure 90: Different activation functions.

We use a 3 x 3 pixel kernel for convolution. The size of the kernel affects the size of relative correlation between pixels (simply by the nature of the convolution operation). Hence this size should be roughly representative of the data.

A kernel constraint is used to directly regularise the loss penalty on the weights matrix. An L_2 norm will normally penalise high weights, and so a kernel constraint specifying a maximum L_2 norm m ensures that the matrix is scaled such that the norm is equal to m. This also reduces the capability of overfitting.

5.4.2.2 *Activation Functions*

A few choices of activation function are widely used, such as ReLU, tanh and sigmoid, as shown in Figure 90.

Aside from the output layer, each hidden layer in our network uses ReLU activation. ReLU works well to avoid saturation during backpropagation (from Figure 90, the sigmoid activation function saturates at values close to 0 and 1), but the signal can still flow poorly during backpropagation, leading to vanishing or exploding gradients (Goh, Hodas, and Vishnu, 2017). To alleviate this, each layer with ReLU activation uses He initialisation (He et al., 2015). The final output layer is a normal convolutional layer with the sigmoid activation function. We use this to ensure the output is between 0 and 1, since we primarily use single line profiles whose intensities are in this range.

For now, we limit ourselves to the ReLU and sigmoid activation functions. The ReLU activation can suffer from 'dead' neurons (neurons whose weights are so low they never fire) and this can be improved by using one of its variants (leaky ReLU, for example), but it still works well in our case.

5.4.3 *Denoising Autoencoders*

As autoencoders learn a representation from an input to create reconstructions, it is possible to formulate the supervised machine learning problem to use noisy input data as the labels and cleaned input data as the features. In this way, the network will learn to remove noise from input samples. It is also possible to switch off certain inputs to create gaps in the input dataset that the network must learn to fill in. This is also a method of regularisation that prevents the

network from overfitting and has the added benefit of forcing individual neurons to learn useful features, lessening the probability that they will die during training.

To start with, we choose to simply add noise to the inputs to simulate actual noise present in spectra. We intentionally use a noise value much higher than what we see in our observations to test just the denoising capability of the autoencoder. While we want the network to perform both denoising and feature extraction, these tasks are sometimes performed by separate autoencoders.

5.4.4 *Denoising gaussian signals*

For spectroscopic purposes, we need to be able to remove noise from single-peaked signals, not just monotonically increasing ones. Here, we followed the same procedure as in the quadratic test case, but used randomised Gaussian amplitudes, width and centres to generate the dataset.

Figure 91 shows three example Gaussian signals used for training the network.

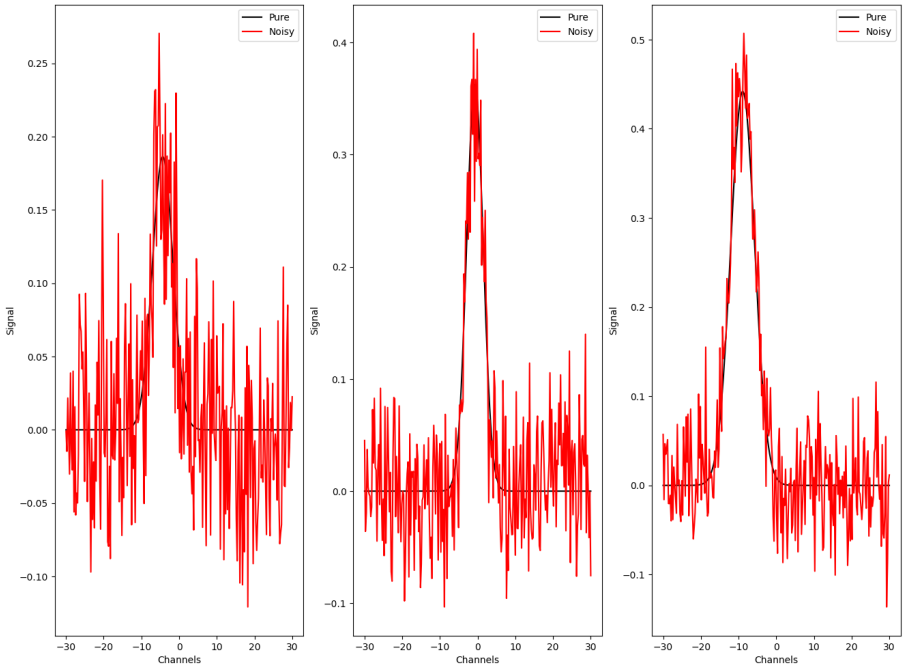

Figure 91: Gaussian signals used in training.

The high level of noise is due to the amplitude and width constraints placed on the Gaussian signal; the noise we use is additive, so weaker signals will see more noise. Again, the network is provided with a noisy sample and attempts to reconstruct the pure one. Figure 92 shows the results of denoising Gaussian signals.

Despite the large amount of noise relative to the signal, the autoencoder successfully denoises the majority of the signal. As this works well for single-peaked functions, we extend the training to spectra that contain multiple Gaussian components. These Gaussian components also have randomised parameters, and additionally, each sample spectrum can have anywhere between 1 and 5 Gaussian components. Again, this is to reflect the solar observations we aim to fit with this method but should be tailored to the problem at hand.

Figure 93 shows the results of training the same model on spectra with multiple Gaussian components.

The autoencoder correctly identifies the Gaussian components in each signal and is able to remove a large amount of the noise. The RMS scatter is more prevalent in narrower signals. However, the autoencoder is able to remove noise from both narrow and broad Gaussian components without specifying anything about the scale of the data. This is a promising result that should also improve its capability to extract the main features of the spectrum.

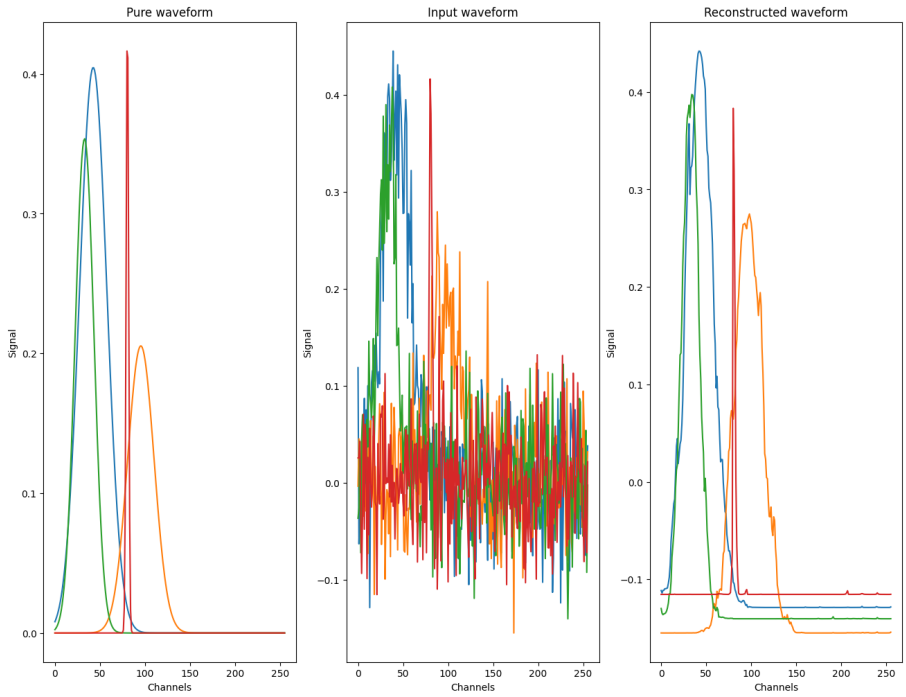

Figure 92: From left to right: pure, noisy and denoised Gaussian signals.

5.4.5 *Training Diagnostics*

The model is trained on 100,000 random Gaussian samples. To ensure the autoencoder would be robust to different signals, the properties of the function is randomised within a suitably determined range, allowing for multiple Gaussian components with differing properties to blend with one another. Each sample comprised of 256 channels and the data were reshaped into a 16×16 array. This does not have a large effect on the outcome, but the consequences are explored further in Section 5.4.6.

The Gaussian samples each have randomised amplitudes, widths and centres, again subject to the condition where the centre could lie outside of the fitting window. This condition directly reflects spectroscopic observations of stars, where line blends outside of the wavelength range used in the fitting affect the intensities of lines within the window. The randomisation ranges for each parameter are summarised in Table 19.

	Amplitude	FWHM	Mean
		[km s^{-1}]	[km s^{-1}]
Min	0.1	0.5	-35
Max	0.5	10	35

Table 19: Randomisation ranges for Gaussian parameters.

Note that both the FWHM and the mean are given in km s^{-1}since we use this velocity-space convention in our data. However, these limits are fairly arbitrary; the fitting window is $[-30, 30]$ km s^{-1}, so the mean could be 5 km s^{-1}outside the edge on either side.

Each model was trained for 5 epochs (meaning the 100,000 samples were shown to the model 5 times) and the batch size parameter (the number of instances the model is shown at a time) was set to 150. These numbers work well with the current example to show convergence to an optimum solution without overfitting. The accuracy of the model does not improve significantly

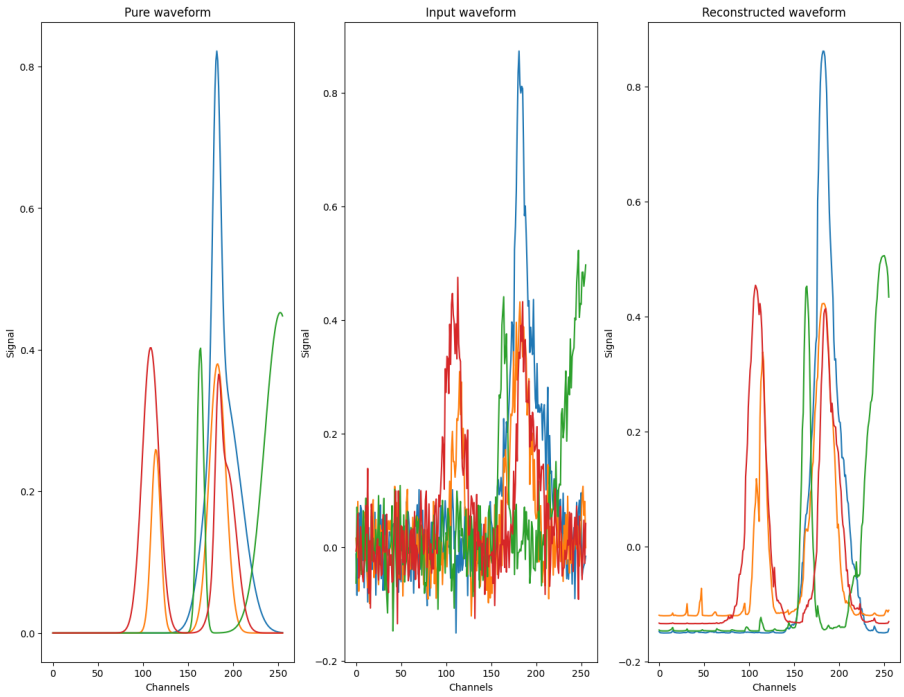

Figure 93: From left to right: pure, noisy and denoised signals with multiple Gaussian components.

past this pointand any improvement is likely due to model overfitting rather than generalisation. We use binary cross-entropy as our loss metric, defined as

$$H_p(q) = -\frac{1}{N}\sum_{i=1}^{N} y_i \cdot \log p(y_i) + (1-y_i) \cdot \log 1 - p(y_i) \tag{131}$$

where N is the number of points in a sample, y_i is the label of a given point and $p(y_i)$ is the predicted probability of a point matching the label. Note that this loss function is often used in binary classification (Parmigiani, 2001), hence its binomial form. However, it can be used in this case to determine the probability that a denoised point comes from the pure sample, i.e. the sample without noise.

After 5 epochs, the model had a loss of 0.0869 and a validation loss of 0.0868, where the unit is the flux amplitude. The similarities between the loss and validation loss of each model shows that overfitting due to a large number of epochs is unlikely.

5.4.6 *Further improvements*

For both the quadratic and Gaussian test cases the autoencoder is able to remove a substantial amount of noise. With the Gaussian samples (weaker signal), the network obtains higher accuracy, suggesting that the network correctly prioritises peaks over noise. In order to improve the results further to apply them in astrophysical contexts, a few things should be tested. Firstly, the scale of noise should be relative to the signal as well as varied between different points. Often, the signal-to-noise ratio in a spectrum changes with wavelength. In the case of the Hamburg spectrum (Neckel and Labs, 1984), the signal-to-noise can vary from $\sim$ 1500 in the optical to $\sim$ 3700 in the near-infrared. To be more representative of actual spectra, then, the noise should be varied between points as well as between samples.

Additionally, the RMS scatter in intensity between neighbouring pixels is often correlated. In the present study, we assume the noise is independent; it is certainly possible that adding this correlation improves the capability of denoising spectra since the network would be able to find a trend instead of a random scatter.

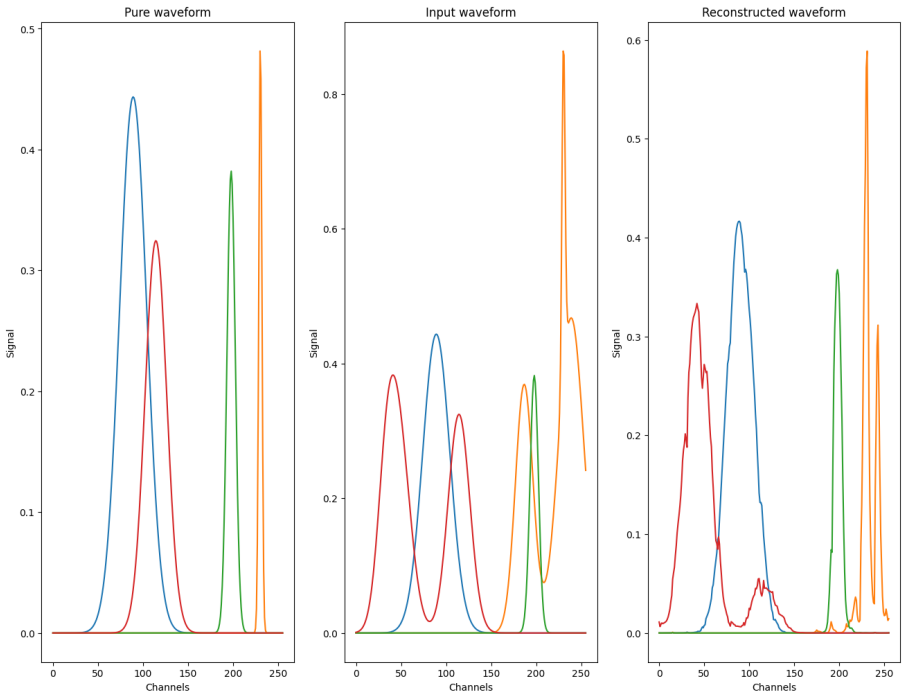

Figure 94: From left to right: Ground truth, input and output from the feature extraction autoencoder.

Finally, the network architecture should be tuned and streamlined to prevent any possible overfitting. By decreasing the size of hidden layers, the autoencoder is forced to learn more efficient representations of the data (up to a point). The 2D convolutional layers should also be replaced with 1D convolutional layers whenever this becomes possible; at the moment, using 1D convolutional layers causes a failure during compilation of the model. By using 2D convolutional layers and reshaping the input data as an image, the convolution kernel will consider points to be correlated that should be independent of one another. Instead of only considering neighbouring points in 1D, it considers neighbouring points in 2D. While this is less of an issue with smaller spectra, large spectra could be reshaped in a way such that pixels normally very far away from one another are considered to be correlated. This also goes hand-in-hand with the correlated noise already present in the spectrum, and falsely adding correlation through the convolution kernel could lead to higher loss when also considering the correlation between neighbouring pixels.

5.4.7 *Feature Extraction*

After ensuring the denoising autoencoder gives satisfactory performance, we train another autoencoder with the same model architecture on feature extraction. The synthetic data with multiple Gaussian components is used as features in the training data while the labels are the data with just the primary Gaussian component in each. To isolate this from the denoising autoencoder, no noise is added to the data. It is possible to do so, though, but keeping these two problems separate is useful to diagnose any potential training issues.

We use the same model architecture for both denoising and feature extraction because the ideal outcome is a single model which can do both. However, in order to properly test the capabilities of each, it would be useful to change the model architecture of the feature extraction network to be a sparse autoencoder (Makhzani and Frey, 2013). These are specifically built to extract the most important features from a dataset.

Figure 94 shows the results of feature extraction with the current model.

The performance of this network for feature extraction is unfortunately rather poor. It is likely that the model architecture is not well suited to this problem given that it has been created for denoising.

For this network to perform both denoising and feature extraction, the number of neurons in each layer should be decreased in order to more closely emulate a sparse autoencoder. This procedure can also lead to better performance with the denoising part of the network, as it is possible that including too many neurons causes the network to interpret noise variations as signal.

The problems of denoising and feature extraction for spectroscopy are two separate problems and it is possible to create two separate networks for this, namely a denoising autoencoder and a spare autoencoder. To link these together, we can turn to ensemble learning (Opitz and Maclin, 1999; Polikar, Third 2006; Rokach, 2010), which has been shown to improve the performance of constituent machine learning algorithms by combining their strengths.

5.5 CONCLUSION AND FUTURE WORK

We have investigated three separate approaches for removing noise and blends from spectra, each with their own strengths and weaknesses. The main conclusions are summarised below:

- Fitting residuals and using Autonomous Gaussian Decomposition both involve purely Gaussian line shapes. Generalisation towards other single-peaked functions may be possible, but it is unclear what effect this would have on the selection criteria for peaks used in both algorithms. On the other hand, autoencoders are insensitive to the shape of the input data when it comes to denoising and are able to handle other kinds of datasets.
- The peak-finding algorithm in fitting residuals works well for identifying Gaussian line shapes, as does AGD. Since they also directly fit the data, both algorithms are able to provide information as to the amplitudes, widths and centres of spectral lines.
- A trained autoencoder is capable of removing a substantial amount of noise from data while keeping the inherent signal, be it quadratic, Gaussian or a combination of components. The small amount of remaining noise in the reconstruction is likely due to suboptimal mdoel architecture.
- An autoencoder with the model architecture described in 5.4.2 performs well on denoising tasks but is unable to generalise to feature extraction. Closer emulation of sparse autoencoders may improve performance, but it is likely that denoising and feature extraction will require separate networks in the context of spectral line profiles.
- Overall, Autonomous Gaussian Decomposition provides the best results for removing blends and noise from the Hamburg atlas. However, it is not able to reproduce the line shapes exactly (as the observations are not pure Gaussians), and training the algorithm for the α_1 and α_2 parameters takes a very long time.
- With these methods, we are able to remove noise from spectra and decompose them into multiple Gaussian components. In terms of stellar spectroscopy, we would be able to run these as a preprocessing step on observations to yield cleaner spectra. Line blends and noise can be difficult to handle during spectral fitting and often lead to poorer estimates of spectroscopic parameters. Handling these issues as a preprocessing step, then, will provide better input data to spectral fitting routines and hence more precise estimates of spectroscopic parameters.

Though promising, it is clear that significant improvements can be made for each method. Fitting the residuals does not seem to be a very viable method for large-scale spectral fitting, since the spectral fits are still calculated with the original data. Additionally, there are issues with discontinuities based on removing line cores as well as autonomously choosing the number of Gaussian components. Here, AGD is able to perform much more efficiently, but still suffers from the caveat that the input data must contain Gaussian components for the decomposition to be accurate. A future project will involve incorporating different single-peaked functions into the algorithm so that it is able to precisely determine the properties of spectral line profiles.

While autoencoders are able to remove noise from many different kinds of data, the model presented here cannot extract the primary line component. It is clear that the model architecture needs to be changed to account for the change in the problem and that the problems of denoising and feature extraction may require separate networks. Also, the use of 2D convolutional layers

and reshaping the data as an image is a drawback that adds incorrect information about pixel-to-pixel correlation. Ideally, 1D convolutions should be used; this would also allow for longer term trends to be detected more easily. Another drawback is the autoencoder is not able to give information about the different components within the signal; it simply applies nonlinear operations to remove noise. A future investigation in this field will involve extracting physical parameters from these networks. This can be used not only for cleaning data and fitting spectra, but also for generating more physically accurate synthetic spectra.

6

MACHINE LEARNING TECHNIQUES FOR CHEMICAL KINETIC PROBLEMS IN STELLAR ATMOSPHERES

6.1 INTRODUCTION

We present a novel method to compute the equilibrium state of a chemical reaction network by training a neural network on input-output data points from stellar atmospheres. This was motivated by the fact that solving a system of ODEs until they reach equilibrium can be a computationally expensive task, and this system needs to be solved for every grid cell in a stellar atmosphere. While it is of course possible to parallelise the problem, we explore the possibility of significant computational speed-up with at run-time by first training a neural network (NN) to map stellar atmospheric parameters to equilibrium number densities. To avoid confusion in the naming scheme, "chemical reaction networks" will be referred to as "CRNs" or "chemical networks", and "neural networks" will be referred to as "NNs" or simply "networks".

We train multiple NN architectures to model the equilibrium state produced by solving the chemical kinetics problem. While many variants of architectures were tested, they all fall into three distinct categories: multi-layer perceptrons (MLPs) (Rosenblatt, 1962), convolutional neural networks (CNNs) (O'Shea and Nash, 2015) and encoder-decoder networks (Ye and Sung, 2019). Each of these architectures consists of an input layer, several hidden layers and an output layer, though the structure of the hidden layers differs between them. A key feature of all of these networks is that the signal flows in a single direction, from input towards output. Other network architectures exist where this is not necessarily the case (Cho et al., 2014; Sherstinsky, 2020; Vaswani et al., 2017), but we focus on the three architectures presented here as they are simpler to train without overfitting and can still provide very precise solutions.

6.1.1 *Multilayer Perceptron*

MLPs are some of the oldest neural network architectures, and are a direct evolution of (single-layer) perceptrons (Rosenblatt, 1957). They consist of multiple fully-connected hidden layers whose outputs go into an activation function. Fig. 95 shows the architecture of the MLP used in this study.

Each fully-connected layer's output h is calculated through

$$h_{\mathbf{W},\vec{b}}(\mathbf{X}) = \phi(\mathbf{X}\mathbf{W} + \vec{b}) \tag{132}$$

where $\mathbf{W}$ is the weights matrix of the neurons in this layer, $\vec{b}$ is the bias vector, $\mathbf{X}$ is the matrix of input features to the layer and ϕ is the activation function. Using a nonlinear activation function alongside multiple hidden layers provides the MLP with the ability to reproduce almost any function, as equation Eq. 132 represents a (nonlinear) function applied to a linear combination of inputs.

6.1.2 *Convolutional Neural Network*

The second architecture we test is a convolutional neural network (CNN). Here, instead of the hidden layer outputs being simple nonlinear combinations of weights, a convolutional kernel is used to learn the relation between neighbouring input features. CNNs are often used for image-classification tasks since the 2D convolutional kernel is naturally suited for these. In our case, the inputs are 1D, so we use a 1D convolutional kernel instead, and the relations are determined between the different input parameters. The MaxPooling layers collect the 2D outputs of the convolutional layers and recombine them into 1D arrays. Fig. 96 shows the architecture of the CNN used in this study.

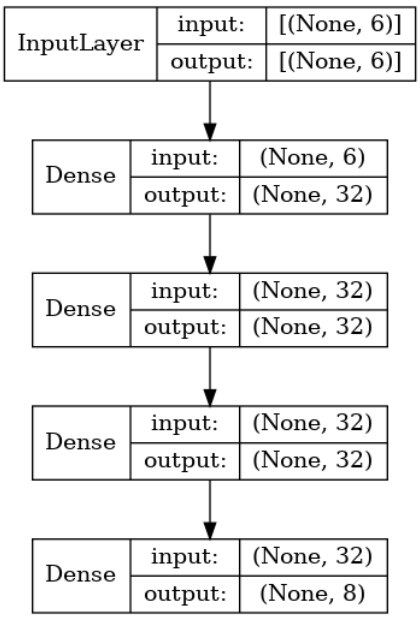

Figure 95: Network architecture for the multilayer perceptron (MLP). All layers use ReLU activation except the final output Dense layer, which uses linear activation.

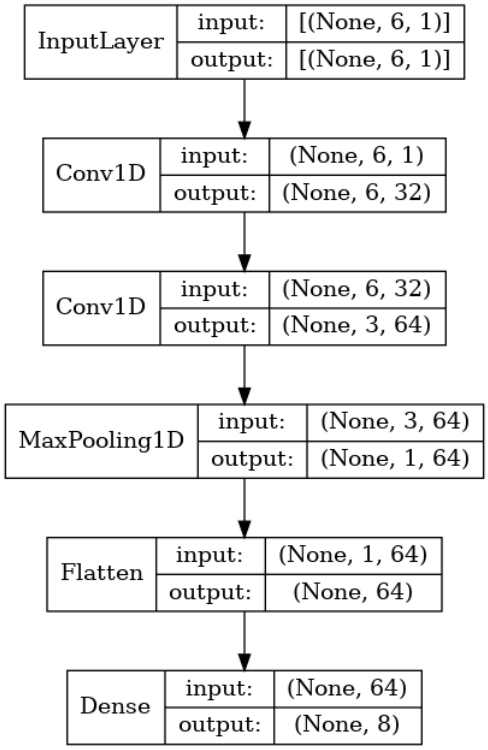

Figure 96: Network architecture for the convolutional neural network (CNN). All layers use ReLU activation except the final output Dense layer, which uses linear activation.

6.1.3 *Encoder-Decoder Network*

Fig. 97 shows the architecture of the encoder-decoder network (EncDec) used in this study.

The EncDec architecture is composed of two different networks that almost mirror one another. The first is the encoder, a feedforward network where there are fewer and fewer neurons in each subsequent hidden layer. The second is the decoder, where the number of neurons in-

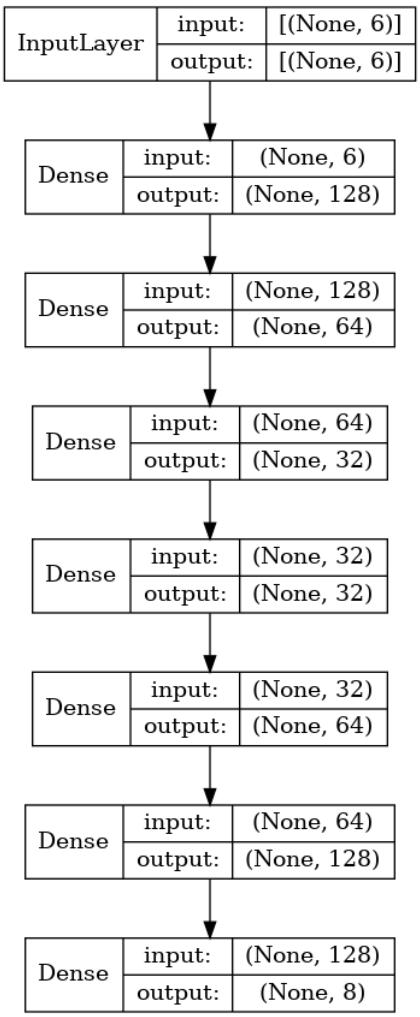

Figure 97: Network architecture for the encoder-decoder network (EncDec). All layers use ReLU activation except the final output Dense layer, which uses linear activation.

crease throughout the hidden layers. The core principle is that the input signal travels through the first network and is encoded as an embedding, and the second network decodes this embedding into the relevant output. In our case, the input abundances, gas density and temperature are encoded into a lower-dimensional embedding before the decoder network reconstructs the output number densities. This architecture automatically regularises the propagating signal to reduce overfitting, as the encoder network is constructed to only retain the most useful information. When trained across a wide range of inputs, this architecture then becomes very robust to changes.

6.1.4 *Data*

We first use the chemical network described in Wedemeyer-Böhm et al. (2005) that models the formation of bimolecular species in stellar atmospheric conditions. This chemical (hereafter CRN1) contains 8 chemical species: C, H, O, CH, OH, CO, H2 and a representative metal M (catalytic). The 27 reactions in this network populate the 8 ODEs that model the time-dependent evolution of the system. We later expand the modelling to the larger network (hereafter CRN2) presented in Deshmukh and Ludwig (2023) (Chap. 3), consisting of 76 reactions and 15 species. As we are only interested in the equilibrium state here, we pre-compute the equilibrium number densities for each species across a 3D model atmosphere snapshot.

As input to the neural network we extract data from 3D model atmosphere snapshots. We experimented with various inputs, and found the best quantities to use were gas density, tem-

perature and the abundances (or log number densities) of the atomic species. The network is then built to output the equilibrium number densities of all species of interest. In summary, every NN has 6 input features and 8 output features when considering CRN1, and 7 input features and 15 output features when considering CRN2. We choose to use data from 3D model atmosphere snapshots since the data used for training is then representative of the environment in the model atmospheres themselves. The datasets used included individual model atmosphere snapshots (only for the dwarf stellar models), and "composite" datasets that combine atmospheric snapshots from all models of a certain type. Three composite datasets were created. The first combines 5 dwarf models, the second combines 7 RGB models, and the third combines all aforementioned models. In each case, these were split into a training/validation and testing dataset. The training/validation dataset consists of a random 75% / 25% split, while the testing dataset uses a completely separate set of snapshots that the NN has never seen. For the combined RGB dataset, the training/validation dataset was created from a total of 6.89×10^6 total data points, and the testing dataset is a full 6.89×10^6 data points from a completely different set of model atmosphere outputs. In short, the training dataset is used for updating NN weights, the validation dataset is used for regularisation and to assess performance during training, and the testing dataset is only used after the training is complete to assess how well the model performs on a completely new dataset.

6.2 RESULTS

To evaluate the performance of the NNs, we consider the mean squared error (MSE) and mean absolute error (MAE). The NNs were trained by minimising MAE, while callbacks to tune learning rate and control early stopping used MAE. For N samples, the MSE is given by

$$\sigma^2_{\text{MSE}} = \frac{1}{N}\sum_{i=1}^{N}(y_i - \hat{y}_i)^2\,, \tag{133}$$

and the MAE is given by

$$\sigma_{\text{MAE}} = \frac{1}{N}\sum_{i=1}^{N}(|\,y_i - \hat{y_i}\,|)\,, \tag{134}$$

where y_i is the ground truth value and $\hat{y_i}$ is the predicted value. Both metrics are calculated across all 8 output number densities and are evaluated for mini-batches during training. For training, a batch size of 1024 was used.

Table 20 shows the MSE and MAE values evaluated on the entire test dataset for each of the model architectures. We also experimented with pre-processing the abundance input into number density ($\log(n)$), and found it slightly improved performance. However, the improvement is comparatively small and allows for less flexibility compared to providing the abundance directly. It does show, though, that adding another layer to the front of the NN to handle this conversion could improve performance further.

It is clear that the EncDec model architecture has the best performance across all atmospheres. As such, we opt to use this architecture for evaluation on the composite datasets. Table 21 shows the same metrics evaluated on the full composite test datasets.

Training the composite dataset NNs took $\sim$ 15 hours in total. Once trained, though, running the NN is extremely fast, with the most complex NN requiring $\sim$ 200 seconds to evaluate on the full test dataset (a composite of 12 model atmospheres) on an AMD Ryzen 7 3700U laptop CPU. For comparison, solving the CRN system for a single model atmosphere snapshot on the same hardware took between 20 minutes to a few hours. For the work presented in Chapters 3 and 4, the equilibrium state for 20 snapshots per model ID need to be calculated. This would amount to a maximum of $\sim$ 1.1 hours with the NN method, compared to a maximum of $\sim$ 60 hours with the conventional method.

The training loss curves for the networks presented in this work are shown in Figs. 98 for the dwarf stellar atmospheric model dataset. Validation loss values follow training loss values well for the entirety of the training process for all models. This demonstrates that the model is not overfitting; halting the training process based on the improvement of validation loss similarly

ID	MSE ($\log(n)$ Input)	MAE ($\log(n)$ Input)	MSE (Abu. Input)	MAE (Abu. Input)
AM1				
MLP	4.26×10^{-5}	3.77×10^{-3}	7.62×10^{-4}	1.44×10^{-2}
CNN	1.14×10^{-5}	2.29×10^{-3}	3.50×10^{-5}	3.57×10^{-3}
EncDec	5.75×10^{-7}	4.98×10^{-4}	1.53×10^{-6}	8.20×10^{-4}
AM2				
MLP	4.17×10^{-4}	1.21×10^{-2}	6.20×10^{-4}	1.37×10^{-2}
CNN	3.65×10^{-5}	4.15×10^{-3}	1.08×10^{-4}	5.49×10^{-3}
EncDec	1.30×10^{-6}	7.63×10^{-4}	6.87×10^{-6}	1.51×10^{-3}
AM3				
MLP	6.93×10^{-4}	1.33×10^{-2}	4.51×10^{-4}	9.57×10^{-3}
CNN	2.81×10^{-4}	6.64×10^{-3}	1.20×10^{-4}	4.37×10^{-3}
EncDec	6.76×10^{-5}	2.74×10^{-3}	4.81×10^{-5}	2.71×10^{-3}
AC1				
MLP	3.00×10^{-4}	1.03×10^{-2}	1.81×10^{-4}	7.81×10^{-3}
CNN	3.90×10^{-4}	9.96×10^{-3}	2.23×10^{-4}	6.30×10^{-3}
EncDec	2.67×10^{-5}	2.45×10^{-3}	2.01×10^{-5}	2.34×10^{-3}
AC2				
MLP	1.02×10^{-4}	5.40×10^{-3}	1.55×10^{-4}	6.99×10^{-3}
CNN	1.92×10^{-4}	7.62×10^{-3}	1.53×10^{-4}	6.25×10^{-3}
EncDec	7.36×10^{-6}	1.54×10^{-3}	9.35×10^{-6}	1.70×10^{-3}

Table 20: Mean squared error (MSE) in dex^2 and mean absolute error (MAE) in dex for the NNs for individual atmospheres evaluated on the test dataset. In all cases, the Encoder-Decoder model (EncDec) performs best.

ID	MSE ($\log(n)$ Input)	MAE ($\log(n)$ Input)	MSE (Abu. Input)	MAE (Abu. Input)
DCEMP chem1	2.73×10^{-4}	4.81×10^{-3}	2.18×10^{-4}	3.65×10^{-3}
DCEMP chem2	2.25×10^{-4}	4.77×10^{-3}	1.94×10^{-4}	5.48×10^{-3}
RGB chem1	7.21×10^{-4}	5.11×10^{-3}	7.28×10^{-4}	6.04×10^{-3}
RGB chem2	1.49×10^{-4}	4.71×10^{-3}	1.76×10^{-4}	5.64×10^{-3}
Combined chem1	1.33×10^{-3}	1.56×10^{-2}	4.23×10^{-4}	4.37×10^{-3}

Table 21: Mean squared error (MSE) in dex^2 and mean absolute error (MAE) in dex for EncDec NNs evaluated on the test datasets. The "ID" column refers to the training/validation/testing dataset and combines the set of models with the CRN: "DCEMP", "RGB" and "Combined" refer to the model atmospheres in Table 14, Table 18 and the combination of the previous two, respectively; "chem1" and "chem2" refer to the CRNs described in (Wedemeyer-Böhm et al., 2005) and (Deshmukh and Ludwig, 2023) (Chapter 3), respectively.

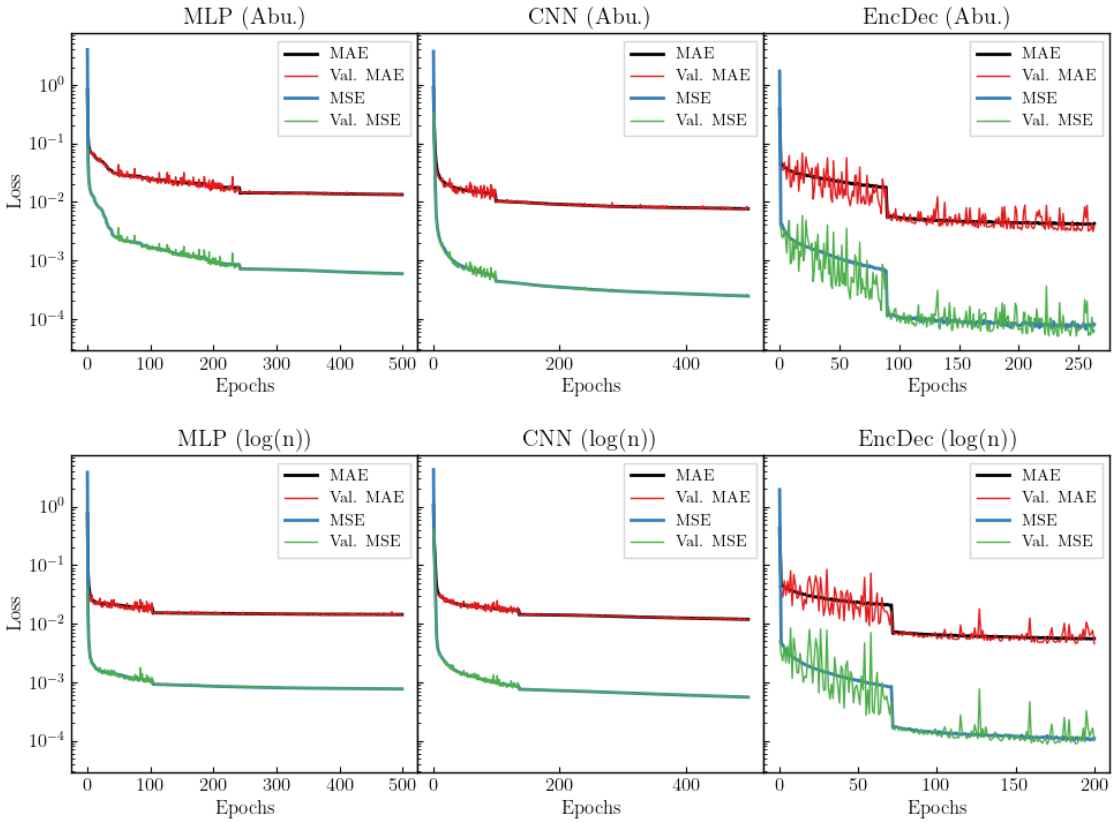

Figure 98: Loss values (MSE, MAE, val. MSE and val. MAE) for each of the networks presented in this work. Validation loss values follow training loss values for the entirety of the training process, showing effective regularisation.

guarantees this. The EncDec models find better solutions in fewer epochs, though do show significantly more variance in their validation loss curves. This suggests that the landscape past this point of significant improvement is a kind of plateau with many local minima (in the training set) which are not necessarily reflected in the validation set. In short, the model is potentially learning very specific features that are not common to both sets, and training is correctly halted before the model overfits to the training set. Fig. 99 shows the training losses for the best-performing EncDec models on each of the composite datasets considered in this work. For the composite models, the "DCEMP chem2" and "RGB chem2" NNs perform much better on the test dataset, but the "Combined chem1" NN performs much worse.

6.3 DISCUSSION

We have seen that using NNs to predict the equilibrium number densities of a CRN can be quite efficient. In this section, we will review some of the shortcomings seen in performing this analysis for RGB stellar atmospheres. Firstly, training and finetuning the NN architectures takes a significant amount of time. Secondly, each NN is trained to predict the equilibrium state of a certain CRN. Finally, the NN is limited to predictions within the range of parameters it has been trained on; it is unable to extrapolate outside of these boundaries effectively.

While training the NNs takes time, their efficiency at runtime makes them well-suited to computing 3D stellar atmospheres. The training and evaluation process can be further sped up by utilising GPUs. A majority of the training time was spent finetuning network architectures. Luckily, this process can be automated somewhat through libraries such as optuna (Akiba et al., 2019), allowing the user to optimise the network architecture quickly.

We tested NNs trained on single model atmospheres as well as those trained on composite atmospheres. In the first case, each model atmosphere (separated by metallicity) is treated completely separately. This is to investigate the effects of metallicity on the training and validation

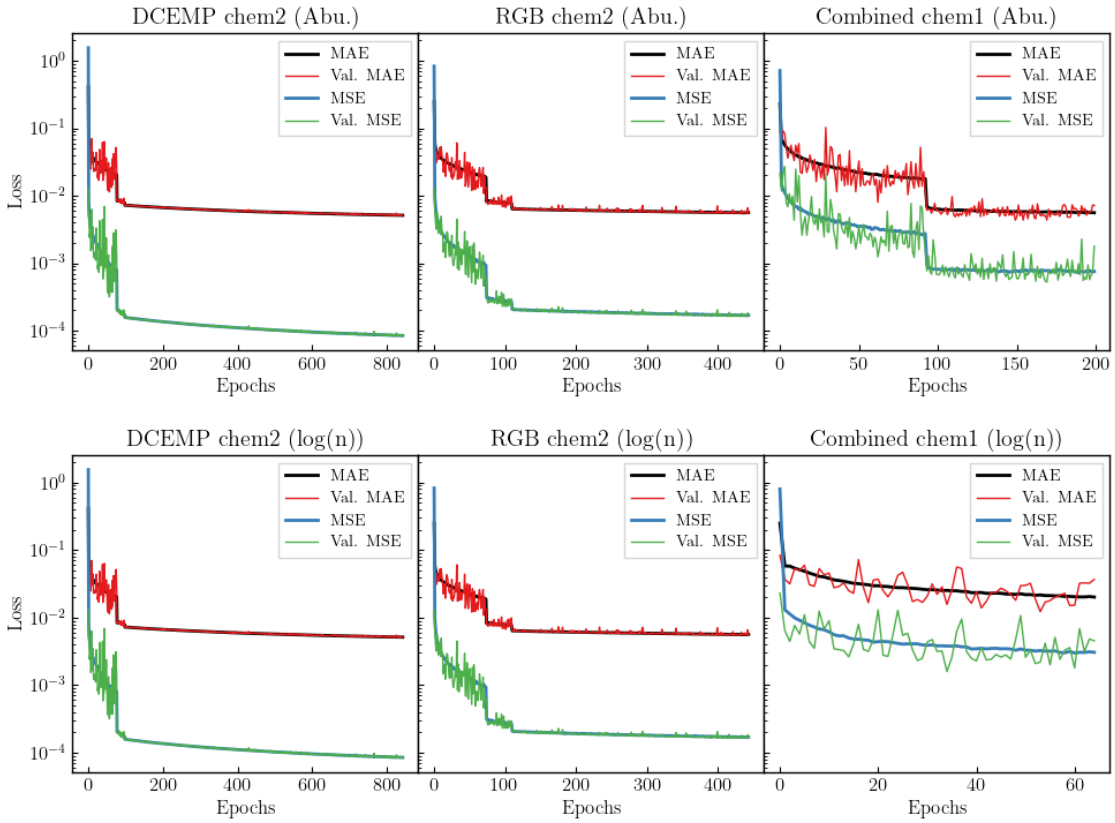

Figure 99: Loss values (MSE, MAE, val. MSE and val. MAE) for a sample of the EncDec networks presented in Table 21. Validation loss values follow training loss values for the entirety of the training process, showing effective regularisation for the "DCEMP chem2" and "RGB chem2" models, while the "Combined chem1" model shows much larger fluctuations.

process. It was found that metal-rich atmospheres have a slightly higher overall accuracy; the difference is quite minor, though. However, an issue is that the NN trained on model AM1 cannot be used on model AM3 outputs since the abundance inputs will be offset by the wrong value, and the output number densities fall in different regimes. This can be remedied in two ways. One involves creating an ensemble learning model, in which one NN for each model atmosphere is trained simultaneously, and the results from each are compared to the ground truth. In this way, certain NNs will perform better at certain metallicities, and the entire system will perform better as a result. However, this obviously does not scale well, and involves a second round of training. The other way is to include all atmospheric inputs into the NN during training. This is far simpler and preferable, as the training process does not change, and will result in an NN that is robust against changes in input abundance. Future work will include such a NN, as well as including different kinds of stellar atmospheres.

It is also important to note that the NNs used here were trained on outputs from 7 different atmospheres, meaning they can also be used to predict equilibrium chemistry for any of these atmospheres' snaphosts. This can of course be expanded further; continuing training on other atmospheric outputs would allow the NN to effectively predict equilibrium chemistry in those atmospheres as well.

Figs. 100 & 101 show the range of gas density and temperature seen in the training and test datasets. The NNs are accurate within this set of atmospheric parameters, and at metallicities ranging from [Fe/H] $= 0.0$ to [Fe/H] $= -3.0$. There are clear peaks visible in the density and temperature histograms; this bias is mainly physical (due to the effective temperatures and surface gravities of the models chosen), and partially due to the compositing scheme. When combining into a single dataset, we chose to use a coarser selection in the $x-$ and y-directions. These biases may be reflected in the final output, in that predictions may be better for better-

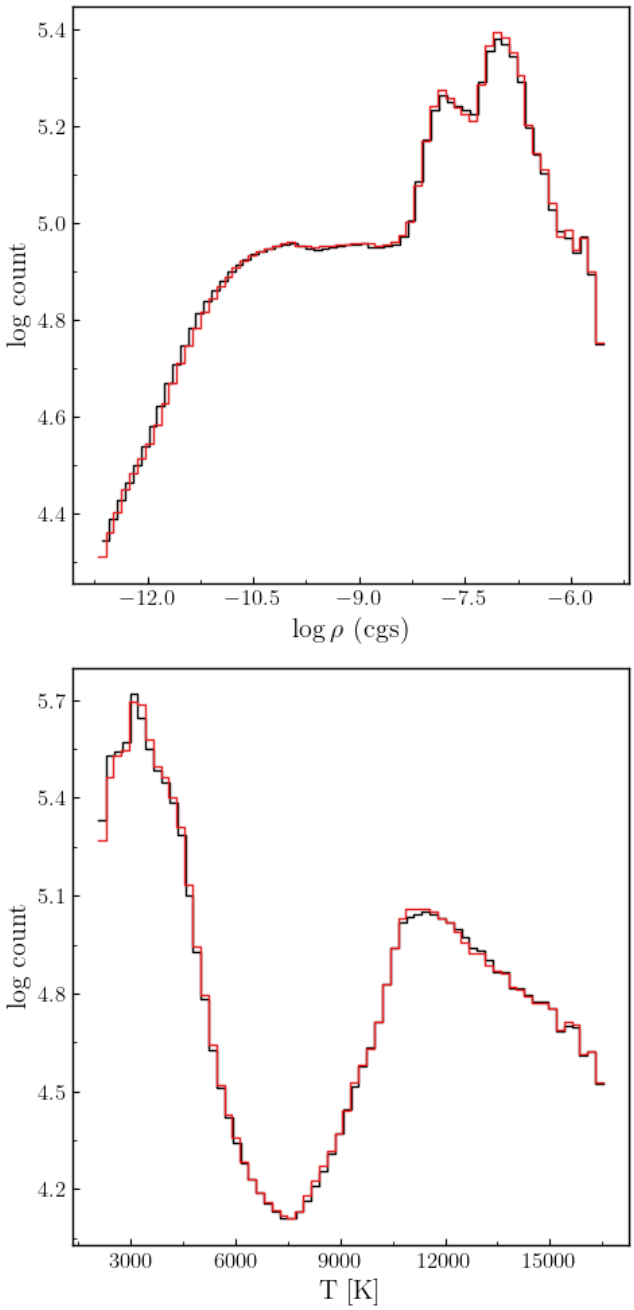

Figure 100: Histograms of gas density and temperature for the training (black) and test (red) datasets. Compositing the 7 3D atmospheres allows for a large range of atmospheric parameters to be explored.

sampled points. However, our sample size is significant across the majority of atmospheric parameters, and so this bias is unlikely to be a major source of error across a large majority of the dataset.

Perhaps the largest drawback is still the accuracy. The encoder-decoder model is quite accurate, but still does not achieve perfect accuracy for every data point. We look forward to further advances in this aspect, since techniques exist for improving the modelling of physical relations through machine learning, such as physics-informed neural networks (Raissi, Perdikaris, and Karniadakis, 2019), Hamiltonian neural networks (Greydanus, Dzamba, and Yosinski, 2019), and neural ODEs (Chen et al., 2018).

The NNs presented in the current work were trained solely on the CRNs from Wedemeyer-Böhm et al. (2005) and Deshmukh and Ludwig (2023). It is also not possible to retrain the NN

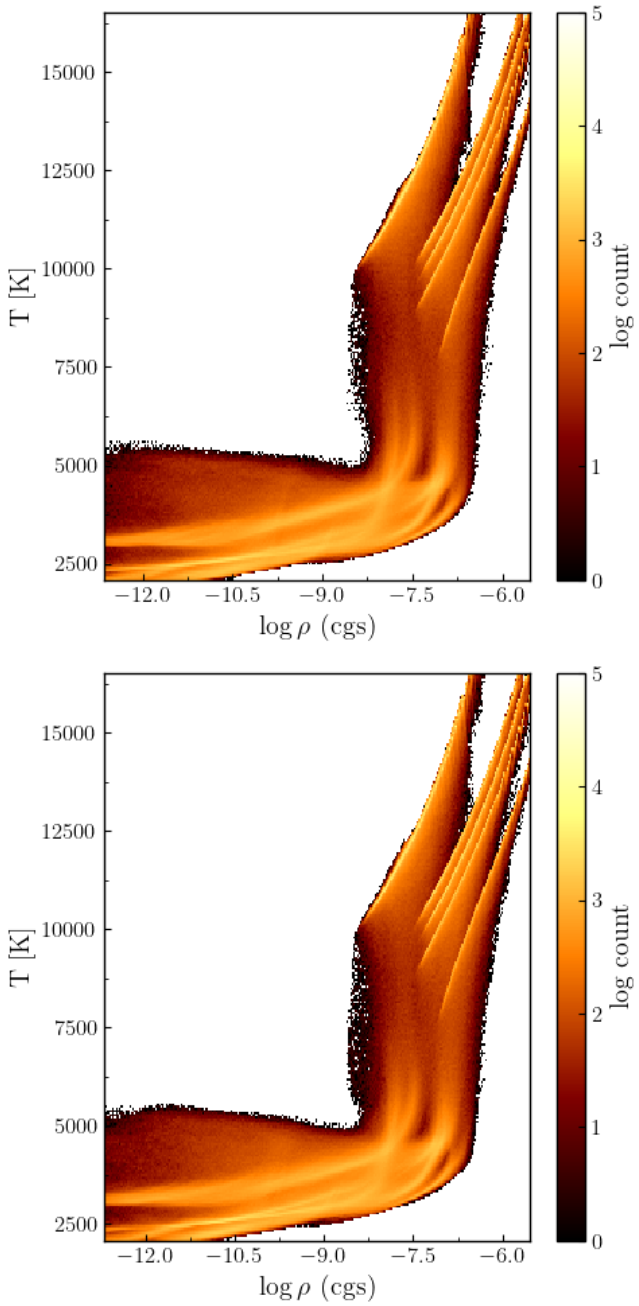

Figure 101: 2D Histograms of gas density vs temperature for the training (top) and test (bottom) datasets. The influence of the singular atmospheres that went into the composite dataset can be seen.

with new inputs from a different CRN, since the inputs and outputs are confined to those originally used during training. A new CRN would require a new NN to be trained. That being said, we have restricted ourselves to simple feedforward networks in this work, as they are simpe to train and analyse, though many more complex layers can be used to overcome these issues. For example, convolutional layers can also be used as inputs and outputs to allow for varying-length sequences. Recent advances in natural language processing has shown transformers utilising attention to be extremely versatile and precise. These techniques can also help the NN to make accurate predictions outside of its training set, since it learns embeddings in a latent space rather than a direct mapping (analogous to learning a mapping in phase space).

Finally, while we set up a chemical kinetics ODE system, we only solve for the steady-state. This was motivated by the long wall-clock times required to solve the ODE system to steady-

state, but this problem extends of course to time-dependent solutions as well. However, this adds another layer of dimensionality to the prediction problem, and requires many more inputs. One way of remedying this is through on-the-fly training, where the NN and the true model are fed inputs simultaneously during the training process. This is beyond the scope of this work, though we aim to model time-dependent kinetics using NNs in the future.

6.4 CONCLUSION

Equilibrium number densities of a CRN can be efficiently predicted with NNs, as has been shown in this chapter. The key takeaways are summarised as follows:

- Predicting the equilibrium state of a CRN via a trained NN achieves a speed-up of 60x compared to the conventional method of solving the chemical ODE system. The training process is time-consuming, and restricts the NN to learn a single CRN. However, the improvements in efficiency make the NN method preferable when relatively large, static CRNs need to be used, such as in the applications of Chaps. 3 and 4.
- The Encoder-Decoder architecture performed best across all atmospheres, with an overall MAE of $\sim 5 \times 10^{-3}$ dex. Both the MLP and CNN architectures require a greater number of epochs to reach a minimum, and their loss values are higher in all circumstances. The EncDec model includes more trainable parameters, but crucially, the architecture encourages the NN to learn efficient mappings between parameters to form a low-dimensional embedding that contains the necessary information to make accurate predictions.
- Combining atmospheric outputs to create composite datasets comprised of the conditions present in multiple atmospheres improves the robustness of the model while simultaneously allowing it to make predictions in a larger parameter space. However, combining both dwarf and giant stellar atmosphere outputs together resulted in worse overall performance, as the parameter space becomes too large for the models presented in this work to predict with high accuracy. Increasing the model complexity and adding mechanisms such as attention (Vaswani et al., 2017) could lead to further improvements in this area.
- Pre-processing the inputs to use number densities instead of abundance marginally improves performance. However, this comes at the cost of simplicity and ease-of-use, since in a larger application, it is often more convenient to specify the abundance set rather than calculating the number densities explicitly.

7

SUMMARY AND OUTLOOK

7.1 SUMMARY

This work has covered work encompassing conventional modelling techniques and machine learning ones. In this section, the main conclusions from each chapter are summarised. A future outlook is presented in Sec. 7.2.

In Chap. 2, the photospheric solar silicon abundance was determined with CO^{5}BOLD model atmospheres and the LINFOR3D spectrum synthesis code. The determined abundance was $\log \varepsilon_{\mathrm{Si}} = 7.57 \pm 0.04$, including a -0.01 dex correction for NLTE effects (Amarsi and Asplund, 2017). From a total of 39 spectral lines, 11 were carefully chosen for the abundance analysis, comprising of 7 optical Si I lines, 3 near-infrared Si I lines, and 1 Si II line. New oscillator strengths from Pehlivan Rhodin (2018) provided smaller uncertainties and facilitated the use of the near-infrared lines. Overall, the 0.06 dex with resepect to recent studies by Asplund, Amarsi, and Grevesse (2021) shows that the determination of the solar silicon abundance is not yet a firmly solved problem. Several factors complicate the fitting process, and it was found that the synthesised lines were too broad to fit observations without applying negative broadening during the process. These over-broadened line syntheses are not specific to CO^{5}BOLD atmospheres, and were also seen in lines synthesised with STAGGER + BALDER . Meteoritic abundances are increased with respect to the previous study by Palme, Lodders, and Jones (2014) due to the increase in the determined photospheric silicon abundance.

Chap. 3 considered the validity of the assumption of chemical equilibrium in the atmospheres of 5 metal-poor and carbon-enhanced metal-poor dwarf stars. Time-dependent molecular formation and dissociation calculations were performed alongside hydrodynamics and radiative transfer in order to make a differential comparison with chemical equilibrium models. A new chemical reaction network was constructed for this work, building upon the network presented in Wedemeyer-Böhm et al. (2005), comprising of 76 reactions and 14 chemical species. Overall, molecular species are generally in equilibrium throughout the model photosphere, with molecular species reaching a maximum deviation from equilibrium of 0.15 dex at $\log \tau = -4$. Generally, the deviations from equilibrium stem from a slowing of chemical timescales due to a reduction in metallicity, and the finite timescales associated with chemical reactions in the time-dependent case. These finite timescales are usually still much faster than hydrodynamical timescales in the majority of the atmosphere, but around features such as shock waves, molecular species are seen to dissociate slower than predicted by equilibrium chemistry around the hot shock front. Additionally, the uppermost, coolest layers ($T \lesssim 3500$ K) show a depletion in CO as there is insufficient time to form it to its equilibrium value before the material is advected. The deviations are unlikely to contribute significantly to spectroscopic measurements for metal-poor dwarfs, as the line cores of key molecular species such as CH, C_2 and CN are formed in deeper layers (Gallagher et al., 2017a, 2016), where the material is in chemical equilibrium.

Chap. 4 extended the treatment of time-dependent molecular formation and dissociation to 7 metal-poor red giant atmospheres. Much like for dwarf stellar atmospheres, the assumption of chemical equilibrium holds well in the spectroscopically relevant region of $-4 \leqslant \log \tau \leqslant 2$, with deviations from equilibrium staying below 0.2 dex. An investigation of various chemical timescales was performed, and the inverse reaction rate timescale was found to give the most plausible result for chemical timescales as a whole. The Damköhler number Da, the ratio of hydrodynamical to chemical timescales, was calculated across the regime. Da was found to be a reasonable approximation to determining which regions in the atmosphere could be out of chemical equilibrium. However, since the analysis considers only mean variations, it does not highlight transient instances that may be interesting, such as shock waves. Together, Chaps. 3 and 4 show that the assumption of chemical equilibrium is valid in the photospheres of metal-poor dwarf and giant atmospheres, but indicate that higher layers, such as chromosphere, are out of chemical equilibrium.

Chap. 5 investigated three machine learning approaches for removing noise and blends from spectral lines. This problem was first encountered in Chap. 2 when many lines were found to contain blending components. Fitting Gaussian line profiles to residuals and Autonomous Gaussian Decomposition (Lindner et al., 2015) work well, but the best overall performance for denoising was achieved by training an autoencoder neural network. This did not extend to feature extraction, though, and AGD performed the best when it came to reproducing the lines from the Hamburg atlas (Neckel and Labs, 1984). However, since AGD is only capable of reproducing Gaussian lines, the Voigt-like profiles of solar photospheric absorption lines were not reproduced. Though promising, significant improvements to the algorithms are required to use them effectively in a standard spectral fitting pipeline.

Chap. 6 presented 3 neural network architectures built and trained to predict the equilibrium state of a chemical reaction network. The problem arose in Chaps. 3 and 4, as solving the chemical ODE system until the equilibrium solution is found can be quite time-consuming. The best trained network (an encoder-decoder) resulted in a $\sim$ 60x speed-up compared to the conventional method. This network achieved an overall mean-absolute-error accuracy around 5×10^{-3} dex. It was found that combining atmospheric outputs to create composite datasets worked well when the composite datasets were of the same kind of atmosphere, that is, if all atmospheres came from dwarf stars. Mixing dwarf and giant stellar atmospheres resulted in worse overall performance, likely due to the relative simplicity of the neural network architectures when compared with the number of data points and the spread of the parameters. Pre-processing the inputs to use number densities instead of abundances resulted in a slight improvement in performance, though it is likely that this could also be achieved by constructing a suitable combination of hidden layers in the neural network.

7.2 FUTURE OUTLOOK

The future landscape holds many possibilities for the merging of conventional and machine learning modelling techniques. Further work on photospheric abundances to determine the consistency of the current solar photospheric silicon abundance derived in Chap. 2 would involve considering radiative NLTE effects as well as diving further into understanding the source of overly broadened spectral line syntheses. Techniques from Chap. 5 should be refined and applied to these analyses in order to further lower uncertainties. It may be feasible to construct high-resolution magnetic model atmospheres that accurately reflect the surface magnetic field strengths of the Sun, and techniques to speed up radiative NLTE calculations would allow for the efficient and precise calculation of solar abundances.

We are fortunate to have increasing access to better data in this age of astronomical surveys, which further helps constrain physical models. Mission such as PLATO take a particular interest in M-type dwarf stars, and applying the methods of time-dependent molecular formation and dissociation seen in Chaps. 3 and 4 would be particularly relevant in the molecule-dominated atmospheres of these stars. Additionally, the presence of magnetic fields alters the structure of the atmosphere. Considering magnetic fields alongside the time-dependent treatment of chemistry is therefore a feasible extension. Recent advancements in radiative NLTE calculations suggest that graph neural networks can provide effective solutions. The structure of a chemical reaction network as a graph lends itself to similar solution mechanisms. Furthermore, constructing a neural network capable of predicting time-dependent chemistry would be an interesting extension to the work presented in Chap. 6. All in all, the future of astrophysical modelling looks bright.

PUBLICATIONS

- Deshmukh, S. A., H.-G. Ludwig, A. Kučinskas, M. Steffen, P. S. Barklem, E. Caffau, V. Dobrovolskas, and P. Bonifacio (Dec. 2022). *The Solar Photospheric Silicon Abundance According to CO5BOLD - Investigating Line Broadening, Magnetic Fields, and Model Effects.* In: A&A 668, A48. issn: 0004-6361, 1432-0746. doi:10.1051/0004-6361/202142072.
- Deshmukh, S. A. and H.-G. Ludwig (July 2023). *Implications of Time-Dependent Molecular Chemistry in Metal-Poor Dwarf Stars.* In: A&A 675, A146. issn: 0004-6361, 1432-0746. doi:10.1051/0004-6361/202345985.

Abramowitz, Milton and Irene A. Stegun (1965). *Handbook of Mathematical Functions: With Formulas, Graphs, and Mathematical Tables*. New York: Dover Publications.

Akerman, C. J., L. Carigi, P. E. Nissen, M. Pettini, and M. Asplund (Feb. 2004). "The Evolution of the C/O Ratio in Metal-Poor Halo Stars." In: *A&A* 414.3, pp. 931–942. ISSN: 0004-6361, 1432-0746. DOI: 10.1051/0004-6361:20034188.

Akiba, Takuya, Shotaro Sano, Toshihiko Yanase, Takeru Ohta, and Masanori Koyama (July 2019). "Optuna: A Next-generation Hyperparameter Optimization Framework." In: *Proc. 25th ACM SIGKDD Int. Conf. Knowl. Discov. Data Min.* KDD '19. New York, NY, USA: Association for Computing Machinery, pp. 2623–2631. ISBN: 978-1-4503-6201-6. DOI: 10.1145/3292500.3330701.

Alfvén, Hannes and B. Lindblad (June 1947). "Granulation, Magneto-Hydrodynamic Waves, and the Heating of the Solar Corona." In: *Monthly Notices of the Royal Astronomical Society* 107.2, pp. 211–219. ISSN: 0035-8711. DOI: 10.1093/mnras/107.2.211.

Allard, France and Peter H. Hauschildt (May 1995). "Model Atmospheres for M (Sub)Dwarfs: I. The Base Model Grid." In: *ApJ* 445, p. 433. ISSN: 0004-637X, 1538-4357. DOI: 10.1086/175708. arXiv: astro-ph/9601150.

Allard, France, Peter H. Hauschildt, David R. Alexander, Akemi Tamanai, and Andreas Schweitzer (July 2001). "The Limiting Effects of Dust in Brown Dwarf Model Atmospheres." In: *ApJ* 556.1, pp. 357–372. ISSN: 0004-637X, 1538-4357. DOI: 10.1086/321547. arXiv: astro-ph/0104256.

Allende Prieto, Carlos (Mar. 2010). "The Stellar Population of the Thin Disk." In: 265, pp. 304–312. DOI: 10.1017/S1743921310000785.

Alpaydin, Ethem (Mar. 2020). *Introduction to Machine Learning, Fourth Edition*. fourth edition. Cambridge, Massachusetts: The MIT Press. ISBN: 978-0-262-04379-3.

Alpher, R. A., H. Bethe, and G. Gamow (Apr. 1948). "The Origin of Chemical Elements." In: *Phys. Rev.* 73, pp. 803–804. ISSN: 1536-6065. DOI: 10.1103/PhysRev.73.803.

Alpher, Ralph A. and Robert C. Herman (Dec. 1948). "On the Relative Abundance of the Elements." In: *Phys. Rev.* 74.12, pp. 1737–1742. DOI: 10.1103/PhysRev.74.1737.

Altrock, Richard C. (Oct. 2004). "The Temperature of the Low Corona During Solar Cycles 21 23." In: *Sol. Phys.* 224, pp. 255–268. ISSN: 0038-0938. DOI: 10.1007/s11207-005-6502-4.

Amarsi, A. M. and M. Asplund (2017). "The Solar Silicon Abundance Based on 3D Non-LTE Calculations." In: *MNRAS* 464.1, pp. 264–273. ISSN: 13652966. DOI: 10.1093/mnras/stw2445.

Amarsi, A. M., P. S. Barklem, R. Collet, N. Grevesse, and M. Asplund (Apr. 2019a). "3D Non-LTE Line Formation of Neutral Carbon in the Sun." In: *A&A* 624, A111. ISSN: 0004-6361. DOI: 10.1051/0004-6361/201833603.

Amarsi, A. M., P. E. Nissen, M. Asplund, K. Lind, and P. S. Barklem (Feb. 2019b). "Carbon and Oxygen in Metal-Poor Halo Stars." In: *Astronomy and Astrophysics* 622, p. L4. ISSN: 0004-6361. DOI: 10.1051/0004-6361/201834480.

Amarsi, A. M., T. Nordlander, P. S. Barklem, M. Asplund, R. Collet, and K. Lind (July 2018). "Effective Temperature Determinations of Late-Type Stars Based on 3D Non-LTE Balmer Line Formation." In: *A&A* 615, A139. ISSN: 0004-6361. DOI: 10.1051/0004-6361/201732546.

Anders, Edward and Nicolas Grevesse (1989). "Abundances of the Elements: Meteoritic and Solar." In: *Geochim. Cosmochim. Acta* 53.1, pp. 197–214. ISSN: 00167037. DOI: 10.1016/0016-7037(89)90286-X.

Anders, F. et al. (Apr. 2014). "Chemodynamics of the Milky Way - I. The First Year of APOGEE Data." In: *A&A* 564, A115. ISSN: 0004-6361, 1432-0746. DOI: 10.1051/0004-6361/201323038.

Anderson, L. D., T. M. Bania, J. M. Jackson, D. P. Clemens, M. Heyer, R. Simon, R. Y. Shah, and J. M. Rathborne (Mar. 2009). "The Molecular Properties of Galactic H II Regions." In: *Astrophys. J. Suppl. Ser.* 181, pp. 255–271. ISSN: 0067-0049. DOI: 10.1088/0067-0049/181/1/255.

Ångström, Anders Jonas (1852). "Kongl. Vetenskaps Academiens Handlingar." In: *R. Swed. Acad. Sci.*

Anstee, S. D. and B. J. O'Mara (Dec. 1991). "An Investigation of Brueckner's Theory of Line Broadening with Application to the Sodium D Lines." In: *MNRAS* 253, pp. 549–560. DOI: 10.1093/mnras/253.3.549.

— (Oct. 1995). "Width Cross-Sections for Collisional Broadening of s-p and p-s Transitions by Atomic Hydrogen." In: *MNRAS* 276, pp. 859–866. DOI: 10.1093/mnras/276.3.859.

Aoki, Wako et al. (Jan. 2013). "High-Resolution Spectroscopy of Extremely Metal-poor Stars from SDSS/SEGUE. I. Atmospheric Parameters and Chemical Compositions." In: *The Astronomical Journal* 145, p. 13. ISSN: 0004-6256. DOI: 10.1088/0004-6256/145/1/13.

Arévalo, A. Vicente, A. Asensio Ramos, and S. Esteban Pozuelo (Nov. 2021). *Accelerating Non-LTE Synthesis and Inversions with Graph Networks*. DOI: 10.48550/arXiv.2111.10552.

Arrhenius, Svante (July 1889a). "Über Die Dissociationswärme Und Den Einfluss Der Temperatur Auf Den Dissociationsgrad Der Elektrolyte." In: *Z. Für Phys. Chem.* 4U.1, pp. 96–116. ISSN: 2196-7156, 0942-9352. DOI: 10.1515/zpch-1889-0408.

— (July 1889b). "Über Die Reaktionsgeschwindigkeit Bei Der Inversion von Rohrzucker Durch Säuren." In: *Z. Für Phys. Chem.* 4U.1, pp. 226–248. ISSN: 2196-7156, 0942-9352. DOI: 10.1515/zpch-1889-0416.

Aschwanden, Markus J. (2006). *Physics of the Solar Corona : An Introduction with Problems and Solutions*. Berlin ; New York : Springer. ISBN: 978-3-540-30765-5.

Asplund, M. (July 2000). "Line Formation in Solar Granulation. III. The Photospheric Si and Meteoritic Fe Abundances." In: *A&A* 359, p. 755. ISSN: 0004-6361.

Asplund, M., A. M. Amarsi, and N. Grevesse (May 2021). "The Chemical Make-up of the Sun: A 2020 Vision." In: *arXiv e-prints* 2105, arXiv:2105.01661.

Asplund, Martin, Nicolas Grevesse, and A Jacques Sauval (2005). "The Solar Chemical Composition." In: p. 14.

Asplund, Martin, Nicolas Grevesse, A. Jacques Sauval, and Pat Scott (Sept. 2009). "The Chemical Composition of the Sun." In: *ARA&A* 47.1, pp. 481–522. ISSN: 0066-4146. DOI: 10.1146/annurev.astro.46.060407.145222.

Avrett, E. H. (Jan. 2003). "The Solar Temperature Minimum and Chromosphere." In: 286, p. 419.

Ayres, Thomas R. and Douglas Rabin (Apr. 1996). "Observations of Solar Carbon Monoxide with an Imaging Infrared Spectrograph. I. Thermal Bifurcation Revisited." In: *Astrophys. J.* 460, p. 1042. ISSN: 0004-637X. DOI: 10.1086/177031.

BRAND, John C. D. (1995). *Lines of Light: The Sources of Dispersive Spectroscopy 1800-1930*. Gordon and Breach Publishers. ISBN: 978-2-88449-162-4.

Baade, W. (Sept. 1944). "The Resolution of Messier 32, NGC 205, and the Central Region of the Andromeda Nebula." In: *Astrophys. J.* 100, p. 137. ISSN: 0004-637X. DOI: 10.1086/144650.

Bahng, J. and M. Schwarzschild (Sept. 1961). "Lifetime of Solar Granules." In: *Astrophys. J.* 134, p. 312. ISSN: 0004-637X. DOI: 10.1086/147160.

Balser, Dana S., Robert T. Rood, T. M. Bania, and L. D. Anderson (Aug. 2011). "H Ii REGION METALLICITY DISTRIBUTION IN THE MILKY WAY DISK." In: *ApJ* 738.1, p. 27. ISSN: 0004-637X. DOI: 10.1088/0004-637X/738/1/27.

Barklem, P. S., S. D. Anstee, and B. J. O'Mara (1998). "Line Broadening Cross Sections for the Broadening of Transitions of Neutral Atoms by Collisions with Neutral Hydrogen." In: *Publ. Astron. Soc. Aust.* ISSN: 13233580. DOI: 10.1071/AS98336.

Barklem, P. S. and J. Aspelund-Johansson (May 2005). "The Broadening of Fe II Lines by Neutral Hydrogen Collisions." In: *A&A* 435.1, p. 373. ISSN: 0004-6361. DOI: 10.1051/0004-6361:20042469.

Barklem, P. S. and R. Collet (Apr. 2016). "Partition Functions and Equilibrium Constants for Diatomic Molecules and Atoms of Astrophysical Interest." In: *A&A* 588, A96. ISSN: 0004-6361. DOI: 10.1051/0004-6361/201526961.

Barklem, P. S. and B. J. O'Mara (Nov. 1998). "The Broadening of Strong Lines of Ca+, Mg+ and Ba+ by Collisions with Neutral Hydrogen Atoms." In: *MNRAS* 300, pp. 863–871. DOI: 10.1046/j.1365-8711.1998.01942.x.

Bartelmann, Matthias (Sept. 2013). *Theoretical Astrophysics: An Introduction*. John Wiley & Sons. ISBN: 978-3-527-66977-6.

Bartels, J. (Jan. 1934). "Twenty-Seven Day Recurrences in Terrestrial-Magnetic and Solar Activity, 1923-1933." In: *Terr. Magn. Atmospheric Electr. J. Geophys. Res.* 39, p. 201. ISSN: 0148-0227. DOI: 10.1029/TE039i003p00201.

Bastian, Nate and Carmela Lardo (Sept. 2018). "Multiple Stellar Populations in Globular Clusters." In: *Annu. Rev. Astron. Astrophys.* 56, pp. 83–136. ISSN: 0066-4146. DOI: 10.1146/annurev-astro-081817-051839.

Baulch, D. L., D. Drysdale, J. Duxbury, and S. J. Grant (1976). *Evaluated Kinetic Data for High Temperature Reactions. Homogeneous Gas Phase Reactions of the 02-03 System, the CO-O2-H2 System, and of Sulphur-Containing Species*. 1st. Vol. 3. London: Butterworths.

Baulch, D. L., D. Drysdale, D. G. Horne, and A. Lloyd (1972). *Evaluated Kinetic Data for High Temperature Reactions*. Vol. 1.

Becker, U., P. Zimmermann, and H. Holweger (Dec. 1980). "Solar and Meteoritic Abundance of Silicon." In: *Geochimica et Cosmochimica Acta* 44.12, pp. 2145–2149. ISSN: 0016-7037. DOI: 10.1016/0016-7037(80)90210-0.

Beer (1852). "Bestimmung Der Absorption Des Rothen Lichts in Farbigen Flüssigkeiten." In: *Ann. Phys.* 162.5, pp. 78–88. ISSN: 1521-3889. DOI: 10.1002/andp.18521620505.

Beers, Timothy C. and Norbert Christlieb (2005). "The Discovery and Analysis of Very Metal-Poor Stars in the Galaxy." In: *Annu. Rev. Astron. Astrophys.* 43.1, pp. 531–580. DOI: 10.1146/annurev.astro.42.053102.134057.

Beers, Timothy C., George W. Preston, and Stephen A. Shectman (June 1992). "A Search for Stars of Very Low Metal Abundance. II." In: *Astron. J.* 103, p. 1987. ISSN: 0004-6256. DOI: 10.1086/116207.

Bekki, K. and K. C. Freeman (Dec. 2003). "Formation of ω Centauri from an Ancient Nucleated Dwarf Galaxy in the Young Galactic Disc." In: *Mon. Not. R. Astron. Soc.* 346, pp. L11–L15. ISSN: 0035-8711. DOI: 10.1046/j.1365-2966.2003.07275.x.

Benjamin, R. A. (May 2008). "The Spiral Structure of the Galaxy: Something Old, Something New..." In: 387, p. 375.

Bensby, T., A. Alves-Brito, M. S. Oey, D. Yong, and J. Meléndez (July 2011). "A First Constraint on the Thick Disk Scale Length: Differential Radial Abundances in K Giants at Galactocentric Radii 4, 8, and 12 Kpc." In: *Astrophys. J.* 735, p. L46. ISSN: 0004-637X. DOI: 10.1088/2041-8205/735/2/L46.

Bensby, Thomas and Sofia Feltzing (Mar. 2010). "The Galactic Thin and Thick Disks in the Context of Galaxy Formation." In: 265, pp. 300–303. DOI: 10.1017/S1743921310000773.

Bergemann, Maria, Rolf-Peter Kudritzki, Matthias Würl, Bertrand Plez, Ben Davies, and Zach Gazak (2013). "Red Supergiant Stars as Cosmic Abundance Probes. II. NLTE Effects in J-band Silicon Lines." In: *ApJ* 764.2, p. 115. ISSN: 0004-637X. DOI: 10.1088/0004-637X/764/2/115.

Bergemann, Maria et al. (Nov. 2019). "Observational Constraints on the Origin of the Elements. I. 3D NLTE Formation of Mn Lines in Late-Type Stars." In: *A&A* 631, A80. ISSN: 0004-6361. DOI: 10.1051/0004-6361/201935811.

Berners-Lee, C. M. (July 1968). "Cybernetics and Forecasting." In: *Nature* 219.5150, pp. 202–203. ISSN: 1476-4687. DOI: 10.1038/219202b0.

Beveridge, Renee C. and Cristopher Sneden (July 1994). "The Chemical Compositions of Two Nitrogen-Rich, Metal-Poor Halo Dwarf Stars." In: *Astron. J.* 108, p. 285. ISSN: 0004-6256. DOI: 10.1086/117068.

Bidelman, William P. and Philip C. Keenan (Nov. 1951). "The Ba II Stars." In: *Astrophys. J.* 114, p. 473. ISSN: 0004-637X. DOI: 10.1086/145488.

Bland-Hawthorn, J. and S. Sharma (Sept. 2016). "GALAH Survey: Chemical Tagging and Disk Reconstruction." In: *Astron. Nachrichten* 337, p. 894. ISSN: 0004-6337. DOI: 10.1002/asna.201612393.

Blecic, Jasmina, Joseph Harrington, and M. Oliver Bowman (July 2016). "TEA: A CODE CALCULATING THERMOCHEMICAL EQUILIBRIUM ABUNDANCES." In: *ApJS* 225.1, p. 4. ISSN: 0067-0049. DOI: 10.3847/0067-0049/225/1/4.

Böhm-Vitense, E. (1958). "Über Die Wasserstoffkonvektionszone in Sternen Verschiedener Effektivtemperaturen Und Leuchtkräfte. Mit 5 Textabbildungen." In: *Zeitschrift fur Astrophysik* 46, p. 108. ISSN: 0372-8331.

Bok, Bart J. (Jan. 1948). "Dimensions and Masses of Dark Nebulae." In: *Harv. Obs. Monogr.* 7, p. 53.

Boltzmann, Ludwig (July 2003). "Further Studies on the Thermal Equilibrium of Gas Molecules." In: *Hist. Mod. Phys. Sci.* 1, pp. 262–349. DOI: 10.1142/9781848161337_0015.

— (1872). "Weitere Studien Über Das Wärmegleichgewicht Unter Gasmolekülen." In: *Sitzungsberichte Akad. Wiss.* 66, pp. 275–370.

Bonifacio, P. et al. (May 2018). "Gaia Confirms That SDSS J102915+172927 Is a Dwarf Star." In: *Res. Notes Am. Astron. Soc.* 2, p. 19. ISSN: 2515-5172. DOI: 10.3847/2515-5172/aac0f4.

Borrero, J. M. (Jan. 2008). "On the Role of Magnetic Fields in Abundance Determinations." In: *ApJ* 673.1, pp. 470–476. ISSN: 0004-637X, 1538-4357. DOI: 10.1086/524099. arXiv: 0709.3809.

Borrero, J. M., L. R. Bellot Rubio, P. S. Barklem, and J. C. del Toro Iniesta (June 2003). "Accurate Atomic Parameters for Near-Infrared Spectral Lines." In: *A&A* 404.2, pp. 749–762. ISSN: 0004-6361, 1432-0746. DOI: 10.1051/0004-6361:20030548.

Bostock, John and H. T. Riley (1898). *The Natural History of Pliny*. Vol. 6. London: George Bell and Sons.

Boulangier, Jels, N Clementel, A J van Marle, L Decin, and A de Koter (Feb. 2019). "Developing a Self-Consistent AGB Wind Model – I. Chemical, Thermal, and Dynamical Coupling." In: *Monthly Notices of the Royal Astronomical Society* 482.4, pp. 5052–5077. ISSN: 0035-8711. DOI: 10.1093/mnras/sty2560.

Bromm, Volker and Richard B. Larson (2004). "The First Stars." In: *Annu. Rev. Astron. Astrophys.* 42.1, pp. 79–118. DOI: 10.1146/annurev.astro.42.053102.134034.

Bubeck, Sébastien et al. (Apr. 2023). *Sparks of Artificial General Intelligence: Early Experiments with GPT-4*. DOI: 10.48550/arXiv.2303.12712. arXiv: 2303.12712 [cs].

Bueno, J. Trujillo, N. Shchukina, and A. Asensio Ramos (July 2004). "A Substantial Amount of Hidden Magnetic Energy in the Quiet Sun." In: *Nature* 430.6997, pp. 326–329. ISSN: 0028-0836, 1476-4687. DOI: 10.1038/nature02669. arXiv: astro-ph/0409004.

Burbidge, E. Margaret, G. R. Burbidge, William A. Fowler, and F. Hoyle (Oct. 1957). "Synthesis of the Elements in Stars." In: *Rev. Mod. Phys.* 29.4, pp. 547–650. DOI: 10.1103/RevModPhys.29.547.

Burgess, C. and K. D. Mielenz (Dec. 2012). *Advances in Standards and Methodology in Spectrophotometry*. Elsevier. ISBN: 978-0-444-59905-6.

Burstein, D. (Dec. 1979). "Structure and Origin of So Galaxies. III. The Luminosity Distribution Perpendicular to the Plane of the Disks in So's." In: *Astrophys. J.* 234, pp. 829–836. ISSN: 0004-637X. DOI: 10.1086/157563.

Cabrera-Lavers, A., C. González-Fernández, F. Garzón, P. L. Hammersley, and M. López-Corredoira (Dec. 2008). "The Long Galactic Bar as Seen by UKIDSS Galactic Plane Survey." In: *Astron. Astrophys.* 491, pp. 781–787. ISSN: 0004-6361. DOI: 10.1051/0004-6361:200810720.

Caffau, E., H.-G. Ludwig, M. Steffen, B. Freytag, and P. Bonifacio (Feb. 2011a). "Solar Chemical Abundances Determined with a CO5BOLD 3D Model Atmosphere." In: *Sol Phys* 268.2, pp. 255–269. ISSN: 1573-093X. DOI: 10.1007/s11207-010-9541-4.

Caffau, E., H.-G. Ludwig, M. Steffen, W. Livingston, P. Bonifacio, J.-M. Malherbe, H.-P. Doerr, and W. Schmidt (July 2015). "The Photospheric Solar Oxygen Project. III. Investigation of the Centre-to-Limb Variation of the 630 Nm [O I]-Ni I Blend." In: *A&A* 579, A88. ISSN: 0004-6361. DOI: 10.1051/0004-6361/201526331.

Caffau, Elisabetta et al. (Sept. 2011b). "An Extremely Primitive Star in the Galactic Halo." In: *Nature* 477, pp. 67–69. ISSN: 0028-0836. DOI: 10.1038/nature10377.

Calder, Alan C., Bruce Fryxell, T. Plewa, Robert Rosner, L. J. Dursi, V. G. Weirs, T. Dupont, H. F. Robey, J. O. Kane, and B. A. Remington (2002). "On Validating an Astrophysical Simulation Code." In: *Astrophys. J. Suppl. Ser.* 143.1, p. 201.

Cannon, Annie J. and Edward C. Pickering (Jan. 1901). "Spectra of Bright Southern Stars Photographed with the 13-Inch Boyden Telescope as Part of the Henry Draper Memorial." In: *Ann. Harv. Coll. Obs.* 28, 129–P.6.

Cannon, Annie Jump and Edward Charles Pickering (Jan. 1912). "Classification of 1,688 Southern Stars by Means of Their Spectra." In: *Ann. Harv. Coll. Obs.* 56, pp. 115–164.

Carollo, Daniela, Ken Freeman, Timothy C. Beers, Vinicius M. Placco, Jason Tumlinson, and Sarah L. Martell (June 2014). "CARBON-ENHANCED METAL-POOR STARS: CEMP-sand CEMP-no SUBCLASSES IN THE HALO SYSTEM OF THE MILKY WAY." In: *ApJ* 788.2, p. 180. ISSN: 0004-637X. DOI: 10.1088/0004-637X/788/2/180.

Carroll, Bradley W. and Dale A. Ostlie (2014). *An Introduction to Modern Astrophysics*. Pearson. ISBN: 978-1-292-02293-2.

Cattaneo, Fausto, Thierry Emonet, and Nigel Weiss (May 2003). "On the Interaction between Convection and Magnetic Fields." In: *ApJ* 588.2, p. 1183. ISSN: 0004-637X. DOI: 10.1086/374313.

Caudal, J., B. Fiorina, M. Massot, B. Labégorre, N. Darabiha, and O. Gicquel (Jan. 2013). "Characteristic Chemical Time Scales Identification in Reactive Flows." In: *Proceedings of the Combustion Institute* 34.1, pp. 1357–1364. ISSN: 1540-7489. DOI: 10.1016/j.proci.2012.06.178.

Cayrel, R. et al. (Feb. 2001). "Measurement of Stellar Age from Uranium Decay." In: *Nature* 409.6821, pp. 691–692. ISSN: 1476-4687. DOI: 10.1038/35055507.

Chabrier, Gilles, Patrick Hennebelle, and Stéphane Charlot (Nov. 2014). "VARIATIONS OF THE STELLAR INITIAL MASS FUNCTION IN THE PROGENITORS OF MASSIVE EARLY-TYPE GALAXIES AND IN EXTREME STARBURST ENVIRONMENTS." In: *ApJ* 796.2, p. 75. ISSN: 0004-637X. DOI: 10.1088/0004-637X/796/2/75.

Chen, Ricky T. Q., Yulia Rubanova, Jesse Bettencourt, and David Duvenaud (June 2018). *Neural Ordinary Differential Equations*. DOI: 10.48550/arXiv.1806.07366.

"Front Matter" (Jan. 1974). In: *Spectroscopy in Biology and Chemistry*. Ed. by Sow-Hsin Chen and Sidney Yip. Academic Press, p. iii. ISBN: 978-0-12-170850-4. DOI: 10.1016/B978-0-12-170850-4.50001-8.

Cheung, M. C. M., M. Schuessler, T. D. Tarbell, and A. M. Title (Nov. 2008). "Solar Surface Emerging Flux Regions: A Comparative Study of Radiative MHD Modeling and Hinode SOT Observations." In: *ApJ* 687.2, pp. 1373–1387. ISSN: 0004-637X, 1538-4357. DOI: 10.1086/591245. arXiv: 0810.5723.

Cho, Kyunghyun, Bart van Merrienboer, Caglar Gulcehre, Dzmitry Bahdanau, Fethi Bougares, Holger Schwenk, and Yoshua Bengio (Sept. 2014). *Learning Phrase Representations Using RNN Encoder-Decoder for Statistical Machine Translation*. DOI: 10.48550/arXiv.1406.1078. arXiv: 1406.1078 [cs, stat].

Churchwell, Ed et al. (Mar. 2009). "The Spitzer/GLIMPSE Surveys: A New View of the Milky Way." In: *Publ. Astron. Soc. Pac.* 121, p. 213. ISSN: 0004-6280. DOI: 10.1086/597811.

Cirtain, J. W. et al. (Jan. 2013). "Energy Release in the Solar Corona from Spatially Resolved Magnetic Braids." In: *Nature* 493.7433, pp. 501–503. ISSN: 1476-4687. DOI: 10.1038/nature11772.

Close, Laird M., Niranjan Thatte, Eric L. Nielsen, Roberto Abuter, Fraser Clarke, and Matthias Tecza (Aug. 2007). "New Photometry and Spectra of AB Doradus C: An Accurate Mass Determination of a Young Low-Mass Object with Theoretical Evolutionary Tracks*." In: *ApJ* 665.1, p. 736. ISSN: 0004-637X. DOI: 10.1086/518207.

Cohen, Judith G., Stephen Shectman, Ian Thompson, Andrew McWilliam, Norbert Christlieb, Jorge Melendez, Franz-Josef Zickgraf, Solange Ramírez, and Amber Swenson (Nov. 2005). "The Frequency of Carbon Stars among Extremely Metal-poor Stars." In: *Astrophys. J.* 633, pp. L109–L112. ISSN: 0004-637X. DOI: 10.1086/498502.

Colella, Phillip and Paul R Woodward (Apr. 1984). "The Piecewise Parabolic Method (PPM) for Gas-Dynamical Simulations." In: *Journal of Computational Physics* 54.1, pp. 174–201. ISSN: 0021-9991. DOI: 10.1016/0021-9991(84)90143-8.

Collaboration, Event Horizon Telescope et al. (May 2022). "First Sagittarius A* Event Horizon Telescope Results. I. The Shadow of the Supermassive Black Hole in the Center of the Milky Way." In: *ApJL* 930.2, p. L12. ISSN: 2041-8205. DOI: 10.3847/2041-8213/ac6674.

Collet, Remo, Zazralt Magic, and Martin Asplund (Dec. 2011). "The StaggerGrid Project: A Grid of 3-D Model Atmospheres for High-Precision Spectroscopy." In: 328, p. 012003. DOI: 10.1088/1742-6596/328/1/012003.

Cowan, John J. et al. (June 2002). "The Chemical Composition and Age of the Metal-poor Halo Star BD +17°3248." In: *Astrophys. J.* 572, pp. 861–879. ISSN: 0004-637X. DOI: 10.1086/340347.

Dame, T. M., Dap Hartmann, and P. Thaddeus (Feb. 2001). "The Milky Way in Molecular Clouds: A New Complete CO Survey." In: *Astrophys. J.* 547, pp. 792–813. ISSN: 0004-637X. DOI: 10.1086/318388.

Dauphole, B., M. Geffert, J. Colin, C. Ducourant, M. Odenkirchen, and H. J. Tucholke (Sept. 1996). "The Kinematics of Globular Clusters, Apocentric Distances and a Halo Metallicity Gradient." In: *Astron. Astrophys.* 313, pp. 119–128. ISSN: 0004-6361.

De, Shaunak, Abhishek Maity, Vritti Goel, Sanjay Shitole, and Avik Bhattacharya (Apr. 2017). "Predicting the Popularity of Instagram Posts for a Lifestyle Magazine Using Deep Learning." In: *2017 2nd Int. Conf. Commun. Syst. Comput. IT Appl. CSCITA*, pp. 174–177. DOI: 10.1109/CSCITA.2017.8066548.

Delbouille, L., G. Roland, and L. Neven (1973). "Atlas Photometrique Du Spectre Solaire de [Lambda] 3000 a [Lambda] 10000." In: *Liege: Universite de Liege, Institut d'Astrophysique, 1973*.

Deshmukh, S. A. and H.-G. Ludwig (July 2023). "Implications of Time-Dependent Molecular Chemistry in Metal-Poor Dwarf Stars." In: *A&A* 675, A146. ISSN: 0004-6361, 1432-0746. DOI: 10.1051/0004-6361/202345985.

Deshmukh, S. A., H.-G. Ludwig, A. Kučinskas, M. Steffen, P. S. Barklem, E. Caffau, V. Dobrovolskas, and P. Bonifacio (Dec. 2022). "The Solar Photospheric Silicon Abundance According to CO5BOLD - Investigating Line Broadening, Magnetic Fields, and Model Effects." In: *A&A* 668, A48. ISSN: 0004-6361, 1432-0746. DOI: 10.1051/0004-6361/202142072.

Dijkstra, E. W. (Dec. 1959). "A Note on Two Problems in Connexion with Graphs." In: *Numer. Math.* 1.1, pp. 269–271. ISSN: 0945-3245. DOI: 10.1007/BF01386390.

Doerr, H.-P., N. Vitas, and D. Fabbian (2016). "How Different Are the Li\'ege and Hamburg Atlases of the Solar Spectrum?" In: *A&A* 590, A118. ISSN: 0004-6361, 1432-0746. DOI: 10.1051/0004-6361/201628570. arXiv: 1604.03748.

Dorfi, E. A. and L. O.C. Drury (1987). "Simple Adaptive Grids for 1 - D Initial Value Problems." In: *J. Comput. Phys.* ISSN: 10902716. DOI: 10.1016/0021-9991(87)90161-6.

Drawin, H. W. (July 1967). *COLLISION AND TRANSPORT CROSS-SECTIONS*. Tech. rep. EUR-CEA-FC-383(Rev.) European Atomic Energy Community. Commissariat a l'Energie Atomique, Fontenay-aux-Roses (France). Centre d'Etudes Nucleaires.

Drimmel, R. (2000). "Evidence for a Two-Armed Spiral in the Milky Way." In: *Astron. Astrophys.* 358, pp. L13–L16. ISSN: 0004-6361. DOI: 10.48550/arXiv.astro-ph/0005241.

Dutta, Jayanta, Sharanya Sur, Athena Stacy, and Jasjeet Singh Bagla (Sept. 2020). "Modeling the Survival of Population III Stars to the Present Day." In: *Astrophys. J.* 901, p. 16. ISSN: 0004-637X. DOI: 10.3847/1538-4357/abadf8.

Einstein, Albert (Jan. 1916). "Strahlungs-Emission Und Absorption Nach Der Quantentheorie." In: *Dtsch. Phys. Ges.* 18, pp. 318–323.

Epstein, Paul S. (1916). "Zur Theorie Des Starkeffektes." In: *Ann. Phys.* 355.13, pp. 489–520. ISSN: 1521-3889. DOI: 10.1002/andp.19163551302.

Érdi, Péter and János Tóth (1989). *Mathematical Models of Chemical Reactions: Theory and Applications of Deterministic and Stochastic Models*. Manchester University Press. ISBN: 978-0-7190-2208-1.

Evans, M. J., C. Petre, P. R. Medwell, and A. Parente (Jan. 2019). "Generalisation of the Eddy-Dissipation Concept for Jet Flames with Low Turbulence and Low Damköhler Number." In: *Proceedings of the Combustion Institute* 37.4, pp. 4497–4505. ISSN: 1540-7489. DOI: 10.1016/j.proci.2018.06.017.

F.R.S, Karl Pearson (Nov. 1901). "LIII. On Lines and Planes of Closest Fit to Systems of Points in Space." In: *Lond. Edinb. Dublin Philos. Mag. J. Sci.* 2.11, pp. 559–572. ISSN: 1941-5982. DOI: 10.1080/14786440109462720.

Fabbian, D., E. Khomenko, F. Moreno-Insertis, and Å Nordlund (Dec. 2010). "Solar Abundance Corrections Derived through 3D Magnetoconvection Simulations." In:

ApJ 724.2, pp. 1536–1541. ISSN: 0004-637X, 1538-4357. DOI: 10.1088/0004-637X/724/2/1536. arXiv: 1006.0231.

Fabbian, D. and F. Moreno-Insertis (Mar. 2015). "Continuum Intensity and [O I] Spectral Line Profiles in Solar 3D Photospheric Models: The Effect of Magnetic Fields." In: *ApJ* 802.2, p. 96. ISSN: 1538-4357. DOI: 10.1088/0004-637X/802/2/96. arXiv: 1501.06916.

Fabbian, D., F. Moreno-Insertis, E. Khomenko, and Å Nordlund (Dec. 2012). "Solar Fe Abundance and Magnetic Fields - Towards a Consistent Reference Metallicity." In: *A&A* 548, A35. ISSN: 0004-6361, 1432-0746. DOI: 10.1051/0004-6361/201219335. arXiv: 1209.2771.

Fath, Edward Arthur (Jan. 1909). "The Spectra of Some Spiral Nebulae and Globular Star Clusters." In: *Lick Obs. Bull.* 149, pp. 71–77. ISSN: 0075-9317. DOI: 10.5479/ADS/bib/1909LicOB.5.71F.

Ferziger, Joel H., Milovan Perić, and Robert L. Street (2020). *Computational Methods for Fluid Dynamics*. Cham: Springer International Publishing. ISBN: 978-3-319-99691-2 978-3-319-99693-6. DOI: 10.1007/978-3-319-99693-6.

Fix, John (Mar. 2010). *Astronomy: Journey to the Cosmic Frontier*. 6th edition. New York: McGraw-Hill Education. ISBN: 978-0-07-351218-1.

Foead, Daniel, Alifio Ghifari, Marchel Budi Kusuma, Novita Hanafiah, and Eric Gunawan (Jan. 2021). "A Systematic Literature Review of A* Pathfinding." In: *Procedia Computer Science*. 5th International Conference on Computer Science and Computational Intelligence 2020 179, pp. 507–514. ISSN: 1877-0509. DOI: 10.1016/j.procs.2021.01.034.

Fosbury, R. A. E. et al. (Oct. 2003). "Massive Star Formation in a Gravitationally Lensed H II Galaxy at z = 3.357." In: *Astrophys. J.* 596, pp. 797–809. ISSN: 0004-637X. DOI: 10.1086/378228.

Foucault, Jean Bernard Léon (1849). "Lumière Électrique." In: *Société Philomatique Paris* 13, pp. 1–310. ISSN: 0366-3515.

Foukal, P. V. (Dec. 1976). "The Pressure and Energy Balance of the Cool Corona over Sunspots." In: *Astrophys. J.* 210, pp. 575–581. ISSN: 0004-637X. DOI: 10.1086/154862.

Frebel, A. (May 2010). "Stellar Archaeology: Exploring the Universe with Metal-Poor Stars." In: *Astron. Nachrichten* 331.5, pp. 474–488. ISSN: 0004-6337. DOI: 10.1002/asna.201011362.

Frebel, Anna and Alexander P. Ji (Feb. 2023). *Observations of R-Process Stars in the Milky Way and Dwarf Galaxies*.

Frebel, Anna and John E. Norris (Jan. 2013). *Metal-Poor Stars and the Chemical Enrichment of the Universe*. Vol. 5, p. 55. DOI: 10.1007/978-94-007-5612-0_3.

Freytag, B., M. Steffen, H. G. Ludwig, S. Wedemeyer-Böhm, W. Schaffenberger, and O. Steiner (Feb. 2012). "Simulations of Stellar Convection with CO5BOLD." In: *Journal of Computational Physics*. Special Issue: Computational Plasma Physics 231.3, pp. 919–959. ISSN: 0021-9991. DOI: 10.1016/j.jcp.2011.09.026.

GRAVITY Collaboration et al. (May 2019). "A Geometric Distance Measurement to the Galactic Center Black Hole with 0.3% Uncertainty." In: *Astron. Astrophys.* 625, p. L10. ISSN: 0004-6361. DOI: 10.1051/0004-6361/201935656.

Gabrielse, Gerald and Hans Dehmelt (July 1985). "Observation of Inhibited Spontaneous Emission." In: *Phys. Rev. Lett.* 55, pp. 67–70. ISSN: 0031-9007. DOI: 10.1103/PhysRevLett.55.67.

Gaia Collaboration et al. (June 2022). *Gaia Data Release 3: Chemical Cartography of the Milky Way*.

Gallagher, A. J., E. Caffau, P. Bonifacio, H.-G. Ludwig, M. Steffen, D. Homeier, and B. Plez (Feb. 2017a). "An In-Depth Spectroscopic Examination of Molecular Bands

from 3D Hydrodynamical Model Atmospheres. II. Carbon-enhanced Metal-Poor 3D Model Atmospheres." In: *Astronomy and Astrophysics* 598, p. L10. ISSN: 0004-6361. DOI: 10.1051/0004-6361/201630272.

Gallagher, A. J., E. Caffau, P. Bonifacio, H.-G. Ludwig, M. Steffen, and M. Spite (Sept. 2016). "An In-Depth Spectroscopic Examination of Molecular Bands from 3D Hydrodynamical Model Atmospheres. I. Formation of the G-band in Metal-Poor Dwarf Stars." In: *Astron. Astrophys.* 593, A48. ISSN: 0004-6361. DOI: 10.1051/0004-6361/201628602.

Gallagher, A. J., M. Steffen, E. Caffau, P. Bonifacio, H.-G. Ludwig, and B. Freytag (2017b). "Enhanced Methods for Computing Spectra from CO5BOLD Models Using Linfor3D. Molecular Bands in Metal-Poor Stars." In: *Memorie della Societa Astronomica Italiana* 88, p. 82. ISSN: 0037-8720.

Garaud, Pascale (2020). "The Tachocline Revisited." In: *Dyn. Sun Stars*. Ed. by Mário J. P. F. G. Monteiro, Rafael A. García, Jørgen Christensen-Dalsgaard, and Scott W. McIntosh. Astrophysics and Space Science Proceedings. Cham: Springer International Publishing, pp. 207–220. ISBN: 978-3-030-55336-4. DOI: 10.1007/978-3-030-55336-4_29.

Garcia Ruiz, R. F. et al. (May 2020). "Spectroscopy of Short-Lived Radioactive Molecules." In: *Nature* 581.7809, pp. 396–400. ISSN: 1476-4687. DOI: 10.1038/s41586-020-2299-4.

Garz, T. (1973). "Absolute Oscillator Strengths of Si I Lines between 2500 A and 8000 A." In: *A&A* 26, pp. 471–477.

Gent, Matthew Raymond, Phillip Eitner, Chervin F. P. Laporte, Aldo Serenelli, Sergey E. Koposov, and Maria Bergemann (June 2022a). *The Prince and The Pauper: Co-evolution of the Thin and Thick Disc in the Milky Way*. DOI: 10.48550/arXiv.2206.10949.

Gent, Matthew Raymond et al. (Feb. 2022b). "The SAPP Pipeline for the Determination of Stellar Abundances and Atmospheric Parameters of Stars in the Core Program of the PLATO Mission." In: *A&A* 658, A147. ISSN: 0004-6361, 1432-0746. DOI: 10.1051/0004-6361/202140863.

Genton, Marc G. (Mar. 2002). "Classes of Kernels for Machine Learning: A Statistics Perspective." In: *J. Mach. Learn. Res.* 2, pp. 299–312. ISSN: 1532-4435.

Gerber, Jeffrey M., Ekaterina Magg, Bertrand Plez, Maria Bergemann, Ulrike Heiter, Terese Olander, and Richard Hoppe (June 2022). *Non-LTE Radiative Transfer with Turbospectrum*.

Gerhard, Ortwin (Jan. 2002). "Mass Distribution in Our Galaxy." In: *Space Sci. Rev.* 100, pp. 129–138. ISSN: 0038-6308. DOI: 10.1023/A:1015818111633.

Géron, Aurélien (Nov. 2022). *Hands-On Machine Learning with Scikit-Learn, Keras, and TensorFlow: Concepts, Tools, and Techniques to Build Intelligent Systems*. 3rd edition. Beijing Boston Farnham Sebastopol Tokyo: O'Reilly Media. ISBN: 978-1-09-812597-4.

Gilmore, G. and N. Reid (Mar. 1983). "New Light on Faint Stars - III. Galactic Structure towards the South Pole and the Galactic Thick Disc." In: *Mon. Not. R. Astron. Soc.* 202, pp. 1025–1047. ISSN: 0035-8711. DOI: 10.1093/mnras/202.4.1025.

Gilmore, G. et al. (Mar. 2012). "The Gaia-ESO Public Spectroscopic Survey." In: *The Messenger* 147, pp. 25–31. ISSN: 0722-6691.

Goh, Garrett B., Nathan O. Hodas, and Abhinav Vishnu (2017). "Deep Learning for Computational Chemistry." In: *J. Comput. Chem.* 38.16, pp. 1291–1307. ISSN: 1096-987X. DOI: 10.1002/jcc.24764.

Gontcharov, George A, Maxim Yu Khovritchev, Aleksandr V Mosenkov, Vladimir B Il'in, Alexander A Marchuk, Sergey S Savchenko, Anton A Smirnov, Pavel A Usachev, and Denis M Poliakov (Dec. 2021). "Isochrone Fitting of Galactic Globular Clusters – III. NGC 288, NGC 362, and NGC 6218 (M12)." In: *Monthly Notices of the Royal*

Astronomical Society 508.2, pp. 2688–2705. ISSN: 0035-8711. DOI: 10.1093/mnras/stab2756.

González Hernández, J. I. et al. (Nov. 2020). "The Solar Gravitational Redshift from HARPS-LFC Moon Spectra⋆. A Test of the General Theory of Relativity." In: *A&A* 643, A146. ISSN: 0004-6361. DOI: 10.1051/0004-6361/202038937.

González, M., N. Vaytet, B. Commerçon, and J. Masson (June 2015). "Multigroup Radiation Hydrodynamics with Flux-Limited Diffusion and Adaptive Mesh Refinement." In: *A&A* 578, A12. ISSN: 0004-6361, 1432-0746. DOI: 10.1051/0004-6361/201525971.

Goodfellow, Ian J., Jean Pouget-Abadie, Mehdi Mirza, Bing Xu, David Warde-Farley, Sherjil Ozair, Aaron Courville, and Yoshua Bengio (June 2014). "Generative Adversarial Networks." In: *ArXiv14062661 Cs Stat*. arXiv: 1406.2661 [cs, stat].

Goodstein, David L. (Jan. 1985). *States of Matter*. Courier Corporation. ISBN: 978-0-486-64927-6.

Goodwin, S. P., J. Gribbin, and M. A. Hendry (Aug. 1998). "The Relative Size of the Milky Way." In: *The Observatory* 118, pp. 201–208. ISSN: 0029-7704.

Gorban, A. N. (Jan. 2014). "Detailed Balance in Micro- and Macrokinetics and Micro-Distinguishability of Macro-Processes." In: *Results in Physics* 4, pp. 142–147. ISSN: 2211-3797. DOI: 10.1016/j.rinp.2014.09.002.

Grassi, T., S. Bovino, F. A. Gianturco, P. Baiocchi, and E. Merlin (Sept. 2012). "Complexity Reduction of Astrochemical Networks." In: *Monthly Notices of the Royal Astronomical Society* 425, pp. 1332–1340. ISSN: 0035-8711. DOI: 10.1111/j.1365-2966.2012.21537.x.

Grassi, T., S. Bovino, D. R. G. Schleicher, J. Prieto, D. Seifried, E. Simoncini, and F. A. Gianturco (Apr. 2014). "KROME - a Package to Embed Chemistry in Astrophysical Simulations." In: *Monthly Notices of the Royal Astronomical Society* 439, pp. 2386–2419. DOI: 10.1093/mnras/stu114.

Gratton, Raffaele, Angela Bragaglia, Eugenio Carretta, Valentina D'Orazi, Sara Lucatello, and Antonio Sollima (Nov. 2019). "What Is a Globular Cluster? An Observational Perspective." In: *Astron. Astrophys. Rev.* 27, p. 8. ISSN: 0935-4956. DOI: 10.1007/s00159-019-0119-3.

Gray, D. F. (2008). *The Observation and Analysis of Stellar Photospheres*. Cambridge Univ. Press, Cambridge.

Gray, Richard and Christopher Corbally (2009). *Stellar Spectral Classification*. Princeton University Press.

Green, Paul (Mar. 2013). "Innocent Bystanders: Carbon Stars from the Sloan Digital Sky Survey." In: *Astrophys. J.* 765, p. 12. ISSN: 0004-637X. DOI: 10.1088/0004-637X/765/1/12.

Grevesse, N., M. Asplund, A. J. Sauval, and P. Scott (July 2010). "The Chemical Composition of the Sun." In: *Astrophys Space Sci* 328.1, pp. 179–183. ISSN: 1572-946X. DOI: 10.1007/s10509-010-0288-z.

Grevesse, N. and A. J. Sauval (May 1998). "Standard Solar Composition." In: *Space Science Reviews* 85, pp. 161–174. ISSN: 0038-6308. DOI: 10.1023/A:1005161325181.

Greydanus, Samuel, Misko Dzamba, and Jason Yosinski (2019). "Hamiltonian Neural Networks." In: *Adv. Neural Inf. Process. Syst.* Ed. by H. Wallach, H. Larochelle, A. Beygelzimer, F. dAlché-Buc, E. Fox, and R. Garnett. Vol. 32. Curran Associates, Inc.

Griewank, Andreas (Jan. 2012). "Who Invented the Reverse Mode of Differentiation?" In: *Optimization Stories*, pp. 389–400. ISBN: 978-3-936609-58-5. DOI: 10.4171/dms/6/38.

Gudiksen, B. V., M. Carlsson, V. H. Hansteen, W. Hayek, J. Leenaarts, and J. Martínez-Sykora (July 2011). "The Stellar Atmosphere Simulation Code Bifrost - Code Description and Validation." In: *A&A* 531, A154. ISSN: 0004-6361, 1432-0746. DOI: 10.1051/0004-6361/201116520.

Gustafsson, B. (1975). "A Grid of Model Atmospheres for Metal-Deficient Stars I." In: *A&A* 42, pp. 407–432.

Gustafsson, B., B. Edvardsson, K. Eriksson, U. G. Jørgensen, Å Nordlund, and B. Plez (Aug. 2008). "A Grid of MARCS Model Atmospheres for Late-Type Stars. I. Methods and General Properties." In: *Astron. Astrophys. Vol. 486 Issue 3 2008 Pp951-970* 486.3, p. 951. ISSN: 0004-6361. DOI: 10.1051/0004-6361:200809724.

Hahnloser, Richard H. R., Rahul Sarpeshkar, Misha A. Mahowald, Rodney J. Douglas, and H. Sebastian Seung (June 2000). "Digital Selection and Analogue Amplification Coexist in a Cortex-Inspired Silicon Circuit." In: *Nature* 405.6789, pp. 947–951. ISSN: 1476-4687. DOI: 10.1038/35016072.

Haken, Hermann and Hans Christoph Wolf (1996). *The Physics of Atoms and Quanta*. Berlin, Heidelberg: Springer. ISBN: 978-3-642-97691-9 978-3-642-97689-6. DOI: 10.1007/978-3-642-97689-6.

Hammes, Gordon (2005). "Fundamentals of Spectroscopy." In: *Spectroscopy for the Biological Sciences*. John Wiley & Sons, Ltd. Chap. 1, pp. 1–15. ISBN: 978-0-471-73355-3. DOI: 10.1002/0471733555.ch1.

Han, Jun and Claudio Moraga (1995). "The Influence of the Sigmoid Function Parameters on the Speed of Backpropagation Learning." In: *Nat. Artif. Neural Comput.* Ed. by José Mira and Francisco Sandoval. Lecture Notes in Computer Science. Berlin, Heidelberg: Springer, pp. 195–201. ISBN: 978-3-540-49288-7. DOI: 10.1007/3-540-59497-3_175.

Hansen, C. J., B. Nordström, T. T. Hansen, C. R. Kennedy, V. M. Placco, T. C. Beers, J. Andersen, G. Cescutti, and C. Chiappini (Apr. 2016). "Abundances of Carbon-Enhanced Metal-Poor Stars as Constraints on Their Formation." In: *Astron. Astrophys.* 588, A37. ISSN: 0004-6361. DOI: 10.1051/0004-6361/201526895.

Hansen, Carl J., Steven D. Kawaler, and Virginia Trimble (2004). *Stellar Interiors: Physical Principles, Structure, and Evolution*. Ed. by I. Appenzeller, G. Börner, A. Burkert, M. A. Dopita, M. Harwit, R. Kippenhahn, J. Lequeux, A. Maeder, and V. Trimble. Astronomy and Astrophysics Library. New York, NY: Springer. ISBN: 978-1-4612-6497-2 978-1-4419-9110-2. DOI: 10.1007/978-1-4419-9110-2.

Harmer, D. L. and B. E. J. Pagel (Jan. 1973). "Stellar CN Band Strengths and the Abundance of Nitrogen." In: *Mon. Not. R. Astron. Soc.* 165, pp. 91–120. ISSN: 0035-8711. DOI: 10.1093/mnras/165.1.91.

Harris, W. E. (Dec. 1976). "Spatial Structure of the Globular Cluster System and the Distance to the Galactic Center." In: *Astron. J.* 81, pp. 1095–1116. ISSN: 0004-6256. DOI: 10.1086/111991.

Harris, William E. (Oct. 1996). "A Catalog of Parameters for Globular Clusters in the Milky Way." In: *Astron. J.* 112, p. 1487. ISSN: 0004-6256. DOI: 10.1086/118116.

He, Kaiming, Xiangyu Zhang, Shaoqing Ren, and Jian Sun (Dec. 2015). "Deep Residual Learning for Image Recognition." In: *ArXiv151203385 Cs*. arXiv: 1512.03385 [cs].

Heiter, U. et al. (Jan. 2021). "Atomic Data for the Gaia-ESO Survey." In: *A&A* 645, A106. ISSN: 0004-6361. DOI: 10.1051/0004-6361/201936291.

Henyey, Louis, M. S. Vardya, and Peter Bodenheimer (Oct. 1965). "Studies in Stellar Evolution. III. The Calculation of Model Envelopes." In: *ApJ* 142, p. 841. ISSN: 0004-637X, 1538-4357. DOI: 10.1086/148357.

Herschel, John (1823). "On the Absorption of Light by Coloured Media, and on the Colours of the Prismatic Spectrum Exhibited by Certain Flames; with an Account of a Ready Mode of Determining the Absolute Dispersive Power of Any Medium, by Direct Experiment." In: Transactions of the Royal Society of Edinburgh 2.

Hertzsprung, Ejnar (Jan. 1909). "Über Die Sterne Der Unterabteilungen c Und Ac Nach Der Spektralklassifikation von Antonia C. Maury." In: *Astron. Nachrichten* 179, p. 373. ISSN: 0004-6337. DOI: 10.1002/asna.19081792402.

— (Jan. 1911). "Ueber Die Verwendung Photographischer Effektiver Wellenlaengen Zur Bestimmung von Farbenaequivalenten." In: *Publ. Astrophys. Obs. Zu Potsdam* 63.

Hilborn, Robert C. (Nov. 1982). "Einstein Coefficients, Cross Sections, f Values, Dipole Moments, and All That." In: *Am. J. Phys.* 50, pp. 982–986. ISSN: 0002-9505. DOI: 10.1119/1.12937.

Hills, J. G. (Feb. 1980). "The Effect of Mass Loss on the Dynamical Evolution of a Stellar System - Analytic Approximations." In: *Astrophys. J.* 235, pp. 986–991. ISSN: 0004-637X. DOI: 10.1086/157703.

Hindmarsh, Alan C., Peter N. Brown, Keith E. Grant, Steven L. Lee, Radu Serban, Dan E. Shumaker, and Carol S. Woodward (Sept. 2005). "SUNDIALS: Suite of Nonlinear and Differential/Algebraic Equation Solvers." In: *ACM Trans. Math. Softw.* 31.3, pp. 363–396. ISSN: 0098-3500. DOI: 10.1145/1089014.1089020.

Hinkel, Natalie R., Patrick A. Young, and Caleb H. Wheeler III (Dec. 2022). "A Concise Treatise on Converting Stellar Mass Fractions to Abundances to Molar Ratios." In: *Astron. J.* 164, p. 256. ISSN: 0004-6256. DOI: 10.3847/1538-3881/ac9bfa.

Ho, Anna Y. Q., Melissa Ness, David W. Hogg, and Hans-Walter Rix (Feb. 2016). "The Cannon: Data-driven Method for Determining Stellar Parameters and Abundances from Stellar Spectra." In: *Astrophysics Source Code Library*, ascl:1602.010.

Holweger, H. (Jan. 1967). "Ein Empirisches Modell Der Sonnenatmosphäre Mit Lokalem Thermodynamischem Gleichgewicht." In: *Z. Astrophys.* 65, p. 365. ISSN: 0372-8331.

— (Nov. 2001). "Photospheric Abundances: Problems, Updates, Implications." In: *AIP Conference Proceedings* 598.1, pp. 23–30. ISSN: 0094-243X. DOI: 10.1063/1.1433974. arXiv: astro-ph/0107426.

— (July 1973). "The Solar Abundance of Silicon." In: *A&A* 26, p. 275. ISSN: 0004-6361.

Holweger, H. and E. A. Mueller (Nov. 1974). "The Photospheric Barium Spectrum: Solar Abundance and Collision Broadening of Ba II Lines by Hydrogen." In: *Sol. Phys.* 39, pp. 19–30. ISSN: 0038-0938. DOI: 10.1007/BF00154968.

Hooke, Robert (1665). *MicrographiaSome Physiological Descriptions of Minute Bodies Made by Magnifying Glasses with Observations and Inquiries Thereupon*.

Horn, F. (Jan. 1972). "Necessary and Sufficient Conditions for Complex Balancing in Chemical Kinetics." In: *Arch. Rational Mech. Anal.* 49.3, pp. 172–186. ISSN: 1432-0673. DOI: 10.1007/BF00255664.

Horn, F. and R. Jackson (Jan. 1972). "General Mass Action Kinetics." In: *Arch. Rational Mech. Anal.* 47.2, pp. 81–116. ISSN: 1432-0673. DOI: 10.1007/BF00251225.

Huang, T. (1996). *Computer Vision: Evolution And Promise*. CERN.

Hubeny, Ivan, Carlos Allende Prieto, Yeisson Osorio, and Thierry Lanz (Apr. 2021). *TLUSTY and SYNSPEC Users's Guide IV: Upgraded Versions 208 and 54*. DOI: 10.48550/arXiv.2104.02829.

Hubeny, Ivan and Dmitri Mihalas (2015). *Theory of Stellar Atmospheres*. Princeton Series in Astrophysics. Princeton University Press.

Huggins, William (1868). "Further Observations on the Spectra of Some of the Stars and Nebulae, with an Attempt to Determine Therefrom Whether These Bodies Are Moving towards or from the Earth, Also Observations on the Spectra of the Sun and of Comet II., 1868." In: *Philos. Trans. R. Soc. Lond.* 158, pp. 529–564. ISSN: 0261-0523. JSTOR: 108925.

Hughes, Arvind C. N. et al. (May 2022). "The GALAH Survey: A New Sample of Extremely Metal-poor Stars Using a Machine-learning Classification Algorithm." In: *Astrophys. J.* 930, p. 47. ISSN: 0004-637X. DOI: 10.3847/1538-4357/ac5fa7.

Huygens, Christiaan (1690). *Treatise on Light: In Which Are Explained the Causes of That Which Occurs in Reflection & Refraction*.

Hyvärinen, Aapo (Feb. 2013). "Independent Component Analysis: Recent Advances." In: *Philosophical Transactions of the Royal Society A: Mathematical, Physical and Engineering Sciences* 371.1984, p. 20110534. DOI: 10.1098/rsta.2011.0534.

Ishigaki, Miho N., Nozomu Tominaga, Chiaki Kobayashi, and Ken'ichi Nomoto (Sept. 2014). "Faint Population III Supernovae as the Origin of the Most Iron-poor Stars." In: *Astrophys. J.* 792, p. L32. ISSN: 0004-637X. DOI: 10.1088/2041-8205/792/2/L32.

Jackson, J. M. et al. (Mar. 2006). "The Boston University-Five College Radio Astronomy Observatory Galactic Ring Survey." In: *Astrophys. J. Suppl. Ser.* 163, pp. 145–159. ISSN: 0067-0049. DOI: 10.1086/500091.

Janes, K. A. and R. L. Phelps (Nov. 1994). "The Galactic System of Old Star Clusters: The Development of the Galactic Disk." In: *Astron. J.* 108, p. 1773. ISSN: 0004-6256. DOI: 10.1086/117192.

Jess, D. B., R. J. Morton, G. Verth, V. Fedun, S. D. T. Grant, and I. Giagkiozis (July 2015). "Multiwavelength Studies of MHD Waves in the Solar Chromosphere. An Overview of Recent Results." In: *Space Sci. Rev.* 190, pp. 103–161. ISSN: 0038-6308. DOI: 10.1007/s11214-015-0141-3.

Johnson, Christian I., Andrea K. Dupree, Mario Mateo, John I. Bailey III, Edward W. Olszewski, and Matthew G. Walker (June 2020). "The Most Metal-poor Stars in Omega Centauri (NGC 5139)." In: *Astron. J.* 159, p. 254. ISSN: 0004-6256. DOI: 10.3847/1538-3881/ab8819.

Johnson, H. L. and W. W. Morgan (May 1953). "Fundamental Stellar Photometry for Standards of Spectral Type on the Revised System of the Yerkes Spectral Atlas." In: *Astrophys. J.* 117, p. 313. ISSN: 0004-637X. DOI: 10.1086/145697.

Kaelbling, L. P., M. L. Littman, and A. W. Moore (May 1996). "Reinforcement Learning: A Survey." In: *jair* 4, pp. 237–285. ISSN: 1076-9757. DOI: 10.1613/jair.301.

Kaeppeler, F., H. Beer, K. Wisshak, D. D. Clayton, R. L. Macklin, and R. A. Ward (June 1982). "S-Process Studies in the Light of New Experimental Cross Sections - Distribution of Neutron Fluences and r-Process Residuals." In: *Astrophys. J.* 257, pp. 821–846. ISSN: 0004-637X. DOI: 10.1086/160033.

Kalari, Venu M., Elliott P. Horch, Ricardo Salinas, Jorick S. Vink, Morten Andersen, Joachim M. Bestenlehner, and Monica Rubio (Aug. 2022). "Resolving the Core of R136 in the Optical." In: *Astrophys. J.* 935, p. 162. ISSN: 0004-637X. DOI: 10.3847/1538-4357/ac8424.

Karimpouli, Sadegh and Pejman Tahmasebi (May 2019). "Segmentation of Digital Rock Images Using Deep Convolutional Autoencoder Networks." In: *Computers & Geosciences* 126, pp. 142–150. ISSN: 0098-3004. DOI: 10.1016/j.cageo.2019.02.003.

Karttunen, Hannu, Pekka Kröger, Heikki Oja, Markku Poutanen, and Karl Johan Donner, eds. (2017). *Fundamental Astronomy*. Berlin, Heidelberg: Springer. ISBN: 978-3-662-53044-3 978-3-662-53045-0. DOI: 10.1007/978-3-662-53045-0.

Kasen, Daniel, Brian Metzger, Jennifer Barnes, Eliot Quataert, and Enrico Ramirez-Ruiz (Nov. 2017). "Origin of the Heavy Elements in Binary Neutron-Star Mergers from a Gravitational-Wave Event." In: *Nature* 551, pp. 80–84. ISSN: 0028-0836. DOI: 10.1038/nature24453.

Kasparova, Anastasia V., Ivan Yu. Katkov, Igor V. Chilingarian, Olga K. Silchenko, Alexey V. Moiseev, and Svyatoslav B. Borisov (July 2016). "The Diversity of Thick

Galactic Discs." In: *Mon. Not. R. Astron. Soc.* 460, pp. L89–L93. ISSN: 0035-8711. DOI: 10.1093/mnrasl/slw083.

Keenan, Philip C. (Nov. 1954). "Classification of the S-Type Stars." In: *Astrophys. J.* 120, p. 484. ISSN: 0004-637X. DOI: 10.1086/145937.

— (Sept. 1993). "Revised MK Spectral Classification of the Red Carbon Stars." In: *Publ. Astron. Soc. Pac.* 105, p. 905. ISSN: 0004-6280. DOI: 10.1086/133252.

Keenan, Philip C. and W. W. Morgan (Nov. 1941). "The Classification of the Red Carbon Stars." In: *Astrophys. J.* 94, p. 501. ISSN: 0004-637X. DOI: 10.1086/144356.

Keller, S. C. et al. (Feb. 2014). "A Single Low-Energy, Iron-Poor Supernova as the Source of Metals in the Star SMSS J031300.36-670839.3." In: *Nature* 506.7489, pp. 463–466. ISSN: 1476-4687. DOI: 10.1038/nature12990.

Kerber, L O, M Libralato, S O Souza, R A P Oliveira, S Ortolani, A Pérez-Villegas, B Barbuy, B Dias, E Bica, and D Nardiello (Apr. 2019). "A Deep View of a Fossil Relic in the Galactic Bulge: The Globular Cluster HP 1." In: *Monthly Notices of the Royal Astronomical Society* 484.4, pp. 5530–5550. ISSN: 0035-8711. DOI: 10.1093/mnras/stz003.

Khomenko, E., N. Vitas, M. Collados, and A. de Vicente (Aug. 2017). "Numerical Simulations of Quiet Sun Magnetic Fields Seeded by the Biermann Battery." In: *Astron. Astrophys.* 604, A66. ISSN: 0004-6361. DOI: 10.1051/0004-6361/201630291.

Kippenhahn, Rudolf, Alfred Weigert, and Achim Weiss (2012). *Stellar Structure and Evolution*. Astronomy and Astrophysics Library. Berlin, Heidelberg: Springer. ISBN: 978-3-642-30255-8 978-3-642-30304-3. DOI: 10.1007/978-3-642-30304-3.

Kirchhoff (1861). *Untersuchungen ueber das Sonnenspektrum und die Spektren der chemischen Elemente*.

Kirchhoff, G. (1860). "Ueber Das Verhältniss Zwischen Dem Emissionsvermögen Und Dem Absorptionsvermögen Der Körper Für Wärme Und Licht." In: *Ann. Phys.* 185.2, pp. 275–301. ISSN: 1521-3889. DOI: 10.1002/andp.18601850205.

Kirchhoff, G. and R. Bunsen (1860). "Chemische Analyse Durch Spectralbeobachtungen." In: *Ann. Phys.* 186.6, pp. 161–189. ISSN: 1521-3889. DOI: 10.1002/andp.18601860602.

Klimchuk, James (2004). "How Do We Solve the Coronal Heating Problem?" In: *Proc. SOHO 15 Workshop - Coronal Heat.*

Kobayashi, Chiaki, Amanda I. Karakas, and Maria Lugaro (Sept. 2020). "The Origin of Elements from Carbon to Uranium." In: *ApJ* 900.2, p. 179. ISSN: 0004-637X. DOI: 10.3847/1538-4357/abae65.

Koch, Andreas, Eva K. Grebel, and Sarah L. Martell (May 2019). "Purveyors of Fine Halos: Re-assessing Globular Cluster Contributions to the Milky Way Halo Buildup with SDSS-IV." In: *A&A* 625, A75. ISSN: 0004-6361, 1432-0746. DOI: 10.1051/0004-6361/201834825.

Kolpak, Michal A., James M. Jackson, T. M. Bania, and John M. Dickey (Oct. 2002). "The Radial Distribution of Cold Atomic Hydrogen in the Galaxy." In: *Astrophys. J.* 578, pp. 868–876. ISSN: 0004-637X. DOI: 10.1086/342659.

Konnov, A. A. (2000). In: *28th Symp Int Combust. Edinb.* Abstr. Symp. Pap. P. 317.

Kordopatis, G., A. Recio-Blanco, P. de Laverny, G. Gilmore, V. Hill, R. F. G. Wyse, A. Helmi, A. Bijaoui, M. Zoccali, and O. Bienaymé (Nov. 2011). "A Spectroscopic Survey of Thick Disc Stars Outside the Solar Neighbourhood." In: *Astron. Astrophys.* 535, A107. ISSN: 0004-6361. DOI: 10.1051/0004-6361/201117373.

Kramer, Mark A. (1991). "Nonlinear Principal Component Analysis Using Autoassociative Neural Networks." In: *AIChE J.* 37.2, pp. 233–243. ISSN: 1547-5905. DOI: 10.1002/aic.690370209.

Kraus, J. D., H. C. Ko, and S. Matt (Dec. 1954). "Galactic and Localized Source Observations at 250 Megacycles per Second." In: *Astron. J.* 59, pp. 439–443. ISSN: 0004-6256. DOI: 10.1086/107059.

Kravtsov, V. V. (June 2001). "Globular Clusters and Dwarf Spheroidal Galaxies of the Outer Galactic Halo: On the Putative Scenario of Their Formation." In: *Astron. Astrophys. Trans.* 20, pp. 89–92. ISSN: 1055-6796. DOI: 10.1080/10556790108208191.

Krumholz, Mark R., Richard I. Klein, Christopher F. McKee, Stella S. R. Offner, and Andrew J. Cunningham (Feb. 2009). "The Formation of Massive Star Systems by Accretion." In: *Science* 323, p. 754. ISSN: 0036-8075. DOI: 10.1126/science.1165857.

Kumar, Mukul and Chi Wang (Aug. 2019). "Magnetic Reconnection in the Solar Corona." In: Balkan, Black sea and Caspian sea Regional Network for Space Weather Studies. DOI: 10.31401/SunGeo.2019.01.06.

Kuperus, M., J. A. Ionson, and D. S. Spicer (Jan. 1981). "On the Theory of Coronal Heating Mechanisms." In: *Annu. Rev. Astron. Astrophys.* 19, pp. 7–40. ISSN: 0066-4146. DOI: 10.1146/annurev.aa.19.090181.000255.

Kupka, F. G., T. A. Ryabchikova, N. E. Piskunov, H. C. Stempels, and W. W. Weiss (Jan. 2000). "VALD-2 – The New Vienna Atomic Line Database." In: *Balt. Astron.* 9, pp. 590–594. ISSN: 1021-6766. DOI: 10.1515/astro-2000-0420.

Kupka, F., N. Piskunov, T. A. Ryabchikova, H. C. Stempels, and W. W. Weiss (July 1999). "VALD-2: Progress of the Vienna Atomic Line Data Base." In: *Astron. Astrophys. Suppl. Ser.* 138, pp. 119–133. ISSN: 0365-0138. DOI: 10.1051/aas:1999267.

Kurucz, R. L. (May 1979). "Model Atmospheres for G, F, A, B, and O Stars." In: *Astrophys. J. Suppl. Ser.* 40, pp. 1–340. ISSN: 0067-0049. DOI: 10.1086/190589.

— (2007). *Robert L. Kurucz on-Line Database of Observed and Predicted Atomic Transitions*.

— (2014). *Robert L. Kurucz on-Line Database of Observed and Predicted Atomic Transitions*.

Kurucz, Robert L. (2005). "ATLAS12, SYNTHE, ATLAS9, WIDTH9, et Cetera." In: *Memorie della Societa Astronomica Italiana Supplementi* 8, p. 14.

— (Oct. 2017). "ATLAS9: Model Atmosphere Program with Opacity Distribution Functions." In: *Astrophys. Source Code Libr.*, ascl:1710.017.

Larmor, Joseph (Jan. 1897). "A Dynamical Theory of the Electric and Luminiferous Medium. Part III. Relations with Material Media." In: *Philos. Trans. R. Soc. Lond. Ser. A* 190, pp. 205–300+493. ISSN: 1364-503X0080-46140962-8436. DOI: 10.1098/rsta.1897.0020.

LeVeque, Randall J. (2002). *Finite Volume Methods for Hyperbolic Problems*. Cambridge Texts in Applied Mathematics. Cambridge: Cambridge University Press. ISBN: 978-0-521-00924-9. DOI: 10.1017/CBO9780511791253.

— (1992). *Numerical Methods for Conservation Laws*. Basel: Birkhäuser. ISBN: 978-3-7643-2723-1 978-3-0348-8629-1. DOI: 10.1007/978-3-0348-8629-1.

Leenaarts, Jorrit (Mar. 2020). "Radiation Hydrodynamics in Simulations of the Solar Atmosphere." In: *Living Rev Sol Phys* 17.1, p. 3. ISSN: 1614-4961. DOI: 10.1007/s41116-020-0024-x.

Leenaarts, Jorrit and Mats Carlsson (2009). "MULTI3D: A Domain-Decomposed 3D Radiative Transfer Code." In: *ASP Conf. Ser.* 415, p. 4.

Leitner, P., B. Lemmerer, A. Hanslmeier, T. Zaqarashvili, A. Veronig, H. Grimm-Strele, and H. J. Muthsam (Aug. 2017). "Structure of the Solar Photosphere Studied from the Radiation Hydrodynamics Code ANTARES." In: *Astrophys Space Sci* 362.9, p. 181. ISSN: 1572-946X. DOI: 10.1007/s10509-017-3151-7.

Levine, E. S., Leo Blitz, and Carl Heiles (June 2006). "The Spiral Structure of the Outer Milky Way in Hydrogen." In: *Science* 312.5781, pp. 1773–1777. ISSN: 0036-8075, 1095-9203. DOI: 10.1126/science.1128455.

Li, Ting, Eric Priest, and Ruilong Guo (May 2021). "Three-Dimensional Magnetic Reconnection in Astrophysical Plasmas." In: *Proc. R. Soc. Math. Phys. Eng. Sci.* 477.2249, p. 20200949. DOI: 10.1098/rspa.2020.0949.

Lian, Jianhui et al. (Sept. 2020). "The Milky Way's Bulge Star Formation History as Constrained from Its Bimodal Chemical Abundance Distribution." In: *Monthly Notices of the Royal Astronomical Society* 497.3, pp. 3557–3570. ISSN: 0035-8711. DOI: 10.1093/mnras/staa2205.

Lindner, Robert R., Carlos Vera-Ciro, Claire E. Murray, Snežana Stanimirović, Brian Babler, Carl Heiles, Patrick Hennebelle, W. M. Goss, and John Dickey (Apr. 2015). "Autonomous Gaussian Decomposition." In: *The Astronomical Journal* 149, p. 138. DOI: 10.1088/0004-6256/149/4/138.

Lodders, K., H. Palme, and H.-P. Gail (2009). "Abundances of the Elements in the Solar System." In: *Landolt-Bornstein*. Vol. VI/4B. Astronomy and Astrophysics, pp. 560–630. DOI: 10.1007/978-3-540-88055-4_34.

Lodders, Katharina (Apr. 2021). "Relative Atomic Solar System Abundances, Mass Fractions, and Atomic Masses of the Elements and Their Isotopes, Composition of the Solar Photosphere, and Compositions of the Major Chondritic Meteorite Groups." In: *Space Sci. Rev.* 217.3, p. 44. ISSN: 0038-6308. DOI: 10.1007/s11214-021-00825-8.

— (Dec. 2019). "Solar Elemental Abundances." In: *arXiv e-prints* 1912, arXiv:1912.00844.

— (July 2003). "Solar System Abundances and Condensation Temperatures of the Elements." In: *ApJ* 591, pp. 1220–1247. DOI: 10.1086/375492.

Löhner-Böttcher, J., W. Schmidt, R. Schlichenmaier, T. Steinmetz, and R. Holzwarth (Apr. 2019). "Convective Blueshifts in the Solar Atmosphere. III. High-accuracy Observations of Spectral Lines in the Visible." In: *Astron. Astrophys.* 624, A57. ISSN: 0004-6361. DOI: 10.1051/0004-6361/201834925.

Lucey, Madeline, Nariman Al Kharusi, Keith Hawkins, Yuan-Sen Ting, Nesar Ramachandra, Timothy C. Beers, Young Sun Lee, Adrian M. Price-Whelan, and Jinmi Yoon (June 2022). *Over 2.7 Million Carbon-Enhanced Metal-Poor Stars from BP/RP Spectra in $Gaia$ DR3*.

Ludwig, H. G. and M. Steffen (Jan. 2013). "Opacities in CO5BOLD." In: *Mem. Della Soc. Astron. Ital. Suppl.* 24, p. 53. ISSN: 0037-8720.

Ludwig, Hans-Günter, Elisabetta Caffau, Matthias Steffen, Piercarlo Bonifacio, Bernd Freytag, and Roger Cayrel (Mar. 2010). "Solar Abundances and 3D Model Atmospheres." In: 265, pp. 201–204. DOI: 10.1017/S1743921310000542.

MacConnell, D. J. (Jan. 1979). "Discoveries on Southern, Red-Sensitive Objective-Prism Plates II : New S/MS, Carbon and SC Stars." In: *Astron. Astrophys. Suppl. Ser.* 38, pp. 335–339. ISSN: 0365-0138.

Magg, Ekaterina et al. (May 2022). "Observational Constraints on the Origin of the Elements. IV. Standard Composition of the Sun." In: *Astron. Astrophys.* 661, A140. ISSN: 0004-6361. DOI: 10.1051/0004-6361/202142971.

Magic, Z., R. Collet, M. Asplund, R. Trampedach, W. Hayek, A. Chiavassa, R. F. Stein, and Å Nordlund (Sept. 2013). "The Stagger-grid: A Grid of 3D Stellar Atmosphere Models - I. Methods and General Properties." In: *A&A* 557, A26. ISSN: 0004-6361, 1432-0746. DOI: 10.1051/0004-6361/201321274. arXiv: 1302.2621.

Magic, Zazralt (May 2014). "Theoretical stellar atmosphere models for cool stars." Text.PhDThesis. Ludwig-Maximilians-Universität München.

Makhzani, Alireza and Brendan Frey (Dec. 2013). "K-Sparse Autoencoders." In: *arXiv e-prints* 1312, arXiv:1312.5663.

Maoz, Dan (2016). *Astrophysics in a Nutshell*. ISBN: 978-0-691-16479-3.

March, J and D Smith (2001). *Advanced Organic Chemistry*. 5th. New York: Wiley.

Markwardt, C. B. (Sept. 2009). "Non-Linear Least-squares Fitting in IDL with MPFIT." In: *ASP Conf. Ser.* 411, p. 251.

Martig, Marie, Ivan Minchev, Melissa Ness, Morgan Fouesneau, and Hans-Walter Rix (Nov. 2016). "A Radial Age Gradient in the Geometrically Thick Disk of the Milky Way." In: *Astrophys. J.* 831, p. 139. ISSN: 0004-637X. DOI: 10.3847/0004-637X/831/2/139.

Mashonkina, Lyudmila (Apr. 2020). "Non-Local Thermodynamic Equilibrium Line Formation for Si I-II-III in A-B Stars and the Origin of Si II Emission Lines in ι Her." In: *Mon. Not. R. Astron. Soc.* 493, pp. 6095–6108. ISSN: 0035-8711. DOI: 10.1093/mnras/staa653.

Masseron, Thomas (Mar. 2008). "Stellar Nucleosynthesis in the Galactic History: The Carbon Stars." In: 990, pp. 178–180. DOI: 10.1063/1.2905535.

Mayorga, L. C., J. Lustig-Yaeger, E. M. May, Kristin S. Sotzen, Junellie Gonzalez-Quiles, Brian M. Kilpatrick, Emily C. Martin, Kathleen Mandt, K. B. Stevenson, and N. R. Izenberg (July 2021). "Transmission Spectroscopy of the Earth–Sun System to Inform the Search for Extrasolar Life." In: *Planet. Sci. J.* 2.4, p. 140. ISSN: 2632-3338. DOI: 10.3847/PSJ/ac0c85.

McClure, R. D. (Dec. 1985). "The Carbon and Related Stars." In: *J. R. Astron. Soc. Can.* 79, pp. 277–293. ISSN: 0035-872X.

McComas, D. J., H. A. Elliott, N. A. Schwadron, J. T. Gosling, R. M. Skoug, and B. E. Goldstein (May 2003). "The Three-Dimensional Solar Wind around Solar Maximum." In: *Geophys. Res. Lett.* 30, p. 1517. ISSN: 0094-8276. DOI: 10.1029/2003GL017136.

McCulloch, Warren S. and Walter Pitts (Dec. 1943). "A Logical Calculus of the Ideas Immanent in Nervous Activity." In: *Bulletin of Mathematical Biophysics* 5.4, pp. 115–133. ISSN: 0007-4985, 1522-9602. DOI: 10.1007/BF02478259.

McElroy, D., C. Walsh, A. J. Markwick, M. A. Cordiner, K. Smith, and T. J. Millar (Feb. 2013). "The UMIST Database for Astrochemistry 2012." In: *A&A* 550, A36. ISSN: 0004-6361, 1432-0746. DOI: 10.1051/0004-6361/201220465.

Mel'Nik, A. (Aug. 2005). "Outer Pseudoring in the Galaxy." In: *Astron. Nachrichten* 326, p. 599. ISSN: 0004-6337.

Mel'nik, A. M. and P. Rautiainen (Sept. 2009). "Kinematics of the Outer Pseudorings and the Spiral Structure of the Galaxy." In: *Astron. Lett.* 35.9, pp. 609–624. ISSN: 1063-7737, 1562-6873. DOI: 10.1134/S1063773709090047.

Meyer, Bradley S. (Jan. 1994). "The R-, s-, and p-Processes in Nucleosynthesis." In: *Annu. Rev. Astron. Astrophys.* 32, pp. 153–190. ISSN: 0066-4146. DOI: 10.1146/annurev.aa.32.090194.001101.

Milone, Antonino P. and Anna F. Marino (June 2022). "Multiple Populations in Star Clusters." In: *Universe* 8.7, p. 359. DOI: 10.3390/universe8070359.

Mohri, Mehryar, Afshin Rostamizadeh, and Ameet Talwalkar (Aug. 2012). *Foundations of Machine Learning*. Cambridge, MA: The MIT Press. ISBN: 978-0-262-01825-8.

Monier, R., B. Smalley, G. Wahlgren, Ph Stee, and L. Mashonkina (Jan. 2010). "Resonance Broadening and van Der Waals Broadening." In: *Eur. Astron. Soc. Publ. Ser.* 43, pp. 135–141. ISSN: 1633-4760, 1638-1963. DOI: 10.1051/eas/1043009.

Moore, Charlotte E. (Jan. 1970). "Silicon in the Sun." In: *Vistas in Astronomy* 12, pp. 307–312. ISSN: 0083-6656. DOI: 10.1016/0083-6656(70)90045-0.

Morgan, W. W. and P. C. Keenan (Jan. 1973). "Spectral Classification." In: *Annu. Rev. Astron. Astrophys.* 11, p. 29. ISSN: 0066-4146. DOI: 10.1146/annurev.aa.11.090173.000333.

Morgan, William Wilson, Philip Childs Keenan, and Edith Kellman (Jan. 1943). *An Atlas of Stellar Spectra, with an Outline of Spectral Classification*.

Nakajima, Tadashi and Satoko Sorahana (Oct. 2016). "CARBON-TO-OXYGEN RATIOS IN M DWARFS AND SOLAR-TYPE STARS." In: *Astrophys. J.* 830.2. ISSN: 0004-637X. DOI: 10.3847/0004-637X/830/2/159.

Neckel, H. and D. Labs (Feb. 1984). "The Solar Radiation between 3300 and 12500 A." In: *Solar Physics* 90, pp. 205–258. DOI: 10.1007/BF00173953.

Neckel, Heinz and Dietrich Labs (Aug. 1994). "Solar Limb Darkening 1986-1990 Lambda 303-NANOMETERS to 1099-NANOMETERS." In: *Sol. Phys.* 153, pp. 91–114. ISSN: 0038-0938. DOI: 10.1007/BF00712494.

Ness, M. and K. Freeman (Jan. 2016). "The Metallicity Distribution of the Milky Way Bulge." In: *Publ. Astron. Soc. Aust.* 33, e022. ISSN: 1323-3580, 1448-6083. DOI: 10.1017/pasa.2015.51.

Newton, Isaac (1704). *Opticks: Or, A Treatise of the Reflexions, Refractions, Inflexions and Colours of Light: Also Two Treatises of the Species and Magnitude of Curvilinear Figures*. London: Printed for S. Smith, and B. Walford.

Nishiyama, Shogo et al. (Mar. 2005). "A Distinct Structure inside the Galactic Bar." In: *Astrophys. J.* 621, pp. L105–L108. ISSN: 0004-637X. DOI: 10.1086/429291.

Nissen, P. E. (Apr. 2013). "The Carbon-to-Oxygen Ratio in Stars with Planets." In: *A&A* 552, A73. ISSN: 0004-6361, 1432-0746. DOI: 10.1051/0004-6361/201321234.

Nordlund, Åke, Robert F. Stein, and Martin Asplund (Apr. 2009). "Solar Surface Convection." In: *Living Reviews in Solar Physics* 6, p. 2. DOI: 10.12942/lrsp-2009-2.

Norris, John E., N. Christlieb, A. J. Korn, K. Eriksson, M. S. Bessell, Timothy C. Beers, L. Wisotzki, and D. Reimers (Nov. 2007). "HE 0557-4840: Ultra-Metal-Poor and Carbon-Rich." In: *Astrophys. J.* 670, pp. 774–788. ISSN: 0004-637X. DOI: 10.1086/521919.

O'Brian, T. R. and J. E. Lawler (Dec. 1991a). "Radiative Lifetimes in Si i from Laser-Induced Fluorescence in the Visible, Ultraviolet, and Vacuum Ultraviolet." In: *Phys. Rev. A* 44, pp. 7134–7143. ISSN: 1050-29470556-2791. DOI: 10.1103/PhysRevA.44.7134.

— (Feb. 1991b). "Vacuum Ultraviolet Laser Induced Fluorescence on a Si Atimic Beam." In: *Phys. Lett. A* 152, pp. 407–411. ISSN: 0375-9601. DOI: 10.1016/0375-9601(91)90834-U.

O'Shea, Keiron and Ryan Nash (2015). "An Introduction to Convolutional Neural Networks." In: *CoRR* abs/1511.08458. arXiv: 1511.08458.

Ohkubo, Takuya, Ken'ichi Nomoto, Hideyuki Umeda, Naoki Yoshida, and Sachiko Tsuruta (Dec. 2009). "Evolution of Very Massive Population III Stars with Mass Accretion from Pre-main Sequence to Collapse." In: *Astrophys. J.* 706, pp. 1184–1193. ISSN: 0004-637X. DOI: 10.1088/0004-637X/706/2/1184.

OpenStax (Mar. 2022). *Astronomy 2e by OpenStax*. Second edition. XanEdu Publishing Inc. ISBN: 978-1-71147-057-3.

Opitz, D. and R. Maclin (Aug. 1999). "Popular Ensemble Methods: An Empirical Study." In: *J. Artif. Intell. Res.* 11, pp. 169–198. ISSN: 1076-9757. DOI: 10.1613/jair.614.

Palme, H., K. Lodders, and A. Jones (2014). "Solar System Abundances of the Elements." In: *Planets, Asteriods, Comets and The Solar System*, pp. 15–36.

Parmigiani, G. (Jan. 2001). "Decision Theory: Bayesian." In: *International Encyclopedia of the Social & Behavioral Sciences*. Ed. by Neil J. Smelser and Paul B. Baltes. Oxford: Pergamon, pp. 3327–3334. ISBN: 978-0-08-043076-8. DOI: 10.1016/B0-08-043076-7/00403-4.

Payne, Cecilia Helena (Jan. 1925). "Stellar Atmospheres; a Contribution to the Observational Study of High Temperature in the Reversing Layers of Stars." PhD thesis.

Peebles, P. J. (Mar. 1966). "Primeval Helium Abundance and the Primeval Fireball." In: *Phys. Rev. Lett.* 16, pp. 410–413. ISSN: 0031-9007. DOI: 10.1103/PhysRevLett.16.410.

Pehlivan Rhodin, Asli (2018). "Experimental and Computational Atomic Spectroscopy for Astrophysics: Oscillator Strengths and Lifetimes for Mg I, Si I, Si II, Sc I, and Sc II." PhD thesis. Lund: Department of Astronomy and Theoretical Physics, Lund University. ISBN: 9789177535331.

Peloso, E. F. del, L. da Silva, G. F. Porto de Mello, and L. I. Arany-Prado (Sept. 2005). "The Age of the Galactic Thin Disk from Th/Eu Nucleocosmochronology - III. Extended Sample." In: *A&A* 440.3, pp. 1153–1159. ISSN: 0004-6361, 1432-0746. DOI: 10.1051/0004-6361:20053307.

Pereira, T. M. D., M. Asplund, R. Collet, I. Thaler, R. Trampedach, and J. Leenaarts (June 2013). "How Realistic Are Solar Model Atmospheres?" In: *A&A* 554, A118. ISSN: 0004-6361, 1432-0746. DOI: 10.1051/0004-6361/201321227.

Pereira, Tiago M. D., Bart De Pontieu, and Mats Carlsson (Oct. 2012). "QUANTIFYING SPICULES." In: *ApJ* 759.1, p. 18. ISSN: 0004-637X. DOI: 10.1088/0004-637X/759/1/18.

Planck Collaboration et al. (Nov. 2014). "Planck 2013 Results. XVI. Cosmological Parameters." In: *Astron. Astrophys.* 571, A16. ISSN: 0004-6361. DOI: 10.1051/0004-6361/201321591.

Plez, B. (May 2012). "Turbospectrum: Code for Spectral Synthesis." In: *Astrophys. Source Code Libr.*, ascl:1205.004.

Plez, B. and J. G. Cohen (May 2005). "Analysis of the Carbon-Rich Very Metal-Poor Dwarf G77-61." In: *Astron. Astrophys. Vol. 434 Issue 3 May II 2005 Pp1117-1124* 434.3, p. 1117. ISSN: 0004-6361. DOI: 10.1051/0004-6361:20042082.

Polikar, R. (Third 2006). "Ensemble Based Systems in Decision Making." In: *IEEE Circuits Syst. Mag.* 6.3, pp. 21–45. ISSN: 1558-0830. DOI: 10.1109/MCAS.2006.1688199.

Popa, S. A., R. Hoppe, M. Bergemann, C. J. Hansen, B. Plez, and T. C. Beers (Dec. 2022). *NLTE Analysis of the Methylidyne Radical (CH) Molecular Lines in Metal-Poor Stellar Atmospheres*. DOI: 10.48550/arXiv.2212.06517.

Pope, S.B. (Jan. 1997). "Computationally Efficient Implementation of Combustion Chemistry Using in Situ Adaptive Tabulation." In: *Combust. Theory Model.* 1.1, pp. 41–63. ISSN: 1364-7830. DOI: 10.1080/713665229.

Preston, G. W. (Jan. 1974). "The Chemically Peculiar Stars of the Upper Main Sequence." In: *Annu. Rev. Astron. Astrophys.* 12, pp. 257–277. ISSN: 0066-4146. DOI: 10.1146/annurev.aa.12.090174.001353.

Prša, Andrej et al. (Aug. 2016). "Nominal Values for Selected Solar and Planetary Quantities: IAU 2015 Resolution B3." In: *Astron. J.* 152, p. 41. ISSN: 0004-6256. DOI: 10.3847/0004-6256/152/2/41.

Pudil, Pavel and Jana Novovičová (1998). "Novel Methods for Feature Subset Selection with Respect to Problem Knowledge." In: *Feature Extraction, Construction and Selection: A Data Mining Perspective*. Ed. by Huan Liu and Hiroshi Motoda. The Springer International Series in Engineering and Computer Science. Boston, MA: Springer US, pp. 101–116. ISBN: 978-1-4615-5725-8. DOI: 10.1007/978-1-4615-5725-8_7.

Raissi, M., P. Perdikaris, and G. E. Karniadakis (Feb. 2019). "Physics-Informed Neural Networks: A Deep Learning Framework for Solving Forward and Inverse Problems Involving Nonlinear Partial Differential Equations." In: *Journal of Computational Physics* 378, pp. 686–707. ISSN: 0021-9991. DOI: 10.1016/j.jcp.2018.10.045.

Ramírez Vélez, J. C., A. López Ariste, and M. Semel (Aug. 2008). "Strength Distribution of Solar Magnetic Fields in Photospheric Quiet Sun Regions." In: *A&A* 487, pp. 731–740. ISSN: 0004-6361. DOI: 10.1051/0004-6361:20078654.

Rankine, William (Dec. 1870). "On the Thermodynamic Theory of Waves of Finite Longitudinal Disturbance." In: *Phil. Trans. R. Soc.* 160, pp. 277–288. ISSN: 0261-0523, 2053-9223. DOI: 10.1098/rstl.1870.0015.

Riener, M., J. Kainulainen, J. D. Henshaw, J. H. Orkisz, C. E. Murray, and H. Beuther (Aug. 2019). "GAUSSPY+: A Fully Automated Gaussian Decomposition Package for Emission Line Spectra." In: *Astronomy and Astrophysics* 628, A78. ISSN: 0004-6361. DOI: 10.1051/0004-6361/201935519.

Rinke-Kneapler, C. N. and M. E. Sigman (Jan. 2014). "15 - Applications of Laser Spectroscopy in Forensic Science." In: *Laser Spectroscopy for Sensing*. Ed. by Matthieu Baudelet. Woodhead Publishing, pp. 461–495. ISBN: 978-0-85709-273-1. DOI: 10.1533/9780857098733.3.461.

Robinson, James W. (July 1996). *Atomic Spectroscopy, Second Edition*, CRC Press. ISBN: 978-0-8247-9742-3.

Roe, P L (1986). "Characteristic-Based Schemes for the Euler Equations." In: *Annu. Rev. Fluid Mech.* 18.1, pp. 337–365. DOI: 10.1146/annurev.fl.18.010186.002005.

Roederer, Ian U. and Paul S. Barklem (Apr. 2018). "A New Test of Copper and Zinc Abundances in Late-type Stars Using Ultraviolet Cu II and Zn II Lines." In: *ApJ* 857, p. 2. ISSN: 0004-637X. DOI: 10.3847/1538-4357/aab71f.

Rokach, Lior (Feb. 2010). "Ensemble-Based Classifiers." In: *Artif Intell Rev* 33.1, pp. 1–39. ISSN: 1573-7462. DOI: 10.1007/s10462-009-9124-7.

Rosenblatt, F. (1957). *The Perceptron, a Perceiving and Recognizing Automaton Project Para*. Cornell Aeronautical Laboratory.

Rosenblatt, Frank (1962). *Principles of Neurodynamics: Perceptrons and the Theory of Brain Mechanisms*. Spartan Books.

Rossi, Martina, Stefania Salvadori, Ása Skúladóttir, and Irene Vanni (June 2023). "Understanding the Origin of CEMP – No Stars through Ultra-Faint Dwarfs." In: *Monthly Notices of the Royal Astronomical Society: Letters* 522.1, pp. L1–L5. ISSN: 1745-3925. DOI: 10.1093/mnrasl/slad029.

Rowland (1882). "LXI. Preliminary Notice of the Results Accomplished in the Manufacture and Theory of Gratings for Optical Purposes." In: *Lond. Edinb. Dublin Philos. Mag. J. Sci.* 13.84, pp. 469–474. DOI: 10.1080/14786448208627217. eprint: https://doi.org/10.1080/14786448208627217.

Russeil, D. (Jan. 2003). "Star-Forming Complexes and the Spiral Structure of Our Galaxy." In: *Astron. Astrophys.* 397, pp. 133–146. ISSN: 0004-6361. DOI: 10.1051/0004-6361:20021504.

Russell, Henry Norris (July 1929). "On the Composition of the Sun's Atmosphere." In: *ApJ* 70, p. 11. DOI: 10.1086/143197.

— (May 1914). "Relations Between the Spectra and Other Characteristics of the Stars." In: *Pop. Astron.* 22, pp. 275–294. ISSN: 0197-7482.

Ryabchikova, T., N. Piskunov, R. L. Kurucz, H. C. Stempels, U. Heiter, Yu Pakhomov, and P. S. Barklem (May 2015). "A Major Upgrade of the VALD Database." In: *Phys. Scr.* 90, p. 054005. ISSN: 0031-8949. DOI: 10.1088/0031-8949/90/5/054005.

Rydberg, Claes-Erik, Erik Zackrisson, Peter Lundqvist, and Pat Scott (Mar. 2013). "Detection of Isolated Population III Stars with the James Webb Space Telescope." In: *Mon. Not. R. Astron. Soc.* 429, pp. 3658–3664. ISSN: 0035-8711. DOI: 10.1093/mnras/sts653.

Salpeter, Edwin E. (Jan. 1955). "The Luminosity Function and Stellar Evolution." In: *Astrophys. J.* 121, p. 161. ISSN: 0004-637X. DOI: 10.1086/145971.

Samet, H. (2006). *Foundations of Multidimensional and Metric Data Structures*. /paper/Foundations-of-multidimensional-and-metric-data-Samet/e8da033f03c679e87b95a9e8cc1cfdd8c6ccb526.

Sbordone, L., P. Bonifacio, F. Castelli, and R. L. Kurucz (Jan. 2004). "ATLAS and SYNTHE under Linux." In: *Mem. Della Soc. Astron. Ital. Suppl.* 5, p. 93. ISSN: 0037-8720.

Schaffenberger, W., S. Wedemeyer-Böhm, O. Steiner, and B. Freytag (Nov. 2005). "Magnetohydrodynamic Simulation from the Convection Zone to the Chromosphere." In: 596, p. 65.1.

Schaschke, Carl (2014). *A Dictionary of Chemical Engineering*. OUP Oxford. ISBN: 978-0-19-965145-0.
Schatzman, Evry (Jan. 1949). "The Heating of the Solar Corona and Chromosphere." In: *Ann. Astrophys.* 12, p. 203. ISSN: 0365-0499.
Schaye, Joop et al. (Jan. 2015). "The EAGLE Project: Simulating the Evolution and Assembly of Galaxies and Their Environments." In: *Mon. Not. R. Astron. Soc.* 446, pp. 521–554. ISSN: 0035-8711. DOI: 10.1093/mnras/stu2058.
Schölkopf, Bernhard, Alexander Smola, and Klaus-Robert Müller (July 1998). "Nonlinear Component Analysis as a Kernel Eigenvalue Problem." In: *Neural Comput.* 10.5, pp. 1299–1319. ISSN: 0899-7667. DOI: 10.1162/089976698300017467.
Schönrich, Ralph and James Binney (June 2009). "Chemical Evolution with Radial Mixing." In: *Mon. Not. R. Astron. Soc.* 396, pp. 203–222. ISSN: 0035-8711. DOI: 10.1111/j.1365-2966.2009.14750.x.
Scott, Pat, Nicolas Grevesse, Martin Asplund, A. Jacques Sauval, Karin Lind, Yoichi Takeda, Remo Collet, Regner Trampedach, and Wolfgang Hayek (2015). "The Elemental Composition of the Sun I. The Intermediate Mass Elements Na to Ca." In: *A&A* 573, pp. 1–19. ISSN: 14320746. DOI: 10.1051/0004-6361/201424109.
Seneca, Lucius Annaeus and John Clarke (1910). *Physical Science in the Time of Nero: Being a Translation of the Quaestiones Naturales of Seneca*. Macmillan and Company, Limited.
Serenelli, Aldo, Pat Scott, Francesco L. Villante, Aaron C. Vincent, Martin Asplund, Sarbani Basu, Nicolas Grevesse, and Carlos Peña-Garay (Nov. 2016). "Implications of Solar Wind Measurements for Solar Models and Composition." In: *MNRAS* 463, pp. 2–9. DOI: 10.1093/mnras/stw1927.
Shaltout, A. M K, M. M. Beheary, A. Bakry, and K. Ichimoto (2013). "The Abundance of Silicon in the Solar Atmosphere." In: *MNRAS* 430.4, pp. 2979–2985. ISSN: 00358711. DOI: 10.1093/mnras/stt103.
Sharma, Mahavir, Tom Theuns, Carlos S. Frenk, and Ryan J. Cooke (Jan. 2018). "Origins of Carbon-Enhanced Metal-Poor Stars." In: *Mon. Not. R. Astron. Soc.* 473, pp. 984–995. ISSN: 0035-8711. DOI: 10.1093/mnras/stx2392.
Shchukina, N., A. Sukhorukov, and J. Trujillo Bueno (Feb. 2016). "Impact of Surface Dynamo Magnetic Fields on the Solar Abundance of the CNO Elements." In: *A&A* 586, A145. ISSN: 0004-6361. DOI: 10.1051/0004-6361/201526452.
— (2012). "Non-Lte Determination of the Silicon Abundance Using a Three-Dimensional Hydrodynamical Model of the Solar Photosphere." In: *ApJ* 755.2. ISSN: 15384357. DOI: 10.1088/0004-637X/755/2/176.
Shchukina, Nataliya G., Andrii V. Sukhorukov, and Javier Trujillo Bueno (Oct. 2015). "The Impact of Surface Dynamo Magnetic Fields on the Chemical Abundance Determination." In: 305, pp. 368–371. DOI: 10.1017/S1743921315005062.
Shen, Juntai, R. Michael Rich, John Kormendy, Christian D. Howard, Roberto De Propris, and Andrea Kunder (Sept. 2010). "Our Milky Way as a Pure-disk Galaxy—A Challenge for Galaxy Formation." In: *Astrophys. J.* 720, pp. L72–L76. ISSN: 0004-637X. DOI: 10.1088/2041-8205/720/1/L72.
Sherstinsky, Alex (Mar. 2020). "Fundamentals of Recurrent Neural Network (RNN) and Long Short-Term Memory (LSTM) Network." In: *Phys. Nonlinear Phenom.* 404, p. 132306. ISSN: 0167-2789. DOI: 10.1016/j.physd.2019.132306.
Shi, J. R., T. Gehren, K. Butler, L. I. Mashonkina, and G. Zhao (2008). "Statistical Equilibrium of Silicon in the Solar Atmosphere." In: *A&A* 486.1, pp. 303–310. ISSN: 00046361. DOI: 10.1051/0004-6361:200809452.
Shi, J. R., M. Takada-Hidai, Y. Takeda, K. F. Tan, S. M. Hu, G. Zhao, and C. Cao (2012). "Silicon Abundances in Nearby Stars from the Si i Infrared Lines." In: *ApJ*. ISSN: 15384357. DOI: 10.1088/0004-637X/755/1/36.

Sivarani, T. et al. (Nov. 2006). "First Stars X. The Nature of Three Unevolved Carbon-Enhanced Metal-Poor Stars." In: *Astronomy and Astrophysics* 459, pp. 125–135. ISSN: 0004-6361. DOI: 10.1051/0004-6361:20065440.

Sokasian, Aaron, Naoki Yoshida, Tom Abel, Lars Hernquist, and Volker Springel (May 2004). "Cosmic Reionization by Stellar Sources: Population III Stars." In: *Monthly Notices of the Royal Astronomical Society* 350.1, pp. 47–65. ISSN: 0035-8711. DOI: 10.1111/j.1365-2966.2004.07636.x.

Sparke, Linda S. and John S. Gallagher III (Aug. 2000). *Galaxies in the Universe : An Introduction*.

— (Feb. 2007). *Galaxies in the Universe*.

Spruit, H. C. (Dec. 1976). "Pressure Equilibrium and Energy Balance of Small Photospheric Fluxtubes." In: *Solar Physics* 50, pp. 269–295. DOI: 10.1007/BF00155292.

Stark, J. and H. Kirschbaum (1914). "Beobachtungen Über Den Effekt Des Elektrischen Feldes Auf Spektrallinien. III. Abhängigkeit von Der Feldstärke." In: *Ann. Phys.* 348.7, pp. 991–1016. ISSN: 1521-3889. DOI: 10.1002/andp.19143480704.

Starkenburg, Else et al. (Nov. 2017). "The Pristine Survey - I. Mining the Galaxy for the Most Metal-Poor Stars." In: *Mon. Not. R. Astron. Soc.* 471, pp. 2587–2604. ISSN: 0035-8711. DOI: 10.1093/mnras/stx1068.

Steen, William M. (1998). *Laser Material Processing*. London: Springer. ISBN: 978-3-540-76174-7 978-1-4471-3609-5. DOI: 10.1007/978-1-4471-3609-5.

Steenbock, W. and H. Holweger (Jan. 1984). "Statistical Equilibrium of Lithium in Cool Stars of Different Metallicity." In: *A&A* 130.2, p. 319. ISSN: 0004-6361.

Steffen, M. (Jan. 2017). "Radiation Transport in CO5BOLD. A Short-Characteristics Module for Local Box Models." In: *Mem. Della Soc. Astron. Ital.* 88, p. 22. ISSN: 0037-8720.

Steffen, M., D. Prakapavičius, E. Caffau, H.-G. Ludwig, P. Bonifacio, R. Cayrel, A. Kučinskas, and W. C. Livingston (Nov. 2015). "The Photospheric Solar Oxygen Project. IV. 3D-NLTE Investigation of the 777 Nm Triplet Lines." In: *A&A* 583, A57. ISSN: 0004-6361. DOI: 10.1051/0004-6361/201526406. arXiv: 1508.03487.

Steigman, Gary (Nov. 2007). "Primordial Nucleosynthesis in the Precision Cosmology Era." In: *Annu. Rev. Nucl. Part. Sci.* 57, pp. 463–491. ISSN: 0163-8998. DOI: 10.1146/annurev.nucl.56.080805.140437.

Stein, Robert F. and Åke Nordlund (Mar. 2000). "Realistic Solar Convection Simulations." In: *Solar Physics* 192.1, pp. 91–108. ISSN: 1573-093X. DOI: 10.1023/A:1005260918443.

Stock, Joachim W., Daniel Kitzmann, A. Beate C. Patzer, and Erwin Sedlmayr (Sept. 2018). "FastChem: A Computer Program for Efficient Complex Chemical Equilibrium Calculations in the Neutral/Ionized Gas Phase with Applications to Stellar and Planetary Atmospheres." In: *Monthly Notices of the Royal Astronomical Society* 479, pp. 865–874. DOI: 10.1093/mnras/sty1531.

Strang, Gilbert (Sept. 1968). "On the Construction and Comparison of Difference Schemes." In: *SIAM J. Numer. Anal.* 5.3, pp. 506–517. ISSN: 0036-1429. DOI: 10.1137/0705041.

Susmitha, A., T. Sivarani, D. K. Ojha, Joe P. Ninan, A. Bandyopadhyay, A. Surya, and U. Athira (Dec. 2020). "Oxygen Abundances of Carbon-Enhanced Stellar Population in the Halo." In: *J Astrophys Astron* 41.1, p. 50. ISSN: 0250-6335, 0973-7758. DOI: 10.1007/s12036-020-09672-5.

Talbot, William (1826). "Experiments on Coloured Flames." In: *Edinb. J. Sci.* 5–6.

Taori, Rohan, Ishaan Gulrajani, Tianyi Zhang, Yann Dubois, Xuechen Li, Carlos Guestrin, Percy Liang, and Tatsunori B. Hashimoto (2023). *Stanford Alpaca: An Instruction-Following LLaMA Model*.

Teske, Johanna K., Katia Cunha, Verne V. Smith, Simon C. Schuler, and Caitlin A. Griffith (May 2014). "C/O RATIOS OF STARS WITH TRANSITING HOT JUPITER EX-

OPLANETS*,†." In: *ApJ* 788.1, p. 39. ISSN: 0004-637X. DOI: 10.1088/0004-637X/788/1/39.

Thielemann, F. K. et al. (Apr. 2011). "What Are the Astrophysical Sites for the R-Process and the Production of Heavy Elements?" In: *Prog. Part. Nucl. Phys.* 66, pp. 346–353. ISSN: 0146-6410. DOI: 10.1016/j.ppnp.2011.01.032.

Thomas, Nicholas C. (Aug. 1991). "The Early History of Spectroscopy." In: *J. Chem. Educ.* 68.8, p. 631. ISSN: 0021-9584. DOI: 10.1021/ed068p631.

Ting, Yuan-Sen, Charlie Conroy, Hans-Walter Rix, and Phillip Cargile (July 2019). "The Payne: Self-consistent Ab Initio Fitting of Stellar Spectra." In: *ApJ* 879, p. 69. DOI: 10.3847/1538-4357/ab2331.

Toro, Eleuterio F. (2009). *Riemann Solvers and Numerical Methods for Fluid Dynamics: A Practical Introduction*. Berlin, Heidelberg: Springer. ISBN: 978-3-540-25202-3 978-3-540-49834-6. DOI: 10.1007/b79761.

Touvron, Hugo et al. (Feb. 2023). *LLaMA: Open and Efficient Foundation Language Models*. DOI: 10.48550/arXiv.2302.13971.

Truran, J. W., J. J. Cowan, and A. G. W. Cameron (June 1978). "The Helium-Driven r-Process in Supernovae." In: *ApJ* 222, p. L63. ISSN: 0004-637X, 1538-4357. DOI: 10.1086/182693.

Truran, J.W. and A. Heger (2003). "Origin of the Elements." In: *Treatise on Geochemistry*. Elsevier, pp. 1–15. ISBN: 978-0-08-043751-4. DOI: 10.1016/B0-08-043751-6/01059-8.

Tsai, Shang-Min, Daniel Kitzmann, James R. Lyons, João Mendonça, Simon L. Grimm, and Kevin Heng (July 2018). "Toward Consistent Modeling of Atmospheric Chemistry and Dynamics in Exoplanets: Validation and Generalization of the Chemical Relaxation Method." In: *Astrophys. J.* 862, p. 31. ISSN: 0004-637X. DOI: 10.3847/1538-4357/aac834.

Tsai, Shang-Min, James R. Lyons, Luc Grosheintz, Paul B. Rimmer, Daniel Kitzmann, and Kevin Heng (Feb. 2017). "VULCAN : An Open-source, Validated Chemical Kinetics Python Code for Exoplanetary Atmospheres." In: *ApJS* 228.2, p. 20. ISSN: 0067-0049. DOI: 10.3847/1538-4365/228/2/20.

Unsöld, Albrecht (1955). *Physik Der Sternatmosphären Mit Besonderer Berücksichtigung Der Sonne*.

— (Nov. 1928). "Über die Struktur der Fraunhofersehen Linien und die quantitative Spektralanalyse der Sonnenatmosphäre." In: *Z. Physik* 46.11, pp. 765–781. ISSN: 0044-3328. DOI: 10.1007/BF01391014.

Valueva, M. V., N. N. Nagornov, P. A. Lyakhov, G. V. Valuev, and N. I. Chervyakov (Nov. 2020). "Application of the Residue Number System to Reduce Hardware Costs of the Convolutional Neural Network Implementation." In: *Mathematics and Computers in Simulation* 177, pp. 232–243. ISSN: 0378-4754. DOI: 10.1016/j.matcom.2020.04.031.

Vanhollebeke, E., M. A. T. Groenewegen, and L. Girardi (Apr. 2009). "Stellar Populations in the Galactic Bulge. Modelling the Galactic Bulge with TRILEGAL." In: *Astron. Astrophys.* 498, pp. 95–107. ISSN: 0004-6361. DOI: 10.1051/0004-6361/20078472.

Vaswani, Ashish, Noam Shazeer, Niki Parmar, Jakob Uszkoreit, Llion Jones, Aidan N. Gomez, Lukasz Kaiser, and Illia Polosukhin (June 2017). *Attention Is All You Need*. DOI: 10.48550/arXiv.1706.03762.

Villalobos, Álvaro and Amina Helmi (Dec. 2008). "Simulations of Minor Mergers - I. General Properties of Thick Discs." In: *Mon. Not. R. Astron. Soc.* 391, pp. 1806–1827. ISSN: 0035-8711. DOI: 10.1111/j.1365-2966.2008.13979.x.

Vinyoles, Núria, Aldo M. Serenelli, Francesco L. Villante, Sarbani Basu, Johannes Bergström, M. C. Gonzalez-Garcia, Michele Maltoni, Carlos Peña-Garay, and Ningqiang Song

(Feb. 2017). "A New Generation of Standard Solar Models." In: *ApJ* 835, p. 202. DOI: 10.3847/1538-4357/835/2/202.

Vögler, A., S. Shelyag, M. Schüssler, F. Cattaneo, T. Emonet, and T. Linde (Jan. 2005). "Simulations of Magneto-Convection in the Solar Photosphere. Equations, Methods, and Results of the MURaM Code." In: *A&A* 429, pp. 335–351. ISSN: 0004-6361. DOI: 10.1051/0004-6361:20041507.

Wartha, Eva-Maria, Markus Bösenhofer, and Michael Harasek (Dec. 2021). "Characteristic Chemical Time Scales for Reactive Flow Modeling." In: *Combust. Sci. Technol.* 193.16, pp. 2807–2832. ISSN: 0010-2202. DOI: 10.1080/00102202.2020.1760257.

Washinoue, Haruka, Munehito Shoda, and Takeru K. Suzuki (Oct. 2022). "The Effect of the Chromospheric Temperature on Coronal Heating." In: *ApJ* 938.2, p. 126. ISSN: 0004-637X. DOI: 10.3847/1538-4357/ac91c8.

Wedemeyer-Böhm, S., I. Kamp, J. Bruls, and B. Freytag (Aug. 2005). "Carbon Monoxide in the Solar Atmosphere. I. Numerical Method and Two-Dimensional Models." In: *Astronomy and Astrophysics* 438, pp. 1043–1057. ISSN: 0004-6361. DOI: 10.1051/0004-6361:20042550.

Wedemeyer-Böhm, S., I. Kamp, B. Freytag, J. Bruls, and M. Steffen (Dec. 2006). "A First Three-Dimensional Model for the Carbon Monoxide Concentration in the Solar Atmosphere." In: 354, p. 301.

Wedemeyer, S. (July 2001). "Statistical Equilibrium and Photospheric Abundance of Silicon in the Sun and in Vega." In: *A&A* 373, pp. 998–1008. ISSN: 0004-6361. DOI: 10.1051/0004-6361:20010663.

Wedemeyer, S., B. Freytag, M. Steffen, H. G. Ludwig, and H. Holweger (Jan. 2003). "3-D Hydrodynamic Simulations of the Solar Chromosphere." In: *Astron. Nachrichten* 324, pp. 410–411. ISSN: 0004-6337. DOI: 10.1002/asna.200310150.

Westley, Francis (1980). *Table of Recommended Rate Constants for Chemical Reactions Occurring in Combustion*. Tech. rep. NBS NSRDS 67. Gaithersburg, MD: National Bureau of Standards. DOI: 10.6028/NBS.NSRDS.67.

Wheatstone, Charles (1836). "On the Prismatic Decomposition of Electrical Light." In:

Wissenschaften, Bayerische Akademie der (1817). *Denkschriften der Königlichen Akademie der Wissenschaften zu München*. Die Akademie.

Wollaston, William Hyde (1802). "XII. A Method of Examining Refractive and Dispersive Powers, by Prismatic Reflection." In: *Philos. Trans. R. Soc. Lond.* 92, pp. 365–380. DOI: 10.1098/rstl.1802.0014.

Ye, Jong Chul and Woon Kyoung Sung (Jan. 2019). *Understanding Geometry of Encoder-Decoder CNNs*. DOI: 10.48550/arXiv.1901.07647.

Yong, David, John E. Norris, M. S. Bessell, N. Christlieb, M. Asplund, Timothy C. Beers, P. S. Barklem, Anna Frebel, and S. G. Ryan (Jan. 2013). "THE MOST METAL-POOR STARS. II. CHEMICAL ABUNDANCES OF 190 METAL-POOR STARS INCLUDING 10 NEW STARS WITH [Fe/H] $\leqslant -3.5$, ," in: *ApJ* 762.1, p. 26. ISSN: 0004-637X, 1538-4357. DOI: 10.1088/0004-637X/762/1/26.

Yoon, Suk-Jin and Young-Wook Lee (July 2002). "An Aligned Stream of Low-Metallicity Clusters in the Halo of the Milky Way." In: *Science* 297, pp. 578–581. ISSN: 0036-8075. DOI: 10.1126/science.1073090.

Yun, Joao Lin and Dan P. Clemens (Dec. 1990). "Star Formation in Small Globules: Bart BOK Was Correct!" In: *Astrophys. J.* 365, p. L73. ISSN: 0004-637X. DOI: 10.1086/185891.

Zeeman, P. (Jan. 1896). "Over de Invloed Eener Magnetisatie Op Den Aard van Het Door Een Stof Uitgezonden lichtOver de Invloed Eener Magnetisatie Op Den Aard van Het Door Een Stof Uitgezonden lichtOn the Influence of Magnetism on the Nature

of the Light Emitted by a Substance." In: *Versl. En Meded. Kon Acad. Van Wet. Afd Natuurkunde* 5, pp. 181–184.
de Ferrer, Jose Joaquin (1809). "Observations of the Eclipse of the Sun, June 16th, 1806, Made at Kinderhook, in the State of New-York." In: *Trans. Am. Philos. Soc.* 6, pp. 264–275. ISSN: 0065-9746. DOI: 10.2307/1004801. JSTOR: 1004801.
de Grijs, Richard and Devika Kamath (Nov. 2021). "Stellar Chromospheric Variability." In: *Universe* 7, p. 440. DOI: 10.3390/universe7110440.
de La Fuente Marcos, Raúl (Sept. 1998). "Dynamical Evolution of Open Star Clusters." In: *Publ. Astron. Soc. Pac.* 110, pp. 1117–1117. ISSN: 0004-6280. DOI: 10.1086/316220.
de Vaucouleurs, G. (Jan. 1964). "Interpretation of Velocity Distribution of the Inner Regions of the Galaxy." In: 20, p. 195.
de Wit, Julien et al. (Sept. 2016). "A Combined Transmission Spectrum of the Earth-sized Exoplanets TRAPPIST-1 b and c." In: *Nature* 537.7618, pp. 69–72. ISSN: 1476-4687. DOI: 10.1038/nature18641.
van der Schaft, A. J., S. Rao, and B. Jayawardhana (Apr. 2016). "A Network Dynamics Approach to Chemical Reaction Networks." In: *International Journal of Control* 89, pp. 731–745. ISSN: 0020-7179. DOI: 10.1080/00207179.2015.1095353.
van der Schaft, Arjan, Shodhan Rao, and Bayu Jayawardhana (June 2015). "Complex and Detailed Balancing of Chemical Reaction Networks Revisited." In: *J Math Chem* 53.6, pp. 1445–1458. ISSN: 1572-8897. DOI: 10.1007/s10910-015-0498-2.
von Steiger, R. and T. H. Zurbuchen (Jan. 2016). "Solar Metallicity Derived from in Situ Solar Wind Composition." In: *ApJ* 816, p. 13. DOI: 10.3847/0004-637X/816/1/13.